The University of Nottingham

MULTI-SCALE MODELLING OF DISCONTINUOUS CARBON FIBRE REINFORCED COMPOSITES

MICHAEL DAVID BOND, MEng. (Hons.)

Thesis submitted to the University of Nottingham
for the degree of Doctor of Philosophy

DECEMBER 2013

Abstract

Discontinuous carbon fibre composites are becoming increasingly popular in the automotive and aerospace sectors, as an alternative to textile-based fibre reinforced composites for both semi-structural and structural components. Materials are highly heterogeneous, with the random architecture leading to uncertainties when modelling and predicting mechanical performance. The microscopic characteristics are known to dominate the strength of the composite, which need to be correctly represented to improve mechanical property predictions at the macroscale.

This thesis presents a multi-scale modelling approach that captures the effects of microstructural (filament level) parameters at the macroscale (component level) to predict the mechanical properties of discontinuous composite materials. In the present work, a continuum damage approach has been used to initiate and monitor failure in the models at all scales, via a user defined material (UMAT), allowing strength predictions to be made for the discontinuous material within the ABAQUS solver. Experimental testing of the material constituents (fibre bundle and matrix materials) has been performed to provide input data for the finite element analyses.

Micromechanical models have been developed to calculate the properties of fibre bundles, which are used directly at the meso and macroscale. Debonding criterion has also been established and validated which has been used to demonstrate that a small interface, with a thickness of only 1% of the fibre radius, can strongly influence the stress transfer between fibre and matrix materials. Interactions between multiple fibre bundles have been considered at the mesoscale, at a range of bundle orientations and separation distances. As the separation distance between the fibre bundles decreased there was an increase in stiffness of the unit cell (~1.9%) across the bundle orientations considered, however, this also coincided with greater stress concentrations (up to 9.6%) being found in the bundles aligned to the direction of loading. These stress concentrations have been used to produce a comprehensive stiffness reduction scheme at the macroscale to account for the 3D nature of the bundle interactions.

A 2D macroscale model is presented for generating discontinuous random fibre architectures consisting of high filament count bundles, with interfacial debonding permitted between the bundle and matrix materials. The fibre bundles are deposited randomly in a 2D plane to provide a representative material. The model has shown that the interface between the bundle and matrix material is critical at short fibre bundle lengths (~5mm) when determining the mechanical properties of the material, with reductions in strength of up to 40% observed at low interfacial shear strengths. The results from the macroscale analysis for discontinuous materials provide predictions within ~10% for tensile stiffness and ~18% for tensile strength when compared with experimental validations.

Acknowledgements

The author wishes to acknowledge the advice and support of his academic supervisors, Dr Lee Harper and Professor Nicholas Warrior. The author gratefully acknowledges the financial support of Bentley Motors Limited, in particular Antony Dodworth for his support of the project.

Special thanks to all the members of the Polymer Composites research group I have been fortunate enough to work with during my time at the University of Nottingham. Thanks also to Roger Smith and Geoffrey Tomlinson for their technical assistance during the practical aspects of this work.

The support and encouragement from my parents, Anne and Andrew, and the rest of my family and friends has been invaluable at all times.

Finally, I would like to thank my girlfriend, Hannah, for the patience, love and support she has given me throughout the past few years.

Contents

Chapter 1 Introduction

1.1 Introduction to polymer matrix composite materials

A composite material is made up of two or more components, which typically comprise a reinforcement material and a binding material. The reinforcement typically has high strength and modulus, with the binding material used to connect the reinforcement material together to permit the transmission of load. Polymer matrix composites (PMCs) can be split into two distinct groups; continuous fibre composites, shown in Figure 1a, and discontinuous fibre composites, shown in Figure 1b. PMCs have become increasingly popular over the past 20 years in the aerospace and automotive sectors, due to developments in raw materials and advances in the manufacturing processes.

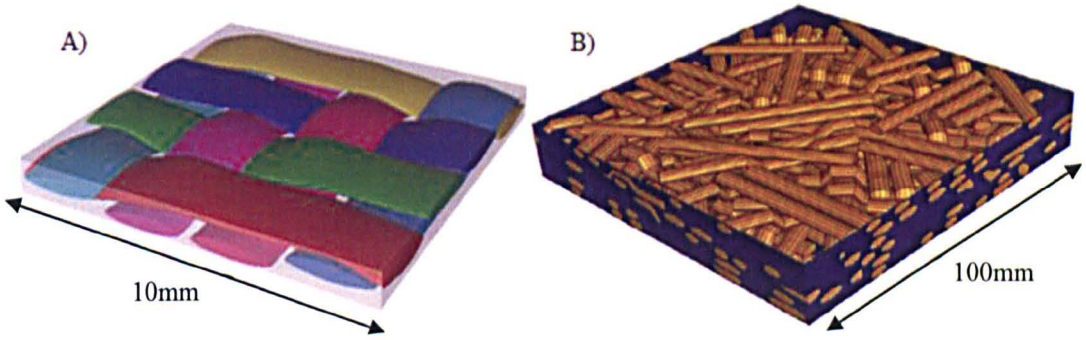

Figure 1 – A) Textile based continuous fibre composite produced by TexGen [1] and B) geometric representation of a discontinuous fibre composite [2].

Currently textile based composites dominate the aerospace market as they offer the greatest specific strength and stiffness properties, with greater repeatability and consistency in their mechanical properties. The repeatable geometry also enables the prediction of mechanical properties when using different lay-ups and configurations, with high levels of accuracy achieved using packages such as TexGen [1] to generate the fibre architecture. Weight savings of 40-60% can be seen for equivalent performance composite components when compared to a metallic counterpart [3]. However, this performance increase comes at a cost, circa £15 per kilogram for the material [4] and between £35-125 per kilogram for the finished part, including manufacturing costs [5]. This has limited the use of carbon-epoxy textile composites to the aerospace and high-end automotive

markets, with production volumes of fewer than 1000 parts per annum. Alternatives to textiles are required if composites are to become a cost effective and viable alternative to metallic materials for the mainstream automotive industry.

Discontinuous fibre composites, such as SMC and BMC, typically cost less to produce than their textile counterparts as they are automated processes that do not require material preparation stages, such as weaving and resin pre-impregnation. The weaving and pre-impregnation required for textiles ramps up the material cost, rendering them unfeasible to use at medium to high production volumes. However, recent developments in discontinuous fibre composites have led to greatly improved mechanical performance characteristics.

1.2 Applications and characteristics of discontinuous fibre composites

Discontinuous fibre composites have been used for over 50 years in a wide variety of applications, with over 80% of the total composite materials used in the automotive industry manufactured from discontinuous fibres [6]. One of the first notable uses in the automotive industry was the fibre glass body panels used in the production of the 1953 Chevrolet Corvette [7]. Discontinuous fibre composites can be split into a number of different categories, and these can be seen in Figure 2, alongside their textile and continuous fibre competitors.

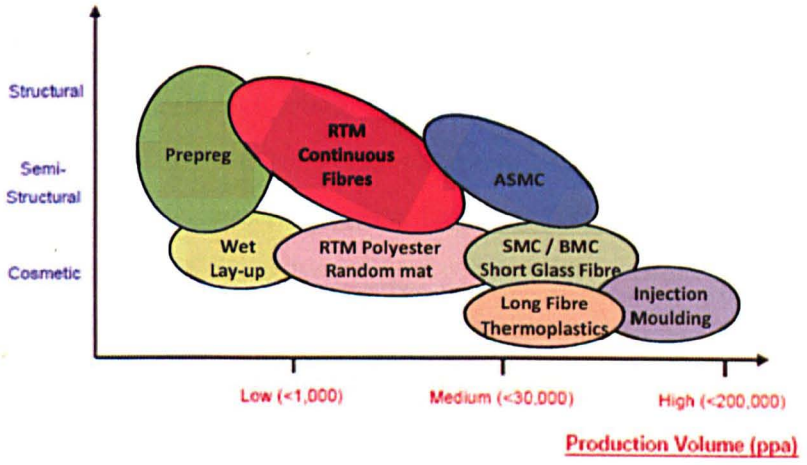

Figure 2 - Mechanical performance vs. production volume for composite manufacturing processes. Modified and reproduced from [8].

Sheet moulding compounds (SMCs) and bulk moulding compounds (BMCs) are made from strands, usually under 50mm in length, of chopped glass in polyester resin and are typically used in cosmetic applications along with a filler – such as calcium carbonate. SMCs and BMCs have short cycle times, low labour requirements and are capable of producing complex shapes. However, they are unsuitable for structural applications due to their relatively low mechanical properties (e.g. E=10GPa, UTS=80MPa), caused by their discontinuous nature, random orientation and low achievable volume fractions; 15-20% for BMCs [9] and 20-30% for SMCs [10, 11]. Advanced SMCs [12] have also been developed, which substitute glass fibres with higher performance, lower density carbon fibres. This improves the mechanical properties of the SMC material (e.g. E=50GPa, UTS=300MPa); however the volume fractions limitations associated with SMCs are still apparent.

Directed fibre preforming (DFP) is an established process [13] which utilizes robotics to produce low cost, low scrap, high volume (>20,000ppa) preform fabrications [14]. Directed fibre preforms are produced by spraying chopped fibres and binder onto a part shaped tool, followed by a resin moulding process to produce the composite component. Mechanical properties are comparable with chopped strand mat at similar fibre volume fractions [15], with wastage levels down from 30wt% to 3wt% [16].

In response to the limitations of SMCs, BMCs and DFP, and the high manufacturing cost and long cycle times associated with textile reinforcements, materials such as Directed Carbon Fibre Preforming (DCFP) [17] have been developed. DCFP utilises automation to provide low levels of touch-labour, design flexibility and consistency when forming complex shapes [3]. This can provide a cost saving of up to two orders of magnitude when compared to pre-impregnated textile composites [18]. Currently, discontinuous carbon composites are used commercially for semi-structural applications on the Dodge Viper [19], whilst 2009 saw the first structural application within the aerospace industry - producing window surrounds on the Boeing 787 Dreamliner [20].

DCFP generates a lot of interest from the automotive sector, as an alternative to aluminium and textile-based fibre reinforced composites. The potential use for structural applications has also been investigated within the aerospace industry [21, 22] and in large wind turbine applications [23, 24]. Tensile stiffness and strength values for DCFP are typically approaching 50GPa and 500MPa (55% V_f) for random fibre architectures [25, 26], and 80GPa and 1000MPa (55% V_f) for aligned fibre architectures [27], making these materials suitable for secondary and primary structures. However, this increase in performance by orientating the chopped tows leads to substantially longer cycle times [28], preventing use in high volume production. DFP and DCFP have been shown to be cost effective at annual production volumes of up to 50,000 parts per annum [29, 30].

Industrial development of DCFP has continued [31-35], with the most recent advancement known as the BRAC3D process (Bentley-RayCell Automated Carbon Composite Charge Deposition) [36]. DCFP relies on a vacuum to adhere the fibres to the tool shape, making it challenging to manufacture thick-section and deep-draw parts. Alternatively, the BRAC3D process produces a powdered epoxy charge, which is sprayed simultaneously in an air stream with the strands of chopped carbon directly onto a 3D tool face from the arm of an industrial 6-axis robot. The BRAC3D process provides greater control of fibre placement, with low void levels observed in the material as the epoxy is evenly distributed across the component as it deposited with the fibre bundles onto the tool face [36]. In addition to this, cycle time savings of approximately 45% have been achieved when comparing the BRAC3D process to conventional DCFP [36]. These recent developments have led to a greater acceptance that discontinuous materials are a viable alternative to their textile counterparts when producing semi-structural and structural components.

The biggest barrier to the acceptance of discontinuous materials is material variability and the associated problems in predicting their performance, which prevents designers using them with confidence. In addition to this, the perception is that the mechanical properties of discontinuous materials are too low. This isn't the case for tensile stiffness, which has been seen to be consistent (coefficient of variation COV ~10%) and retention values of over 90% quoted compared to

continuous fibre counterparts [27]. Conversely, ultimate tensile strength (UTS) values have been shown to vary by as much as 50% [27], and strength retention is currently limited to a maximum of ~60% [17]. However, it has been shown in [37] that with efficient design, discontinuous materials can potentially replace woven fibre architectures with almost no reduction in performance, particularly for stiffness driven components in the automotive industry.

1.3 Modelling of discontinuous composite materials

Discontinuous materials have historically suffered from poor repeatability, leading to variable part quality. Inconsistent volume fractions through the part and the presence of voids have rendered it difficult to validate their usage in structural applications. Recent advancements in discontinuous composites have allowed fibre architectures to be tailored with varying fibre length, bundle size, alignment and fibre volume fraction [38, 39]. With this increased control over discontinuous materials, the performance gap to continuous materials has been reduced, potentially increasing the usage of discontinuous materials in structural applications. With these recent developments, notably in ASMC (Advanced Structural Moulding Compound) [40-42] and DCFP [36, 38, 39], there is a need for a reliable predictive model to enable designers to efficiently design discontinuous composite components.

Textile fabrics are repeatable and can thus be modelled as a relatively small periodic unit cell; discontinuous fibre composites are highly heterogeneous and hence non-repeating. Figure 1b shows the variation in fibre bundle architecture that can be observed across a discontinuous composite, with a much larger geometric entity required to capture this material heterogeneity. In addition to this, there is currently a lack of understanding of discontinuous materials with complex stress transfer mechanisms dictating material performance. Stress concentrations at bundle ends and fibre cross-overs through the thickness of the material greatly influence the performance characteristics of the discontinuous composite [43], and these factors are not always considered in macroscopic models.

A review in [44] has shown that conventional analytical models for predicting tensile properties are inaccurate, since they overlook the high levels of heterogeneity of discontinuous architectures. This heterogeneity exists particularly if they consist of high filament count bundles and the component thickness is of the same order of magnitude as the reinforcement (<10mm). Numerical models are being developed at the macro mechanical (coupon) scale [2, 36, 45, 46] using random sequential adsorption (RSA) schemes to introduce material variability into the model, which give predictions within ~10% for tensile stiffness compared with experimental validations. Few authors however, have attempted to predict the ultimate strength in this way, because of the complex array of failure mechanisms associated with discontinuous carbon fibre composites.

The microscopic characteristics of the material have been shown to dominate the strength of the composite at the macro-scale [47, 48]. In all composite materials the load is transferred between the reinforcement and matrix by shear [49, 50], so the interface between the two constituents is critical when predicting the performance of the material. Each component made from discontinuous fibres is unique; no fibre bundle architecture is the same from one component to the next. The presence of multiple bundle ends and the relationship at the interface between bundle and matrix becomes increasingly important when determining the material stiffness and strength. Some existing models only consider the degradation of each constituent material, neglecting the other potential failure mechanisms such as interfacial debonding and bundle pull-out, without fully understanding their significance. More information is therefore needed from the microscale and mesoscale, including fibre-matrix and bundle to bundle interactions, to provide a material model of improved accuracy, which can be used to drive future process and material developments.

1.4 Project overview

The research in this thesis was conducted as part of the RayCell project, funded by Bentley Motors Ltd. The aim of the project was to develop the BRAC3D manufacturing process for the production of high performance discontinuous carbon composite components for use, primarily, in automotive applications. To

complement the process development, the work in this thesis develops a multi-scale material model to characterise the mechanical performance of discontinuous fibre composites.

Multi-scale modelling allows the prediction of material properties at the macroscale, based on knowledge of the relationships obtained at the mesoscale, and prior to that at the microscale. At each scale there are parameters that can influence the mechanical performance of the discontinuous material. For example, at the microscale the level of adhesion between fibre and matrix needs to be established, whilst at the mesoscale bundle-bundle interactions must be considered to quantify any stress concentrations that may arise due to the bundle architecture. A schematic detailing the multi-scale modelling scheme used in this thesis can be seen in Figure 3.

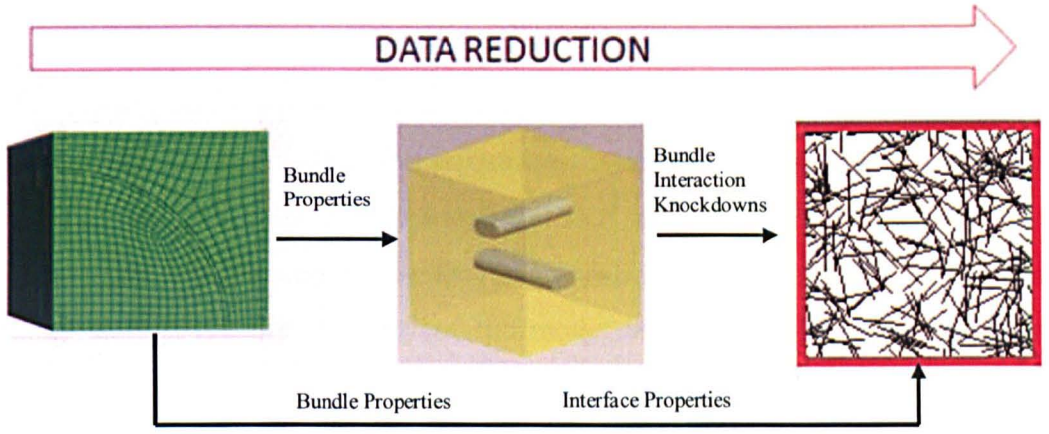

Figure 3 - Multi-scale modelling scheme adopted to characterise the discontinuous composite material, (left to right – micro, meso and macroscale).

1.5 Theme of work

1.5.1 Microscale modelling

A single fibre composite model has been developed to analyse the influence of the interfacial strength between the filament and matrix. The methodology used at this scale will be used to simulate debonding at the macroscale between the carbon bundles and epoxy resin. The second study predicts the ineffective length of a broken fibre in a two fibre composite material for the carbon fibres and epoxy

resin used in this analysis. These models analyse how stress is redistributed around the site of a fibre break, with a full factorial study performed to look at the influence of the moduli of the constituents on the fibre ineffective length. In the final study, periodic unit cells with a hexagonal packing arrangement have been developed to predict the mechanical properties of fibre bundles at a range of bundle volume fractions. The calculated bundle properties will be used in the mesoscale and macroscale analyses.

1.5.2 Mesoscale modelling

The first study at the mesoscale analyses the influence of the cross-sectional shape of the fibre bundle when transferring load between two bundles in a unit cell. The finite element study is performed to predict the bundle ineffective length of a fractured bundle and stress concentration factors (SCFs) in the neighbouring bundle as the aspect ratio of the bundle is increased, similar to the fibre ineffective length study at the microscale.

The second study at the mesoscale looks at the interaction of the fibre bundles at a range of angular orientations and separation distances, allowing the calculation of SCFs in the fibre bundles. SCFs will be used to produce a stiffness reduction scheme that will be adopted at the macroscale level at the bundle cross-over points to improve the accuracy of the model when predicting the mechanical properties of discontinuous composite materials.

1.5.3 Macroscale modelling

A macroscale model has been developed to predict the mechanical properties of discontinuous composite materials. The 2D fibre bundle architecture from the model in [27] has been adapted as a starting point to produce the macroscale model, which allows high volume fraction (~50% V_f) RVEs to be produced that are computationally inexpensive. The fibre bundle properties used in the analysis have been calculated at the microscale, with the assumption that the fibre bundles behave as a unidirectional composite material. An unstructured free meshing strategy has been developed to allow debonding between the fibre bundle and matrix materials. Debonding criterion has been established at the microscale, with

connector elements used to tie the fibre bundles and matrix together to allow the separation of the materials once a failure threshold has been exceeded.

A modified Delaunay meshing algorithm has been utilised in the model, with mesh refinement techniques used to improve the quality of the mesh along the length of the fibre bundles and at the points of bundle intersection. Mesoscale models were developed to look at the interaction between two fibre bundles in a 3D unit cell, with SCFs calculated at the bundle intersection points. These SCFs have been used to produce a stiffness reduction scheme at the bundle crossovers to improve the accuracy of the 2D models. The mechanical properties obtained from the model will be validated against existing analytical and numerical models for discontinuous materials at a range of fibre volume fractions, bundle lengths and interfacial shear strengths. The user interface for the developed program is shown in Appendix B.

1.5.4 Material characterisation

Individual fibres (micro), fibre bundles (meso and macro), and epoxy matrix (micro, meso and macro) materials are used in the analysis contained in this thesis. An experimental testing procedure has been adopted to determine the mechanical properties of the materials under different loading conditions. Initially, the properties of individual filaments are derived from manufacturer's data sheets, before experimental tests are performed to determine the tensile strength of unidirectional fibre bundles.

The matrix used in the development of the BRAC3D process [36] was a prototype material, with little data available for the mechanical properties of the material, therefore experimental testing was essential to provide the necessary inputs for the FE models. Tensile, compressive and in-plane shear tests were conducted to determine the modulus, yield stress and failure stress/strain of the matrix material for each load case.

To capture the behaviour of the materials and to monitor and track damage in the FE analysis, a User Defined Material (UMAT) model has been developed in FORTRAN that runs in conjunction with the models in ABAQUS/Standard.

Chapter 2 Literature Review

2.1 Damage modelling and failure criterion for composite materials

The worldwide failure exercise (WWFE) [51-53] was an extensive study that looked at existing failure theories for composite materials. It was conducted in three parts; prediction, experiments and comparisons. A summary of the WWFE can be found in [54], with recommendations for composite designers on which failure criterion to select and the influence on results obtained in numerical studies. Failure theories can be split into two categories; independent and interactive. Independent failure theories consider each mode of failure individually, each with its own distinctive failure criterion, before determining whether the material has failed. Interactive failure theories use a single criterion, combining modes of failure to establish if the material has failed [55]. Independent and interactive failure criterions will be reviewed in this section, allowing for appropriate criterion to be selected for the FE modelling work contained in this thesis. Stiffness reduction schemes will also be discussed.

2.1.1 Stiffness degradation in composite materials

Damage modelling consists of two stages; the detection of damage via the use of appropriate failure criterion and the degradation of local material properties to simulate damage initiation and propagation. Rujiter [56] highlighted the importance of the prediction of initial damage, with most high-performance applications of composite materials associated with brittle failure mechanisms.

Continuum damage mechanics (CDM) is often used to model damage in composite materials, where the effects of damage are analysed by using degraded properties in regions where the material has found to have failed [56]. Blacketter et al [57] used CDM to model failure in textile composites, with knockdowns applied to the stiffness properties of the material to simulate damage onset and progression. It has since become common practice in simulating material damage in composites to reduce the stiffness (or stiffness in a certain direction) to a near zero value [36, 55, 58-61]. The stiffness of the material is reduced to a marginal value, and not zero, to prevent instabilities in the FE analysis.

Once damaged, the failure criterion has been satisfied, there are generally two approaches for stiffness reduction - selective and non-selective methods. For non-selective reduction, the stiffness is reduced to a near-zero value irrespective of the failure direction. For isotropic materials, such as polymer resin, damage is independent of the material orientation, so a non-selective stiffness reduction can be applied regardless of the failure criterion used. Typically a degradation factor of 0.01 is used on the materials properties [36, 61], which reduces all tensile, compressive and shear stiffness's to 1% of their initial value. Non-selective stiffness reduction schemes can also be used for anisotropic materials where the failure direction cannot be determined from the failure criterion, i.e. Hoffman, Tsai-Hill and Tsai-Wu.

Selective stiffness reduction schemes only reduce the stiffness in the direction in which the material has failed. In composite materials, transverse failure of the material can occur without breaking the longitudinal fibres, which does not completely destroy the load bearing capability of the material [61]. Selective stiffness reduction schemes can be used if the failure criterion indicates the failure direction to the user, such as Maximum Stress criterion (MSC). Blacketter [57] used the selective stiffness reduction scheme with MSC, with degradation factors assigned to each mode of failure. If a particular failure mode was met, i.e. tensile failure in the 1-direction, the relevant stiffness parameters were reduced accordingly.

In [61], if the failure was detected in the transverse direction, the transverse modulus was reduced to 1% of its original value, but the longitudinal modulus remained unchanged. The shear modulus was also degraded, but a degradation factor used of 0.2 was used as opposed to 0.01, with the composite able to support some shear stress along the length of the fibre due to friction between the fibre and matrix [57, 62]. A similar methodology was adopted in [36], with the degradation factors, $d_E = 0.01$ and $d_G = 0.2$, assigned to apply knockdowns to the relevant terms in the stiffness matrix, Equation 1, once the material was damaged.

$$[C] = [S]^{-1} = \begin{bmatrix} \frac{1}{d_E E} & \frac{-v}{d_E E} & 0 \\ \frac{-v}{d_E E} & \frac{1}{d_E E} & 0 \\ 0 & 0 & \frac{1}{d_G G} \end{bmatrix}^{-1}$$

Equation 1

Reduction of local material properties allows damage to be monitored and tracked across a composite material. With the complex array of failure mechanisms associated with composite materials, and in particular discontinuous composite materials, it is beneficial to know dominant failure modes. If the mode of failure can be identified, it is possible to identify ways to improve the mechanical properties of the composite.

2.1.2 Failure theories for fibres and fibre bundles

Carbon fibres are transversely isotropic, with a much greater stiffness along the axis of the fibre (E_1) compared to the off-axis, transverse properties ($E_2 = E_3$). It is therefore necessary to define the modulus and failure strength in relation to the material orientation, to allow accurate prediction of the failure of the fibres in FE models. At the mesoscale, fibre bundles are often treated as a unidirectional composite [61], the properties of which can be determined by using Rule of Mixtures (ROM) or by performing FE analysis on an RVE of a fibre bundle, as in section 4.1.3. The behaviour of a fibre bundle is similar to that of a single fibre [63, 64],with the same failure criterion applicable for both filaments and bundles. It was shown in [61] that Maximum Stress criterion, Hoffman criterion, Tsai-Hill criterion and Tsai-Wu criterion are all appropriate failure models for fibres and fibre bundles. The limitations of each of these failure criterions will be discussed in this section. For simplicity, the 2D case of each failure criterion has been selected for comparison.

Maximum Stress criterion

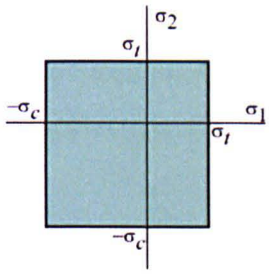

Figure 4 - Maximum Stress criterion failure envelope for a 2D component [65].

The Maximum Stress criterion (MSC) for composites was initially developed by Jenkins [66, 67] and is typically used to predict the failure of brittle materials, such as fibres and bundles [36, 60, 61, 68, 69]. A material is assumed to have failed if the principal stress, σ_1 or σ_2, exceeds σ_t or σ_c; the failure strength in tension and compression respectively. It should be noted that different values can be specified for σ_t and σ_c based on the orientation. MSC is an independent failure criterion, as it assesses the stress state in each principal direction before determining if failure has occurred in the material – no interaction between stresses is considered. For example, if a composite reached 99% of its transverse tensile strength, it would also be expected to support 99% of its in-plane shear strength without failing [55]. As the failure strength of carbon fibres is much greater along its axis than in the transverse direction ($\sigma_1 >> \sigma_2$), MSC is an appropriate criterion to define the onset of failure in the material. Equation 2 outlines the bounds for the principal stresses, σ_1 and σ_2, for which failure will not occur, with Equation 3 highlighting the failure criterion used for shear failure.

$$-\sigma_c < \{\sigma_1, \sigma_2\} < \sigma_t \qquad \text{Equation 2}$$

$$|\tau_{12}| \geq \tau_{12u} \qquad \text{Equation 3}$$

Maximum Strain criterion

The Maximum Strain criterion [67] is analogous to MSC, with the failure determined by the strains in each direction of the material. It is an independent failure theory and therefore has the same limitations as MSC. Equation 4 shows the bounds of the principal strains in tension, compression and shear.

$$-\varepsilon_c < \{\varepsilon_1, \varepsilon_2\} < \varepsilon_t \;\; ; \;\; |\gamma_{12}| \geq \gamma_{12u} \qquad \text{Equation 4}$$

For brittle materials, such as carbon fibres and bundles, a stress-based criterion is primarily used as the material behaviour is linear elastic up until the point of failure. Maximum strain criterion is often used for ductile materials where plastic deformation occurs once the material has exceeded its yield strength.

Tsai-Wu criterion

Tsai-Wu theory [70] was developed based on experimental observation and curve fitting. The values of the tensile, compressive and shear strengths of the composite in its principal directions need to be determined by experimental testing in order to use the Tsai-Wu criterion [71]. It allows different tensile and compressive failure strengths to be assigned, unlike Tsai-Hill criterion, and evaluates the interaction between the principal stresses before determining if failure has occurred. Equation 5 shows the mathematical function used to define the Tsai-Wu criterion.

$$F_1\sigma_1 + F_2\sigma_2 + F_{11}{\sigma_1}^2 + F_{22}{\sigma_2}^2 + F_{66}{\tau_{12}}^2 + 2F_{12}\sigma_1\sigma_2 = 1 \qquad \text{Equation 5}$$

F_1, F_2, F_{11}, F_{22}, F_{66} and F_{12} are constants derived using the strengths of the composite in each principal direction, with unique values permitted for tensile and compressive failure. σ_{1ut}, σ_{1uc}, σ_{2ut} and σ_{2uc} are the tensile and compressive strengths in the 1 and 2 directions, with τ_{12u} used to define the shear strength of the composite material and σ_{biax} defining the strength of the material under equal biaxial loading. The constants are defined as follows:

$$F_1 = \frac{1}{\sigma_{1ut}} + \frac{1}{\sigma_{1uc}} \; ; \; F_2 = \frac{1}{\sigma_{2ut}} + \frac{1}{\sigma_{2uc}} \; ;$$

$$F_{11} = \frac{1}{\sigma_{1ut}\sigma_{1uc}} \; ; \; F_{22} = \frac{1}{\sigma_{2ut}\sigma_{2uc}} \; ; \; F_{66} = \frac{1}{{\tau_{12u}}^2} \; ;$$

$$F_{12} = \frac{1}{\sigma_{biax}^2}\left[1 - \left(\frac{1}{\sigma_{1ut}} + \frac{1}{\sigma_{1uc}} + \frac{1}{\sigma_{2ut}} + \frac{1}{\sigma_{2uc}}\right)\sigma_{biax} + \left(\frac{1}{\sigma_{1ut}\sigma_{1uc}} + \frac{1}{\sigma_{2ut}\sigma_{2uc}}\right)\sigma_{biax}^2\right]$$

The value of F_{12} is usually estimated to avoid the need for biaxial tests to be conducted on the composite material, with Tsai and Hahn [72] deriving the

approximation shown in Equation 6, with an average value of f^* = -0.5 typically used to predict failure [73].

$$F_{12} = f^*\sqrt{F_{11}F_{22}} \quad \text{where } -1 \leq f^* \leq 1 \qquad \text{Equation 6}$$

Tsai-Wu essentially fits an ellipsoid to the uniaxial strengths of the composite material, with it noted in [55] that this could lead to over-predictions in strength when the material is subjected to biaxial loading. Based on these findings, Tsai-Wu will not be considered for predicting the failure of the fibres and bundles in this thesis.

Hoffman criterion

Hoffman criterion [74] is an interactive failure criterion that has no unknown interaction term, such as a biaxial strength component which is required for Tsai-Wu criterion. Separate tensile, compressive and shear strengths can be specified for all material orientations, with experimental testing required to determine these properties [71]. The Hoffman criterion for 2D composites is shown in Equation 7, with the constants C_1–C_3 outlined below. σ_{1ut}, σ_{1uc}, σ_{2ut} and σ_{2uc} are the tensile and compressive strengths in the longitudinal (1) and transverse (2) directions, with τ_{12u} used to define the shear strength.

$$C_1(\sigma_1 - \sigma_2)^2 + C_2(\sigma_1 + \sigma_2) + C_3{\tau_{12}}^2 = 1 \qquad \text{Equation 7}$$

The constants C_1–C_3 are defined as follows.

$$C_1 = \frac{1}{2\sigma_{1ut}\,\sigma_{1uc}}\,;\, C_2 = \left(\frac{1}{2\sigma_{2ut}} - \frac{1}{2\sigma_{2uc}}\right)\,;\, C_3 = \frac{1}{{\tau_{12u}}^2}$$

Hoffman criterion was used to model fibre bundle failure by Huysmans et al. [75], with it stated that if small fibre twist is ignored then the fibre bundle can be treated as a unidirectional reinforced transversely isotropic rod. Zhao et al [61] also used Hoffman criterion to define the failure in fibre bundles.

Tsai-Hill criterion

Tsai [76] applied the criterion developed by Hill [77] for anisotropic materials to the failure of composite materials and found that this approach is suitable for predicting the onset of failure in fibre bundles that contain fibre and matrix materials. The Tsai-Hill failure criterion developed in [76] is shown in Equation 8. Tsai-Hill is an interactive failure criterion that considers the stresses in all principal directions, before evaluating if failure has occurred in the composite. However, the accuracy of Tsai-Hill is limited as it does not allow for different tensile and compressive failure thresholds to be considered, as in Tsai-Wu, with only one failure stress value permitted for each principal direction. It was noted in [55] that although Tsai-Hill does not distinguish between tensile and compressive failure, it is possible to assess the contribution of each principal stress on the failure of the composite.

$$\left(\frac{\sigma_1{}^2}{\sigma_{1u}{}^2} - \frac{\sigma_1\sigma_2}{\sigma_{1u}{}^2} + \frac{\sigma_2{}^2}{\sigma_{2u}{}^2} + \frac{\tau_{12}{}^2}{\tau_{12u}{}^2}\right) = 1 \qquad \text{Equation 8}$$

Note: σ_{1u} and σ_{2u} are the strengths in the 1 and 2 directions, with τ_{12u} defining the shear strength of the composite material.

Zhao et al. [61] performed a study to look at the influence of using different combinations of failure criterion on the mechanical properties of a unit cell containing fibre bundles and matrix materials. MSC, Tsai-Wu [70] and Hoffman [74] criterion were used to model the carbon fibre bundles in the analysis. MSC, Tsai-Wu and Hoffman are all appropriate failure criterion for fibres and fibre bundles, however, the way in which they determine if failure has occurred varies. Tsai-Wu and Hoffman employ a non-selective stiffness reduction scheme once failure has been reached, whereas MSC allows a selective stiffness reduction scheme to be applied to the failed elements in the model. Full details on selective and non-selective stiffness reduction schemes can be found in section 2.1.1. The study in [61] found that Tsai-Wu and Hoffman criterion models failed prematurely at approximately 25% of the load required to cause failure in the MSC models in textile materials; attributable to the non-selective stiffness reduction scheme used by these models. Based on the findings in [61], MSC has

been selected to predict the onset of damage in fibres and fibre bundles in this thesis. It has been chosen as it allows different modulus values to be specified for each principal direction, essential for the transversely isotropic fibres and bundles, in addition to allowing a selective stiffness reduction scheme to be adopted.

2.1.3 Review of appropriate epoxy matrix failure criterion

The polymer resins used to bond fibres and fibre bundles together in composites are typically isotropic materials, with the same modulus and failure strengths in all directions. Matrix materials can behave in a brittle manner like fibres and bundles, but some matrix materials can exhibit non-linearity before they completely fail. Maximum Stress, von Mises and Drucker-Prager failure criterions were recommended by Zhao et al. [61] for polymer matrix materials.

Maximum Stress and Maximum Strain criterion

Full details of how Maximum Stress and Maximum Strain criterion determine failure is outlined in section 2.1.2. For the case of an isotropic material the failure strengths (or strains) in each direction are equal.

Tresca (Maximum Shear Stress) criterion

Tresca, or Maximum Shear Stress, criterion can be used to model the failure of ductile, isotropic materials, such as polymer resins. Figure 5 graphically shows the yield surface defined by the Tresca criterion outlined in Equation 9.

$$|\sigma_1| \leq \sigma_y; \quad |\sigma_1 - \sigma_2| \leq \sigma_y; \quad |\sigma_2| \leq \sigma_y \qquad \text{Equation 9}$$

Tresca is usually regarded as conservative when predicting the yield surface of an isotropic material, with the shape of the Tresca yield surface an irregular hexagon that is circumscribed by the von Mises criterion.

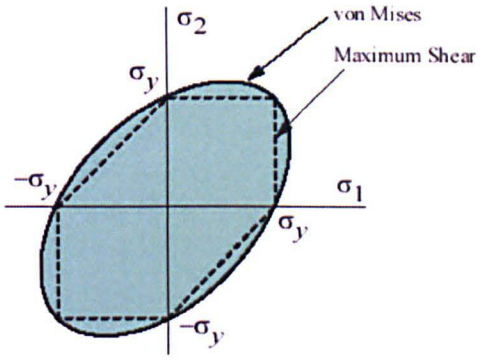

Figure 5 - von Mises and Tresca criterion failure envelopes for a 2D component [78].

von Mises criterion

The von Mises criterion can be used to predict the yield of ductile, isotropic materials. Equation 10 defines the yield surface for von Mises criterion, in 2D, with Figure 5 showing a comparison of the Tresca (Maximum Shear) and von Mises yield surfaces.

$$\sqrt{\frac{1}{6}(\sigma_1 - \sigma_2)^2} = \frac{\sigma_y}{\sqrt{3}} \qquad \text{Equation 10}$$

von Mises is an interactive failure criterion, where the principal stresses in all directions are assessed before determining if the yield stress of the material has been exceeded. However, the von Mises criterion is still limited, with no distinction made between tensile and compressive failure.

Drucker-Prager criterion

The Drucker–Prager failure criterion [79], sometimes referred to as the extended von Mises model, was originally developed for plastic deformation of soils, but has since been applied to polymers and other pressure dependent materials. The Drucker–Prager model is used to model frictional materials, which exhibit pressure dependent yield or failure as the material becomes stronger as the pressure increases [61]. It is also ideally suited for materials where the compressive strength is greater than the tensile strength, such as polymer resins, as the compressive and tensile strengths can both be specified, σ_c and σ_t respectively. The Drucker-Prager yield surface can be defined in many ways, but

to allow direct comparison to von Mises yield criterion it is defined here in terms of the principal stresses of the 2D isotropic material:

$$\sqrt{\frac{1}{6}(\sigma_1 - \sigma_2)^2} = A + B\,(\sigma_1 + \sigma_2) \qquad \text{Equation 11}$$

The constants A and B in Equation 11 are defined below.

$$A = \frac{2}{\sqrt{3}}\left(\frac{\sigma_c \sigma_t}{\sigma_c + \sigma_t}\right) \; ; \; B = \frac{1}{\sqrt{3}}\left(\frac{\sigma_t - \sigma_c}{\sigma_c + \sigma_t}\right)$$

Zhao et al [61] compared the response of a unit cell, with Maximum Stress criterion, von Mises and Drucker-Prager used to define failure in the matrix. The load-strain curves obtained from the numerical study are shown in Figure 6. The failure point of the unit cell varies significantly depending on the criterion used for the matrix material, with Drucker-Prager providing the highest and von Mises the lowest strength prediction. It was suggested by Edgren et al [80] that von Mises or Drucker-Prager failure criterions were best suited to matrix materials when modelling a E-glass/vinylester composite, based on comparisons with experimental test results.

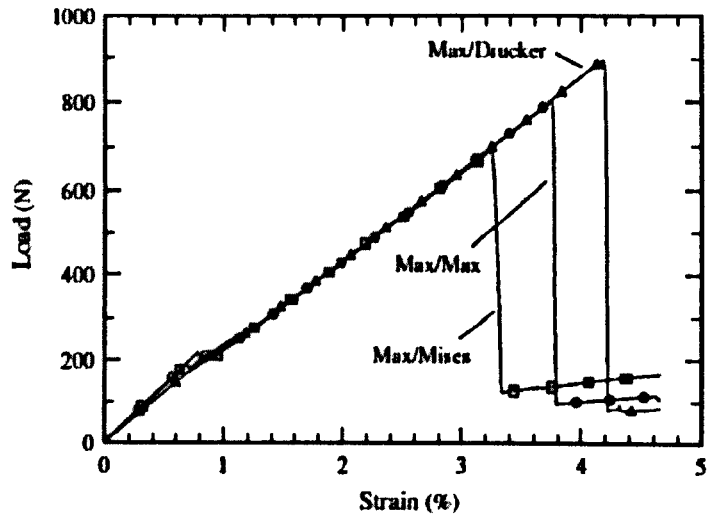

Figure 6 - Comparison of load-strain curves for the different failure criterion used for matrix material in [61].

It is important to select a failure criterion that is suitable for isotropic materials, with Drucker-Prager, von Mises and MSC used to evaluate epoxy resin failure in [61], and von Mises also used in [47]. Drucker-Prager and von Mises employ non-selective reduction schemes, where the stiffness is degraded to a near zero value regardless of the failure direction. Non-selective failure criterions calculate whether or not an element has failed by combining the stresses in each principal direction, allowing failure to be determined with one simple calculation. In contrast to this, MSC considers the stress in each direction independently before determining if failure has occurred, without any consideration for the interaction between the principal stresses.

The von Mises failure criterion was selected for the DLS 1776 epoxy resin for the analysis contained in this thesis as it is widely used in the literature for isotropic matrix materials. The equation used for 2D analysis can be seen in Equation 10, with the criterion for 3D analysis detailed in Appendix C. When implementing the von Mises failure criterion, a yield function (σ_y) is required in order to initiate when the elements begin to behave plastically in tension. Once the tensile yield criterion has been exceeded, a plasticity softening law is applied to gradually reduce the stiffness of the element until final failure occurs. Implementation of this stiffness reduction is discussed further in the UMAT development - section 3.2.

2.2 Review of existing single fibre composite models

2.2.1 Single fibre composite failure mechanisms

The bonding between the fibre and matrix is critical in all composite materials when determining the mechanical properties. Many authors have attempted to characterise the bonding relationship between fibre and matrix by analysing a single fibre embedded in a matrix region. A full review was conducted by Goh et al. [81] and a flow chart highlighting these failure mechanisms is shown in Figure 7. Initially the stress transfer between the matrix and fibre is elastic, and the failure of the system can progress in two ways from this point. The matrix may be

brittle and fail elastically, shown in Figure 8, or alternatively the matrix will reach its yield point before exhibiting plastic behaviour.

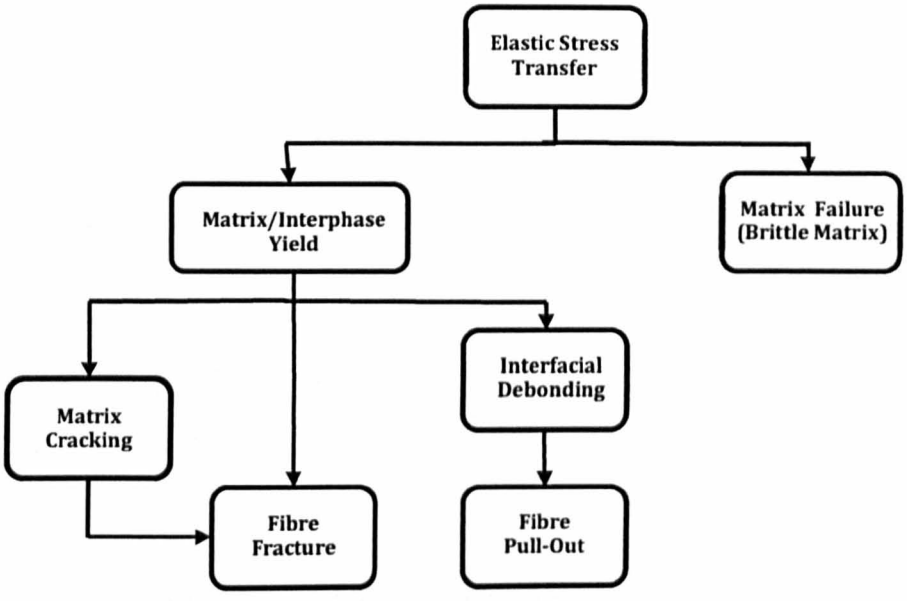

Figure 7 - Potential failure mechanisms for single fibre composite systems

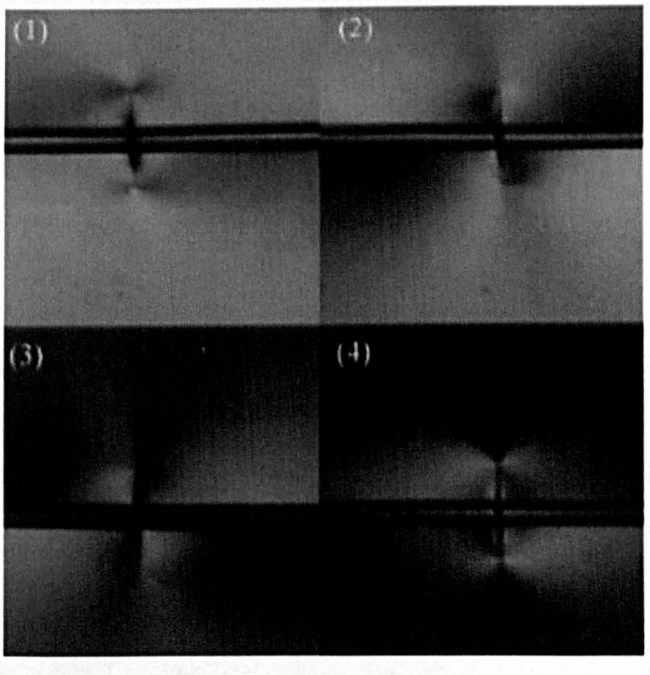

Figure 8 - Development and progression of matrix cracks of an α-alumina fibre in epoxy resin [82]. Images 1 and 4 are bright field and dark field images, and images 2 and 3 are greyscale images at 0.188% applied strain.

From this point forward, there are multiple factors that can influence the failure mechanism of the single fibre system. For experimental coupons, the composite

material will inherently contain imperfections. Matrix voids may be present in the sample, which would increase the likelihood of matrix cracking [83]. Alternatively, the fibre may have been damaged in the manufacture of the sample, or during handling, and this could result in fibre fracture. An image showing fibre fracture in a glass fibre composite is shown in Figure 9.

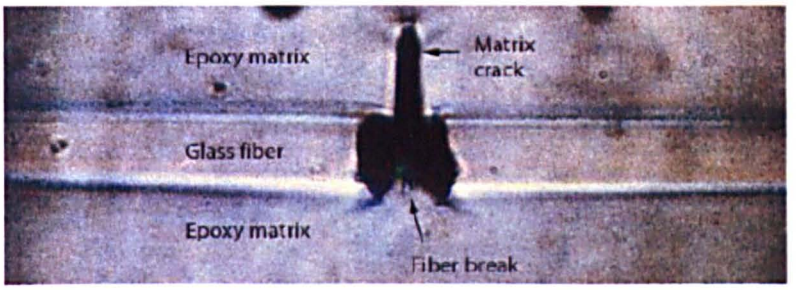

Figure 9 - Fibre break in a glass fibre-epoxy composite system [84].

Figure 10 shows the potential failure mechanisms in a unidirectional composite material based on the level of adhesion between fibre and matrix. Poor adhesion results in fibre-matrix debonding, with intermediate adhesion reducing the amount of debonding in the model, thus it is more likely fibre fracture will occur. With strong adhesion between fibre and matrix, very high stress concentrations will be apparent around the site of a fibre break, resulting in brittle failure of the composite due to failure in the resin material [85].

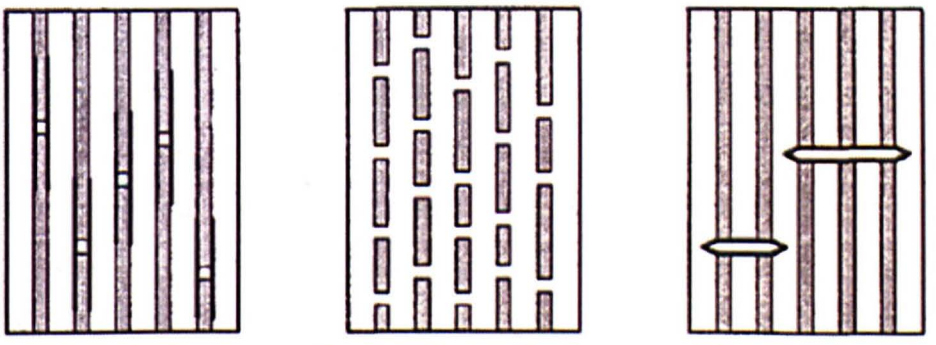

Figure 10 - Graphical representation of failure in continuous fibre composite materials based on the levels of adhesion between fibre and matrix [85].

For short fibre lengths, the contact surface area between fibre and matrix is small, increasing the likelihood of fibre pull-out. In addition to this, if the surface

adhesion is poor between the fibre and matrix, either due to coatings or the lack of sizing applied to the fibre, then the fibre is likely to debond and pull-out will occur. The level of fibre-matrix adhesion is determined by the amount of reactive groups on the surface of the fibre and it has been shown that the surface treatments can greatly influence the failure process in composite materials. It was found in [85] that with an oxidative surface treatment (10% of the fibre diameter) there was a substantial decrease (~60%) in the debonded length when compared to fibres with no surface treatments, indicating an improvement in the fibre/matrix interface strength.

Manufacturing defects, material imperfections and the level of fibre-matrix adhesion will contribute to which failure mechanism is observed in a single fibre composite system. However, if a finite element approach is taken, then the failure mechanism of the system becomes more controllable. The user can control the applied boundary conditions, as well as the utilisation of element elimination techniques to simulate fibre fracture, previously used in [86]. With this greater control, it is possible to study the effect of these parameters independently, allowing optimisation of composite materials at the microscale level.

2.2.2 Interfacial debonding

The single fibre fragmentation (SFF) test is often used to obtain information about the interface between fibre and matrix in a composite material. It is a simple test in which a single filament is embedded in a resin dog-bone specimen before being subjected to a tensile load. When the shear stress transferred to the fibre through the interface reaches the breaking stress of the fibre; fibre failure occurs. If the applied stress on the sample is increased after this point then the fragmentation process continues, until the fibre fragments reach a length where the transferred stress from matrix to fibre is insufficient to cause fibre fracture [85]. A common experimental set up for the single fibre fragmentation test can be seen in Figure 11.

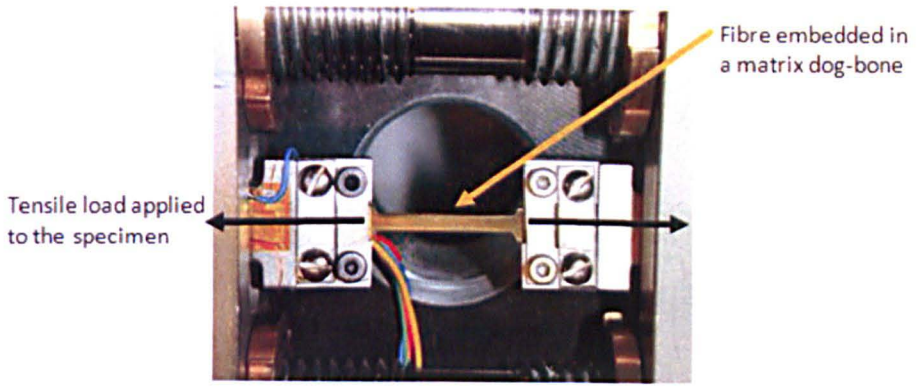

Figure 11 - Schematic of single fibre fragmentation test, reproduced from [84].

By analysing the length of the fibre fragments in the tensile sample, the interfacial shear strength (ISS) between fibre and matrix can be calculated. Short fibre fragments imply stress transfer by a high interfacial shear stress; therefore high ISS. Long fibre fragments indicate stress transfer by a low interfacial shear stress; attributable to a low ISS or yielding matrix [85]. The values obtained in the literature for the ISS range between 20MPa and 70MPa [47, 87-93], based on the material constituents used in the model. For a carbon fibre composite with a strong interface, the shear stress found in the interface approached the resin shear yield strength (67MPa), whereas in a weaker interface model the obtained shear stress was much lower (33% less – 45MPa), attributable to fibre debonding [87].

Debonding is likely to occur at the site of a fibre fracture, or fibre end, in the material, with Figure 12 showing the debonding length along the fibre as the fibre and matrix begin to separate. When debonding occurs in a composite, the load bearing capability of the material is reduced as stress cannot be transferred from the matrix to the fibre in the debond zone. The application of coatings to fibres reduces the debonding length to ensure there is strong adhesion between fibre and matrix, which will therefore increase the strength of the composite. The parameters which influence the rate of debonding will be investigated at the microscale, with matrix plasticity, interface strength and fracture toughness considered in the analysis.

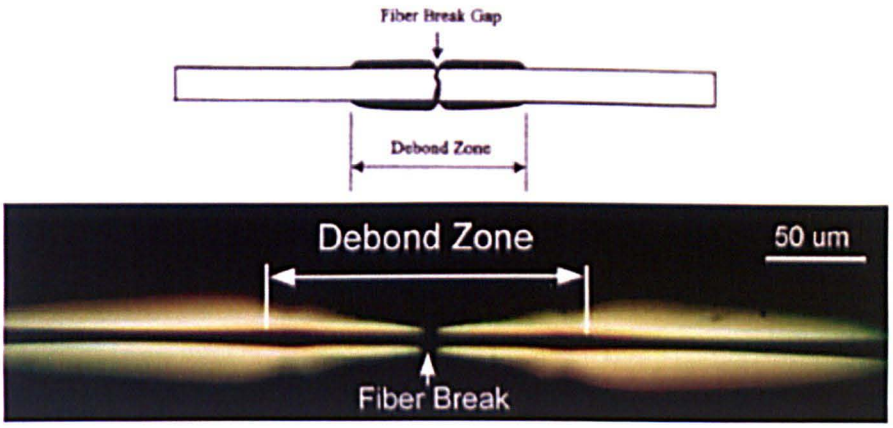

Figure 12 - Debonding from around the site of a fibre fracture for an AS4-carbon fibre embedded in epoxy matrix, modified from [94].

2.2.3 Single fibre composite modelling strategies

To complement the experimental research on fibre-matrix debonding, many authors have produced numerical and finite element models to predict the ISS between the fibre and matrix. Early two-phase models were analytical solutions, namely by Cox [50] and Kelly-Tyson [49]. Cox [50] developed the shear lag model which assumed linear elastic behaviour for both the fibre and matrix constituents. This enabled the axial fibre stress and shear stress between the fibre and matrix to be determined, but it was assumed that no load transfer occurs through the fibre ends. A study by Galiotis et al [95] found that strains of up to 0.5% can be present at the fibre ends for $E_f/E_m = 16$, but the strain levels at the fibre ends dropped for higher E_f/E_m ratios (~100), such as carbon/epoxy composites [96]. The Cox model is therefore limited in its application as there will be some stress/strain transfer at the fibre ends.

Kelly-Tyson [49] used an elastic-perfectly plastic material to model the matrix region and this allows the critical length of a fibre to be determined, in addition to the axial fibre stress and shear stress that was previously calculated by the Cox model. The critical length of a fibre is defined as the minimum fibre length that will permit the tensile stress induced by the interfacial shear strength, to reach the tensile strength of the fibre [97]. The Kelly-Tyson model, however, assumes that the shear stress is constant along the length of the fibre, which again is an idealisation.

The Cox and Kelly-Tyson models provide analytical solutions to the single-fibre problem. However, in order to study the stress transfer characteristics between the fibre and matrix constituents in detail, a more comprehensive finite element model is often used. Two-phase single-fibre models were developed [89, 98] to look at the stress transfer characteristics between fibre and matrix, but it has been widely documented that an interfacial region exists between the two constituent materials in carbon-fibre/epoxy composites. This region is known to dominate the stress transfer between fibre and matrix, as shown by experimental studies in [92] for unsized and sized fibres. It is therefore acknowledged that two-phase material models [99, 100] (top, Figure 13) fail to fully capture the behaviour of the single fibre composite system, with a third material or connection required between fibre and matrix (bottom, Figure 13) to accurately predict composite behaviour [47, 86, 101, 102]. The bond between the fibre and matrix has been modelled in a variety of ways in the literature. For simplicity, some authors assume a "perfect" bond between fibre and matrix [49, 50, 103], whilst others model the interface as a third material with perfect bonding between all three material phases [47, 48, 60, 104].

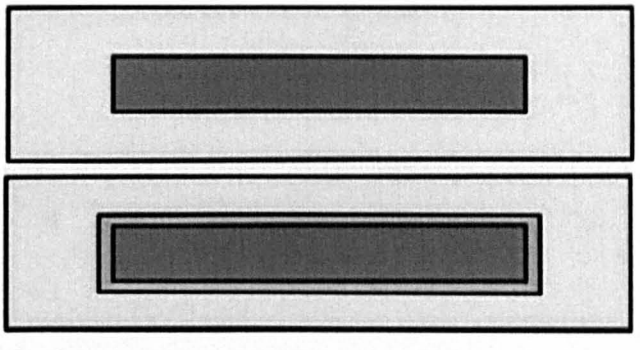

Figure 13 – Two-phase (top) and three-phase (bottom) material models used in single fibre analysis.

Interfacial regions can be formed by two mechanisms. The first of which is caused by residual stresses that form in the matrix when the resin is cooled during the moulding process [104, 105]. These residual stresses form as a result of the volumetric shrinkage of the resin around the fibre, which alters the region immediately surrounding the fibre, with its own unique mechanical properties. The thickness of this region is dependent on the rate of curing and also on any surface treatments that may have been applied to the fibre. The second mechanism

is a result of the sizings or coatings that are typically applied to the fibre during manufacture [92, 93, 106]. Paipetis and Galiotis [92] found that the axial stresses in a sized fibre (Soficar M40B-40B MEBS) were approximately 1.6% higher than that of its unsized equivalent (Soficar M40B). At the point of saturation, the interfacial shear strength of the sized samples were approximately 42MPa, compared to 35MPa for the unsized equivalent [92] – both of which were at least 25% greater than Kelly-Tyson's predictions.

Kari et al [107] looked at the effect of increasing the interfacial modulus between fibre and matrix. It was found that an increase in interface modulus from 10GPa to 250GPa saw just a 5% increase in longitudinal modulus for a unidirectional composite. However, when the unidirectional composite was loaded in the transverse direction there was a significant increase (~18%) in the transverse modulus, shown in Figure 14.

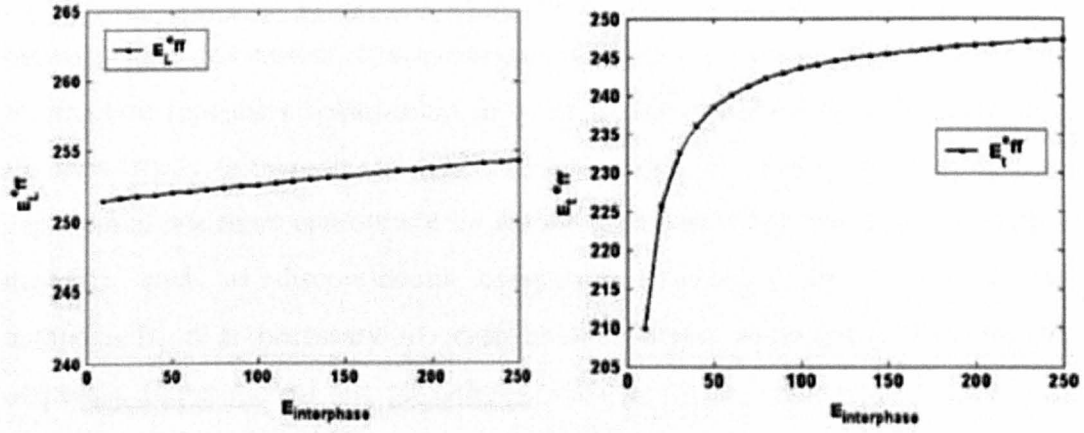

Figure 14 – Longitudinal (left) and transverse (right) modulus of a unidirectional composite with increasing interfacial modulus, reproduced from [107]

(Note: Fibre material in this study is tungsten with modulus of 345GPa and the matrix is nickel with modulus of 214GPa).

Wu et al. [89, 102, 108, 109] modelled two-phase and three-phase single fibre models, initially assuming a perfect bond in both models before introducing debonding criterion. Johnson et al. [86] concluded that a three phase model with debonding was the most representative of a single fibre composite system, as it allowed separation of the fibre and matrix and a discrete interphase region to be

modelled to replicate sizings applied to the fibre. The assumption of a perfect bond between fibre and matrix oversimplifies the composite material, with common failure mechanisms such as debonding and pull-out excluded in the analysis, leading to over predictions in stiffness and strength.

2.2.4 Traction-separation laws for cohesive and connector elements

Based on the findings of Wu [108], Johnson [86] and Pan [69], debonding between the fibre and matrix material is known to be critical when predicting the strength of the single fibre composite. Cohesive elements or similar, such as spring/connector elements, are often placed between the fibre and matrix to tie the surfaces of the fibre and matrix together. Both cohesive and spring/connector elements use traction-separation laws or energy based relationships to define the point at which debonding will occur in the models [107, 110, 111].

The constituent materials used in a fibre reinforced composite material, along with any sizings that may be applied to the fibres, will dictate the bonding strength between fibre and matrix. It is important to select the correct shape function for the traction-separation relationship in order to accurately model debonding in a FE simulation, with a linear softening law ideal for brittle materials and an exponential law more appropriate for ductile materials [112]. For a more complex material, such as discontinuous composites containing ductile and brittle components, it is necessary to establish the correct relationship between the materials. Experimental test procedures, such as the microdroplet fibre pull-out test specified in [90] and the SFF test shown in Figure 11, are typically performed to extrapolate the interfacial strengths and displacements required to produce the traction-separation curves in Figure 15.

Sun and Jin [113] have developed cohesive laws to model debonding in composite materials, with three examples of typical cohesive laws shown in Figure 15. In most applications the cohesive zone is initially taken to be of zero (or small) volume, with the relationship between the traction and separation governing the constitutive response of the zones [113]. It has been noted that the initial cohesive traction should not be zero, as stress singularities would exist at the tip of the cohesive zone [114, 115].

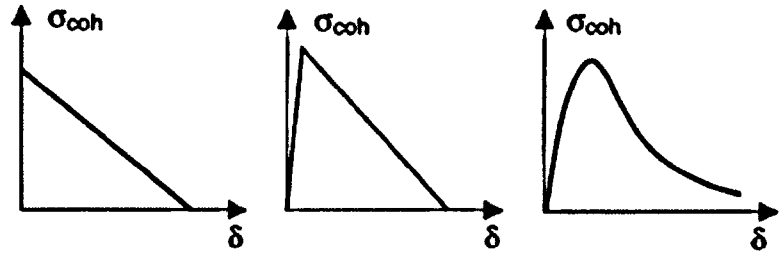

Figure 15 - Sample of cohesive laws that are commonly used to model debonding in composite materials. (Left) linear softening law, (centre) bi-linear softening law and (right) exponential law, modified from [113].

Scheider [112] performed numerical studies and found that a modified bi-linear/exponential law was appropriate for a ductile matrix containing multiple fibre reinforcement. However, other authors have chosen to use a range of different traction-separation laws in their numerical analysis. Lin et al. [116] used a rate-independent bi-linear cohesive law that accounted for frictional contact at the interface, an extension of the work by Geubelle and Baylor [117]. Needleman [118, 119] used an exponential law, Li et al. [120] used a linear softening law, whilst Tvergaard and Hutchison [121] used a trapezoidal relationship to model the interfacial behaviour between carbon fibre and matrix material. However, it was noted in [120] that numerical simulations have shown that the precise shape of the traction–separation law does not fundamentally affect the results of an analysis, with the interfacial strength value the most critical parameter for the cohesive law.

Nishikawa et al. [122] proposed two methods for characterising the cohesive law from experimental testing, one based on the number of fibre breaks and the other based on the debonding length. Kim and Nairn [94] performed single fibre fragmentation tests to calculate the length of the debonded zone in glass/epoxy and carbon/epoxy fibre composites, with photoelasticity fringes around fibre breaks used to measure the debond lengths that occurred instantaneously after each fibre break, shown in Figure 12. In both studies, experimental and simulation data were compared in order to establish suitable cohesive parameters for analysis.

For the analysis contained in this thesis, a bi-linear softening law has been selected to model the interface between the fibre and matrix, similar to the methodology employed by Pan [69] who had success in implementing this law for predicting the debonding length in a single fibre composite model with glass fibre and epoxy. The following properties are required for a bi-linear constitutive equation for cohesive and connector elements, shown in Figure 16:

- K, Penalty Stiffness (N/mm^3)
- τ_o, Interfacial Shear Strength (MPa)
- G_c, Fracture Toughness (J/m^2)

The penalty stiffness defines the stiffness of the cohesive / connector elements before the onset of damage at point A, shown in Figure 16. Turon et al [123] developed a relationship to calculate the penalty stiffness for composite materials, using the equation below:

$$K = \frac{\propto E_2}{t} \qquad \text{Equation 12}$$

Where E_2 = transverse modulus of the fibre (MPa or N/mm^2), t = thickness of the cohesive element (mm), and α is a dimensionless parameter significantly greater than 1 ($\alpha >> 1$). It was noted in [123] that the interface penalty stiffness should be large enough to provide a reasonable stiffness, but small enough to avoid numerical problems such as spurious oscillations of the tractions in an element. Typically, α values of 50 are used which gives penalty stiffness values of the order of 10^5 to 10^6 N/mm^3 [69, 123-125].

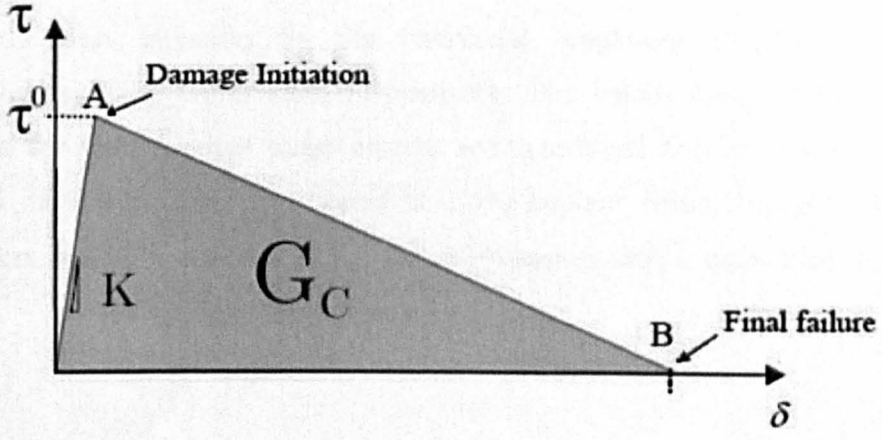

Figure 16 - Bi-linear constitutive response for cohesive / connector elements [123].

The Interfacial Shear Strength (ISS), τ_o, is required to define the stress needed to initiate damage in the cohesive element (point A highlighted in Figure 16). Typically, values in the range of 20MPa to 70MPa [47, 87-93] are observed in experimental tests for the ISS of carbon-epoxy composites. Shear strain and force values can also be used to determine the onset of damage for the cohesive elements.

Fracture toughness, or critical fracture energy, G_C, is the area underneath the traction-separation curve and is defined as the energy dissipation per unit area of the crack once it has formed at the interface [126]. The fracture toughness dictates the rate of failure of the cohesive element, from the point of damage initiation (point A) to final failure (point B), shown in Figure 16. For simplicity, it is common to consider each mode of fracture independently using an uncoupled traction-separation law to avoid the complexity of mixed mode failure [69]. This methodology is acceptable for a single fibre composite model as the cohesive surface is only subjected to mode II (in-plane shear) fracture [69], with the influence of mode I (opening) and mode III (out-of-plane shear) negligible for this load case.

For multi-fibre composites the fracture toughness should account for all three modes of fracture that could occur in the composite material. Typically a fracture toughness value is used that accounts for all three modes of fracture, with values of the order of 100 J/m^2 [69, 126] used for glass/epoxy models. Experimental tests conducted by Kim and Nairn [94] found that values of 120 J/m^2 and 220 J/m^2 were the best estimates for the interfacial toughness of glass/epoxy and carbon/epoxy fibre composites, respectively. The values obtained in [94] also account for both residual stress effects and interfacial friction, with debonded lengths of 3 fibre diameters found at 1.5% applied strain, rising to 12 fibre diameters at 2.5% applied strain for AS4-carbon fibres embedded in epoxy matrix.

2.3 Review of existing multi-fibre composite models

2.3.1 Fibre ineffective length

An important issue when calculating the axial strength of composite materials is the redistribution of stress after a fibre failure has occurred. Fibres that immediately surround a broken fibre in a composite are responsible for carrying additional load, with the ineffective length of a broken fibre defined as the length of fibre over which 90% recovery in axial stress/strain occurs from the site of a fibre fracture [85]. A reduction in fibre ineffective length would indicate greater stress transfer efficiency, which will increase the mechanical properties of the discontinuous composite at the macroscale as the fibre can carry greater axial stress, leading to fibre failure rather than fibre pull-out.

All of the fibres in an ideal composite material would have uniform failure stress and strain, which would make it a straightforward task to determine the stiffness and strength. However, this is not the case, with significant variations found when determining the mechanical properties of the fibres. This variation in strength gives rise to a complicated array of failure mechanisms in composite materials, such as fibre breaking, interfacial debonding and matrix cracking [85].

When a single fibre failure occurs in a composite, a large fraction of the load is transferred to the surrounding matrix material, which results in high shear stresses at the interface between fibre and matrix. If the interfacial bond is insufficient, fibre pull out will occur, otherwise the overload is redistributed to neighbouring fibres, which provides stress concentrations in these fibres and increased probability of failure [127]. The region in the adjacent fibre affected by the fibre break is often referred to as the Positively Affected Length (PAL). The ineffective length of the broken fibre determines the PAL of the neighbouring fibres and also dictates the stress/strain concentration observed [48]. Figure 17 shows the stress distribution in a broken fibre and the fibre adjacent to the break.

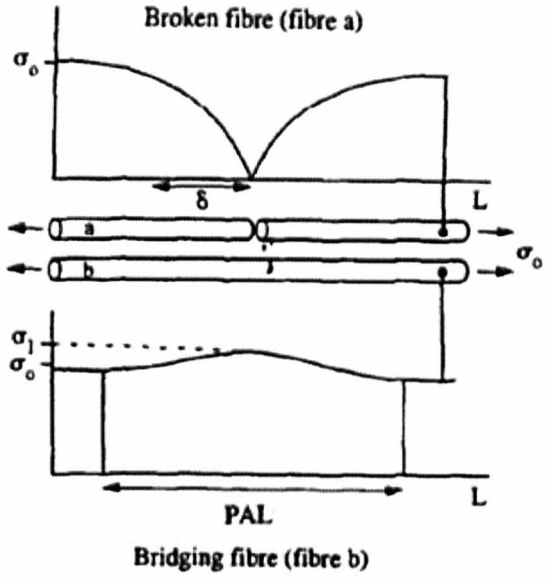

Figure 17 – Ineffective length of a broken fibre (top) and the positively affected length in a fibre adjacent to the fibre break (bottom), reproduced from [128].

Stress concentration factors (SCFs) are often calculated to quantify the overload experienced by bridging fibres neighbouring a fractured fibre, see Figure 17. High SCFs in intact fibres adjacent to a fibre break can lead to further fibre fractures in a composite material, which can dramatically reduce the mechanical properties of the composite [129]. Coatings are often applied to fibres to promote more efficient stress transfer between the fibre and matrix, with it noted that a soft interface (low modulus) increases the ineffective length of a broken fibre but reduces the SCFs in the surrounding fibres. In contrast to this, a stiffer interface (high modulus) yields less; therefore the adjacent fibres will experience higher SCFs [48].

Nedele and Wisnom [130, 131] developed models to predict stress concentration factors in fibres surrounding a fibre fracture. A linear elastic material was used for the matrix, limiting the accuracy of the model since it is widely acknowledged that an elastic-plastic model is essential when predicting the behaviour of the matrix material. The elastic-plastic relationship is necessary for ductile matrix materials, which exhibit a clear yield point after which irreversible plastic deformation will occur. Many authors [132-134] have incorporated matrix plasticity into their analysis; with a decrease in the SCF in neighbouring fibres observed when compared to elastic matrix models, primarily due to local matrix

yielding in the models around the point of fibre fracture. Fielder et al [133] reported SCF values for glass fibre composites of approximately 1.2 for linear-elastic matrix models, reducing to 1.1 for elastic-plastic matrix models at applied strains greater than 2.0%.

Behzadi et al. [135] found that with an elastic-plastic matrix the applied strain can never be fully recovered in the broken fibre, with the threshold of 90% recovery used to define the ineffective length, which was determined to be 0.149mm for the carbon-epoxy unidirectional composite considered in the analysis. A perfect interphase is assumed between fibre and matrix in the model, but it was noted that if the interphase was more ductile the ineffective length would increase. Studies were also conducted in [135] to look at the impact of multiple fibre fractures in a unidirectional composite, with the strain concentrations monitored in fibres surrounding the fractures. The fracture patterns used, with the resulting strain concentration factors in the adjacent fibres, are shown in Figure 18. The strain concentration factor in the surrounding fibres increases as the number of fractured fibres increases; with the strain concentration rising by up to 22% (1.09 to 1.33) in adjacent fibres from the one fibre fracture model (a) to the model with two coincident fractures (b).

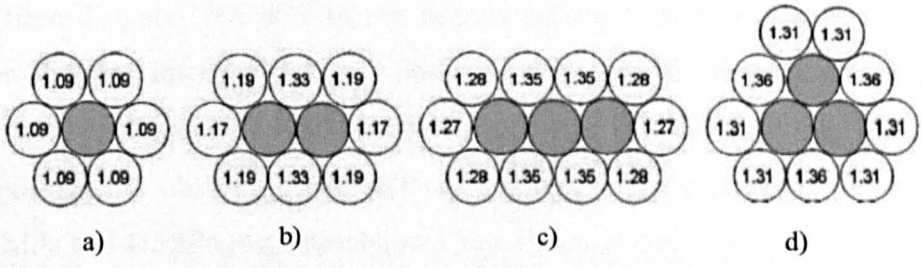

Figure 18 - Strain concentration factor values in neighbouring fibres. (Note: Grey fibres denote the fibres that are fractured), reproduced from [135].

Van den Heuvel et al. [129] performed a finite element study to compare predictions of stress concentration factors (SCF) in unidirectional carbon-epoxy composites with experimental results obtained using Raman spectroscopy in [136, 137]. The SCFs were recorded in the closest adjacent fibre, with good agreement - less than 10% error at an inter-fibre spacing of one fibre diameter - observed between analytical and experimental results. Two models were considered, one with perfect fibre-matrix adhesion, whilst the other model allowed for debonding

between the fibres and matrix by specifying an initial debonded length along the broken fibre. The SCF in the nearest adjacent fibre is shown in Figure 19, as the debond length was increased from 0 to 30 fibre diameters.

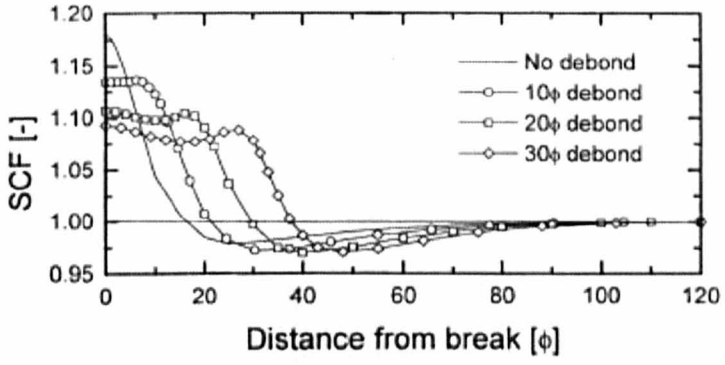

Figure 19 - Stress Concentration Factor (SCF) in the nearest adjacent fibre to a fibre break, with increasing debonding length along the broken fibre [129].

Behind the debonded zone in the models, matrix yielding occurs which prevents the applied load being transferred to the neighbouring fibres, thus a reduction in SCF and an increase in the PAL is observed in the first adjacent fibre. For the case of perfect fibre-matrix adhesion in [129], the inter-fibre distance was varied along with the yield stress of the matrix material. It was found that by decreasing the inter-fibre distance, the SCF in the nearest adjacent fibre increased. Peak SCF values of approximately 1.20 were observed at an inter-fibre spacing of one fibre diameter. An increase in yield stress of the matrix led to a slight increase in the value of the SCF observed, with SCFs of 1.19 and 1.21 obtained for yield stresses of 20MPa and 80MPa respectively, at a separation distance of one fibre diameter. It was noted that a matrix with a higher yield stress can transfer a fibre overload more efficiently to the intact fibres, resulting in a higher SCF in the intact fibre and a reduced ineffective length in the fractured fibre [129].

In [138] a 3D finite element study of a hexagonal packing array was conducted, with SCFs of around 1.07 calculated for high volume fraction (25-70%) models in the fibre immediately next to the broken fibre. The SCFs obtained in [138] were similar in magnitude to the values reported by Nedele and Wisnom [130, 131] and Behzadi et al. [135] for one fibre fracture, but significantly lower than the SCFs of 1.25 observed in experimental tests in [136]. In contrast to this, Van den Heuvel et

al. [129] and Hedgepeth and Van Dyke [132] calculated SCFs to be approximately 1.20 and 1.104, respectively, in the nearest neighbouring fibre. The difference in values of the SCF from these studies is attributable to the number of intact fibres that immediately surround the fibre break. A larger number of intact fibres in the 3D models allowed the overload to be redistributed between them, resulting in a lower SCF values. However, it was noted that a SCF value of the order of 1.07 was still high enough to play a role on the macroscopic failure of a composite material [138].

Mehan and Schadler [139] investigated the effect of interfacial strength on the strain concentration factor and overload transfer length (OTL), which is equivalent to the PAL of the fibre adjacent to the fibre break. Figure 20 shows the variation in OTL and strain concentration factor that can be expected by altering the interfacial strength between fibre and matrix. The stronger interphase allows for greater strain transfer efficiency from the point of the fibre break to the adjacent fibre, thus a higher strain concentration factor is expected with increasing interfacial strength.

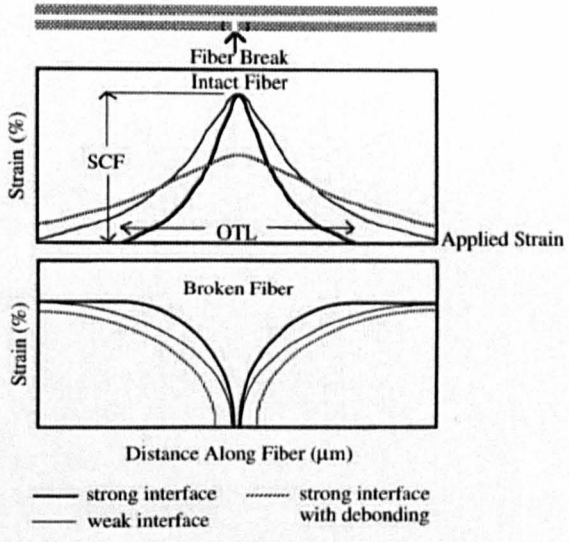

Figure 20 - Strain profiles for an intact (top) and broken fibre (bottom) with varying interfacial strength, reproduced from [139].

Lane et al. [48] developed a three-phase material model to predict the strain concentration factors in a square packing arrangement at three separate volume fractions; 38, 48 and 58%. An interface of 0.2μm thickness was used in the

analysis, with two grades of epoxy used for the matrix and interface properties. The characteristics of the two epoxies are detailed below in Table 1 and a summary of the strain concentration factors in the nearest neighbouring fibre is detailed in Table 2. At low applied strains (approximately 0.1%) an increase in fibre volume fraction in the models led to an increase in the strain concentration factor in the nearest fibre to the fibre fracture, for both of the models under consideration. However, at 1.0% applied strain, when the strain transfer is largely plastic, the strain concentration factor was unaffected by the volume fraction in the cell, with the resin used for the matrix and interface also having no effect on the strain concentration factors observed.

At 0.1% strain the 5050 matrix/6040 interface model provides lower strain concentration factor values than the higher performance 6040 matrix/5050 interface model, across the range of volume fractions in the analysis. It was concluded that when plasticity occurs, the presence of a soft interface reduces the reinforcing efficiency of a broken fibre, therefore limiting the strain concentration in the surrounding fibres [48]. A stiff interface yields less than a soft interface and the surrounding fibres will experience a higher strain concentration factor, with the matrix properties then crucial as the matrix is more likely to yield than a stiff interface under increased loading [48].

Table 1 - Material properties for matrix/interphase in analysis by Lane et al. [48]

	Resin System	
Property	5050	6040
Initial Modulus (GPa)	1.76	3.48
Average Modulus to yield point (GPa)	0.79	0.84
Yield Stress (MPa)	35.16	53.50
Yield Strain (%)	4.40	6.37
Assumed value of Poisson's ratio	0.36	0.36

Table 2 - Summary of strain concentration factors from study by Lane et al. [48]

Resin System		0.1% Applied Strain			1.0% Applied Strain		
Matrix	Interphase	0.38 V_f	0.48 V_f	0.58 V_f	0.38 V_f	0.48 V_f	0.58 V_f
6040	5050	1.10	1.12	1.14	1.05	1.05	1.05
5050	6040	1.08	1.10	1.13	1.05	1.05	1.05

Behzadi and Jones [127] used a two-phase material model to investigate the effect of temperature on strain transfer between a broken fibre and adjacent fibres in a unidirectional fibre composite. Square packing with four fibres was used in a uniaxial compressive test and it was found that the strain concentration factor in adjacent fibres decreased with an increase in temperature. This was attributable to a decrease in yield strength and increase in plasticity of the matrix with increased temperature, which allowed more of the energy released from the fibre fracture to be absorbed by the matrix material and not by the neighbouring fibres. In addition to this, it was found that there was less efficient strain transfer back into the broken fibre with increasing temperature, providing an increase in the ineffective length [127].

2.3.2 Review of unit cells used to determine fibre bundle properties

Fibre bundles contain thousands of filaments and it is therefore unfeasible to model each individual filament when determining the mechanical properties of the bundle. Each fibre bundle used to create a discontinuous component will have its own unique filament architecture; therefore a methodology is needed to provide an approximate solution for fibre bundles of varying volume fraction. A common modelling strategy is to use a unit cell of the cross-section of the fibre bundle to calculate bundle properties.

Two packing arrays are typically considered, a square packing array [48, 127, 140, 141] and a hexagonal arrangement [135, 141-143], with these shown in Figure 21. The two arrangements are an idealisation of what would be expected across the fibre bundle; however they do not take into account resin rich regions which could be present in the bundle. Inter-fibre distance can be varied to adjust the volume fraction of the bundle to allow the full range of fibre bundle properties to be calculated. Both unit cells shown in Figure 21 require appropriate boundary conditions to accurately predict the bundle properties, with the correct procedure outlined in section 2.3.3.

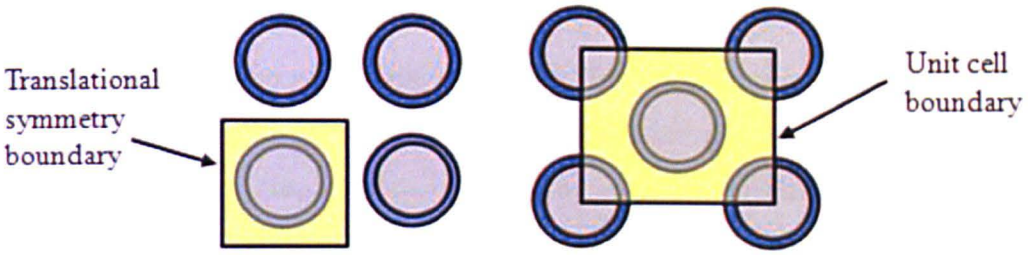

Figure 21 – Square packing array (left) and hexagonal packing array (right) used to determine fibre bundle properties, three-phase material models with an interface between the fibre and matrix.

Kari et al. [107, 110] developed a randomly distributed fibre model and compared this directly to a square and hexagonal packing arrangement at a range of volume fractions. It was found that in the longitudinal direction of the fibres the modulus of the material was constant regardless of the packing arrangement. However, when the unit cells were loaded transversely it was found that the square packing array predicted the highest stiffness at all volume fractions, with the hexagonal array predicting the lowest stiffness. The stiffness of the random model was bounded by the square and hexagonal models, with the results obtained from this study shown in Figure 22.

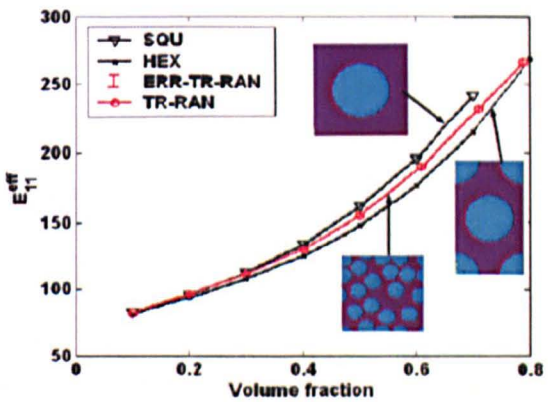

Figure 22 - Comparison of square, hexagonal and random packing arrangements as a function of volume fraction, reproduced from [110].

Mishnaevsky et al. [144] also modelled 3D random unit cells of glass fibre composites, but the mechanical properties of the fibres were varied throughout the thickness of the model, according to a Weibull distribution, to simulate fibre fracture. FE models with 20 fibres were produced (Figure 23) and it was found

that the simulated fibre fractures led to matrix failure, with cracks in the matrix growing from the site of the fibre crack to the neighbouring fibres. The fibres adjacent to the broken fibres were then responsible for carrying the load and higher stresses were found in these fibres, leading to a reduction in strength (~7%) when compared to the model with constant fibre strength, shown in the in Figure 24.

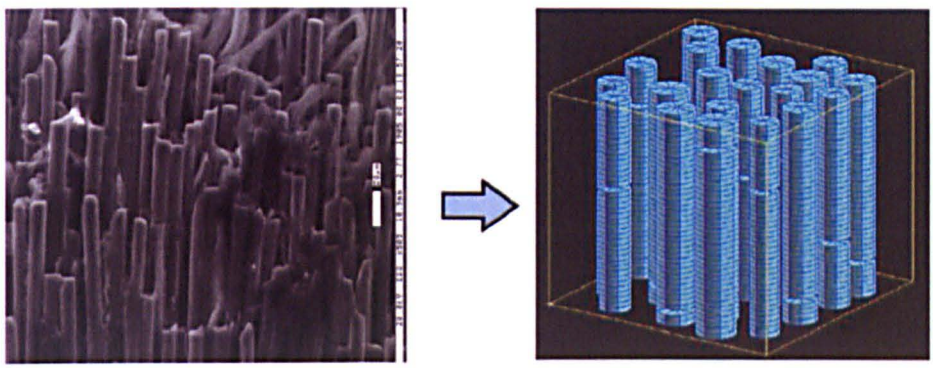

Figure 23 - Micrograph of a unidirectional fibre reinforced composite material with failed fibres (left) and an FE model with 20 fibres and layers removed to simulate fibre fracture (right), reproduced from [144].

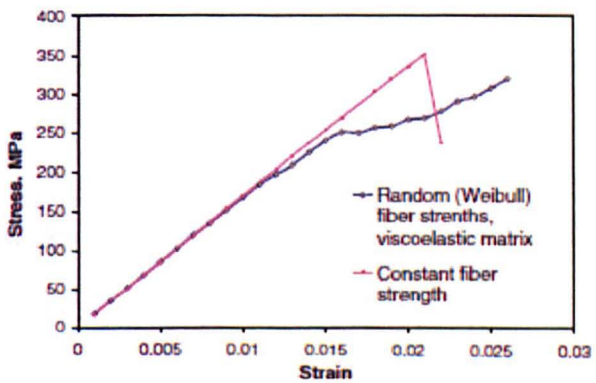

Figure 24 - Stress-strain curve for glass-epoxy composite models developed by Mishnaevsky et al. [144].

Fibre diameter is known to vary during the manufacturing process, with values reported from 5μm to 10μm [92, 105, 145, 146] for PAN based carbon fibres. A central point of 7μm has been selected to determine the fibre bundle properties in this analysis, which is consistent with the manufacturer data for Toray T700 12k 50C. Coatings are often applied to fibres to promote stress transfer between the

fibre and matrix, leading to varying levels of interfacial thickness on the fibres. The literature shows that the interfacial thickness can vary between 0.2μm [48] and 1.5μm [88]. A mean interfacial thickness of 0.5μm has been used in this analysis, since it was found by Hayes et al [47] and Jacobs and Verpoest [147] that this is approximately the width that the fibre alters the matrix properties during curing.

Hayes et al. [47] and Johnson et al. [86] performed studies to look at the effect of the stress transfer between multiple fibres embedded in a matrix region. Various grades of epoxy were modelled for the matrix and interfacial regions, with both authors finding that the level of plasticity in the epoxy has a significant influence on the strain development in the model. The matrix and interface will be modelled as elastic-plastic materials (rather than elastic-perfectly-plastic as used previously) when determining the mechanical properties of the fibre bundle in section 4.1.3. Experimental tests were conducted to fully characterise the elastic-plastic behaviour of the DLS 1776 epoxy, with the mechanical properties obtained from the testing (section 3.1) used in this analysis.

2.3.3 RVEs and boundary conditions for composite microstructures

A representative volume element (RVE) is defined as the volume of a heterogeneous material that is sufficiently large to be statistically representative of the composite, ensuring a sample is taken of all micro-structural heterogeneities that occur in the material [110, 148]. Determining the size of the RVE is important when calculating the material properties, with Figure 25 showing three possible RVEs (A, B and C) for a random distribution of fibres in a unidirectional composite, such as a fibre bundle. The RVEs in Figure 25 are of varying size and it is not obvious which RVE is the optimum for calculating the properties of the unidirectional composite. It was noted by Wongsto and Li [149] that the RVE size must accommodate the randomness without interfering. Approximate boundary conditions must then be applied to the RVE to consider it as a unidirectional composite to calculate the mechanical properties. It is acknowledged, however, that the models can never be fully representative of a fibre bundle due to the random distribution of the fibres across the transverse cross-section.

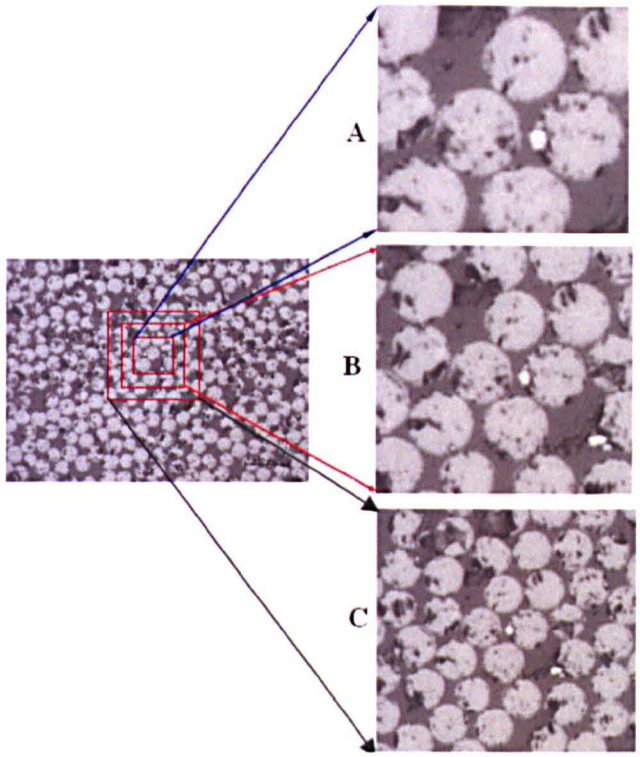

Figure 25 - Typical microstructure of a transversely randomly distributed unidirectional fibre composite (cross-section) [110]

The interaction between multiple fibres has also been extensively modelled in the literature, with authors varying inter-fibre distance to calculate the properties of fibre bundles of varying volume fraction. However, the boundary conditions imposed on the models in these simulations is inconsistent, leading to uncertainties in the fibre bundle properties obtained. A review of these boundary conditions is necessary to clarify and establish the correct boundary conditions to calculate fibre bundle properties.

An idealised composite with a regular structure is typically considered to determine the fibre bundles mechanical properties, with hexagonal and square packing arrangements used to approximate the material properties. There are many different unit cells that can be used to model the cross-section of the fibre bundle, with Figure 26 showing how symmetry can be exploited for a hexagonal packing arrangement. Li et al. [150, 151] advocated the need for the use of a hexagonal packing arrangement over a square packing arrangement, as it is more representative of a physical material and preserves the statistical transverse isotropy of the composite.

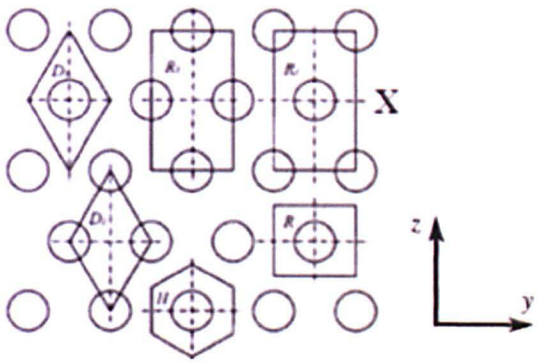

Figure 26 - Unit cells for hexagonal packing arrangements [150]

The periodicity of unit cell models implies that each RVE in the composite has the same deformation mode and there is no separation or overlap between the neighbouring RVEs after deformation [110]. The boundary conditions on the unit cell allow for relatively small models to be considered when conducting analysis to determine the properties of a unidirectional composite, as the relationships imposed infer that the unit cell is part of a more extensive structure.

Li [152] outlined the correct methodology to derive boundary conditions to exploit symmetry in microstructures when generating unit cells. Each RVE configuration, i.e. for the hexagonal packing arrangements in Figure 26, will have its own unique set of boundary conditions relating to the translational, rotational and reflectional symmetry of the unit cell. Once symmetry conditions have been established, the boundary conditions can be obtained for the unit cell. For example, unit cell X, highlighted in Figure 26, has translational symmetry in the y and z direction that covers the whole region of interest.

Boundary conditions can be prescribed in terms of displacements or stresses on the outer surfaces of the unit cell, with [150] containing a comprehensive review of the constraints required for different unit cells. Figure 27 shows the horizontal constraints on a unit cell, between faces A and B, for a square packing arrangement. Surfaces C and D will also have equivalent constraints between the surfaces to ensure the translational symmetry is also maintained in the vertical directions.

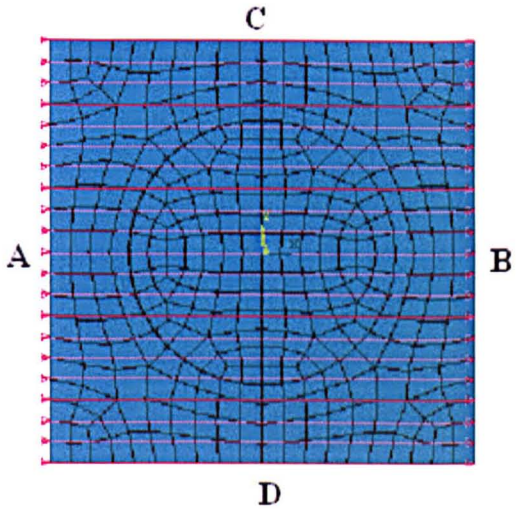

Figure 27 - Square packing arrangement with nodal constraints shown in the horizontal direction, reproduced from [110]

2.4 Review of literature related to the mesoscale of discontinuous composite materials

2.4.1 Fibre bundling in discontinuous composites

It was reported by Harper [8] that filaments tend to remain in bundles when they are chopped to form discontinuous laminates, with the bundled filaments behaving in a different manner when compared to the same volume of evenly dispersed fibres. Mulligan et al. [153, 154] analysed the effect of fibre bundling on the performance of discontinuous materials and found that a material with dispersed fibres had a greater strength than that of a material with high levels of fibre bundling, with the alignment of the fibres in the bundles causing stress concentrations to develop in the material. Many authors therefore acknowledge that discontinuous materials containing bundles have a unique mesoscale structure [153-158], with Figure 28 showing a discontinuous preform with the fibres bundled together.

Figure 28 - Discontinuous fibre preform produced from the BRAC3D process [159].

Studies in [63, 64] have shown that the behaviour of the fibre bundle is similar to that of a single fibre, with bundle pull-out a common failure mechanism in short fibre discontinuous materials and bundle fracture common in components containing longer fibre bundle lengths. Therefore, it is a fair assumption to consider the fibre bundle as a single volume, which is a convenient modelling strategy as each bundle contains thousands of filaments (3k, 6k, 12k or 24k), making it unfeasible to model them individually at the meso and macroscale. The idealisation that a fibre bundle can be modelled as a single entity simplifies the analysis and it is commonly accepted that the material properties of fibre bundles can be determined at the microscale, with the volume fraction of fibres in the bundle dictating the stiffness and strength. This strategy was adopted in [68, 160] with fibre bundles modelled as beam elements embedded in an epoxy matrix. However, using beam elements neglects common failure mechanisms that occur in the bundle, such as fibre-matrix debonding and transverse bundle fracture.

The other two factors that influence the mechanical properties of the fibre bundle are the length and cross-sectional shape of the bundle. Coleman [161] demonstrated that the strength of a fibre bundle can be between 50-65% less than the strength of the filaments contained in the bundle. Bader and Priest [162] also reported that the mean strength of 1K carbon tows is reduced by 10% with an increase in length from 20mm to 300mm. The cross-sectional shape of the fibre bundle also influences the mechanical properties of the manufactured component.

As bundles come into contact with other fibre bundles, the local cross-sectional shape of the bundle changes, with bundle spreading likely to occur at the contact point. The methodology used to determine fibre bundle shape is discussed in the following section.

2.4.2 Bundle shape in composite materials

Rujiter [56] and Crookston [55] performed studies to determine the cross-sectional shape of a yarn in textile composites, highlighting the difficulty of predicting the shape due to multiple factors. Yarn manufacturing, yarn processing (weaving, braiding, contact with other yarns), preforming (stacking, handling, compacting), impregnation of the resin and the curing (chemical and thermal shrinkage) of the composite can all influence the cross-sectional shape of the yarn [56]. This has led to a number of approximations being used to represent the shape, shown in Figure 29.

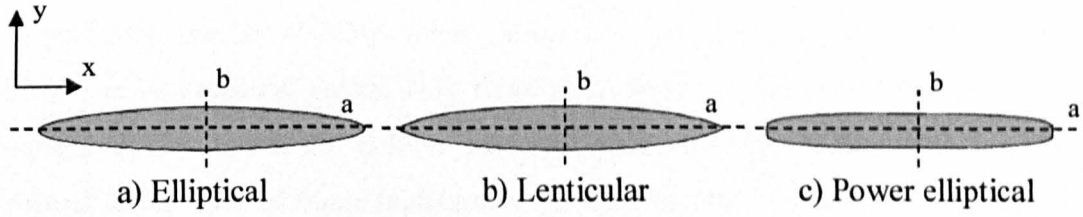

Figure 29 - Geometrical representations used for bundle cross-sectional shapes in textile materials.

Sherburn [1] performed extensive numerical studies to look at the effects of forming on yarn geometry in dry textile composites, however, it was found in [56] that it is difficult to attribute deformations in bundle shape to stages in the production process, therefore predicting the final shape of the bundle in the manufactured part is difficult. To overcome this difficulty, the bundle shape is often extracted from the finished composite using microscopy, as shown in Figure 30, with an assumption that the original bundle shape is not important if the final shape of the bundle can be obtained. The fibre density and fibre volume fraction across the bundle is plotted in Figure 30. The volume fraction across the width of

the bundle is relatively constant (~60%) and the shape is approximately lenticular in this study.

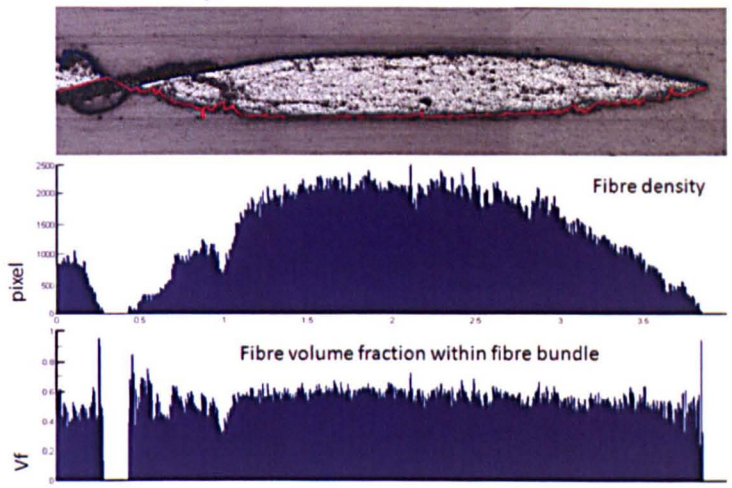

Figure 30 - Fibre volume fraction distribution across a fibre bundle in a textile composite material, reproduced from [163].

The production methods used to manufacture discontinuous composite materials, in particular the BRAC3D process, makes it even more complex to predict the bundle cross-sectional shape, with three main factors contributing to this shape variation. The first is the random orientation of the chopped fibre bundles, the second is the level of filamentisation in the fibre bundle, with the third attributed to the compaction levels in part forming. All of these factors change the cross-sectional shape of the bundle, with a range of shapes likely across a component, which makes predicting the mechanical properties at the macroscale a complex procedure when compared to a textile material. In addition to this, it has also been noted that in discontinuous composites the end effects of the bundles play a significant role in the mechanical performance of the material [164], which is another factor that has not been considered previously in textile models.

The bundle cross-section in discontinuous composites varies significantly across a component and is not as regular and repeatable as in textile materials, but to simplify the analysis at the mesoscale an elliptical approximation has been used, based on the microscopy of a discontinuous specimen, shown in Figure 31. The

bundle shape in a discontinuous component was shown to be more elliptical than the lenticular shapes found in woven textile composites.

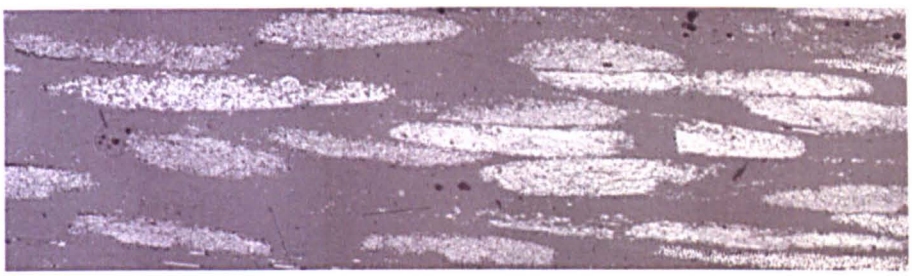

Figure 31 - Micrograph of 3k carbon tow discontinuous composite [8].

2.4.3 Review of modelling strategies employed in the literature

Pan et al. [43] studied the interaction of fibres in a discontinuous material using circular profiled inclusions encased in a unit volume of matrix material. The distance between the fibres was varied and the peak stress found in the matrix material between fibres was recorded to calculate the stress concentration factor (SCF). Two separate studies were conducted in [43]. In the first study one interacting fibre pair was considered, whilst in the second study 20 interacting fibre pairs were analysed. Each interacting pair contained two fibres that were orientated at 90^{o} to one another.

It can be seen from a summary of the results presented in Table 3 that by increasing the number of interacting pairs in the unit volume, the SCF increases significantly by 226% from 2.14 at a separation distance of 1.5d to 6.98 at 1.05d. Even when only one interacting fibre pair is considered, a SCF of 4.96 is observed in the matrix material between the fibre pairs. The SCFs observed are high in this study as the stress is monitored in the matrix material between the fibres. Figure 32 shows the local stress distributions that were obtained for the one and 20 interacting fibre pairs at a separation distance of 1.05 fibre diameters.

Table 3 - Summary of results obtained in the interacting fibre pair study by Pan [43].

One Interacting Fibre Pair		20 Interacting Fibre Pairs	
Stress Concentration Factor (SCF)	**Inter-fibre distance (d = diameter of fibre)**	**Stress Concentration Factor (SCF)**	**Inter-fibre distance (d = diameter of fibre)**
1.37	5d	-	-
1.78	1.5d	2.14	1.5d
4.96	1.05d	6.98	1.05d

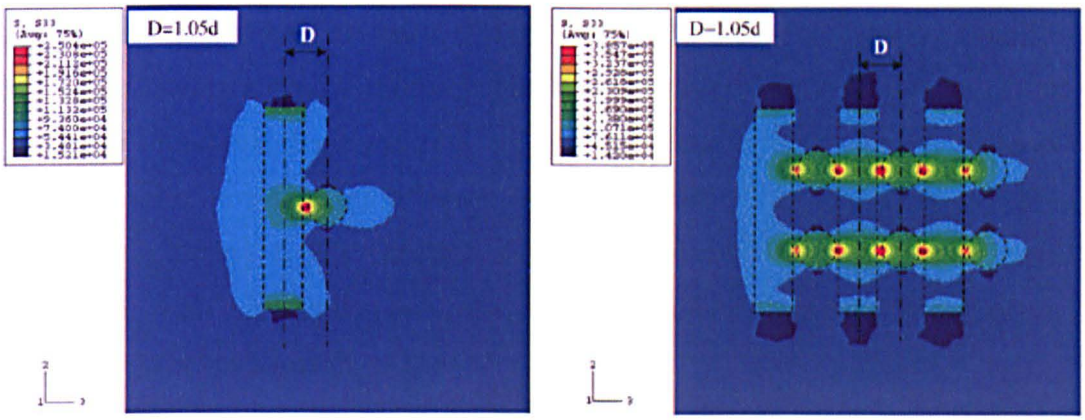

Figure 32 - (Left) One interacting fibre pair with separation distance 1.05d, (right) 20 interacting fibre pairs with 1.05d separation distance, reproduced from [43].

Toll [165] established a relationship to estimate the average number of contact points for a fibre in a short fibre reinforced composite material:

$$N_c = \frac{8}{\pi} V_f a f + 4 V_f (g + 1)$$

N_c is the average number of contact points, a is the fibre aspect ratio, V_f is fibre volume fraction, and f and g are the scalar invariants of the fibre orientation distribution. Pan et al. [43] used the equation derived by Toll for a 2D random distribution, with $f = g = 2/\pi$ and $a = 5$. Using these parameters it was calculated that an RVE with 139 fibres (~55% V_f) would have 1112 contact points, or 556 interacting fibre pairs, which could affect the elastic constants of the unit cell by up to 34.5%, using the results obtained from the FE studies.

Harper [8] produced a DCFP process simulation to study fibre orientation and homogeneity, with a wide range of fibre orientations found across the surface of a part manufactured from discontinuous fibres. Pan et al. [43] investigated the effect

of in-plane angular orientation between two interacting fibres on the elastic properties, initially having two fibres at 90° from one another and incrementing the angle by 15° until the fibres were parallel at 0°. As the angle was reduced from 90° to 0° the interaction region between the two fibres became maximised, leading to an increase in the modulus of the RVE. The out-of-plane effect on the elastic properties of the RVE was studied in [43], for the out-of-plane angles in a discontinuous composite within the range of -10° to +10°. It was found that the elastic properties of the RVE only decreased slightly, less than 0.01%, when the out-of-plane angle was increased from 0° to 10°, with the in-plane angular orientation having a greater influence on the properties of the RVE. Luchoo et al [166] also found that there was only a small reduction (~5%) in tensile stiffness with increasing levels of out-of-plane curvature, from 1° to 35°. However, the change in ultimate tensile strength (UTS) of the material was much more significant, with a reduction of 34% observed as the maximum out-of-plane orientation was increased from 1° to 35°.

2.5 Review of literature related to the macroscale of discontinuous composite materials

2.5.1 Characteristics of discontinuous materials and recent manufacturing developments

Textile composites have continuous fibres that are woven in a repeatable weave across the component, allowing for relatively small mesoscale unit cells to be produced when predicting the mechanical performance of the material. This repeatable bundle architecture provides a constant volume fraction across a component, with few voids across a manufactured part. In contrast to this, discontinuous composite materials, such as DCFP and SMCs, can have large variations in the local volume fraction as the filaments tend to remain in bundles, which has previously limited their use to non-structural applications [153]. The mesostructure of discontinuous materials can vary greatly across a component, attributable to the random nature in which the bundles are deposited, with the mechanical properties of the material dominated by this heterogeneity [167].

The development of new manufacturing methods for discontinuous fibre architectures has seen void content reduced (~2%) and volume fractions up to 54% achieved [36]. An optical micrograph showing the void levels in a specimen of BRAC3D material can be seen in Figure 33. These recent developments allow more complex parts to be produced with greater thickness, with the possibility to control fibre placement and alignment to meet local loading criteria [168].

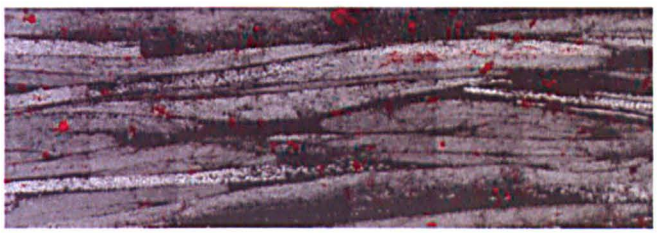

Figure 33 - Cross-sectional micrograph for a BRAC3D specimen at 54% V_f, bundle length 30mm, showing void levels (red) in the material, reproduced from [36].

Recent advancements in discontinuous fibre preforming have enabled aligned fibre architectures to be produced, which are competitive against woven fabrics in terms of mechanical performance and cost, allowing them to be used for semi-structural and structural applications. Partial alignment of fibres in the principal loading direction has proven to be an effective way of increasing tensile stiffness and strength by over 200% compared with the random fibre counterpart, when utilising 24K carbon tows [17, 27]. In addition to fibre alignment, smaller bundle sizes are known to offer improved mechanical properties over larger bundle sizes for discontinuous composites, attributable to the more homogeneous fibre bundle distribution [169]. Modulus and strength increases of 72% and 500%, respectively, were observed in [168] when comparing plaques manufactured from 48K and 1K tow sizes, however it was noted that the fibre cost rises by over 1200% when substituting a 48K tow for a 1K tow. To improve the mechanical properties of discontinuous composites, the fibre coverage needs to be more uniform, whilst keeping the cost of the component to a minimum. One solution is the mechanism of filamentisation.

Filamentisation, dispersion of the fibres in the bundle to provide a more homogenous coverage of the tool face, can be induced to improve the mechanical properties of discontinuous composites. Harper [8] found that in general, filamentisation increased the tensile properties of discontinuous carbon composites over the range of bundle lengths tested (3mm to 115mm), with tensile modulus increasing by 18.9% and tensile strength up 44.1%. However, filamentisation is not always desirable for the manufacture of discontinuous materials. It has been reported that preform loft can increase by up to 650%, making it much more difficult to process the material with fibre volume fractions limited to under 30% due to the inefficient fibre packing [8].

The effect of fibre length and filamentisation on the strength of discontinuous composites is shown in Figure 34. It can be clearly seen that shorter fibre bundles improve the strength of the composite (to a critical length between 3mm and 6mm), with preform coverage more uniform and lower filament counts present due to natural filamentisation of the bundles [169]. At low levels of filamentisation, bundle pull-out will be the dominant mode of failure for the discontinuous composite; with bundle fractures likely to dominate the failure of the material as the level of filamentisation increases. By increasing the level of filamentisation of the fibre bundle more of the filament's surface area is exposed to the matrix material, enabling more efficient stress transfer between the two material constituents [13, 170].

It can be seen in Figure 34 that the strength of the composite decreases with increasing fibre length. Homogeneity of the composite improves at shorter bundle lengths as there is a reduction in bundle integrity, caused by higher levels of natural filamentisation [8]; therefore it is difficult to quantify the effect of bundle length on the composites mechanical properties at shorter fibre lengths (<20mm). However, in a separate study in [171], it was found that the modulus and strength decreased by 7% and 16.8% respectively with an increase in fibre length from 25mm to 75mm, attributable to an increase in local volume fraction variation with the increasing fibre length.

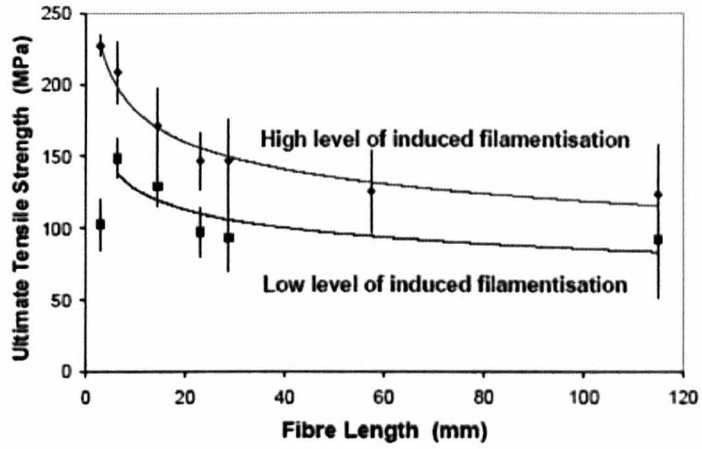

Figure 34 – Ultimate tensile strength as a function of fibre length and level of induced filamentisation for discontinuous composite samples [8].

2.5.2 Review of existing numerical models and their limitations

Many authors have attempted to generate random fibre architectures for the modelling of discontinuous materials, using their different strategies. Some have opted to produce computationally efficient 2D models, which allows for quick determination of the materials stiffness and strength but do not truly capture the geometry of the fibre bundles in the unit volume. The development of 3D models in the literature has allowed for closer representation of the fibre bundle distribution, but the algorithms required to produce the bundle networks can be computationally expensive.

Harper et al. [68] developed a 2D random fibre bundle network model, using 1D linear beam elements to represent fibre bundles. Bundles were limited to just axial material properties, with an effective circular cross section used to represent the shape of the fibre bundle. 2D resin elements, with a representative thickness, hosted the beams using the ABAQUS *Embedded Element technique. Bundle-bundle contacts were permitted, as overlapping fibres were embedded in the same resin cell, providing no upper limit for fibre volume fraction or fibre aspect ratio. Figure 35 shows the random fibre network produced using the model developed in [68]. Fibres are initially deposited over an area (A'B'C'D') which is two fibre lengths ($2l$) longer and wider than the specified region of interest (ROI), with the fibres then cropped to the ROI boundary (ABCD).

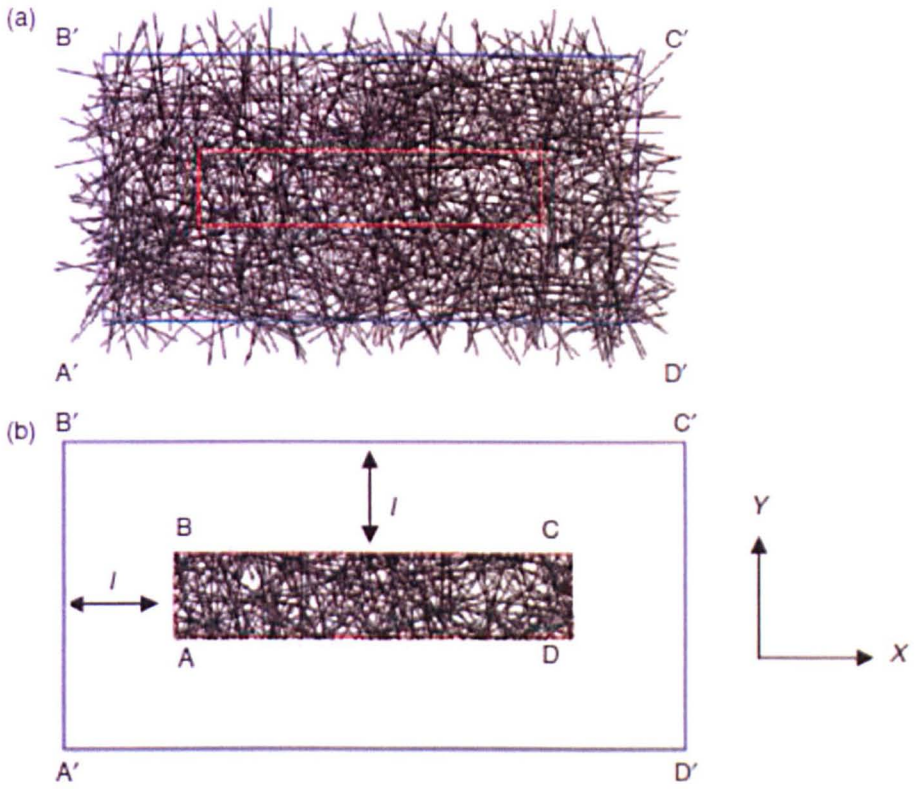

Figure 35 - Fibre distribution in the 2D model developed by Harper et al. [68]. The uncropped state is shown in (a), with the fibre distribution after cropping shown in (b).

Tensile predictions from the model developed in [68] were found to be within 10% and 20% for tensile modulus and strength respectively, when compared to experimental results for studies of varying volume fraction and length in [36]. The model was found to be computationally inexpensive, enabling large volumes (200mm×200mm×3mm) to be analysed, but simulations were limited to in-plane tension because of the 2D fibre architecture and the hosting of the fibre elements in the resin using the *Embedded Element technique. The embedded element technique is simple and efficient for meshing the models, with a square grid generated across the ROI. However, the hosting of the fibres in the resin elements is computationally expensive when running the FE analysis of the models, compared with more conventional meshing.

The 2D fibre bundle network in [68] does not account for the out-of-plane orientation of the bundles and the interaction between bundles at the bundle-

bundle crossovers, potentially leading to the discrepancy observed between numerical and experimental results in [36]. In addition to this, the fibre bundles are hosted by the resin elements, limiting the failure mechanisms that can be observed in the models. For example, interfacial debonding between the bundle and matrix is not possible using the embedded element technique, which will inherently lead to inaccuracies when predicting the strength of the material, as bundle pull out is a common failure mechanism in discontinuous composite materials.

The beam model was extended to three dimensions by Luchoo et al. [166] to account for out-of-plane fibre curvature effects. A typical fibre network generated by the model is shown in Figure 36. A non-contact algorithm was developed, enabling more realistic fibre architectures to be produced with volume fractions of up to 60% achievable. 1D elements were again used to represent the fibre bundles, with 3D continuum resin elements used to host the bundles. It was found that the out-of-plane fibre curvature had little effect on the in-plane tensile modulus, but the ultimate tensile strength (UTS) decreased by up to 34% with an increase in fibre bundle curvature from 1 to 35 degrees in the unit cell [166].

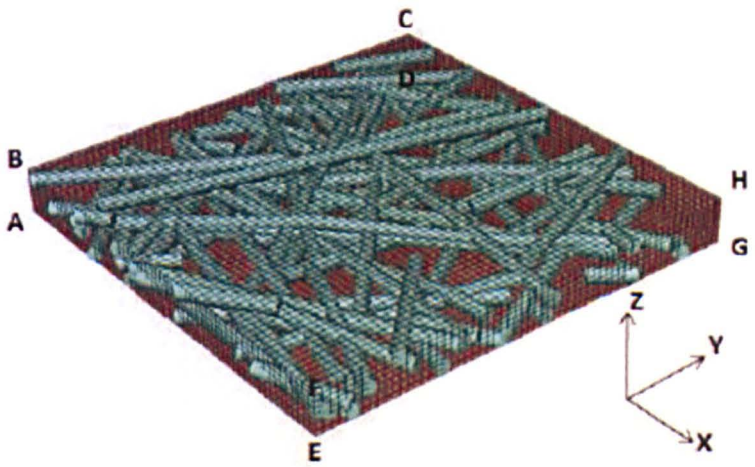

Figure 36 - 3D fibre bundle network model developed by Luchoo et al. [166]

The model still hosted the fibre bundles in the resin using the *Embedded Element technique, preventing failure mechanisms such as interfacial debonding and bundle pull out from occurring. The processing time of the 3D fibre network FE models also increased by two orders of magnitude when compared to the 2D

models produced in [68], attributable to the additional degrees of freedom of the bundles in the 3D model [166].

Pan et al. [2, 43, 172] have produced 3D macroscale models for discontinuous materials with glass fibre bundles represented by a dodecagonal approximation of an elliptical cross-section, shown in Figure 37. Linear segments were used to model the fibres; however there is a sharp change in orientation as the fibres pass through sub-layers of the model at intersection points, resulting in large local stress concentrations at the inflection points. This is not physically representative of a discontinuous composite material, with Figure 38 showing the fibre network generated. It was observed in [166] that the fibres out-of-plane orientation changes gradually without abruptly changing direction, with the approach adopted in [2] unable to capture the effects of fibre compaction and redistribution in areas of high volume fraction. The results from the model were compared to experimental results, with errors of less than 5% observed between the predicted UTS of the model and test coupons [69].

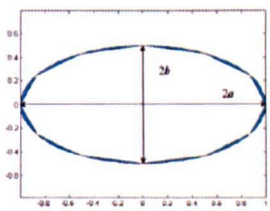

Figure 37 - Dodecagonal approximation of bundle cross-section adopted by Pan [2]

Figure 38 –3D fibre network produced by Pan [2] (left), with the inflection points shown to allow fibres to pass through sub-layers in the model (right).

A random sequential fibre absorption scheme was adopted in [2], limiting volume fractions to 35-40% due to fibre 'jamming'. Random sequential absorption (RSA) and Monte Carlo (MC) methods add fibres to layers in an RVE and avoid fibre-fibre intersection by discarding contacting fibres. Random numbers are generated for the orientation and position of the centre of the fibres, with 'jamming' occurring when regions of free space are too small to accept additional fibres as intersections become unavoidable in the remaining free volume [173]. RSA adds successive fibres to an RVE, whilst the MC method initially deposits all fibres inside the RVE, before algorithms are implemented to rearrange the fibres in the volume, without violating the contact algorithm [174, 175]. RSA and MC can therefore inadvertently homogenise the material, which is unrepresentative of a discontinuous material which can have areas of high and low volume fraction across a component. Both methods produce architectures that appear random on a global scale, but clusters of aligned fibres are introduced at the local level [176].

Dumont at al [177] developed macroscale models using the methodology outlined in [178, 179], with slender fibre bundles immersed in an incompressible Newtonian fluid, allowing a connected fibre bundle network to be produced. The interaction between two individual bundles is shown in Figure 39, with the sheared zone between the inclusions highlighted. The full fibre bundle network produced by the model, Figure 40, was developed to predict the orientation change of fibre bundles in a short fibre bundle composite induced during the forming process. Bundles are allowed to bend along their length as the volume fraction in the cell is increased, with variation also found in the elliptical bundle cross-section in areas of high bundle density [177]. The model produced in [177] has an upper limit of 30% for the volume fraction of fibre bundles contained in the RVEs, limiting its use as it cannot be used to model high volume fraction parts produced from techniques such as the BRAC3D process [36].

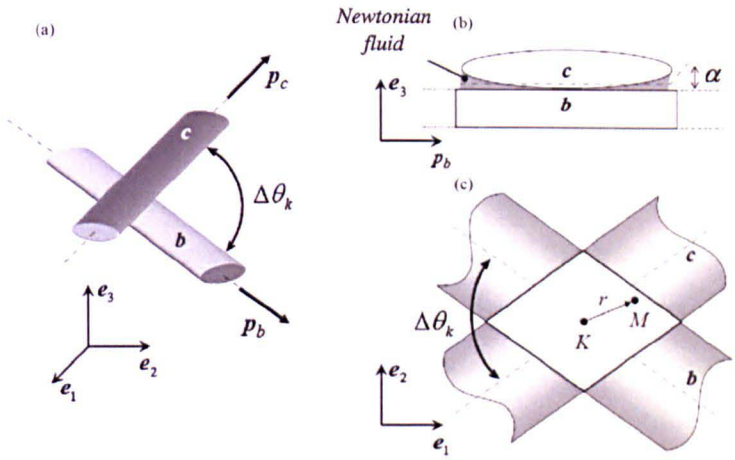

Figure 39 - Bundle-bundle interactions. (a) Isometric view of connected bundles, (b) side view of the sheared zone between the bundles, and (c) plan view of the overlapping surfaces. Reproduced from [177].

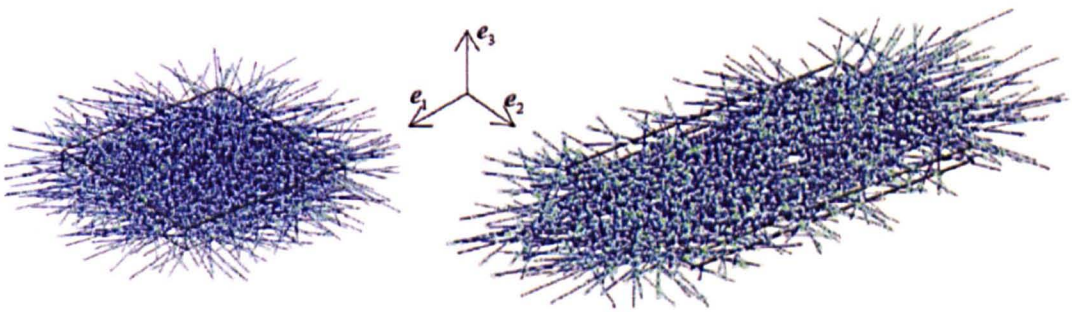

Figure 40 - Macroscale model developed by Dumont et al [177] to predict orientation change in short fibre bundle composites during the forming process. (Left - 25mm x 25mm x 2.5mm RVE with 437 bundles of length 25mm. Right - RVE after flowing under plane strain deformation.)

Evans and Ferrar [176] demonstrated that achievable fibre volume fractions with RSA techniques is a function of the fibre AR. Volume fractions as high as 60% can be achieved for ARs of 1 (sphere), but this reduces to less than 40% for ARs of 6. Kari [110] created discontinuous fibre RVEs with inclusions of different AR, which allowed for volume fractions of up to 40% to be generated. MC methods are limited to volume fractions of 20-25%, depending on the AR of the fibres [110, 174]. Both the RSA and MC method fall short of the 55% volume fractions that are achievable in discontinuous materials [36, 180], with Duschlbauer et al

[174] concluding that forced packing and the introduction of agglomerations are required to produce higher volume fraction RVEs. The difficulty of generating the fibre architecture at higher volume fractions (~50%) was highlighted in [159], due to the computational expense and complexity of the algorithms needed to deposit bundles without self-intersection. Another issue is the meshing of the models, with a very fine mesh required close to the fibre intersections due to the close proximity of the fibres and also to capture the stress transfer between the fibres, which can lead to a significant increase in computational run time for the models.

Luchoo et al. [159] used an alternative strategy to avoid the problem of fibre 'jamming', using 2D shell elements embedded in a 3D volume of resin. A force-directed attraction-repulsion algorithm is used to redistribute the 2D fibres as pressure is applied from the matched mould tool, shown in Figure 41. This allows a randomly distributed fibre network to be produced that is smoothly interpolated in 3D space (Figure 42). This strategy allows representative high volume fraction RVEs to be produced, but the model still uses the *Embedded Element technique employed in [68]. By hosting the fibre bundles in the 3D resin elements debonding between the two constituents is prohibited, limiting the failure mechanisms that can be observed in the FE analysis. The model is also computationally expensive, in the generation of the RVEs themselves, due to the complexity of the algorithms required to deposit and then relocate the fibre bundles, and in the running of the FE analysis.

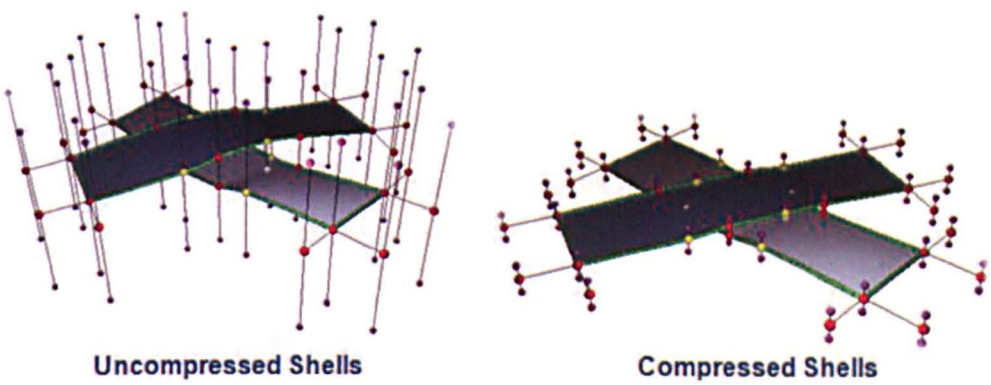

Figure 41 – Force-directed algorithm used by Luchoo et al [159] to generate discontinuous fibre architectures.

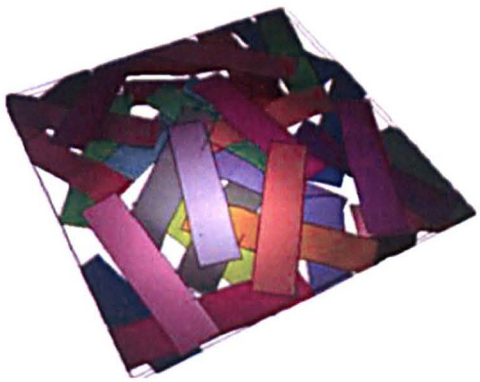

Figure 42 - Sample RVE produced by Luchoo et al [159].

2.5.3 Review of macroscale RVEs and associated boundary conditions

Fibre bundle length, bundle aspect ratio and volume fraction all contribute to the bundle architecture observed in a discontinuous composite and can influence the size of the RVE required, with these factors also dictating the stiffness and strength of the material. To avoid the need for large, computationally inefficient unit volumes it is necessary to establish a methodology to determine the RVE size for discontinuous materials. A review of current RVE generation techniques for macroscale models is detailed in this section, with appropriate boundary conditions identified to allow a reduction in RVE size for FE analysis of discontinuous materials.

Periodicity is often imposed on material models to reduce the size of the RVE required for FE analysis [43, 110, 175, 181, 182]. Fibres, or bundles, that cross the RVE boundary are cut and shifted to the opposite face to maintain periodicity. Gitman et al [183] used periodic boundary conditions for randomly heterogeneous transverse bundles and spherical inclusions, and found that smaller RVEs (~30%) are required when compared to models with non-periodic conditions. Pan et al [43] used periodicity, shown in Figure 43, to ensure that each fibre deposited was fully contained in the RVE. By cropping the fibres, a representative number of bundle ends will be contained in the RVE. However, it was found in [184] that enforcing periodicity for long slender fibres with larger aspect ratios can cause a boundary effect, influencing the local fibre volume fraction distribution around the edge of the model, which can affect the critical size of the RVE. This

boundary effect can eliminate the randomness in a material and can create a pseudo-random situation as the randomness is compromised.

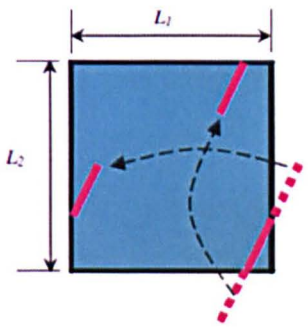

Figure 43 - RVE geometry periodicity of fibres after being cut at the boundary and translated to opposite faces [43]

Some authors have opted to use an alternative approach to avoid imposing periodicity, where the region of interest (ROI) is embedded in a homogenous material to transmit the applied load [185-187]. The embedding of the cell leads to perturbations in the local stress and strain fields at the boundary of the ROI, similar to the periodic approach [184]. A study was conducted in [184] to compare the embedding of the ROI in a homogenous and heterogeneous material, to determine the critical decay length for both models. Figure 44 shows the approach adopted in the study, with a critical decay length of 0.5 and 2 fibre lengths found for the homogenous and heterogeneous models, respectively. The heterogeneous approach resulted in larger models being required for analysis, however this approach was considered to be more reliable than the homogeneous approach, which had large stress perturbations at the bundle ends at the boundary. The critical decay length of two fibre lengths found in the study in [184] was consistent with the findings in [149], where a decay length of two times the reinforcement scale was found for a unidirectional fibre reinforced composite with fibres distributed at random over a transverse cross-section.

Saint-Venant's principle [188] was exploited in [184] on the inner region of the model, defined as the RVE in Figure 44, with periodic boundary conditions imposed on the outer model boundary. Saint-Venant allows an approximation to the exact solution to be calculated if the RVE is a critical 'decay length' away

from the boundary. The distribution of nodal displacements can be integrated with respect to the nodal position along the boundary in question, in order to obtain the average displacement of the RVE [184]. By utilising Saint-Venant's principle, the effects of the boundary conditions are removed from the analysis, thus improving the accuracy of the model when predicting the modulus and strength of the discontinuous material.

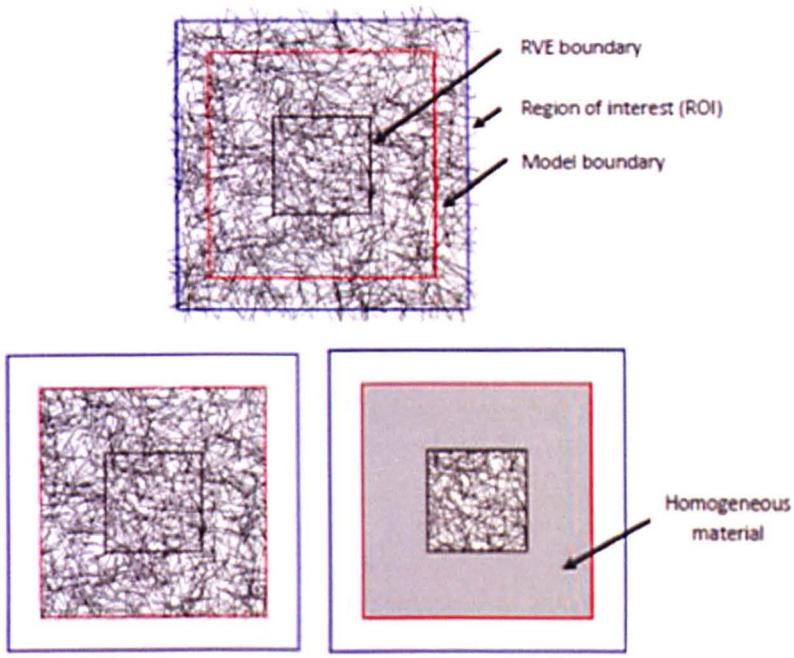

Figure 44 - Schematic of models in [184]. (Top) As-deposited state, (bottom - left) trimmed state for heterogeneous approach and (bottom - right) trimmed state for homogeneous approach. (Note: Black lines represent the bundle centre lines).

Limited data exists in the literature for defining the critical size of RVEs for non-aligned discontinuous fibre composites. A study was conducted in [189] to determine the critical (minimum) size for discontinuous RVEs, and it was found that it is more efficient to test fewer larger models than many smaller models, for the same level of statistical confidence (~95%) when determining the elastic material properties. In [172] the RVE boundary length was set to at least two times the fibre length, with the study in [189] determining that an optimum RVE edge length is 4 times the fibre length. Convergence of the effective mean values for E_1, E_2 and G_{12} was found in [189] with this greater RVE edge length, with the results independent of the fibre volume fraction of the material. The Poisson's ratio was largely unaffected by the RVE size of the FE models. The model

developed in [184, 189] uses the embedded element technique adopted in [36], which has limitations in the failure mechanisms that can be observed in the material as the resin elements host the fibre bundles.

2.6 Summary

2.6.1 Material characterisation

Interactive failure criterions, such as von Mises, Tresca and Drucker-Prager, are ideally suited to isotropic materials as they combine the principal stresses in all directions before determining if failure has occurred. Independent failure criterions, such as Maximum Stress criterion and Maximum Strain criterion, are better suited to transversely isotropic materials as they allow different stiffness and strength values to be assigned in each principal direction. In this thesis, Maximum Stress criterion has been selected to predict the onset of failure in the fibres and bundles for analysis, with von Mises selected to define the onset of failure for the matrix material.

2.6.2 Microscale modelling

The use of cohesive elements, or equivalent spring/connector elements, is necessary to simulate debonding, with this methodology adopted at the microscale to predict the debonded lengths of single fibre composites. The cohesive parameters established in this section will be used to define the behaviour of the cohesive elements used in the microscale analysis of a single fibre composite. The traction-separation laws developed at the microscale will then be directly used at the macroscale when simulating debonding of high volume fraction discontinuous composite materials.

The factors that influence the ineffective length of a broken fibre and the positively affected length (PAL) of a neighbouring, intact fibre have been reviewed. It was noted that the presence of a soft interface reduces the reinforcing efficiency of a broken fibre, therefore limiting the strain concentration in the surrounding fibres, whilst a stiff interface yields less and the surrounding fibres will experience a higher strain concentration factor [48]. When debonding occurs in a composite material the ineffective length of the broken fibre increases, with

the PAL of the fibres adjacent to the fibre break also increasing, which could lead to further fibre fractures in the composite [129].

Appropriate boundary conditions have been identified to generate unit cells to determine the mechanical properties of fibre bundles, using the methodology outlined by Li et al. [150, 151]. A hexagonal packing arrangement has been selected to determine the bundle properties in this analysis, as it was found in [150, 151] that a hexagonal arrangement is more representative of the fibre bundle and preserves the transverse isotropy of the unidirectional composite model.

2.6.3 Mesoscale modelling

Numerical models have been developed to look at the interaction of fibres at crossover points, to establish the influence of orientation and separation when determining the mechanical properties of composite unit cells. In [43] the influence of in-plane and out-of-plane orientations of the fibres were investigated, with it shown that the out-of-plane angle has little impact (~0.01%) on the stiffness of the unit cell. The number of intersection points in a discontinuous composite, as estimated by Toll [165], is known to impact the elastic constants of unit cells, with potential errors of up to 34.5% estimated when predicting the elastic constants of composites with 55% V_f [43].

2.6.4 Macroscale modelling

It has been shown that the macroscale structure of a discontinuous composite material is complex and is influenced by multiple variables. Filaments tend to remain in bundle form, especially at longer bundle lengths (>20mm), which provides variations in local volume fraction across a component. At shorter bundle lengths (<20mm), natural filamentisation is likely to occur as the bundle loses its integrity, increasing the homogeneity across the discontinuous material [8].

A review of numerical models has shown that producing random fibre bundle architectures is a complex process. Some models are limited on achievable fibre

volume fractions [2, 43, 110, 172, 174], whilst others do not allow for the full range of failure mechanisms of the composite material because of the use of the *Embedded Element technique [36, 68, 159, 166]. Replicating the in-plane orientations and out-of-plane waviness that can be observed in the discontinuous materials, in addition to the interactions between the fibre bundles, has proven to be difficult. The correlation of results with experimental data is also limited, with error margins in the order of 10% and 20% for the prediction of modulus and strength, respectively, in current models [68, 159].

An optimum macroscale model should be able to model volume fractions approaching 50%, with the full array of failure mechanisms associated with discontinuous materials permitted; matrix cracking, bundle fracture, bundle pull-out and interfacial debonding between bundle and matrix. Currently, there is no published work in the literature that can satisfy all of these requirements. The findings from [189] will assist the macroscale model development in this thesis, with RVE boundary lengths set to a minimum of 2 times the fibre length in the analysis [149].

Chapter 3 Methodology

3.1 Material characterisation

3.1.1 Individual filament properties

Manufacturer data for the carbon fibres used in the development of the BRAC3D process is detailed in Table 4. These values will be used when looking at microscale models of discontinuous composite materials. Transverse and shear mechanical properties of fibre bundles will be calculated, to complement axial tensile tests conducted in sections 3.1.2.

Table 4 - Carbon filament properties supplied by Toray for T700 12k 50C. [190]

Axial Tensile Modulus, E_{33} (GPa)	230.00
Diameter (μm)	7.0
Axial Tensile Strength, σ_{33T} (MPa)	4,900
Density (g/cm^3)	1.80
Strain (%)	2.1
Sizing (%)	1.0

Determining the strength of filaments is complex as the length of the filaments is known to be critical, with many studies [191-195] showing that the tensile strength of single brittle filaments decreases with increasing length. According to Weibull's weakest link theory [196], the strength of a brittle material, such as carbon filaments, is size dependent as there is a higher probability that a larger volume of material will contain a critical flaw. The Weibull relationship for the mean fibre strength, $\bar{\sigma}_f$, is a function of the fibre length, l, shown in Equation 13. The gamma function, Γ, is a constant determined experimentally, m is the Weibull modulus and σ_0 is the filament strength at l = 1mm.

$$\bar{\sigma}_f(l) = (\sigma_0)\,\Gamma\left(1+\frac{1}{m}\right) l^{-\frac{\gamma}{m}} \qquad \text{Equation 13}$$

Values of $m = 9.7060$, $\gamma = 1.5083$ and $\sigma_0 = 5199.4$MPa were used in [8] to predict the strength of carbon filaments, where the tensile strength of the filament was shown to reduce by 37% as the gauge length was increased from 5mm to 100mm.

Van Hattum [197] used a Weibull modulus value, m, of 20 for carbon filaments based on the findings in [198, 199], with the strength of 80mm carbon fibres shown to be 40% lower than the strength of 5mm fibres in that study. Experimental work was conducted by Pardini et al [200] on single carbon fibres at different gauge lengths, with the results from this study presented in Table 5. It was shown that as the gauge length increased from 25mm to 100mm the tensile strength reduced by approximately 12%, whilst the tensile modulus was largely unaffected.

Table 5 - Variation in tensile strength of carbon fibres as a function of the gauge length, reproduced from [200].

Specimen Gauge Length (mm)	Tensile Strength (GPa)	Extension at break (mm)	Calculated Strain (%)*	Young's Modulus (GPa)
25	2.90 ±0.97	0.3250	1.318	220.00
50	2.70 ±0.72	0.5631	1.126	240.00
75	2.66 ±0.87	0.8351	1.113	240.00
100	2.54 ±0.80	1.0882	1.088	233.00
Average	2.70 ±0.15		1.1612 ±0.10	233.00 ±9.40
* assuming ideal Hookean behaviour (linear elastic material)				

Although the length of the filament has been shown to directly influence the filament strength, the lengths of the filaments in the analysis contained in the microscale analysis in this thesis will not exceed 1mm. Therefore, it will be assumed that the fibre strengths are constant throughout the microscale analysis, with the values used detailed in Table 4. The lengths of the fibre bundles considered in the analysis at the meso and macroscale are much greater than the fibre lengths considered in the analysis at the microscale. Therefore, Weibull effects must be incorporated at the meso and macroscale to quantify the reduction in strength of the fibre bundles with increasing length.

3.1.2 Fibre bundle tensile testing

3.1.2.1 Background

Fibre bundles are comprised of thousands of filaments and a matrix material when formed in a composite, with the rule of mixtures (ROM) approach traditionally adopted to determine the mechanical properties of the bundle in the longitudinal direction. The volume fraction of filaments in the bundle is determined, typically using microscopy, with the bundle considered to be a unidirectional composite for the purpose of calculating the modulus and strength along the axis of the bundle. This method has its limitations, as it does not typically account for fractures that may exist along the lengths of the fibres that make up the bundle. In addition to this, coatings are also applied to fibres and the ROM approach overlooks this in the determination of the mechanical properties of the bundle.

Weibull theory has also been applied at the mesoscale to fibre bundles which contain thousands of filaments, but the results are less conclusive [8]. Bader and Priest [162] reported that the mean strength of 1K carbon tows was reduced by 10% when the gauge length was increased from 20mm to 300mm, which is lower than the reduction seen for individual filaments in section 3.1.1. Weibull theory assumes that failure is sudden and therefore component failure coincides with failure of the weakest link. This oversimplifies the failure of a fibre bundle as the failure can be progressive, with load redistributed to adjacent filaments by shear transfer through the matrix when a single filament fails [201]. With this uncertainty in determining the mechanical properties of carbon fibre bundles, it was deemed essential to perform an experimental study to determine the tensile strength of Toray T700 12k 50C tows at a range of gauge lengths.

3.1.2.1 Tensile testing

Impregnated single fibre bundles were manufactured according to the test standard BS EN ISO 10618:2004. The test standard specifies a method of testing for the determination of the tensile strength, tensile modulus of elasticity and strain at maximum load of a resin-impregnated yarn specimen, applicable to yarns of carbon fibre used as reinforcements in composite materials. The calculation of

tensile strength at a range of bundle gauge lengths was of primary interest in this study.

To manufacture test samples, a bobbin of fibre was placed on a creel stand and pulled through an impregnation bath filled with epoxy resin. The tow was passed over a series of rollers to control the resin content (target of 60% V_f) before being wound onto a frame consisting of four Ø10mm rods configured in a square pattern. The impregnated bundles were hot-air cured at a temperature of 80°C for two hours. Gurit PRIME20 epoxy resin was chosen to comply with the test standard, having a strain to failure of 4.1% (according to the manufacturer's data sheet). Figure 45 shows the bundle test specimens after manufacture.

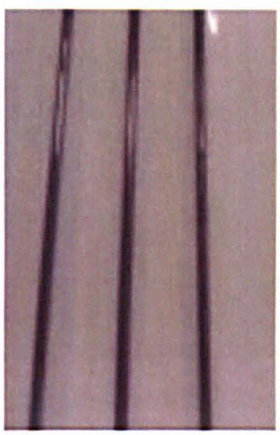

Figure 45 - Bundle test specimens produced for tensile testing according to the test standard BS EN ISO 10618:2004.

A near circular cross-section with no macroscopic voids, approximately 1mm in diameter, was achieved when manufacturing the bundles, with a representative optical micrograph shown in Figure 46. Bundles were tabbed at each end using the two plate method shown in Figure 47, in order to avoid premature failure at the jaws of the testing equipment. Specimens were tested to failure at an extension rate of 1mm/min. The ultimate tensile strength values were calculated based on the effective cross-sectional area of 12,000 filaments with an average filament diameter of 7μm each – based on the manufacturer's data in Table 4. The contribution of the resin was ignored in the calculations as it was deemed to be negligible, with the strength of the individual filaments calculated and compared to the strength specified by the manufacturer (4,900MPa - Table 4), shown in

Figure 48. Fifteen repeats were tested for each gauge length (10mm, 20mm, 50mm, 100mm, and 150mm).

Figure 46 - Typical cross-section of an impregnated Toray T700 12k 50C tow.

Figure 47 - Tabbing configuration used for bundle test specimens.

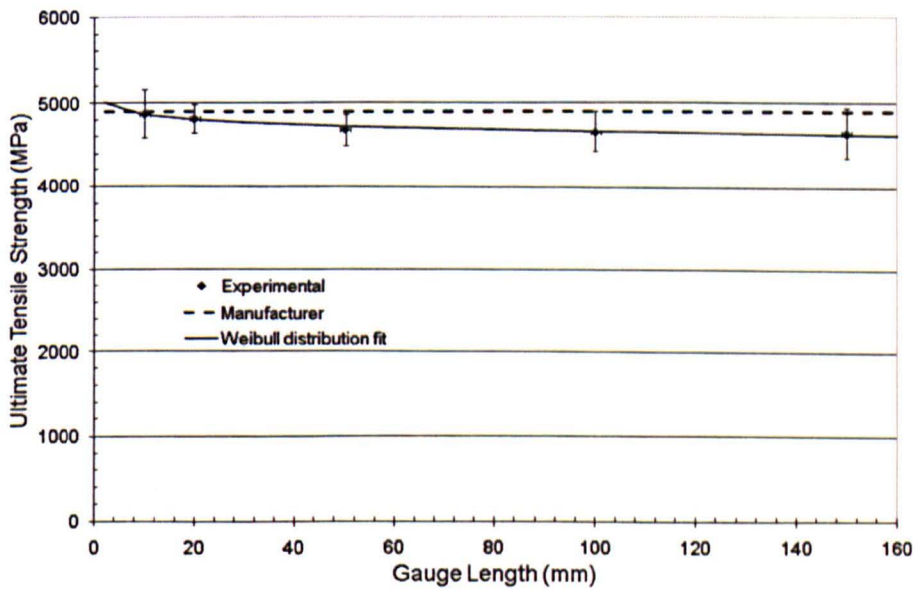

Figure 48 - Ultimate tensile strength results compared to manufacturer data and Weibull distribution fit for the filaments contained in a single impregnated bundle.

At the shortest gauge length of 10mm, the experimental values for the filament strength are shown to be within 0.6% of the UTS values quoted on the manufacturers' data sheet. In general, there is a reduction in UTS with increasing gauge length, with the UTS for a 150mm gauge length being just 4.4% lower than that of a 10mm gauge length. A non-linear regression analysis has been performed using NLREG v6.3 to summarise the experimental data for finite element modelling purposes. A two-parameter Weibull distribution has been used, where σ_{l_0} is the scale parameter, γ is the shape parameter and l_0 is a typical gauge length of 50mm:

$$\sigma_1 = \sigma_{l_0} \left(\frac{l}{l_0}\right)^{-\frac{1}{\gamma}} \qquad \text{Equation 14}$$

σ_{l_0} and γ were estimated to be 4725.21MPa and 55.896 respectively, with a Correlation Coefficient (R^2) of 94.5% between experimental data and the values calculated using Equation 14. The Weibull distribution plot is compared with the experimental data in Figure 48. Using Equation 14, the strength of filaments can be determined at a range of gauge lengths. To calculate the ultimate tensile strength (UTS) of a fibre bundle, the strength calculated by Equation 14 is multiplied by the fibre volume fraction of the bundle, with the UTS predictions for a 60% V_f bundle at a range of gauge lengths shown in Table 6.

Table 6 – Predicted carbon fibre bundle strength (60% V_f) at a range of gauge lengths. (Note: These lengths can currently be cut using the BRAC3D process).

Fibre Bundle Length (mm)	Ultimate Tensile Strength (MPa)
2	3003.18
10	2917.95
18	2887.42
36	2851.84
54	2831.23
90	2805.47
140	2783.38
180	2770.89

The results obtained in this section provide axial strength data that will be used for carbon fibre bundles at the meso and macroscale for finite element predictions.

The strength of the bundle is calculated using Equation 14 based on the bundle length considered in the analysis. The modulus in the axial, transverse and shear directions is calculated using finite element models of a unit cell generated to represent a fibre bundle in section 4.1.3.

3.1.3 Epoxy matrix testing

3.1.3.1 Background

The epoxy resin used in the BRAC3D process [36] is a development system produced by Hexcel called DLS 1776. It is a powdered epoxy that is deposited at the same time as the fibre bundles during the manufacture of discontinuous components. The powdered epoxy is heated momentarily, via the use of a custom burner design shown in Figure 49, to turn the powder into a semi-liquid state. As the powder hits the tooling, held at ambient temperature, it quickly cools and solidifies resulting in a net shape charge with 100% tool coverage. The cycle is completed by transferring the highly conductive tool skin to a separate moulding station (at temperature ~125°C) and curing the charge under heat and pressure in a matched-sided tool for approximately 23 minutes [36].

As the epoxy was a prototype, with an unconventional cure cycle, its mechanical properties were unknown. Testing was therefore necessary to determine the mechanical properties for three key loading scenarios – tension, compression and shear; allowing the calculation of modulus, yield stress and failure stress/strain for each load case.

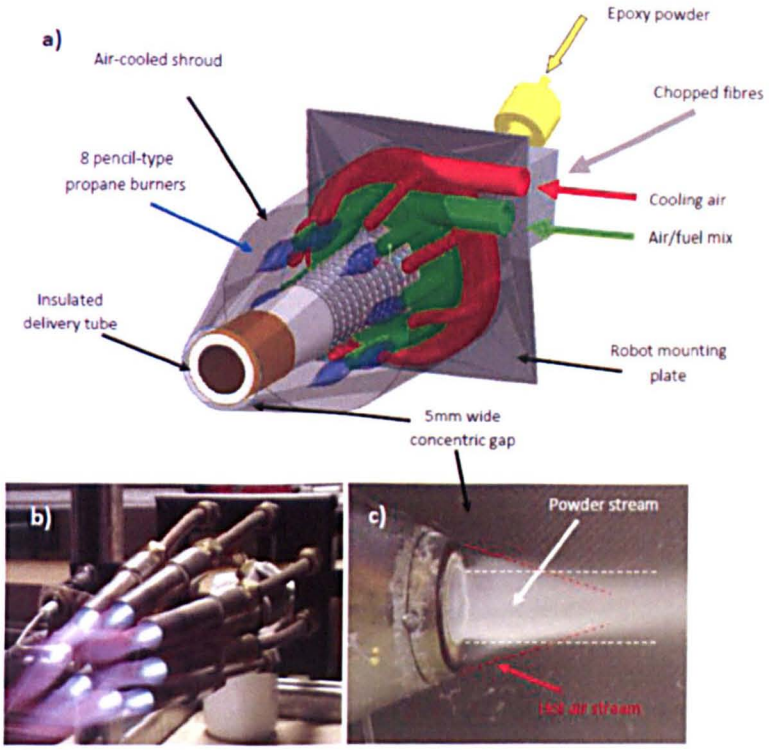

Figure 49 - (a) Propane-fuelled burner. (b) Outer shroud removed to show ignited burners. (c) Burner tip showing air stream convergence with powder stream [1].

3.1.3.2 Preparation of samples

To produce neat resin plaques, the virgin DLS 1776 powder was deposited onto a polished aluminium plate (0.8mm thick) at room temperature. A 5mm thick frame, cut from Rohacell 7IG foam, was used to constrain the flow of the resin and the inner dimensions of the frame were 300mmx400mm. A second 0.8mm thick polished plate, equal in size to the outer frame, was placed on top of the Rohacell dam. This entire arrangement was then placed inside a vacuum bag and evacuated of air, before being loaded into a hot air oven at 125˚C for 23 minutes. The plaques were left to cool to ambient temperature before dismantling to avoid any cracking of the material.

Once the plaques were manufactured, the samples were water-jet cut to the required size, according to the following test standards:

Tension - BS EN 2747-1 [202].

Compression - ISO 604 [203].

Shear - ASTM D7078 [204].

The edges of the specimens were all polished using 400 grit abrasive paper to remove any potential stress raisers. The surfaces and edges of the specimens were then inspected to ensure they were free from scratches or any other visible imperfections that could influence the results. Ten specimens were tested for each of the loading scenarios and the mean results are presented in section 3.1.3.5.

3.1.3.3 DIC experimental testing procedure

Specimens were loaded to failure in a hydraulic Instron 500 tension/compression machine, at an extension rate of 1.0 mm/min. A sampling rate of 1Hz was adopted for the load data acquisition. A Limess Vic3D Digital Image Correlation (DIC) system was used to produce full-field strain measurements of the experimental test specimens. This method was contactless and therefore eliminated the potential risk of premature failure caused by the jaws of a clip-on extensometer, with the use of DIC also ensuring that out-of-plane movement was accounted for in the calculations of modulus.

The surface of each sample was sprayed white and then a black speckle pattern was applied to obtain a randomised grey level distribution. Both layers of paint were applied using a Harder and Steenbeck Evolution Airbrush, with a Ø0.4mm splatter nozzle. Efforts were made to ensure that the diameter of the speckles were as uniform in size, but not distribution, and as small as possible to provide a good spatial resolution.

A white light (6400K colour temperature) was used to illuminate the area of interest. Images of the specimen surface were recorded throughout the test at an acquisition rate of 0.33 Hz, via two 2.0 Megapixel CCD cameras fitted with Pentax C37500 lenses (f = 75mm, 1:2.8 D). The cameras were mounted on a tripod positioned 1.5m away from the subject to provide a 120×120mm field of view. The local displacement resolution of the system is 0.01pixels, which corresponds to 0.24μm for the current set up. An image processing unit was used to calculate a three-dimensional displacement field, based on correlation calculations. The method consists of correlating the grey pixels in each deformed image to the counterpart in the undeformed (reference) image. The area of interest of each image was divided into small square subsets of size 25×25 pixels, using a

step size of 3 pixels (i.e. the subset moves by 3 pixels in the x and y directions – providing a small degree of overlap in the strain calculations). Digital images were recorded in Limess VicSnap during testing, in preparation for post processing analysis in Limess Vic3D.

3.1.3.4 Experimental testing results

Tensile testing

Ten dog-boned tensile specimens were water-jet cut from each plaque in accordance with BS EN 2747-1 [202]. The dimensions of the dog-boned specimen are shown in Figure 50. A digital micrometer was used to measure the thickness, width and length of the specimens to three significant figures, with five measurements of each recorded and averaged to determine the effective cross-sectional area of the specimen.

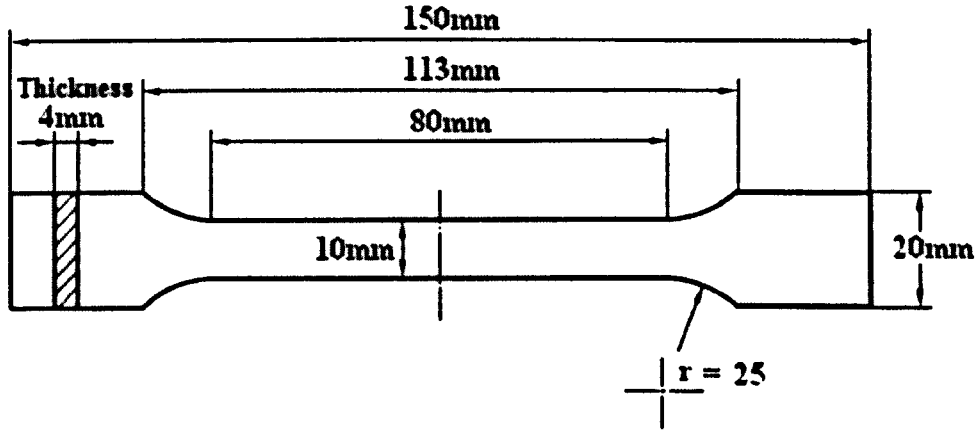

Figure 50 - Specimen dimensions for tensile tests, according to BS EN 2747 [202].

Figure 51 shows images of a tensile specimen undergoing testing with the DIC, with the left image showing the speckle pattern on the sample and the right image showing the local strain field at 2.21% global strain. A summary of the results obtained from the tensile tests is shown in Table 7. The DLS epoxy behaved in an elastic-plastic manner, with a clear yield point at 25MPa. Up until the point of yield, the increase in stress was proportional to the increase in strain, with a constant elastic modulus of 3.35 GPa for the material. After reaching the yield point of 25MPa the resin behaved in a non-linear manner as it began to deform

plastically, failing at an ultimate strain of approximately 2.5%, with an UTS of approximately 65MPa. The stress-strain curve for the DLS 1776 epoxy from the tensile testing is shown in Figure 52. The Poisson's ratio of the epoxy was also calculated using the tensile test results (Table 7) by dividing the strain experienced by the Region of Interest (ROI) in the transverse direction by the strain in the loading direction.

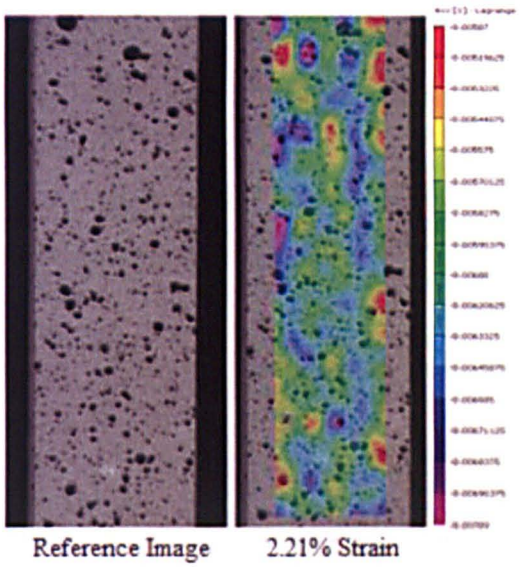

Figure 51 – DIC reference image (left) and image taken prior to final failure at 2.21% global strain (right) for a dog-boned DLS 1776 resin sample.

Table 7 - Summary of results obtained from DIC tensile testing.

Tensile Modulus (E_T)	Yield Strength (σ_y)	Ultimate Tensile Strength - UTS (σ_T)	Strain to Failure (ε_t)	Poisson's Ratio
3.35GPa (± 10.9%)	25MPa	65MPa (± 7.8%)	2.50%	0.38

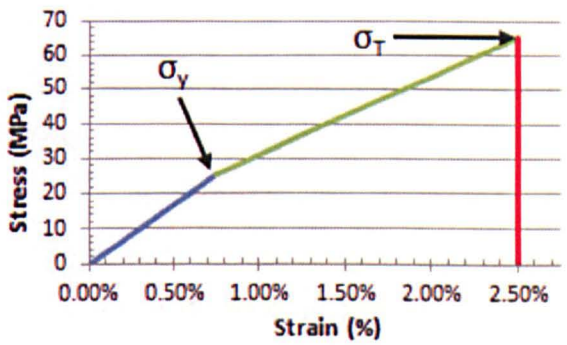

Figure 52 – Approximation of stress-strain curve for DIC tensile testing of DLS 1776 epoxy.

Compression testing

Two sample sizes were required for the compressive testing of the epoxy matrix to comply with the ISO 604 test standard [203], one to determine the modulus and the other to determine ultimate strength (shown in Table 8). Hardened steel compression plates were fitted to the Instron to apply the deformation load to the test specimens. Ten specimens were tested for each test method, at a compression rate of 1.0mm/min. Five measurements of the thickness, width and length of the specimens were taken with a digital micrometer to three significant figures, before being averaged to determine the effective cross-sectional area, to allow calculation of the compressive modulus and strength. Figure 53 shows an image taken using DIC of a compressive strength test, with a specimen undergoing a compressive modulus test shown in Figure 54.

Table 8 - Specimen dimensions for compression tests, according to ISO 604 [203].

Type	Measurement	Length (mm)	Width (mm)	Thickness (mm)
A	Modulus	50 ± 2	10 ± 0.2	4 ± 0.2
B	Strength	10 ± 0.2	10 ± 0.2	4 ± 0.2

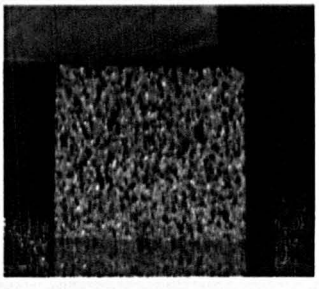

Figure 53 - Sample image from DIC compression testing of DLS 1776 – strength.

The results obtained from the two compressive tests on the DLS 1776 epoxy are detailed in Table 9. The modulus of the resin was determined to be 7.53GPa, which is over two times greater than the calculated tensile modulus. The compressive strength of the resin was approximately 316MPa, almost five times greater than the 65MPa tensile strength. In metals, the compressive and tensile modulus is often very close, however, in polymers the tensile and compressive modulus can vary widely, with the variation often 50% or greater, depending on

the resin type [205]. An epoxy material typically exhibits greater stiffness and strength in compression than it does in tension, with the values obtained from the experimental tests in this section comparable with other commercially used epoxies in composite materials [206]. The behaviour of the epoxy was linear-elastic in the compression tests and this is modelled accordingly in the UMAT developed in section 3.2.

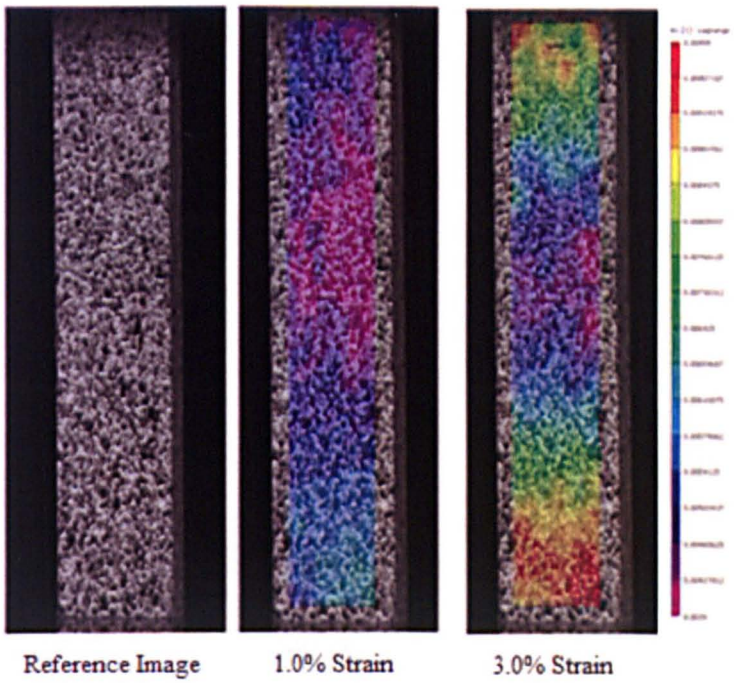

Figure 54 - Sample images from DIC compression testing of DLS 1776 – modulus.

Table 9 - Summary of results obtained from DIC compression tests for DLS 1776. (Note: Strain to failure is calculated using the modulus and strength of the material).

Compressive Modulus (E_C)	**Compressive Strength (σ_c)**	**Strain to Failure (ε_c)**
7.53GPa (± 16.3%)	316.0MPa (± 11.1%)	4.20%

In-plane shear testing

Ten specimens were prepared for the v-notched shear rail test, ASTM D7078 [204], with the dimensions of the samples shown in Figure 55. The shear rail test is typically used to determine in-plane shear properties of composite materials that have fibres parallel and/or perpendicular to the loading direction. It has been used

to determine the in-plane shear properties for DLS 1776 epoxy due to a lack of availability of other test rig facilities, notably ASTM D732–10 [207]. It is accepted that the results obtained from the test are limited, but as the material is a prototype and no manufacturer data is available, it was deemed essential to conduct the tests to provide an initial prediction for the shear modulus and strength of the resin.

The specimens were subjected to an extension rate of 1.0mm/min applied at the shear rails, with DIC used to track the local strain, shown in Figure 56. The central region of the sample is subjected to shear loading and the average shear strain across this region was calculated using the post-processing software Limess Vic3D. Table 10 shows the shear modulus, strength and strain to failure obtained from the ASTM D7078 shear rail test.

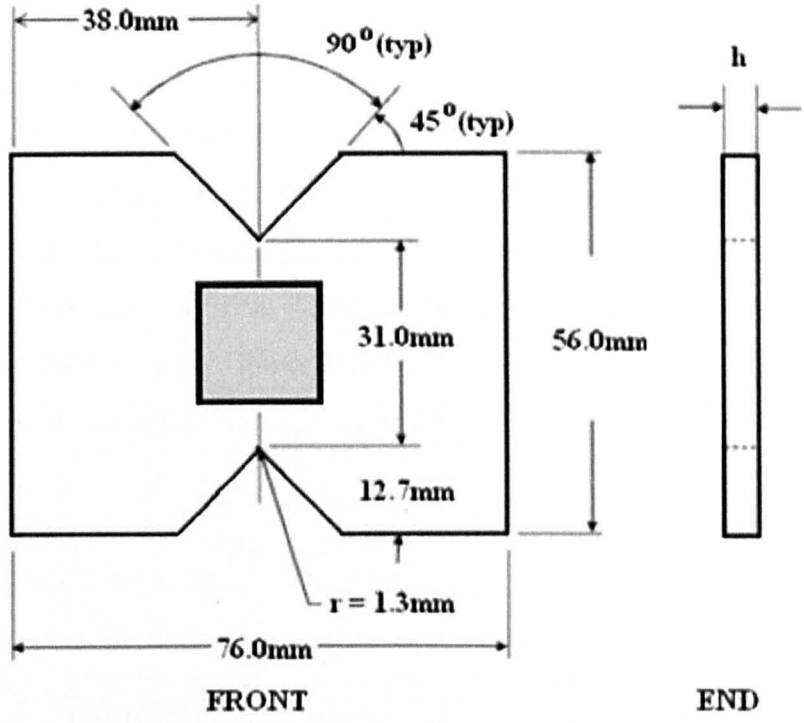

Figure 55 - Specimen dimensions for ASTM D7078 v-notched shear rail test [204]. Strain was averaged across the grey region in the centre of the test sample for the calculations. (Note: The specimen thickness, h, in this analysis was set to 5mm).

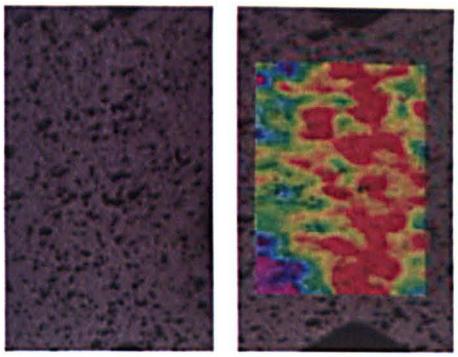

Figure 56 - Sample image from DIC shear testing of the DLS 1776 epoxy.

Table 10 - Summary of results obtained from DIC shear tests for DLS 1776 epoxy. (Note: Strain to failure is calculated using the modulus and strength of the material).

Shear Modulus (G_{xy})	**Shear Strength (σ_{xy})**	**Shear Strain to Failure (ε_{xy})**
2.08GPa (± 18.7%)	32.8MPa (± 13.8%)	1.70%

Although the ASTM D7078 test isn't ideally suited for shear testing of a neat resin sample, the results obtained are comparable to the mechanical properties obtained using the ASTM D-732 test method for neat epoxy resin samples, with shear strength values of 34.5MPa and 37.2MPa quoted in [208] and [209], respectively. If the shear modulus of the material is calculated using the tensile modulus of the material using Equation 15, then the predicted shear modulus is 1.214GPa, which is much lower (~41%) than the actual shear modulus of the material calculated in the experimental testing.

$$G = \frac{E}{2(1+\nu)} \qquad \text{Equation 15}$$

3.1.3.5 Epoxy matrix properties

A summary of the results from the three experimental tests is presented in Table 11. The compressive and shear tests do not have a value for yield stress, as the DLS 1776 behaved in a linear-elastic manner up until the point of failure under these loading conditions. However, the epoxy did show a clear yield point when under tension and this was found to be at 25 MPa. The properties obtained from

the experimental tests were of a similar magnitude to that of manufacturer's data for more conventional and widely available epoxy materials [206].

Table 11 - Summary of DLS 1776 epoxy experimental testing results

	Tension	Compression	In-Plane Shear
Modulus (GPa)	3.350	7.530	2.075
Yield Stress (MPa)	25.0	-	-
Ultimate Strength (MPa)	65.0	316.0	32.8
Failure Strain (%)	2.50	4.20	1.70

Poisson's Ratio - 0.38

3.2 Damage modelling

The mechanical properties for fibres, fibre bundles and DLS 1776 epoxy have been determined in section 3.1. The modulus, strength and strain to failure of the materials have been calculated and this data will be programmed into a material model that can be used for FE analysis of discontinuous composite materials.

This section will outline the development of a user defined material model (UMAT) in FORTRAN that will run in conjunction with input files created for ABAQUS/Standard. The fibre and fibre bundle UMAT is detailed in section 3.2.1, with the epoxy UMAT development discussed in section 3.2.2. A UMAT will be generated that can be used for 2D and 3D analysis at the micro, meso and macroscale.

3.2.1 Elastic damage model development – fibre and fibre bundles

The UMAT for fibres and fibre bundles is simple, as they behave linear elastically with a maximum and minimum stress value used to determine if failure has occurred in tension, compression or shear respectively. To simulate damage onset and progression, it is necessary to evaluate the current stress state at each integration point in the model, at each increment throughout the analysis. If the stress state exceeds the MSC failure threshold (Equation 16 - 2D analysis), in any direction, then the stiffness matrix of the fibre or the fibre bundle is degraded.

$$-\sigma_c < \{\sigma_1, \sigma_2\} < \sigma_t \;\; ; \quad |\tau_{12}| \geq \tau_{12u} \qquad \text{Equation 16}$$

Following failure, the modulus of the fibre or fibre bundle at the integration point is reduced to 1% of the initial value for direct stiffness components (d_E) and 20% of the initial value for shear components (d_G), using the method developed by Blacketter [57]. The stiffness matrix at the relevant integration point is then recalculated as follows (Equation 17), where $d_E = 0.01$ and $d_G = 0.2$. (Note: the stiffness matrix shown below is for a 2D analysis. Damage models have been developed for 1D (beam), 2D (shell) and 3D (continuum) elements), with the failure criterion used for 3D analysis detailed in Appendix C.

$$[C] = [S]^{-1} = \begin{bmatrix} \frac{1}{d_E E_{11}} & \frac{-v_{21}}{d_E E_{22}} & 0 \\ \frac{-v_{12}}{d_E E_{11}} & \frac{1}{d_E E_{22}} & 0 \\ 0 & 0 & \frac{1}{d_G G_{12}} \end{bmatrix}^{-1}$$

Equation 17

An algorithm has been implemented to ensure that only one knockdown is applied to each element if failure is experienced, to prevent double knockdowns leading to FE instabilities. A user-defined state variable within a user defined field (USDFLD) is updated after each increment in the UMAT, to allow the user to monitor whether an element is undamaged or damaged in ABAQUS. The state variable sets undamaged elements to a value of zero (blue), with damaged elements set to a value of 100 (red). The stress-strain curves for a fibre and fibre bundle in tension are shown in Figure 57, with the colour coding on the graph corresponding to the state of the element – undamaged or damaged. The damage models have been validated using periodic unit cells that are subjected to tensile, compressive and shear loading using boundary conditions according to [150, 151].

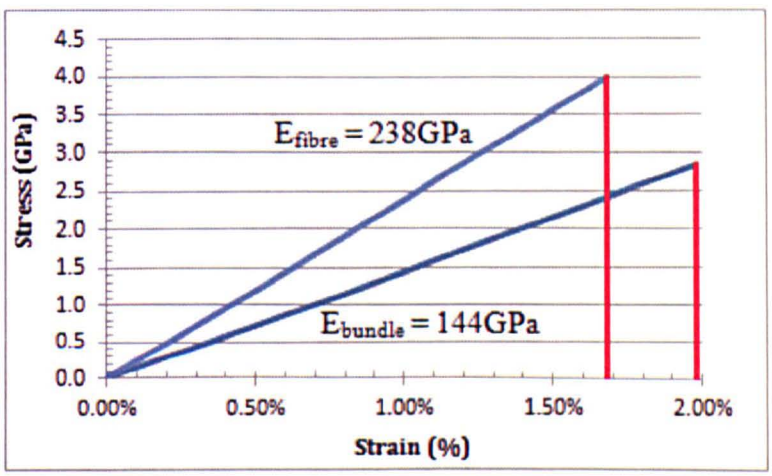

Figure 57 - Stress-strain curves for a unit cell subjected to pure tensile loading in the 1 direction – along the length of the fibre or fibre bundle.

(Note: Fibre length is assumed to be less than 1mm for the filament in this study, with tensile failure strength of 4.00GPa. The bundle, containing fibre and matrix material, has a fibre volume fraction of 60%, with tensile failure strength of 2.85GPa at a gauge length of 36mm, see Table 6).

3.2.2 Elastic-plastic damage model development – epoxy matrix

The direction of loading on each element is computed in the UMAT at the end of the first increment in the analysis. This determines the loading condition for each element and from this the UMAT assigns a yield stress, hardening parameter and failure strain, as required, based on whether dominant stress in the element is in tension, compression or shear. A flow chart detailing this is shown in Figure 58. The epoxy properties used for FE analysis are detailed in section 3.1.3.5. Following the assignment of the mechanical properties the UMAT then continues to evaluate the stress state at each integration point, at each increment throughout the analysis.

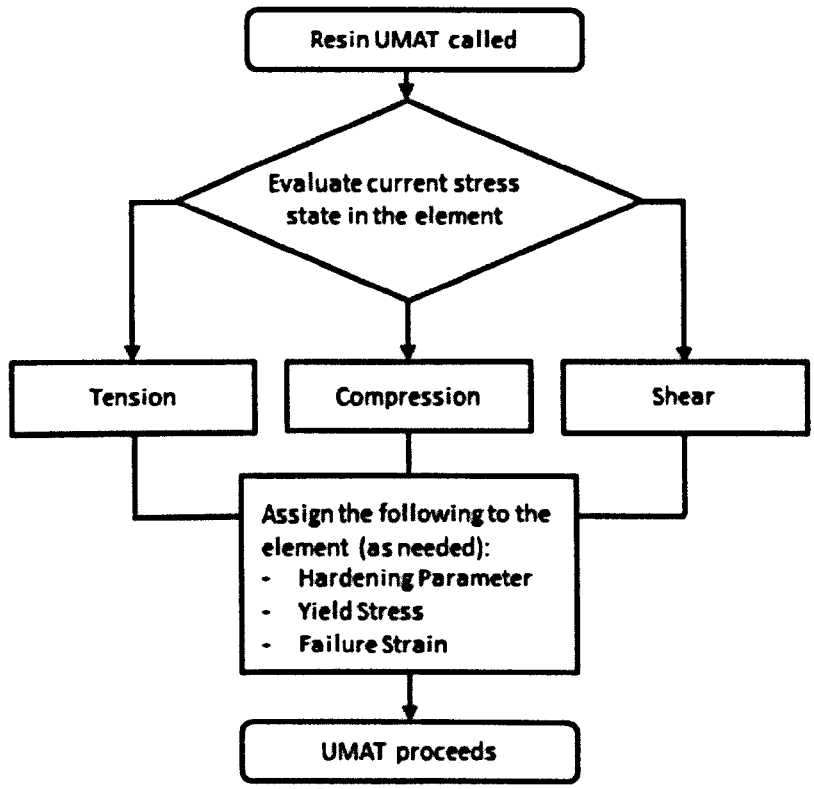

Figure 58 - Flow chart for element property assignment in the matrix UMAT.

The matrix uses a more advanced UMAT than the fibres, which allows the introduction of plasticity into the user-defined material – necessary when the resin is loaded in tension. There are three possible scenarios for the resin: 1) undamaged, 2) plastic (post elastic limit) and 3) damaged (final failure), as shown in Figure 59. If no damage is present and the material is still linear elastic, then the stiffness matrix is calculated using the initial elastic constants (condition 1).

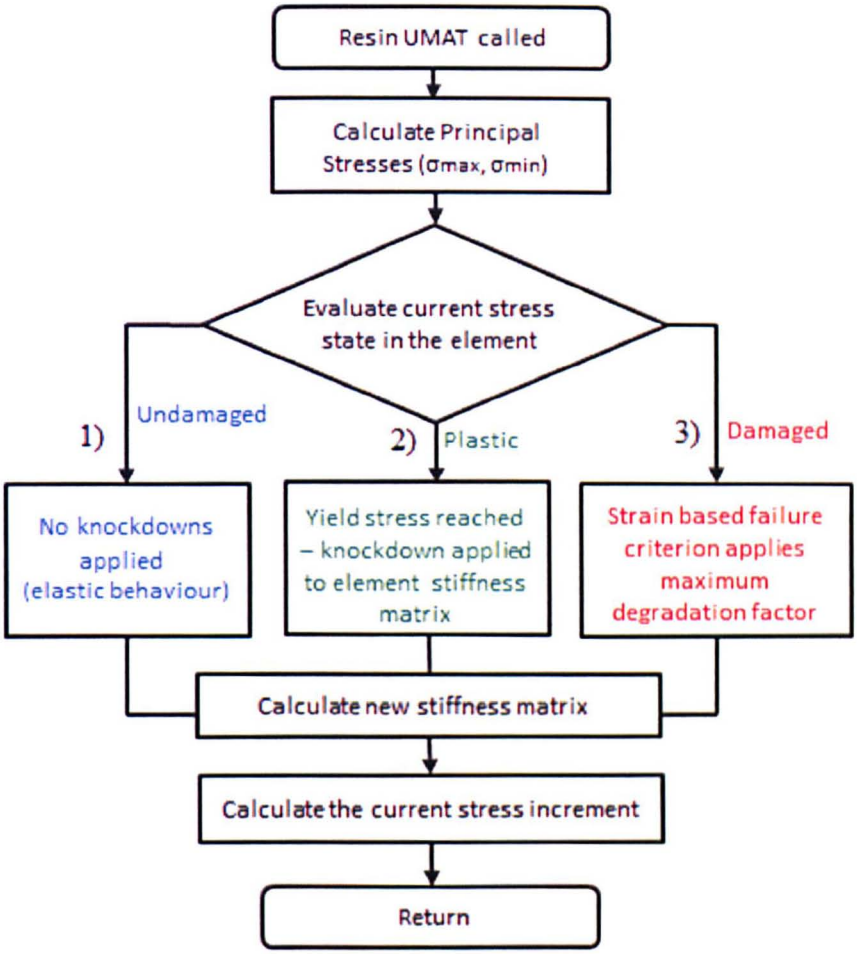

Figure 59 - Flow chart for the elastic-plastic matrix UMAT.

If the onset of damage is detected under tensile loading (σ_y exceeded), but final failure is not met (condition 2), degradation factors are calculated to reduce the terms in the stiffness matrix – the element enters the plastic region. The rate at which the stiffness is degraded is governed by a damage parameter (d) and a shape parameter, n (where $n>1$) – both of which were calculated by performing a regression analysis which is described later in section 3.2.3. The damage parameter is used to calculate the degradation factor (D) as follows:

$$D = 1 - \frac{\left(\frac{\sigma_{Mises}}{\sigma^{t}_{matrix}} - 1\right)^{n}}{d} \qquad \text{Equation 18}$$

where:

σ_{Mises} = von Mises stress in the element under consideration (MPa)

σ^{t}_{matrix} = tensile yield stress of the matrix material (MPa)

D is limited to a lower bound value of 1% for direct stiffness components (d_E), using the same methodology as the fibre and fibre bundle UMAT in section 3.2.1.

$$d_E = \max\ (D, 0.01) \qquad \text{Equation 19}$$

The stiffness matrix at the relevant integration point is then recalculated for the isotropic matrix material using Equation 1. Final failure is triggered (condition 3) when the strain of the element exceeds the failure strain in tension, compression or shear – depending on the loading condition/direction. The stiffness matrix is then reduced by the maximum degradation factor.

Throughout the FE analysis a user-defined state variable is updated after each increment in the UMAT to allow damage initiation and progression to be monitored visually in ABAQUS/Standard. Undamaged elements are set to 0 (blue), plastic elements set to 50 (green) with damaged elements set to 100 (red). The matrix damage model has been validated using a periodic unit cell that is subjected to tensile, compressive and shear loading, with the stress-strain curves plotted in Figure 60.

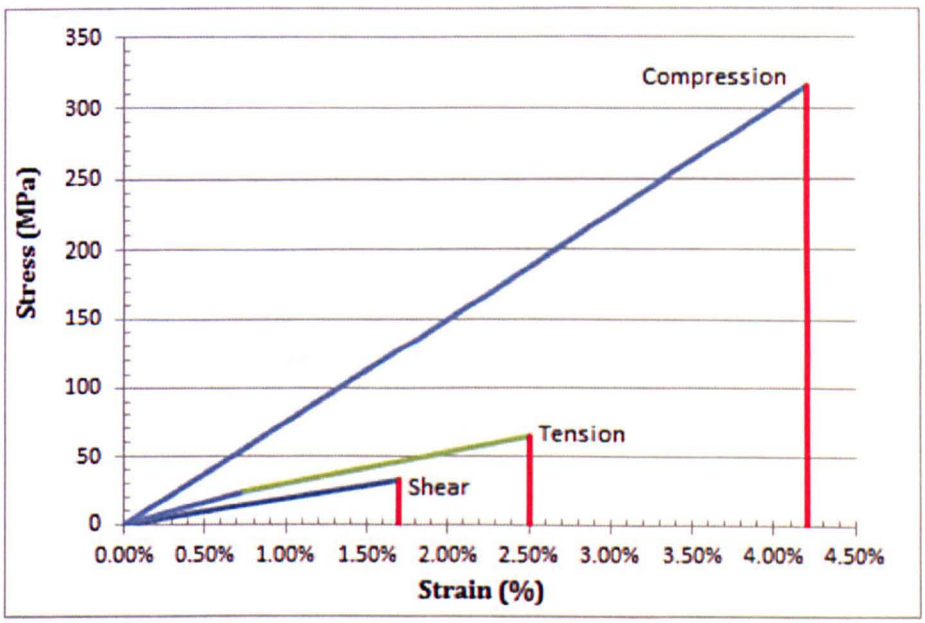

Figure 60 - Stress/strain response of the periodic unit cell loaded in tension, compression and shear (Note: blue - undamaged, green - plastic and red – damaged).

3.2.3 Numerical and experimental comparison

A regression analysis was performed using NLREG v6.3 to calculate the rate of decay after the yield stress when the matrix was loaded in tension. The analysis determined that the damage parameter, d, and the shape parameter, n, were 10 and 1 respectively for the tensile load case – which applied a linear reduction in stiffness beyond the yield point. FE analysis was performed on a periodic unit cell loaded in tension to check the accuracy of the regression, with 99.79% agreement between the elastic-plastic numerical model and the experimental results, shown in Figure 61. For the compression and shear load cases, the elements are assumed to behave in a linear-elastic manner up until the point of failure (Figure 60), therefore no regression analysis was required for these load cases.

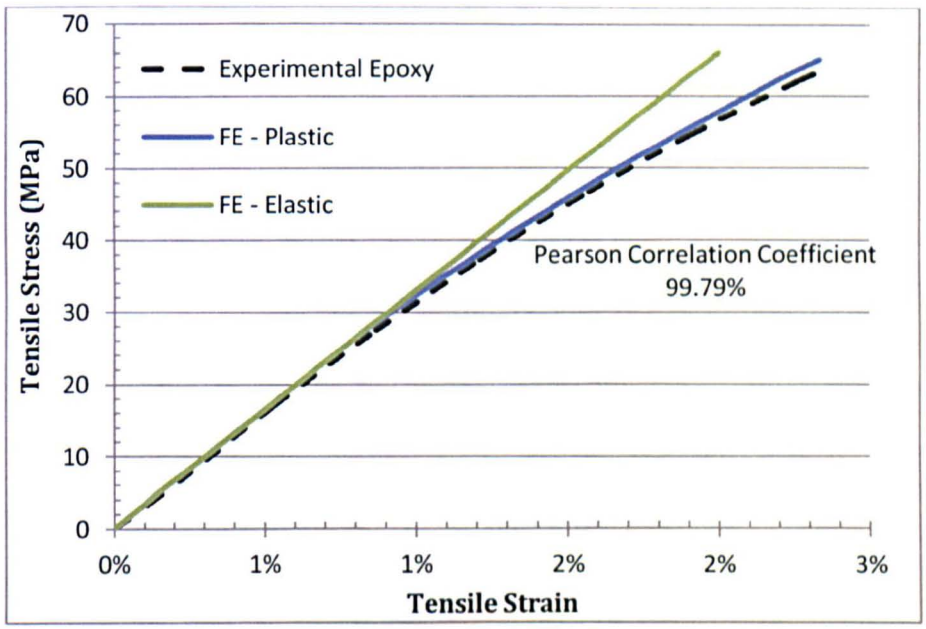

Figure 61 - Stress/strain response of tensile tests on neat resin sample compared to the response of a periodic unit cell in tension (Note: The FE elastic line is plotted merely to highlight the deficiencies in using a linear model for this loading scenario).

3.3 Microscale modelling

3.3.1 Single fibre micromechanical analysis – interfacial debonding

3.3.1.1 Geometric model and boundary conditions

A single cylindrical short fibre embedded in an epoxy matrix region, in isolation from other fibres, has been considered in this analysis, with the fibre considered to be a fragment in a single fibre fragmentation test. By modelling a single fibre composite, it is possible to determine the influence of interfacial strength and fracture toughness on the rate of debonding in the unit cell. The single-fibre composite model makes use of the axial symmetry of the system, which is possible as the interfacial layer undergoes pure mode II loading [69], in order to save computation time, shown in Figure 62. In addition to this, half of the fibre length is modelled which allows a finer mesh to be used and enables the debonding length to be monitored more accurately as the applied tensile strain is increased.

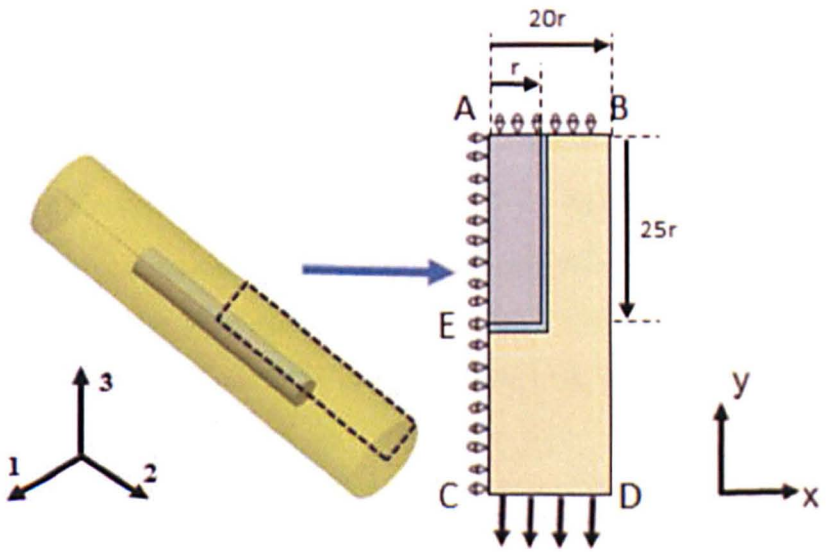

Figure 62 – Diagram to show the axial symmetry exploited in the single-fibre model. (Note: Diagram is not to scale).

The boundary conditions imposed on the model are shown in Figure 62. Edge AB is constrained to prevent movement in the y-direction ($U_y = 0$), part of the plane of symmetry. Edge AC, the fibre centreline, is constrained in the x-direction ($U_x = 0$) to impose the axisymmetric boundary conditions. Edge BD is a free edge in the model. A uniform tensile strain of 3% is applied to the unit cell along edge CD.

The radius of the fibre, r, is 1 unit in this analysis, with the radius of the matrix material (distance AB) 20 times the fibre radius (20r) to ensure the fibre is in isolation so that volume fraction effects are removed from the analysis. The half-length of the fibre modelled (distance AE) is equal to 25r, which would provide a fibre length of 50r if the full length of the fibre was considered in the analysis. The length of the composite (distance AC) is twice the length of the half-length of the fibre, which also equates to 50r for this analysis. A layer of cohesive elements, 1% of the thickness of the fibre radius, have been used to fully encase the fibre to model the interface and allow debonding between the materials.

(Note: Models have also been produced without the interfacial cohesive elements to benchmark the results, with comparisons also made to shear lag predictions from the Cox model).

3.3.1.2 Cohesive parameters for FE models

Cohesive elements governed by an uncoupled bi-linear traction-separation law are used to model the interface between the fibre and matrix. A penalty stiffness, K, value of 10^6 N/mm^3 is used for the traction-separation law for the cohesive elements. The maximum stress criterion is used to initiate failure, with τ_o set to 20MPa to allow comparisons to be made to the debonded lengths obtained by Pan [69] for a single glass fibre composite. The shear stress value of 20MPa is also comparable to the values obtained in the literature for carbon/epoxy ISS [47, 87-93]. The fracture toughness, G_C, of the cohesive elements was set to 220 J/m^2 based on the experimental tests conducted by Kim and Nairn [94].

A study has also been conducted to look at the influence of interfacial fracture toughness on the debonded length in the single fibre composite. Fracture toughness values of 100 J/m^2, 220 J/m^2, 500 J/m^2 and 1000 J/m^2 are considered, with the shear stress kept constant at 20MPa in this analysis. The effect of increasing the interfacial shear strength has not been investigated in this analysis, as Pan [69] concluded that the applied strain required to initiate damage in the interface is linearly proportional to the interfacial strength, with damage initiating

at 0.07%, 0.14% and 0.27% applied strain for an interfacial shear strength values of 20MPa, 40MPa and 80MPa, respectively.

Note: For this analysis the possibility of fibre and matrix failure has been eliminated to allow the failure in the cohesive elements at the interface between the fibre and matrix to be monitored independently. For the elastic-plastic matrix material, the matrix is considered to behave in an Elastic Perfectly Plastic (EPP) manner in this study, with the stress-strain curve used to define the matrix behaviour shown in Figure 63. A von Mises criterion is used to predict the point of yield for the matrix material.

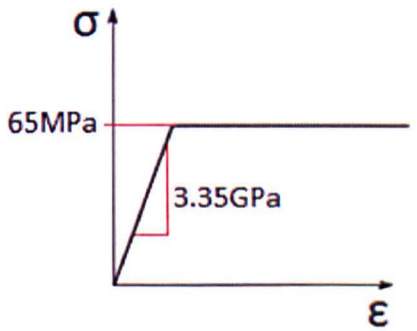

Figure 63 - Elastic Perfectly Plastic (EPP) relationship for epoxy in debonding study.

3.3.1.3 Mesh properties

ABAQUS/CAE has been used to model the single fibre composite model. The models contain approximately 40,000 elements; ~2,000 cohesive elements in the interphase, ~5,000 in the fibre and ~33,000 in the matrix regions. The fine mesh allows close monitoring of the debonding progression in the cohesive elements along the length of the interface. The elements used for the fibre and matrix materials are four node axisymmetric elements, CAX4, with four node axisymmetric cohesive elements, COHAX4, used for the interface elements.

3.3.2 Fibre ineffective length

Finite element studies have been performed to determine the fibre ineffective length and stress concentration factors (SCFs) around the site of a fibre break in a unidirectional composite material. The effect of varying the modulus of the fibre, matrix and interface is investigated by performing a full factorial study, detailed in section 3.3.2.2.

3.3.2.1 Finite element modelling procedure

Three-dimensional finite element models have been generated with two fibres embedded in an epoxy matrix material and a third material is used to model the interfacial region between fibre and matrix. Symmetry has been exploited in the model, with half of the fibres modelled (shown in Figure 64) to allow a finer mesh to be used for the unit cell.

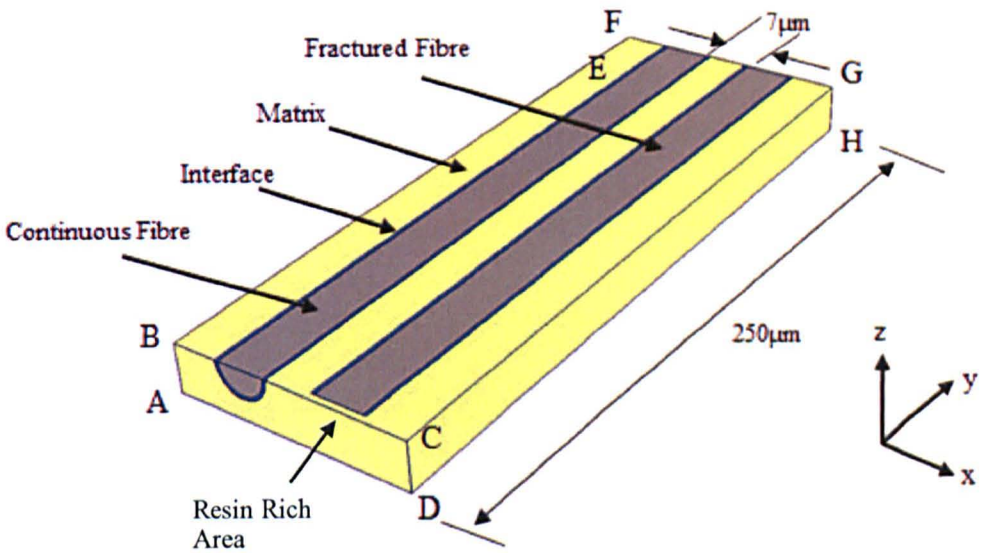

Figure 64 - Fibre ineffective length model used for analysis (Note: the fractured fibre is not continuous across the model, matrix material covers the end at surface ABCD).

The inter-fibre distance is kept constant throughout the analysis, with the fibres one fibre diameter (7μm) apart from each other. The interface thickness was set to 0.5μm to complement the study in section 4.1.3 determining the mechanical properties of fibre bundles. A half-fibre length of 250μm has been selected for the analysis, to allow the variation in the fibre ineffective length to be monitored as

the modulus of the constituents is varied. The volume fraction of the unit cell is kept constant throughout the analysis to provide consistency in the obtained results.

The following boundary conditions for the model use the labels that are designated in Figure 64. To maintain the symmetry of the model, surface BCFG is constrained in the z-direction ($U_z = 0$). Surface ABCD is constrained to prevent movement in the y-direction ($U_y = 0$), with surface CDGH constrained in the x-direction ($U_x = 0$). A tensile displacement is applied to the unit cell along surface EFGH, with 2% strain applied to the model in the y-direction away from the fibre break.

The models contain 83,250 elements; 6,488 in the interphase, 14,970 in the fibre and 61,792 in the epoxy. The fine mesh allows close monitoring of damage progression within the model, with the end view of the mesh (surface EFGH) shown in Figure 65. ABAQUS/Standard was used to model the problem and the elements used in the analysis are C3D8R - reduced integration 8-node linear brick continuum elements.

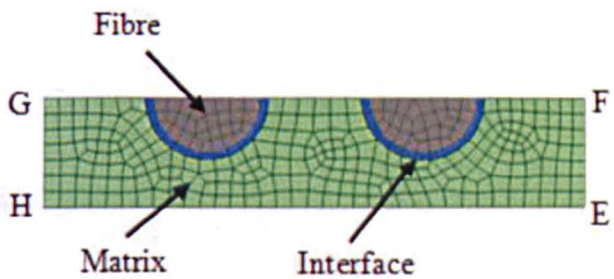

Figure 65 - Sample meshing view of fibre ineffective length model (end view)

3.3.2.2 Full factorial design

The aim of this study was to predict the change in the ineffective length of a broken fibre and the SCF in the unbroken fibre when the stiffness of the materials (fibre, matrix and interface) was varied in a two fibre composite model, shown in Figure 64. The central values used for the mechanical properties of the carbon fibre and matrix materials are detailed in section 3.3.4. For this study, the central value for the interface stiffness is set to the same value as the matrix stiffness.

The full factorial study is detailed in Table 12, with the low and high values corresponding to ±20% of the central values for the moduli detailed in section 3.3.4. Minitab v16 ® was used to derive and analyse the full factorial array by performing a general linear analysis of variance (ANOVA). The importance of the three input variables (fibre, matrix and interface stiffness) were evaluated by comparing the response variable means of two outputs at the different factor levels:

- Fibre ineffective length of the broken fibre.
- Stress concentration factor (SCF) in the unbroken fibre.

Table 12 – Full factorial array generated for fibre ineffective length study

Fibre Diameter (μm)	Interface Thickness (μm)	Fibre Stiffness	Matrix Stiffness	Interface Stiffness
7.0	0.50	High (+20%)	High (+20%)	High (+20%)
7.0	0.50	Low (-20%)	Low (-20%)	High (+20%)
7.0	0.50	Mid	High (+20%)	Mid
7.0	0.50	Mid	Mid	Mid
7.0	0.50	Low (-20%)	High (+20%)	Low (-20%)
7.0	0.50	Low (-20%)	Mid	High (+20%)
7.0	0.50	Mid	Low (-20%)	Low (-20%)
7.0	0.50	High (+20%)	High (+20%)	Low (-20%)
7.0	0.50	High (+20%)	Low (-20%)	Mid
7.0	0.50	Low (-20%)	High (+20%)	Mid
7.0	0.50	Mid	High (+20%)	High (+20%)
7.0	0.50	High (+20%)	Low (-20%)	High (+20%)
7.0	0.50	Low (-20%)	Low (-20%)	Low (-20%)
7.0	0.50	High (+20%)	Low (-20%)	Low (-20%)
7.0	0.50	Mid	Mid	Low (-20%)
7.0	0.50	Mid	Mid	High (+20%)
7.0	0.50	Low (-20%)	Mid	Low (-20%)
7.0	0.50	Mid	Low (-20%)	Mid
7.0	0.50	High (+20%)	High (+20%)	Mid
7.0	0.50	Low (-20%)	High (+20%)	High (+20%)
7.0	0.50	High (+20%)	Mid	Low (-20%)
7.0	0.50	Low (-20%)	Mid	Mid
7.0	0.50	Mid	High (+20%)	Low (-20%)
7.0	0.50	Low (-20%)	Low (-20%)	Mid
7.0	0.50	High (+20%)	Mid	High (+20%)
7.0	0.50	Mid	Low (-20%)	High (+20%)
7.0	0.50	High (+20%)	Mid	Mid

3.3.3 Fibre bundle model

In discontinuous composites, fibre bundles can be subjected to a complex array of loading mechanisms due to their random placement in the material. It is therefore important to calculate the modulus and strength of the fibre bundles in the longitudinal, transverse and shear loading directions, to help improve the accuracy of material models at the meso and macroscale. Typically, a fibre bundle is treated as a unidirectional composite, allowing for relatively small unit cells to be produced which exploit the translational symmetry of the bundle. To account for the discontinuity of the fibre bundles, the longitudinal tensile strength of the bundles has already been calculated experimentally in section 3.1.2 for a range of bundle gauge lengths.

Three-dimensional periodic unit cells have been generated for finite element analysis using the model developed by Lidgett et al [210]. Symmetry has been exploited in the model, with one full fibre and four quarter fibres surrounded by epoxy matrix. A third material is used to model the interfacial region between fibre and matrix, as shown in Figure 66. The fibre diameter (7μm) and interface thickness (0.5μm) were kept constant throughout the analysis, with the inter-fibre distance altered in each model to vary the fibre volume fraction of the unit cell from 10% to 75%. The model depth (z-direction in Figure 66) was constant and set to one fibre diameter (7μm); however there is no variation through the depth of the model and the thickness of the model could have been set to just one element. ABAQUS/Standard has been used to model the problem and the elements used in the analysis are C3D8R - reduced integration 8-node linear brick continuum elements.

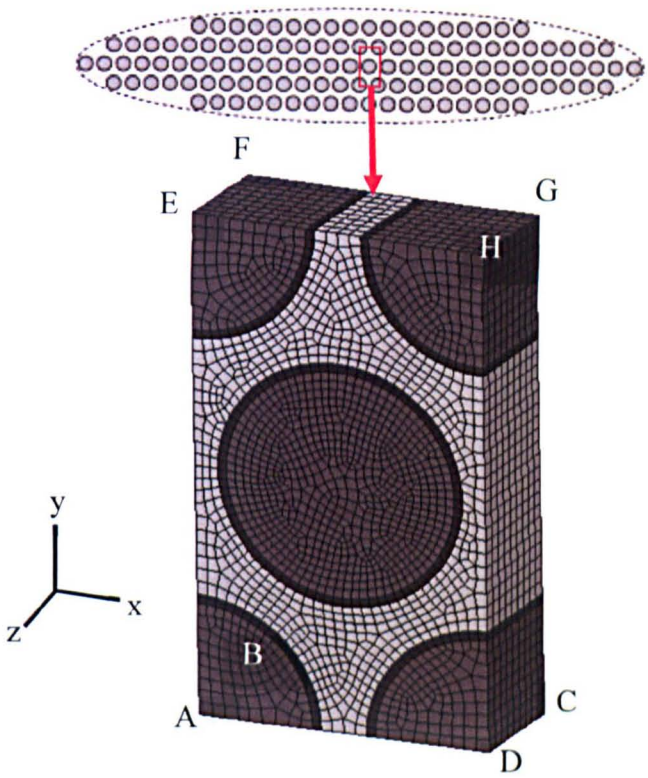

Figure 66 - Periodic unit cell used in micromechanical analysis to determine fibre bundle properties

Periodic boundary conditions have been imposed on the model, shown in Figure 66, adhering to the conditions outlined by Li et al [150, 152] for unit cells with translational symmetry in the x and y directions. The mesh contains approximately 23,000 elements for the 56% V_f model, with the number of elements increasing or decreasing depending on the bundle volume fraction under consideration. The mesh on the opposite boundaries of the unit cell was identical to allow the periodicity to be imposed, with the opposing surfaces on the unit cell (CDGH-ABEF, ABCD-EFGH and ADEH-BCFG – designated in Figure 66) tied with equation constraints to ensure continuity throughout. A uniform global strain was incrementally applied to the models for each loading scenario, with the modulus, strength and failure strain recorded for each bundle volume fraction model.

3.3.4 Material properties for microscale modelling

The carbon fibre is considered to be a transversely isotropic material with linear elastic behaviour. The mechanical properties used in this analysis for the carbon fibre are as follows; E_{11}=238GPa, E_{22}=E_{33}= 22.5GPa, υ_{21}=υ_{31}=0.21 and υ_{23}=0.25. The Maximum Stress criterion is used define the onset of failure for the fibre elements, with the element stiffness reduced to 1% of its initial stiffness once the failure stress has been met. Failure strengths of 4.0GPa (σ_1) and 2.0GPa (σ_2 and σ_3) were used for the fibre in this analysis.

The matrix is considered to be an isotropic material, with Young's modulus and Poisson's ratio set to E_m=3.35GPa and υ_m=0.38, respectively (see Table 11). The interface for the fibre bundle study in section 3.3.3 is also considered to be an isotropic material, with Young's modulus and Poisson's ratio set to E_i=4GPa and υ_i=0.3, respectively. The interface modulus was set at 20% greater than the modulus of the matrix to account for fibre coatings that can be applied to promote stress transfer. The matrix and interfacial regions both behave in an elastic-plastic manner; with the onset of plasticity defined by a von Mises yield criterion and the final failure imposed using a maximum strain criterion. For simplicity, the same failure strains are used for both the matrix and interface materials, with the values used detailed in Table 11. Full details of the user material damage model (UMAT) used and how degradation is applied can be found in section 3.2.

3.3.5 Microscale modelling limitations

The single fibre micromechanical model (section 3.3.1) provides a quantitative assessment of varying the interfacial fracture toughness on the debonding length in the single-fibre composite model.

An idealisation of a unidirectional composite has been used to represent a fibre bundle in this analysis in section 3.3.3. It has been documented in [110] that the fibre distribution can vary greatly across a unidirectional composite material, however it is acknowledged that modelling the bundle as an ideal composite is a convenient modelling strategy to determine the mechanical properties of the

material. The filaments are consistently spaced in the unit cell, with no account made for stress concentrations in the unit cell due to contacting fibres.

The microscale models do not take into consideration the presence of matrix voids, something that would inherently be apparent from the manufacturing of such samples experimentally. It is assumed that no fibre defects are present in the models, which are inevitable during the handling of the carbon fibres, due to their brittle nature. For the models that don't consider interfacial debonding, adhesion is assumed to be perfect with the surfaces tied between fibre and matrix. When interfacial debonding is implemented, the cohesive elements are tied to the surfaces of the fibre and matrix materials. Finally, the residual stresses induced on the system are neglected as they are negligible in this analysis when compared to the stresses in the unit cell due to loading [140].

3.4 Mesoscale modelling

3.4.1 Bundle ineffective length

After a bundle failure has occurred in a composite material, the surrounding bundles are responsible for carrying additional load. When calculating the strength of composite materials, the redistribution of stress after a fibre bundle failure is an important issue. Most studies looking at stress redistribution in composites calculate the ineffective length of fractured fibres at the microscale, as discussed in section 2.3.1. To complement the fibre ineffective length study, the ineffective length of a fractured fibre bundle has been investigated. In discontinuous composite materials the cross-section of the bundle can vary across the component, therefore predicting the redistribution of stress is more complex than for fibres with a relatively constant circular cross-section. Finite element studies have been performed to determine the influence of bundle aspect ratio on the ineffective length of fractured bundles contained in composite materials.

Three-dimensional finite element models have been generated with two bundles embedded in matrix material, with SCFs calculated in the unbroken bundle to quantify how efficient the redistribution of stress is once bundle failure has occurred. Symmetry about the BCFG plane has been exploited in the model, with half of the bundles modelled, shown in Figure 67, to allow a fine mesh to be used to allow close monitoring of the stress redistribution in the unit cell.

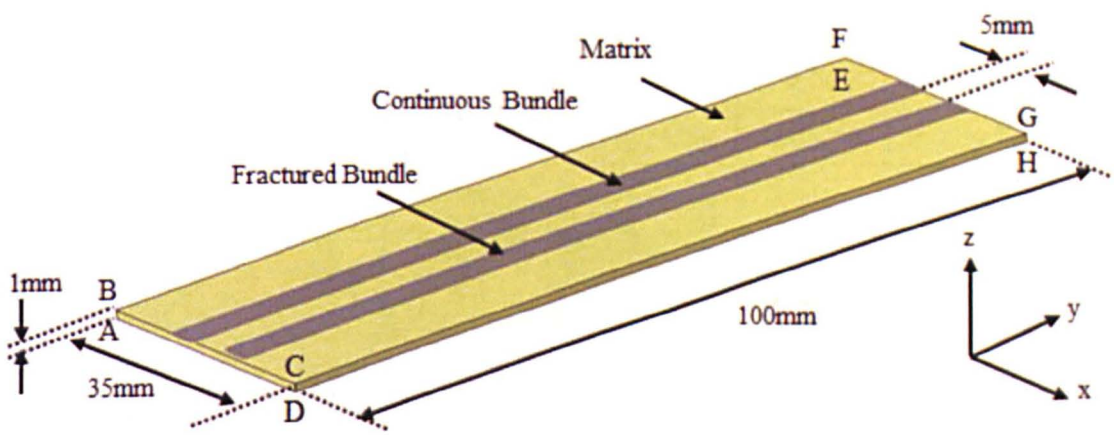

Figure 67 - Bundle ineffective length model. (Note: the fractured bundle is not continuous across the model as the matrix covers the end at surface ABCD).

The following imposed boundary conditions use the labels that are designated in Figure 67. To maintain the symmetry of the model surface BCFG is constrained in the z-direction ($U_z = 0$). Surface ABCD is constrained to prevent movement in the y-direction ($U_y = 0$), with surface CDGH constrained in the x-direction ($U_x = 0$). The strain is applied to the unit cell along surface EFGH, with 2% strain applied to the model in the y-direction away from the fibre break.

The inter-bundle distance was kept constant throughout the analysis, with the inner edge of the bundles kept 5mm apart from each other for the range of bundle shapes. A fibre bundle length of 100mm was selected for the analysis, to allow the variation in the bundle ineffective length to be monitored as the cross-section of the bundle was varied. The volume fraction of the unit cell (4.40% V_f) was kept constant throughout the analysis, by maintaining the same bundle cross-sectional area of 0.7696mm^2, representative of a 12k fibre bundle with a fibre volume fraction of 60%. The dimensions for the bundle cross-sections considered in this analysis are shown in Table 13. In this study T refers to half the bundle height as only half of the bundle is modelled in the analysis due to the exploitation of the model symmetry.

Table 13 – Dimensions of bundle cross-sections used in bundle ineffective length study. (Note: Surface EFGH is shown below Table 13 to show the label designations used to define the fibre bundle width and height).

Model Reference	A (circular)	B	C	D
Bundle Width, W (mm)	0.98980	2.00	4.00	8.00
Half Bundle Height, T (mm)	0.49490	0.24500	0.12250	0.06125

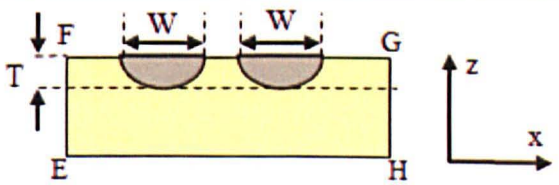

The models contain approximately 325,000 elements, with around 35,000 in the bundles and 290,000 in the matrix. The exact number of elements varies between each model. The fine mesh allows close monitoring of damage progression within

the model, with ABAQUS/Standard used to run the finite element analysis. The elements used in the analysis are C3D8R - reduced integration 8-node linear brick continuum elements.

3.4.2 Bundle interaction

Due to the heterogeneity of discontinuous materials, an infinite number of orientation and separation distance variations can be found between fibre bundles across a component. The aim of this section is to capture a finite number of these variations at the mesoscale to improve the accuracy of the developed macroscale model. A three-dimensional finite element study has been conducted, similar to the study in [43], using two elliptical fibre bundles embedded in matrix material in a unit cell. The orientation of the first bundle remains constant, whilst the other bundle is incrementally rotated through angle ϕ, shown in Figure 68. Using the results from the models, stress concentration factors (SCFs) are calculated in the bundles to produce a stiffness reduction scheme that will be adopted at the macroscale level at the bundle crossover points.

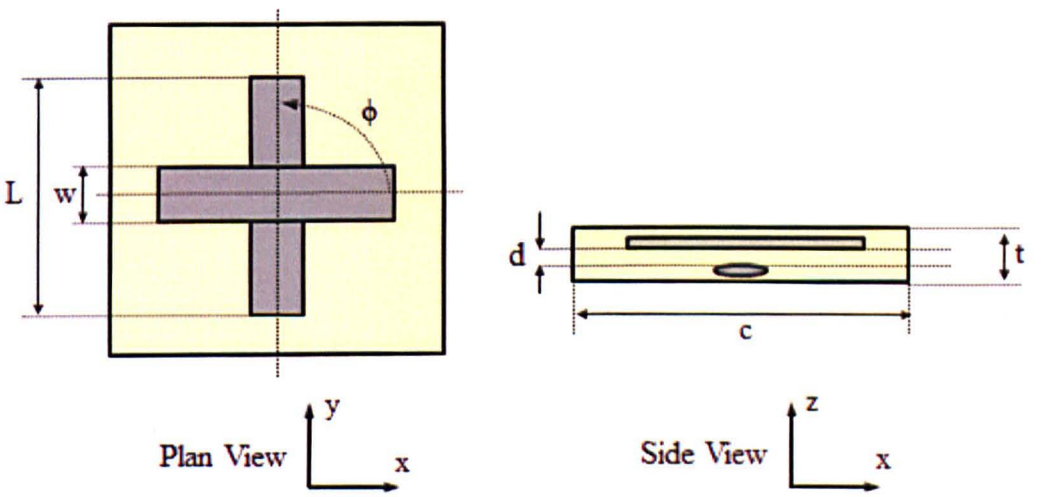

Figure 68 – Model set-up for fibre bundle orientation study. (Note: At $\phi = 0^{\circ}$ the fibre bundles are parallel and at $\phi = 90^{\circ}$ they are perpendicular).

The following dimensions used in the analysis use the label designation in Figure 68:

Unit cell width	c = 40.0mm
Unit cell height	t = 3.00mm

Bundle length	L = 30.0mm
Bundle separation	d = 0.60mm
Bundle width	w = 3.50mm (which gives a bundle height of 0.280mm for a 12k bundle with 60% V_f and area of 0.7696mm^2).

The above values were set to prevent the models from becoming too large, in terms of computational memory and the time taken to run the analysis. The influence of the separation distance, d, is also investigated later in the analysis.

C3D10M elements (10-node modified tetrahedral) were used and the models contain approximately 415,000 elements, with 85,000 in the bundles and 330,000 in the matrix. The mesh plot for the model at $\phi = 90^\circ$ is shown in Figure 69.

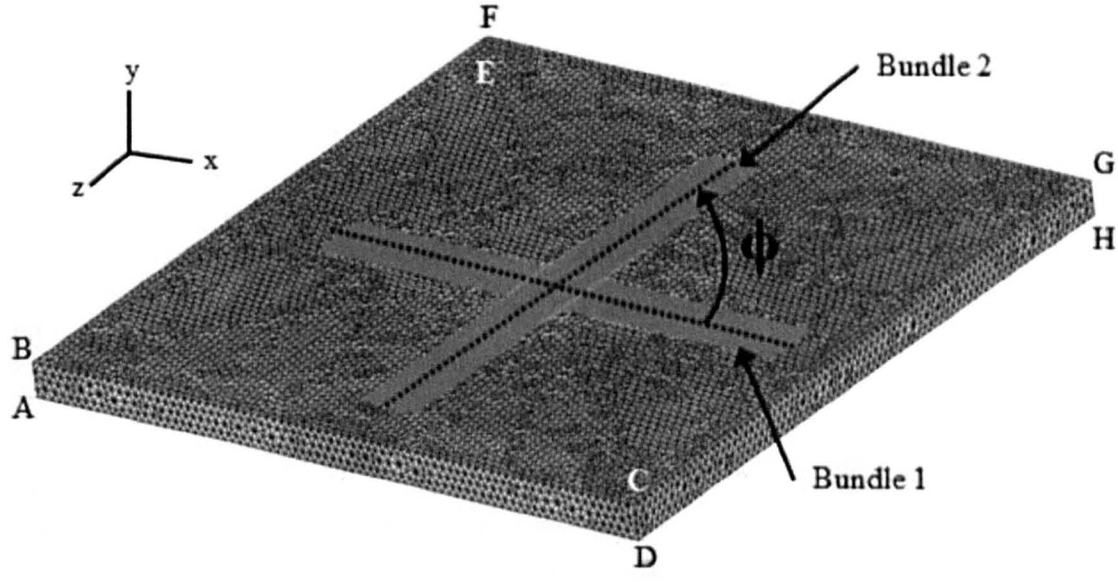

Figure 69 - Mesh plot for bundle orientation study at $\phi = 90^\circ$.
(Note: Labels are assigned to help define the boundary conditions on the models).

A range of angular orientations have been selected and modelled to cover the full range of orientations that could occur between the two fibre bundles. Bundle 1 remains in the same orientation throughout the analysis, whilst bundle 2 is rotated relative to it, at 15° intervals from 0° to 90°, as shown in Figure 69. The unit cell was loaded in the x-direction along the length of principal axis of bundle 1, with a strain of 2% applied to all models, for each load case, over 100 increments.

The following boundary conditions have been imposed on the model (see Figure 69 for the label designation):

Surface - **ABEF**	x-displacement of surface = 0
Surface - **EFGH**	z-displacement of surface = 0
Surface - **CDGH**	2% strain applied in x-direction

The axial stress along the centre of each bundle was monitored at all orientations in order to calculate SCFs induced due to the rotation of bundle 2. To determine the impact of the SCFs on the mechanical properties of the unit cell, a superposition study has been performed to benchmark the results. Models containing only one fibre bundle have been produced at all the angular orientations. The contribution of the fibre bundle on the modulus on the unit cell has been calculated at each orientation. For example, for the 0°/45° scenario two models were produced, one with a bundle oriented at 0° to the loading direction and another model with a bundle at 45° to the loading direction. The modulus contribution of the bundle to each model was then calculated, with the contributions summated to give a predicted modulus for the unit cell. This was then compared directly to the model containing two fibre bundles, oriented at 0°/45°, to quantify the influence of the SCF in the matrix between the bundles when determining the modulus of the unit cell.

A further study has also been conducted at this scale, with the distance between the bundles varied to determine how the separation of the two bundles impacted the SCFs observed in the matrix material. Five separation distances (d, see Figure 68) were modelled in the analysis, with separations of 0.20, 0.60, 1.20, 1.70 and 2.20mm considered in this study for the full range of in-plane orientations from 0° to 90°.

3.4.3 Mesoscale material properties

The bundle is assumed to have linear-elastic behaviour, whereas the matrix behaves in an elastic-plastic manner, with final failure imposed using a strain based criterion. A fibre bundle volume fraction of 60% has been assumed for this analysis, with the mechanical properties used taken from the microscale analysis of the fibre bundle unit cell – section 4.1.3. The matrix is considered to be an isotropic material, with Young's modulus and Poisson's ratio set to E_m=3.35GPa and υ_m=0.38, respectively. Full details of the material damage models used and how degradation is applied can be found in section 3.2.

3.4.4 Mesoscale modelling limitations

The cross-section of the fibre bundles are assumed to be uniform along their length, with no fibre or matrix defects present in the determination of the fibre bundle properties. Interfacial adhesion between the bundles and matrix is perfect in all the models, with surface to surface contact used between the two constituents to ensure they remain in contact with one another in the analysis. In addition to this, for simplicity, the bundles are assumed to be straight, with no bundle curvature present. This allows the influence of bundle shape, orientation and separation distance to be assessed independently when determining the bundle ineffective length and SCFs in the fibre bundles.

3.5 Macroscale modelling

3.5.1 Generation of fibre bundle architecture

3.5.1.1 Fibre bundle deposition

The fibre bundle architecture used for this model is taken from the model developed in [27], where planar 2D bundle architectures have been generated using a modified random sequential adsorption (RSA) scheme. Fibre bundles, represented as 1D beam elements, are deposited over a region of interest (ROI), indicated by the outer square in Figure 44. Random numbers within upper and lower bounds are generated for the x and y coordinates (X_{Mid}, Y_{Mid}) of the centre of mass for each fibre bundle, with a third random number used to generate a bundle orientation (θ) about the centre of mass (ranging from $-\pi/2$ to $\pi/2$), shown in Figure 70. This orientation value can be completely random or can be returned from a statistical distribution depending on the level of fibre alignment specified by the user. It is assumed that the fibre bundles remain straight when deposited, with bundle intersections ignored when generating the fibre bundle architectures; therefore no limitation is imposed on the fibre volume fraction of the unit cell.

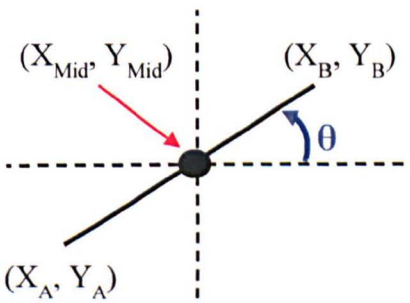

Figure 70 - Orientation (θ) and mid-point (X_{Mid}, Y_{Mid}) of the deposited fibre bundles.

A Cohen-Sutherland [211] line clipping algorithm is used to trim the fibre bundles to the model/RVE boundary (Figure 44), depending on the imposed boundary conditions – discussed later in section 3.5.5. This ensures that both bridging and ending fibre bundles are captured within the model according to the specified fibre bundle length [184]. The cropping of the fibre bundles occurs as each bundle is sequentially deposited in the ROI, to ensure that the target fibre volume fraction

is exactly as specified within the model/RVE boundary (shown in Figure 44). A cumulative total of the bundle length within the model/RVE boundary is used to establish if the volume fraction requirements have been met, with the exact fibre volume fraction of the unit cell returned to the user in the developed program.

The beam elements used to represent the fibre bundles are assumed to have a circular cross-section, where the diameter is assigned as a function of the filament count and bundle volume fraction (V_{bundle}). Bundle diameters can also be randomly assigned using a probability density function to reflect the level of filamentisation in the mesostructure of the material [169]. The mechanical properties of the bundles are taken from the microscale analysis and the internal bundle structure contains matrix material, therefore the volume fraction of the deposited bundles ($V_{deposited}$) is adjusted to ensure the target volume fraction (V_f) is met in the model/RVE boundary:

$$V_{deposited} = \frac{V_f}{V_{bundle}} \qquad \text{Equation 20}$$

One disadvantage of the deposition method used to generate the bundle architecture is that it doesn't fully capture the levels of material heterogeneity and local fibre volume fraction variations across a manufactured discontinuous composite [184]. In addition to this, depositing all the fibre bundles in a 2D distribution limits the level of physical detail that can be modelled, with no matrix material present between the fibre bundles through the thickness of the unit cell. Analysis was completed at the mesoscale looking at the interaction between two fibre bundles in a 3D unit cell. The separation distance and angular orientation between intersecting bundles was shown to be critical when determining the stress in the bundles, with the results from this study presented in section 4.2.2. Stress concentrations were found in the bundles at the intersection points, with the mechanical properties of the fibre bundles modified in the model to account for these SCFs. The full implementation of this is outlined later in section 3.5.4.

It is acknowledged that the 2D bundle architecture is not fully representative of a discontinuous composite material, such as the bundle architectures generated in

[43, 166], but the use of the beam elements allows high volume fraction models to be produced that are computationally inexpensive. It was deemed more important to capture the stochastic fibre distribution in the discontinuous composite, based on the level of variation in material properties experienced experimentally [17, 21, 44, 46], rather than generate a complex 3D bundle network that would produce models requiring high computational memory and run time.

3.5.1.2 Bundle intersections

Once the fibre bundles have been deposited and the volume fraction requirements have been met in the model/RVE boundary, the program finds the intersection points between the bundles. The intersections between the bundles are required for two reasons. Firstly, they are needed to allow nodes to be generated along the lengths of the bundles to create the fibre elements, with the intersection points discretising the bundles into sub-sections. For example, if a bundle is intersected by two other bundles, there will be three segments along the length of the intersected bundle, shown in Figure 71. Secondly, the intersection points are also required to allow the SCFs determined in the mesoscale analysis to be implemented into the model, discussed in section 3.5.4. At the point of bundle intersection the angular orientation (ϕ) between the bundles is stored, shown in Figure 72.

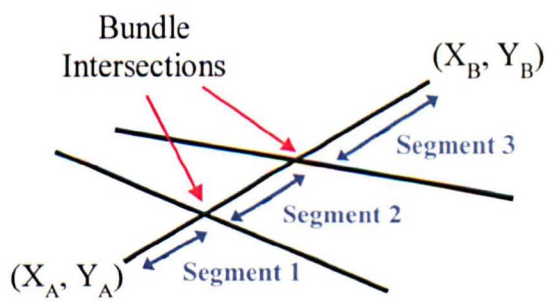

Figure 71 - Schematic of a fibre bundle discretised into segments due to intersections.

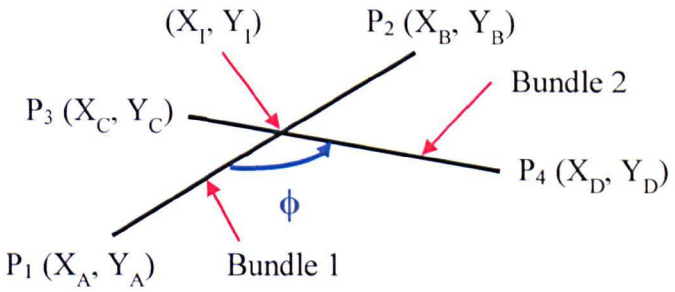

Figure 72 – Schematic of a generic bundle intersection in the macroscale model.

The intersection points between the fibre bundles are calculated by determining if the centrelines of the bundles intersect in the ROI. As the bundles are deposited into the unit cell, they are assigned a sequential deposition number which provides the bundles with a unique identifier. Each bundle is then considered in turn to calculate if any other bundles in the model have intersected it. The following procedure is performed and repeated for each bundle in the model/RVE boundary, with the methodology used detailed in [212]. The equations for the centrelines of bundle 1 (P_a) and bundle 2 (P_b) are as follows:

$$P_a = P_1 + u_a\,(P_2 - P_1) \qquad \text{Equation 21}$$

$$P_b = P_3 + u_b\,(P_4 - P_3) \qquad \text{Equation 22}$$

The end coordinates of bundle 1, P_1 (X_A, Y_A) and P_2 (X_B, Y_B), and the end coordinates of bundle 2, P_3 (X_C, Y_C) and P_4 (X_D, Y_D), are then substituted into the above equations, which are then solved for the case where $P_a = P_b$, with the following two expressions obtained:

$$x_A + u_a\,(x_B - x_A) = x_C + u_b\,(x_D - x_C) \qquad \text{Equation 23}$$

$$y_A + u_a\,(y_B - y_A) = y_C + u_b\,(y_D - y_C) \qquad \text{Equation 24}$$

The above expressions are then rearranged and solved in terms of u_a and u_b:

$$u_a = \frac{(x_D - x_C)(y_A - y_C) - (y_D - y_C)(x_A - x_C)}{(y_D - y_C)(x_B - x_A) - (x_D - x_C)(y_B - y_A)} \qquad \text{Equation 25}$$

$$u_b = \frac{(x_B - x_A)(y_A - y_C) - (y_B - y_A)(x_A - x_C)}{(y_D - y_C)(x_B - x_A) - (x_D - x_C)(y_B - y_A)} \qquad \text{Equation 26}$$

Using the equations for u_a and u_b it can be determined if the centrelines of the fibre bundles intersect. If the denominator for equations u_a and u_b is 0 then the two lines are parallel, and if the denominator and numerator for u_a and u_b are 0 then the two lines are coincident. If the two centrelines are not parallel or coincident, then the values of both u_a and u_b must lie between 0 and 1 if the two bundles intersect. The following equations are obtained if an intersection is found:

$$X_I = x_1 + u_a (x_B - x_A) \qquad \text{Equation 27}$$

$$Y_I = y_1 + u_a (y_B - y_A) \qquad \text{Equation 28}$$

The intersection point (X_I, Y_I) is then stored in an array, with the in-plane orientation angle (ϕ) between bundle 1 and bundle 2 also stored to calculate SCFs at the crossover point. The nodes at the crossover point between the intersecting bundles are then tied together, with a connector element, which releases once a failure stress is met. The implementation of this is discussed in section 3.5.3. Multiple intersections are expected along the length of each bundle, as shown in Figure 72, with the intersections stored in ascending order, in terms of the x-coordinates, from left to right across the width the model/RVE boundary.

3.5.1.3 Generation of fibre bundle elements

Once all of the intersection points have been found along the length of the bundles, the bundles are split into segments (Figure 72). Elements then need to be generated for the bundle, which requires nodes to be created along the lengths of the bundle segments. The segment length is initially calculated using the coordinates of the bundle end points and intersection points. For example, for segment 1 in Figure 73 the length of the bundle segment is calculated as follows:

$$Bundle\ Segment\ Length = \sqrt{(Y_1 - Y_A)^2\ (X_1 - X_A)^2} \qquad \text{Equation 29}$$

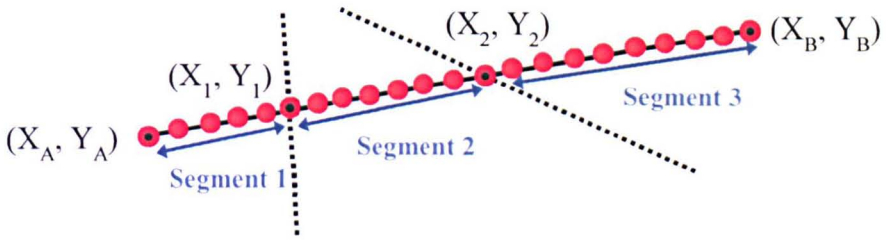

Figure 73 - Schematic showing generated nodes along the length of the fibre bundle.

Using the calculated bundle segment length, the number of nodes along the length of the segment is then determined. The user specifies a global element seed size for the model in the program, with this used to determine the number of nodes along the length of the segment, shown below:

$$Bundle\ Node\ Count = 2 * \left[Int\left(\frac{Bundle\ Segment\ Length}{Global\ Element\ Size}\right)\right] + 1 \qquad \text{Equation 30}$$

Note: Each 1D beam element requires 3 nodes (B22 in ABAQUS/Standard), with the above calculating the integer value of the number of nodes required. If the bundle segment length is less than the initial global element size, the segment is treated as one element with a mid-node inserted to complete the element.

Using the number of nodes required along the segment, a revised element size is calculated:

$$New\ Element\ Size = \frac{Bundle\ Segement\ Length}{(Bundle\ Node\ Count - 1)} \qquad \text{Equation 31}$$

Note: The -1 is present above as the element size calculated is the distance between the nodes. For example, if 5 nodes are to be placed along the length of a segment, 4 fibre spacing's are required between the 5 nodes.

The fibre bundle nodes are then distributed evenly along the length of the segment using the new element size. This process is repeated for every bundle segment contained in the model/RVE boundary. The coordinates of the fibre bundle nodes are also stored in an array, as matrix nodes will need to be created in the same location to allow the bundles and matrix to be tied together with connector elements to allow debonding of the two materials in the analysis.

3.5.2 Delaunay meshing algorithm

3.5.2.1 Background and overview

After generating the discontinuous fibre bundle architecture and creating nodes for the bundle elements, the next step is to generate a mesh in the matrix region across the model/RVE boundary to allow finite element (FE) models to be produced. To allow the bundles and matrix to separate in the analysis, an unstructured mesh is required across the unit cell. As the nodes for the fibre bundle elements are spaced sporadically across the model boundary (Figure 74) a meshing algorithm needs to be implemented that can encapsulate these nodes, with the introduction of additional nodes to keep a consistent element size across the model. A custom meshing algorithm is therefore required to produce FE input files (.inp) ready to submit to ABAQUS/Standard, with no intermediate steps, for analysis with the developed user material models.

The fibre bundle architectures produced by the model are unique for each combination of bundle length, volume fraction, cell size, etc., with the bundles orientated at random to each other across the model/RVE boundary. Due to the complexity of the bundle distribution, especially at high fibre volume fractions, it was deemed appropriate to use triangular elements to generate the mesh for the models in this analysis. Free-meshing techniques often use triangular elements to model complex geometries, such as in the work by Pan et al [2], with meshes of greater quality typically produced over their quad equivalents. In addition to this, at the point of the bundle intersections in the model, the use of triangular elements allows for the quality of the mesh to be maintained. As the angle (θ) between the bundles decreases/increases beyond the point shown in Figure 75, the use of quad elements would lead to poor quality elements being produced at the point of intersection in the model.

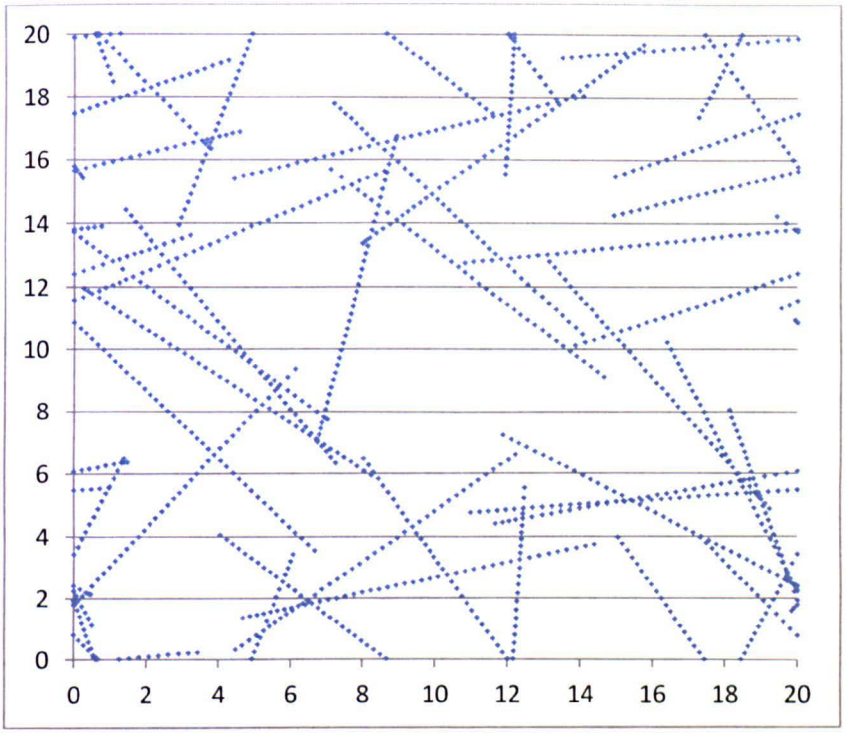

Figure 74 - Typical fibre bundle node plot produced from the model for a bundle length of 10mm in a 20x20mm unit cell at approximately 30% V_f.

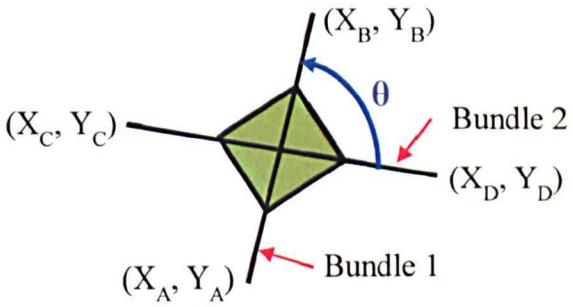

Figure 75 - Schematic of triangular elements produced at the bundle intersection point.

After establishing that triangular elements were to be used in the analysis, a suitable meshing algorithm was required for the model. A common triangulation procedure used to mesh an unstructured region of points is the Delaunay algorithm [213-215]. A Delaunay triangulation algorithm [216, 217] has been selected as it maximises the minimum angle among all possible triangulations of a particular node set. Therefore, to produce a high quality 2D unstructured mesh, Delaunay algorithms are often used as they provide good element quality across the region of interest (ROI). The coding for Delaunay meshing algorithms are

widely available in many programming languages, including Microsoft Visual Basic®, allowing for easy integration into the developed macroscale model.

3.5.2.2 Characteristics of the Delaunay meshing algorithm

A 2D Delaunay triangulation (D), of a set vertices (V) is a set of triangles (T) whose vertices collectively are V, where the interiors of the triangles do not intersect each other [216, 218]. Figure 76 shows two possible triangulations for an arbitrary set of nodes A to E. These triangulations are both valid, but only one of them satisfies the Delaunay criteria.

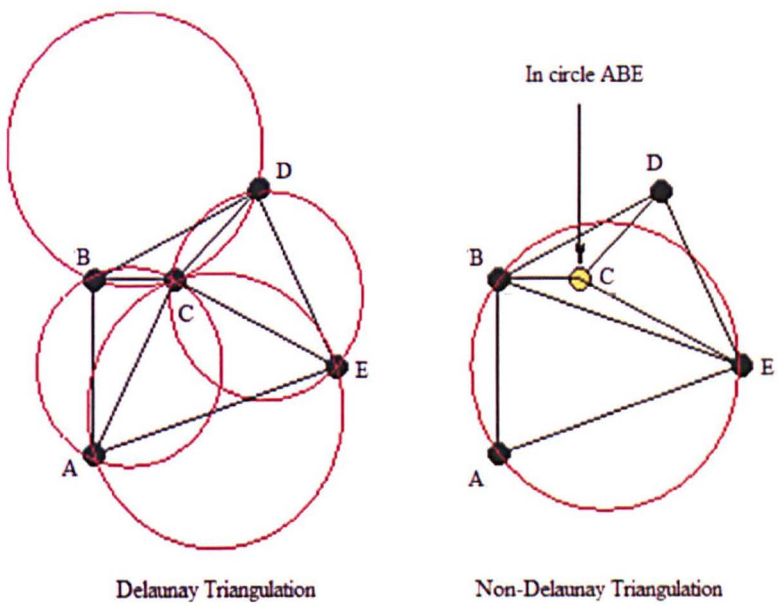

Figure 76 – Triangulations, with prescribed circumcircles, shown for a random set of points A to E [218].

If A and B are two vertices then a circumcircle of the edge AB is any circle that passes through A and B. The edge AB satisfies the Delaunay triangulation criteria if the circle passing through vertices A and B contains no other vertices – e.g. the circumcircle of AB is empty. A Delaunay triangulation is shown on the left of Figure 76, with this triangulation instantly recognisable as Delaunay as all the circumcircles are empty. The triangulation on the right in Figure 76 does not satisfy the Delaunay criteria as node C lies in the circumcircle prescribed by nodes ABE. All triangles in a Delaunay triangulation have empty circumcircles - no nodes lie in the interior of any triangle's circumcircle.

A constrained Delaunay triangulation (CDT) is a generalization of the Delaunay algorithm that includes all the required nodes in a triangulation. All the coordinates of the nodes are specified initially, with all of the nodes included in the triangulation procedure. The generation of the matrix nodes in the developed program, outlined in section 3.5.2.3, makes a CDT an ideal candidate to mesh the model boundary as the coordinates of the nodes are determined before triangulation. However, as a Delaunay triangulation is almost always unique, a CDT may contain elements that do not satisfy the Delaunay condition.

To ensure good quality meshes are produced from the CDT, refinement algorithms have been developed. Delaunay refinement algorithms operate by inserting nodes until the mesh meets a required set of constraints, usually dictated by the minimum interior angle in the triangulations. Inserting a node is a local operation, which makes the refinements computationally inexpensive as the mesh will only be refined around the region which contains the poor quality triangulation. When refining a Delaunay triangulation, it is difficult to know exactly where to place the new node. It is desirable that the new node should be placed as far away as possible from the other nodes in a model, to prevent small edges being created that could produce thin triangles. Two common Delaunay refinement algorithms are detailed below.

Chew's refinement algorithm [219] begins with a CDT of the input nodes, before the quality of the triangles produced are assessed. If a poor quality triangle is detected, an interior angle less than 28.6°, a node is inserted at the circumcentre of that triangle, unless the circumcentre lies on the opposite side of an input segment as the poor quality triangle, in which case the midpoint of the segment is inserted. This process is repeated until no poor-quality triangles exist across the model boundary.

Another commonly used Delaunay refinement algorithm is Ruppert's algorithm [220]. Once again a CDT is completed using the input nodes across the model boundary, with poor quality triangles having interior angles of less than 20.7° identified for refinement. The midpoint of a segment with a non-empty

circumcircle is inserted, along with the circumcentre of the poor quality triangle. This process is also repeated until the triangulation across the model is deemed to be acceptable.

Both Ruppert's and Chew's algorithms improve the quality of the initial CDT by inserting additional nodes across the model boundary, with both methods adopting a different strategy when selecting the location of the additional nodes. It is clear that the distribution of the nodes in the model boundary directly influences the quality of the initial mesh obtained from the CDT. The methodology used to select the placement of the matrix nodes in the model is detailed in section 3.5.2.3, with refinement techniques implemented across the model boundary before the initial CDT is completed to improve the quality of the obtained mesh.

3.5.2.3 Matrix node generation

To produce a mesh across the model/RVE boundary, a cloud of points was generated before performing a constrained Delaunay triangulation (CDT). The coordinates of the fibre bundle nodes must be included in the node set to produce the matrix elements, to allow the matrix to be meshed around the bundles. A coarse grid, referred to as the base level grid, was produced to discretise the model using the global element seed size specified by the user. This is used to calculate the spacing between the nodes in the x and y directions, with a sample grid shown in Figure 77. Nodes have been produced around the perimeter of the model boundary, with a potential node, P (X_P, Y_P), highlighted in the bottom left of Figure 77.

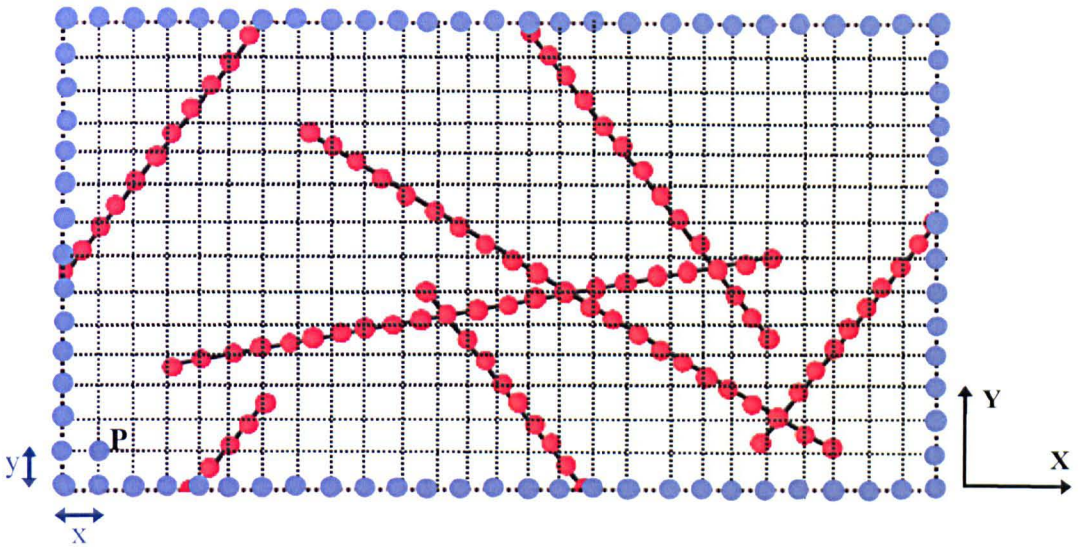

Figure 77 - Schematic showing grid spacing and potential matrix nodes across a model boundary. (Note: The red nodes are nodes with the same coordinates as the fibre bundles, with the blue nodes potential new nodes added into the model).

For each potential node, P (X_P, Y_P) a check is done to ensure that the newly inserted node does not lie too close to an existing node in the model – which could result in a poor quality element after the CDT. A minimum separation distance between the nodes in the model is defined as follows:

$$Minimum\ Node\ Separation < \frac{Global\ Element\ Size}{2} \qquad \text{Equation 32}$$

Using this minimum separation distance, the coordinates of each potential new node P (X_P, Y_P) are checked against the coordinates of each node already present in the model. If the coordinates of the new node satisfy the minimum node separation criterion, then that node is added to the cloud of points ready for triangulation.

To further improve the quality of the CDT, adaptive mesh refinement (AMR) techniques have been adopted when producing the cloud of point across the model boundary. The model is scanned for areas of potential interest, in this case along the lengths of the fibre bundles and at the points of bundle intersection, with these regions then "tagged". All the tagged regions are then further refined, with a finer

grid overlaid over the base level grid. The new element size for the regions identified for refinement is defined as follows:

$$Refinement\ Element\ Size < \frac{Global\ Element\ Size}{2} \qquad \text{Equation 33}$$

The refinement along the length of the fibre bundles, in the tagged regions, is limited to ± 2 global element sizes either side of the bundle. This method provides local refinement for the model, with an increased number of elements at the bundle-matrix interface where debonding occurs. To reduce the number of poor quality elements formed in the CDT in the refinement regions, a new minimum node separation is calculated:

$$Refinement\ Node\ Separation < \frac{Refinement\ Element\ Size}{2} \qquad \text{Equation 34}$$

Without the mesh refinement, the grid used to generate the cloud of points would have to be fine over the whole model to provide a good quality triangulation. This would be computationally expensive, resulting in a large number of nodes being produced for the triangulation procedure. The time taken to perform a Delaunay triangulation for a given number of points rises exponentially; therefore it is beneficial to keep the number of nodes to a minimum whilst maintaining a good quality mesh. In addition to this, the mesh does not need to be that fine for the majority of the model, especially in the regions that contain matrix material and no fibre bundles. A typical cloud of points generated for triangulation is shown in Figure 78, with the nodes for the coordinates of the fibre bundles in blue and the nodes generated for the matrix region, after refinement along the length of the bundles and at the bundle intersections, shown in green.

A number of criteria must be satisfied when producing the cloud of points in order to satisfy to the boundary conditions imposed on the model (section 3.5.5). For periodic boundary conditions, an equal number of nodes must be present on opposite boundaries and dummy nodes are also created to apply strain to the models in the x, y and xy directions. For tensile boundary conditions, a dummy node is generated and tied to the right edge of the model to apply the prescribed strain to the unit cell.

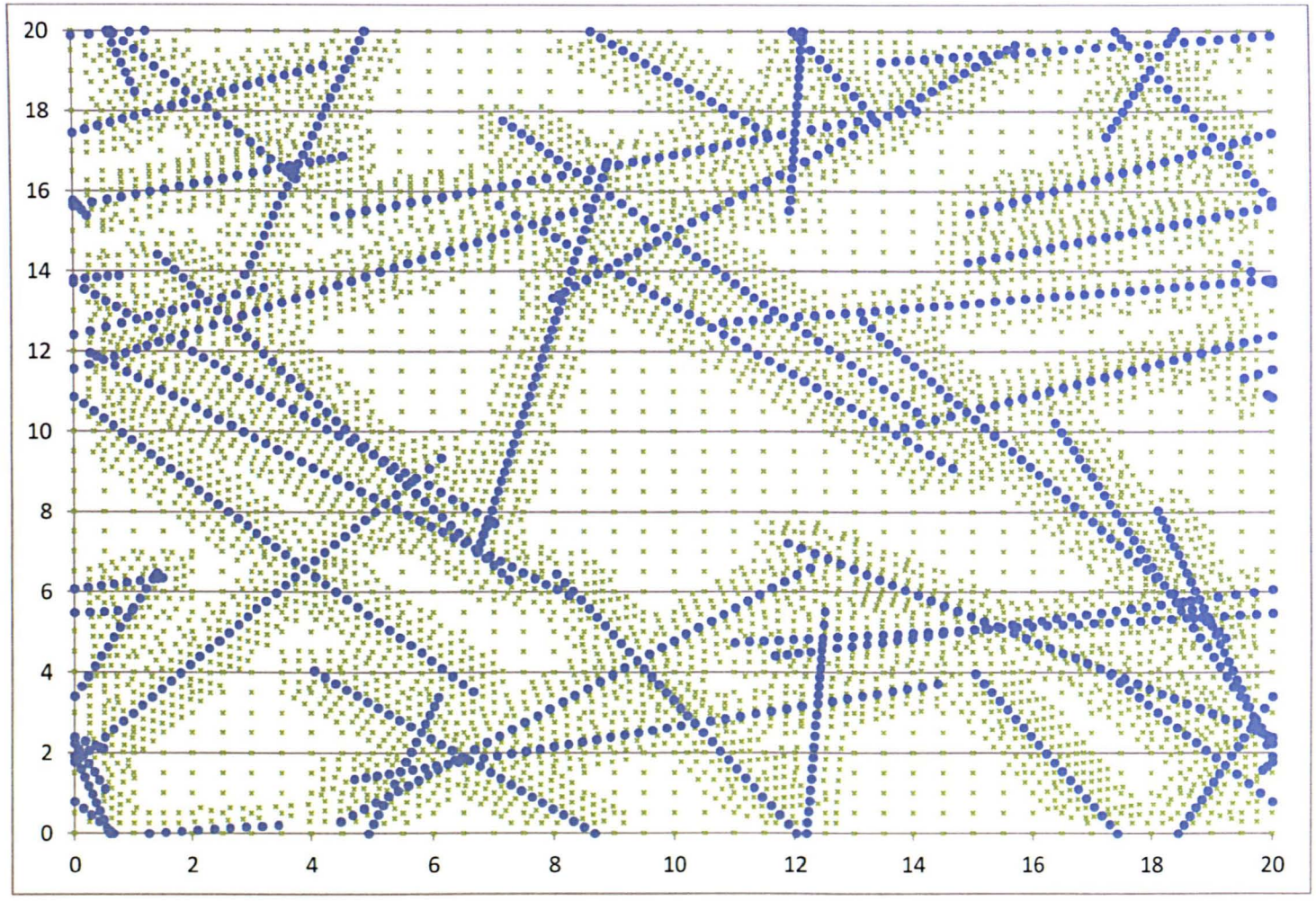

Figure 78 - Cloud of points generated for the Delaunay mesh of a periodic unit cell after refinement grid is plotted.

3.5.2.4 Implementation of Delaunay algorithm into the model

A constrained Delaunay triangulation (CDT) algorithm has been implemented into the macroscale model to mesh the cloud of points generated across model/RVE boundary, as discussed in section 3.5.2.3. A typical mesh produced by the CDT for a tensile unit cell is shown in Figure 79, with the model shown at relatively low fibre volume fraction (~5%) to allow the refinement around the bundles to be clearly observed. The refinement along the length of the bundles provides good quality triangulations, with the criteria used to define the quality of the triangulation detailed in section 3.5.2.5. The fine mesh around the bundle intersections and bundle ends also allows for closer monitoring of debonding, damage initiation and damage progression in the model, with it shown at the microscale and mesoscale that these regions experience elevated stresses as they transfer load from bundle to bundle, and from matrix to bundle.

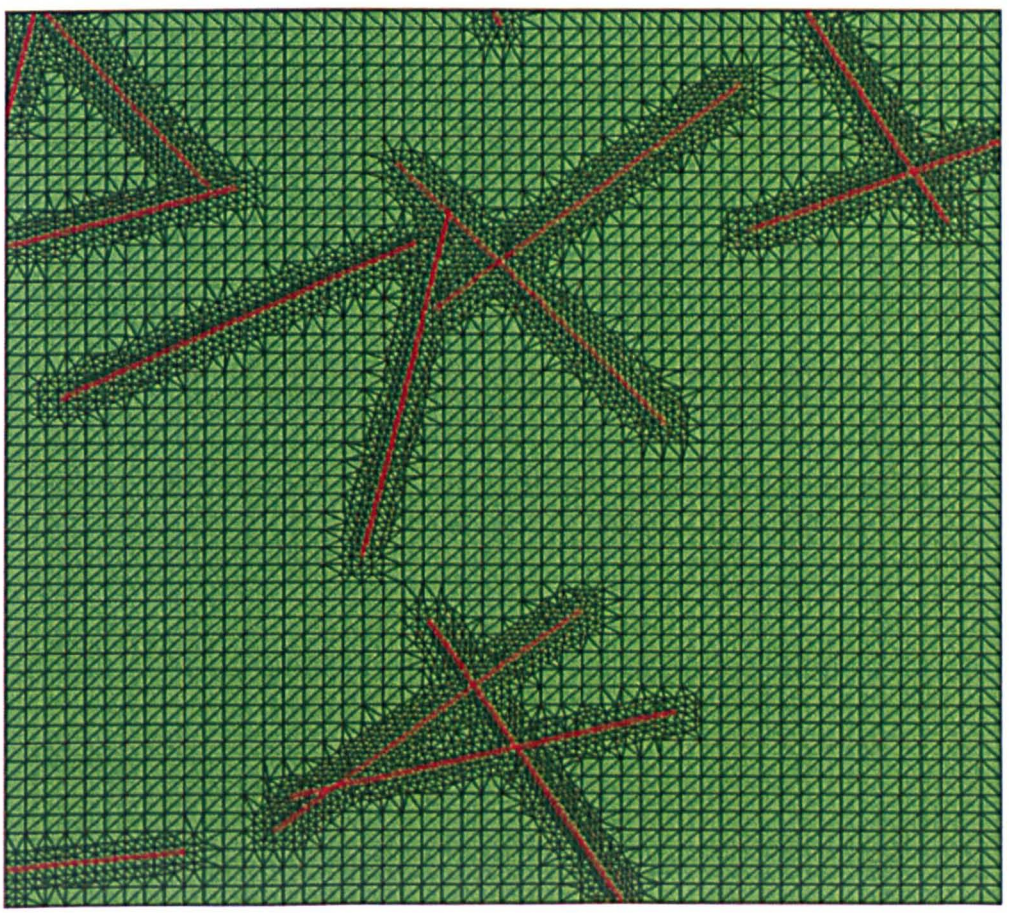

Figure 79 - Typical constrained Delaunay triangulation (CDT) produced by the model after refinement along the length of the fibre bundles (highlighted in red).

3.5.2.5 Mesh quality assessment

The quality of the triangulations of the generated models is important when performing FE analysis. The use of the CDT forces the triangulation to include every node generated in the cloud of points when meshing across the model/RVE boundary, potentially leading to some long slender triangles being formed. Poor quality elements in the models could lead to errors when determining the mechanical properties of the unit cell, therefore it is important to assess the quality of the generated mesh before submitting the model to the FE solver.

Padron et al [221] have developed a criterion to determine the quality of a triangular element for FE analysis. The criterion calculates the area of the triangle (A) and the side lengths (h_1, h_2 and h_3), shown in Figure 80, before feeding these values into a function (q) to quantify the quality of the mesh as follows:

$$q = 4A \frac{\sqrt{3}}{\left(h_1^2 + h_2^2 + h_3^2\right)} \qquad \text{Equation 35}$$

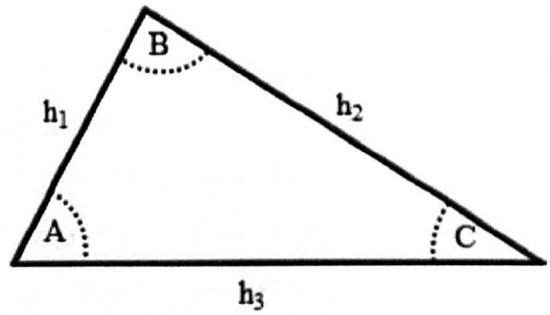

Figure 80 - Label designation for mesh quality assessment of the CDT.

The optimum case for a triangular element is when $q = 1$, where an equilateral triangle is obtained ($h_1 = h_2 = h_3$). Any value of $q > 0.6$ returns an acceptable triangle for FE analysis, with all interior angles (A, B, and C in Figure 80) of the triangle greater than 22.5° if this criterion is satisfied.

A sensitivity study was conducted to look at the number of poor elements ($q < 0.6$) obtained across a 5x5mm unit cell as the global element size was reduced from 1mm to 0.05mm. The graph plotting the percentage of poor shaped elements against the global element size is shown in Figure 81. At a global element size of

1mm, 6.231% of the elements (21 out of 337) in the model returned a q value lower than 0.6. This reduced significantly as the global element size was reduced, with just 0.016% of elements (5 out of 31,077) deemed poor at a global element size of 0.05mm - 1/100th of the model width.

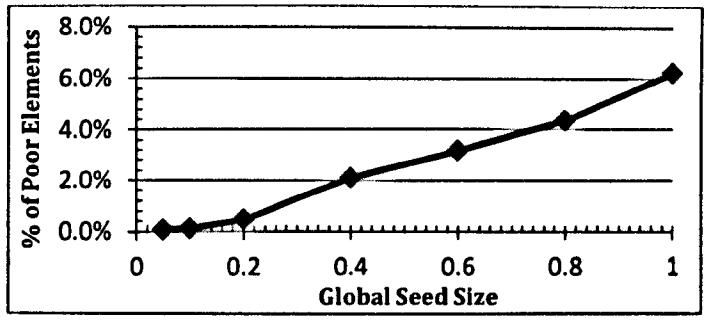

Figure 81 - Percentage of poor elements across a 5x5mm unit cell with 20% V_f at a bundle length of 2mm, as the global element size was reduced from 1mm to 0.05mm.

(Note: Global element size indicates the value used to plot the coarse grid of points across the model, with the refinement element size half of the global size specified).

Of the elements that were poor at a global element size of 0.05mm (refinement grid size of 0.025mm), none of the elements in the model had angles of less than 18° in the model. This level of triangulation quality was considered to be adequate for the models created for FE analysis with no further refinement needed, with a global element size of 1/100th of the cell width adopted for the remainder of the analysis at the macroscale.

3.5.3 Fibre bundle and matrix debonding

3.5.3.1 Element selection for bundle/matrix interface

A review of the methods used to simulate debonding in composite materials is contained in section 2.2.2. Cohesive elements were used at the microscale in section 4.1.1 to simulate debonding in a single fibre composite, with the length of the debonded zone along the fibre calculated as the applied strain was increased on the model. Suitable parameters were established at the microscale that will

now be used to simulate debonding in the developed macroscale model. Some authors have used cohesive elements at the interface at the macroscale [69, 113], whilst others have used spring elements to connect the two materials together. Swaminathan et al. [111] developed a numerical cohesive zone model to represent debonding failure at the fibre-matrix interface using non-linear springs/connectors in the normal and tangential directions, much like the models produced by Kari [107]. The springs initially have zero, or negligible, length and as the strain is increased on the model the traction across the interface increases before a criterion is met to "release" the springs; thus simulating debonding between the fibre and matrix [111].

A spring/connector element was deemed the most suitable option to attach the nodes of the fibre bundles to the matrix in the developed macroscale model, as the elements are simple to integrate into the model at low computational expense. A connector element was selected over a spring element for this analysis as it allowed the element to be removed once it had failed. Initially, the length of the connector elements is zero in the model, as the nodes of the bundle and matrix are coincident. As the traction increases in the connector, the length of the element increases until the interfacial shear strength is reached, before the connector then grows at a rate defined by the fracture toughness. Once the element has failed it is removed from the model. The removal of the connector element allows complete debonding of the bundle and matrix, which can be observed visually by the user in the FE analysis in ABAQUS/Standard.

3.5.3.2 Generation and implementation of connector elements

To allow the fibre bundles and matrix to debond in the analysis it is necessary to modify the matrix elements that were generated during the Delaunay triangulation of the unit cell. Following the completion of the meshing procedure, there is one matrix node present in the same location as each fibre node. To allow separation of the matrix and bundle materials, an additional matrix node is created with the same global x and y coordinates of the coincident bundle and matrix node.

Using this newly created node, the elements either side of the fibre bundle need to be separated to allow them to be connected to the fibre bundle nodes, as shown in Figure 82. An algorithm has been developed to calculate which side of the fibre bundle each matrix element is situated, to allow the correct nodal assignment to be made. The coordinates of the nodes of each element are sequentially checked, with the element "flagged" if it contains a node that is coincident to a bundle node. The flagged elements are then assigned to the left, right or end of the bundle node, based on the coordinates of the other nodes that make up that particular matrix element. A connector element is then generated between the bundle and matrix nodes (Figure 82), with a local coordinate system assigned to each connector in the model. Figure 83 shows the connector elements across a sample model.

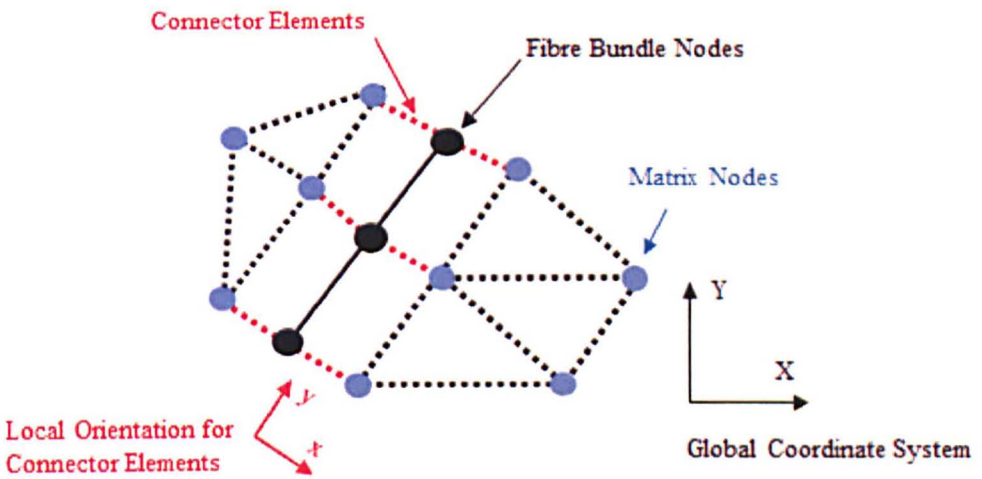

Figure 82 - Schematic showing how the fibre bundle and matrix elements are connected together to allow debonding in the FE analysis.

(Note: The matrix and fibre bundle nodes have the same global x and y coordinates initially, before loading is applied to the unit cell. A separation distance is shown above between bundle and matrix to show how the elements are connected together).

The elements used for the connectors are CONN2D2 in ABAQUS/Standard, which connect two nodes together and allow two degrees of freedom (x and y

direction). Once the connector elements have been generated and positioned in the models, the behaviour of the connectors must be defined for FE analysis.

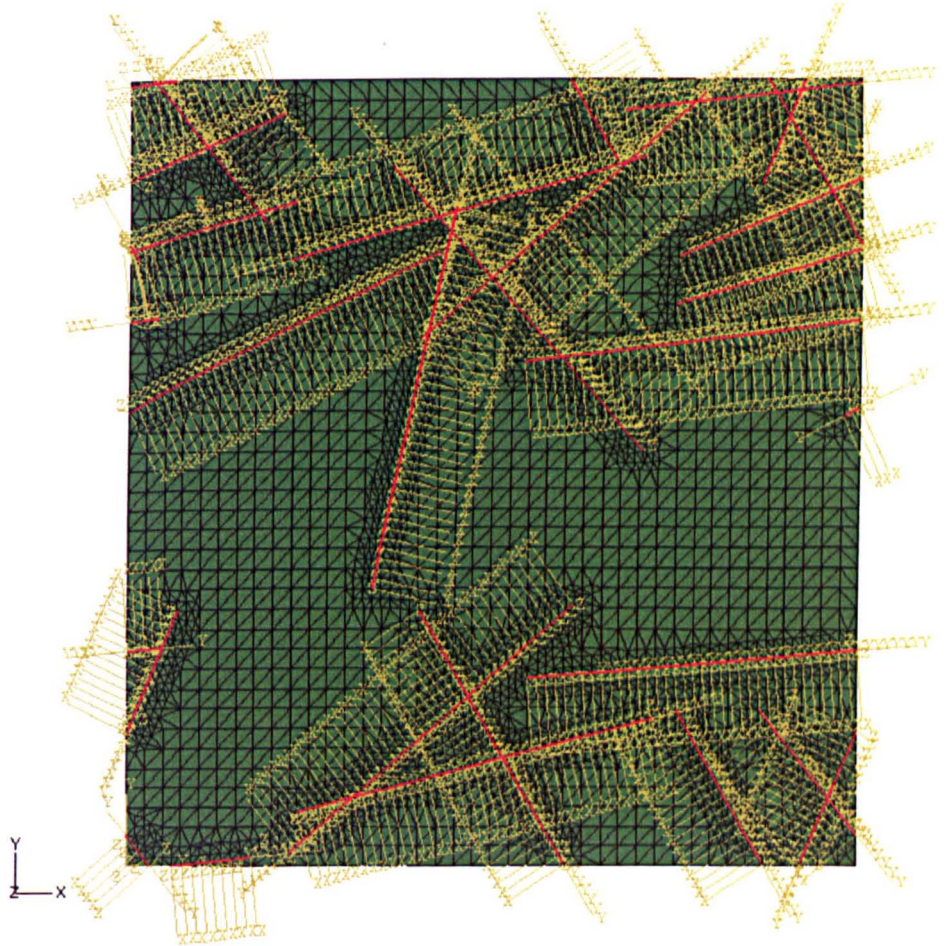

Figure 83 - Connector elements shown across a typical model, with the local x and y directions specified for each connector. (Note: Fibre elements are highlighted in red).

The connector elements use the same mechanical properties that were used in the microscale analysis in section 4.1.1. Their behaviour is governed by an uncoupled bi-linear traction-separation law. A penalty stiffness value, K, of 10^6 N/mm^3 is used for the traction-separation law for the cohesive elements. The maximum stress criterion is used to initiate failure, with τ_o set initially to 23.1MPa (or 23.1N/mm^2) using the results obtained by Gerlach et al [222]. Fibre bundle pull-out tests were performed in [222] on RTM-6 infiltrated TENAX HTS carbon fibre bundles surrounded by pure matrix material, with a mean interfacial shear strength of 23.1MPa calculated between the bundle and matrix, comparable to the values obtained in the literature for single fibre carbon/epoxy composites [47, 87-93].

The fracture toughness, G_C, of the cohesive elements was set to 220 J/m^2 based on the experimental tests conducted by Kim and Nairn [94]. The influence of the interfacial shear strength is investigated later in section 4.3.2.

Connector elements use a force based criterion to define the onset of failure, unlike cohesive elements which allow a stress value to be assigned. Therefore, the shear strength of the interface needs to be converted into a maximum force value for the connector elements. Michaeli and Kocker [223] used Equation 36 to calculate the shear stress at the interface for fibre bundle pull-out tests. Although the equation was initially developed for the single fibre pull-out test, it was found to provide good approximations of the interfacial shear strength when the area of the boundary layer of the bundle was measured optically after the test had been completed.

$$\tau_o = \frac{F_{max}}{A} = \frac{F_{max} d}{\pi l_c} \qquad \text{Equation 36}$$

where:

τ_o = maximum shear stress in the bundle matrix interface (MPa or N/mm^2).

F_{max} = force required to debond the filament from the matrix (N).

A = area of boundary layer (mm^2).

l_c = length of filament encapsulated (mm).

d = filament diameter (mm).

The fibre bundles considered in this analysis (1D beam elements) are assumed to have a circular profile, with Equation 36 adopted to calculate the force required, F_{max}, to initiate debonding in the connectors based on the interfacial shear strength, τ_o, specified for the analysis. Table 14 shows the F_{max} values obtained at constant interfacial shear strength of 23.1MPa, at a range of bundle lengths from 2mm to 100mm for a 12k fibre bundle with 60% fibre volume fraction.

Table 14 - Typical force values used to initiate failure in the connector elements, based on the shear strength specified between the bundle and matrix.

F_{max} (N)	τ_o (N/mm^2)	Bundle Diameter, d, – 12k bundle (mm)	Length of Bundle, l_c (mm)
146.64	23.10	0.9898	2.00
366.59	23.10	0.9898	5.00
733.19	23.10	0.9898	10.00
1832.97	23.10	0.9898	25.00
3665.93	23.10	0.9898	50.00
7331.86	23.10	0.9898	100.00

FE analysis has been performed on the bundle architecture produced in Figure 83 to ensure that the connector elements were functioning as specified, using the properties for the connectors defined in Table 14 for a fibre length of 5mm. The unit cell measured 20x20mm with a low volume fraction of 10% used to allow the connector behaviour to be clearly observed. The von Mises stress plot for the model is shown in Figure 84. A detailed view of the connector elements is shown between the fibre bundle and matrix elements in Figure 84, to show the separation of the bundle and matrix as the applied strain is increased on the unit cell.

Once the connector element has failed the element is "released" from the model, with the debonded fibre bundle no longer able to carry any load that is applied to the unit cell. This will lead to a reduction in strength of the composite material at low interfacial shear strengths, as multiple bundles will debond from the matrix leaving the neighbouring bundles and the surrounding matrix responsible for carrying the additional load. A study is conducted in section 4.3.2 to look at the influence of shear strength on the mechanical property prediction of the discontinuous material model.

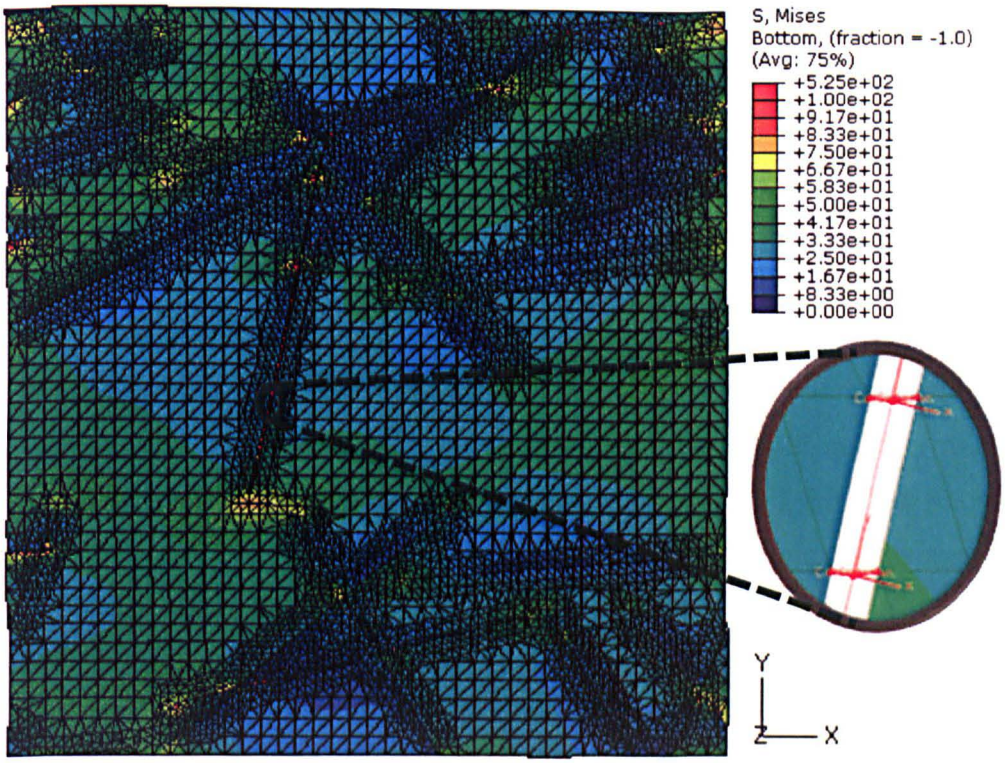

Figure 84 – Typical von Mises stress plot of a periodic unit cell with a detailed view of the connectors between the fibre bundle and matrix elements.

3.5.4 Bundle to bundle interaction

3.5.4.1 Overview

The macroscale model for discontinuous composite materials developed in this section is a 2D idealisation of a 3D problem. It was noted in [184] that the in-situ interaction between fibre bundles in the vicinity of the point where two or more bundles intersect is of a genuine 3D nature, with no attempt made in existing 2D models to capture the 3D behaviour at the intersection points [68, 184]. Macroscale models have been developed to capture the 3D fibre bundle architecture of discontinuous materials, with a review of these models and their limitations discussed in section 2.5.2.

To improve the modulus and strength predictions of the developed 2D model, 3D studies were conducted at the mesoscale to quantify SCFs in the bundles at the point of intersection, at a range of angular orientations. The results obtained in the 3D analysis at the mesoscale have been integrated into the 2D macroscale model with the bundle's mechanical properties modified at the point of intersection. The

implementation of this is discussed in the following section, with the bundle orientations and a separation function used to determine the new element properties for the bundle at the intersection point.

3.5.4.2 Implementation of bundle interactions from mesoscale

The 2D bundle architecture of the developed model does not account for the matrix material between the bundles, in the out-of-plane direction. To account for this, the coincident nodes from the overlapping bundles are tied together using a connector element, using the same methodology in section 3.5.3. The traction-separation parameters used for the connector elements at the bundle intersection are the same values used at the bundle-matrix boundary, with an assumption made that at the point of intersection the bundles are always separated by matrix material through the thickness of the model.

Figure 85 shows the intersection of two fibre bundles, with the elements at the intersection identified ready for the modification based on SCFs found in the bundles and matrix in the 3D mesoscale analysis in section 4.2.2. The reduction in the mechanical properties of the elements at the bundle intersections is dictated by the in-plane orientation angle (ϕ) and a function used to generate an out-of-plane separation distance between the bundles. In the 3D mesoscale analysis of two fibre bundles interacting in a unit cell, orientation angles (ϕ) between 0^{o} and 90^{o} were considered at a range of separation distances from 0.2mm to 2.20mm.

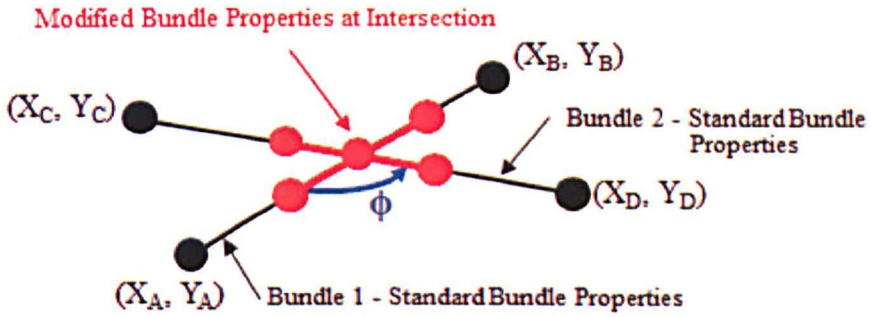

Figure 85 - Schematic to show the bundle mechanical properties that are modified at the point of bundle intersection.

The orientation angle (ϕ) between the fibre bundles is calculated, before being grouped ready for the reduction in the mechanical properties of the elements at the intersection. Seven groups, A to G, were generated using the values of the orientations considered at the mesoscale as their central value, with the angle ranges used to define the groups shown in Table 16. After the bundle intersection has been assigned an angle orientation group, the bundles are assigned an out-of-plane separation distance. A probability density function (Q) is used to assign the separation distance (s) of the bundles, which is a function of the cell depth (d) - specified initially by the user in the program. The function is a skewed normal distribution, which is defined as follows:

$$Q = f(s) = ae^{-\frac{(s-b)^2}{2c^2}} \qquad \text{Equation 37}$$

A probability density function (Q) is defined for a range of volume fractions for the unit cell, with the skew greater with decreasing volume fraction, shown in Figure 86. The function takes into consideration that the fibre bundles are likely to have a greater separation distance through the thickness of the material as the volume fraction is reduced. The values used to define the function shapes are detailed in Table 15.

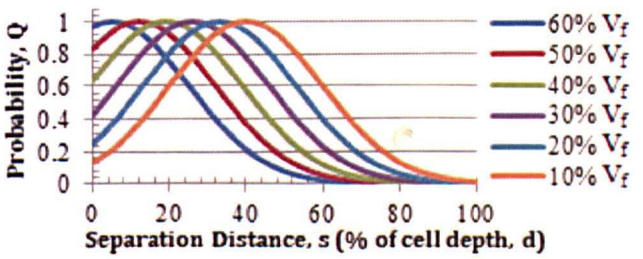

Figure 86 - Skewed probability function (Q) to assign separation distance between the fibre bundles at the point of bundle intersection.

Table 15 - Values used to define the probability function (Q) for the separation distance between the fibre bundles at varying volume fraction, see Figure 86.

V_f	60%	50%	40%	30%	20%	10%
a	1	1	1	1	1	1
b	5	12	19	26	33	40
c	20	20	20	20	20	20

The values used in Table 15 were generated to provide a quantitative variation in separation distance across unit cells of varying volume fraction, with the values used not based on experimental data. For this analysis, the range of separation distances considered at each volume fraction was deemed acceptable; however, the accuracy of the model could be improved in future by calculating the average bundle separation distance across plaques manufactured with different volume fractions.

After the bundle intersection has been allocated a separation distance, based on the volume fraction of the cell and the value returned from the probability density function (Q), the separation distance is then allocated a separation group. The five separation groups used in this analysis are shown in Table 16. The separation distances and angular orientations are grouped as it would be unfeasible to calculate knockdowns for every possible permutation of separation/orientation, with the 35 groups created in Table 16 providing adequate coverage of the full range of possible separation/orientation combinations.

The values given in Table 16 for the knockdowns are percentage values, with the stiffness of the elements either side of the point of intersection, shown in Figure 85, reduced to the value contained in each cell. The knockdown is calculated by dividing the stiffness of the elements by the SCF found at the mesoscale. For example, if an intersection lies in group D (45°) and its separation distance is 30-50% of the unit cell depth, then the stiffness of the bundle elements are reduced to 96.87% of the original bundle mechanical properties. A study has been conducted in section 4.3.3 to quantify the influence of the knockdowns at the bundle intersections on the mechanical properties of the unit cell.

Table 16 - Summary of knockdowns used for modulus of the bundle elements at the point of intersection for the range of orientations and separation distances.

		Angular Orientation						
	Angle Range	0.00° to 7.50°	7.51° to 22.50°	22.51° to 37.50°	37.51° to 52.50°	52.51° to 67.50°	67.51° to 82.50°	82.51° to 90.00°
	Group	**A (0°)**	**B (15°)**	**C (30°)**	**D (45°)**	**E (60°)**	**F (75°)**	**G (90°)**
Separation Distance, s (% of unit cell depth, d)	**100% to 70%**	100.00%	100.00%	100.00%	100.00%	100.00%	100.00%	100.00%
	70% to 50%	100.00%	100.00%	100.00%	99.38%	98.01%	97.35%	96.76%
	50% to 30%	100.00%	100.00%	99.47%	96.87%	95.36%	94.61%	94.16%
	30% to 10%	100.00%	100.00%	97.87%	94.56%	92.92%	92.61%	92.24%
	10% to 0%	100.00%	100.00%	96.85%	93.36%	91.64%	91.42%	91.21%

3.5.5 Boundary conditions

A full review of the boundary conditions used for macroscale RVEs of discontinuous composites is contained in section 2.5.3. The developed macroscale model is capable of producing tensile test coupons and unit cells with periodic boundary conditions, with a summary of these boundary conditions and the subsequent constraints imposed on the models detailed in this section. For the analysis contained in this thesis at the macroscale, periodic boundary conditions have been utilised to subject the unit cells to pure tensile (x and y) and shear (xy) strains.

3.5.5.1 Tensile boundary conditions

The simpler of the two boundary conditions that can be imposed on the macroscale model is the tensile (bi-axial) boundary conditions, shown in Figure 87. The left edge of the model is constrained in the x and y directions to allow no movement along that surface. The right surface is tied to a dummy node, with the prescribed strain applied along the full length of the surface. The right surface is also constrained from moving vertically, to directly simulate a tensile specimen in

the jaws of a testing machine. Both the top and bottom surface are free to contract due to Poisson effects, with no boundary conditions imposed on them.

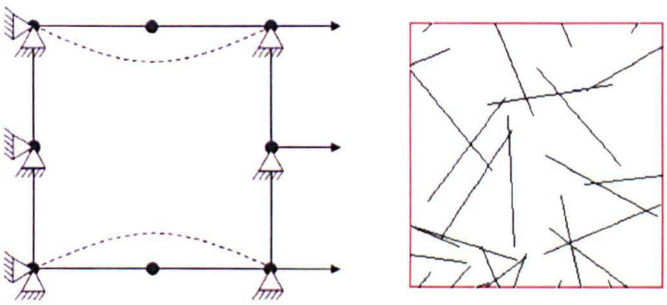

Figure 87 - Schematic of the bi-axial conditions imposed on the model to simulate a tensile test.

3.5.5.2 Periodic boundary conditions

The second set of boundary conditions that can be imposed on the macroscale model are periodic boundary conditions that adhere to the equation constraints outlined by Li et al [150, 151] for cells with translational symmetry in the x and y directions, shown in Figure 88 (left - before loading, middle – after loading). To maintain periodicity across the cell, the fibres are cropped at the boundary of the model, as shown in Figure 43, before being translated across to the opposing surface to ensure a representative number of bridging and ending fibre bundles are captured within the model boundary. The cropped fibres that have been translated to opposing boundaries are highlighted in red in Figure 88 (right).

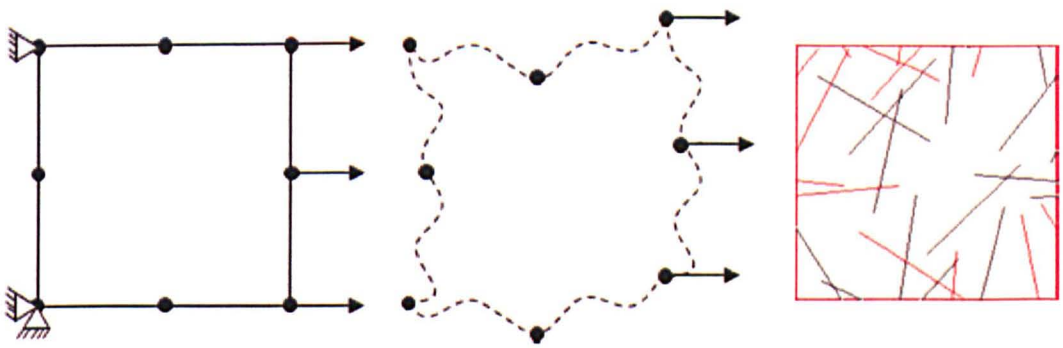

Figure 88 - Schematic of periodic boundary conditions imposed on model.

To impose periodic boundary conditions on the model, an equal number of nodes must be present on opposite boundaries. The number of nodes on the left edge is

equal to the number of nodes on the right edge, and the number of nodes on the top edge is equal to the number of nodes on the bottom edge. Three dummy nodes are also created with equation constraints used to apply strain to the unit cells in the x, y and xy directions. The equation constraints used to impose the periodic boundary conditions on the model are detailed in Appendix D.

3.5.6 Macroscale modelling limitations

The model provides a quantitative assessment of varying the interfacial shear strength between the fibre bundle and matrix materials when determining the mechanical properties of discontinuous composite at the macroscale. As stated previously, the in-situ interaction between fibre bundles in the vicinity of the point where two or more bundles intersect is of a 3D nature [184]. The developed model uses mesoscale studies of interacting bundles to account for this to improve mechanical property predictions. The fibre bundles are considered to be perfectly straight in the models, with the influence of curvature neglected for this analysis.

Chapter 4 Results

4.1 Microscale modelling

4.1.1 Single fibre micromechanical analysis – interfacial debonding

The finite element results for the single fibre composite model are presented in four separate sections. The first section assumes that the fibre and matrix are perfectly bonded and the second section uses cohesive elements between the fibre and matrix to model interfacial debonding. Both studies are performed with the matrix modelled as an elastic and elastic-perfectly-plastic (EPP) material. Comparisons are then made in section 3 with shear lag predictions. The final section looks at the influence of the interfacial fracture toughness on the rate of debonding in the single carbon fibre composite models.

Section 1: Perfect bond between fibre and matrix

The fibre axial stress and interfacial shear stress for the elastic matrix material model are shown in Figure 89. For the graphs in this section, Z is defined as the length along the fibre, with Z/r defined as the ratio of fibre length to fibre radius in the models. The peak values for both the fibre axial stress and interfacial shear stress increase with increasing applied strain on the single fibre composite, with the maximum fibre axial stress observed at the fibre midpoint and the peak interfacial shear stress found at the fibre end. The fibre axial stress is approaching the fibre failure strength at 2.4% applied strain as the interface is assumed to be perfect in the model allowing greater loads to be transferred to the fibre. Interfacial shear stress values are high for the perfect interface model, exceeding the 20-70MPa range typically used to define the interfacial shear strength (ISS) between fibre and matrix materials. In addition to this, the axial stress at the fibre end is non-zero, consistent with the findings of Galiotis [95], with this not captured by the models produced by Cox and Kelly-Tyson.

The fibre axial stress and interfacial shear stress for the EPP matrix material model are shown in Figure 90. The introduction of plasticity into the matrix changes both the fibre axial stress and interfacial shear stress profiles along the length of the fibre. At small applied strains (0.4%), prior to the onset of matrix

plasticity in the models, the fibre axial stress and interfacial shear stress in the elastic matrix model and EPP matrix model closely match each other. As the applied strain is increased on the model, a plateau region is observed in the interfacial shear stress profile as the stress levels exceed the matrix yield stress, similar to the results presented by Pan [69], with the magnitude of the interfacial shear stress values much lower than for the elastic matrix model in Figure 89. The length of the plateau region increases as the applied strain is increased, with this constant interfacial shear stress along the length of the fibre causing the fibre axial stress profiles to be almost linear at applied strains greater than 1.2% as no further load can be applied to the fibre in the plateau region.

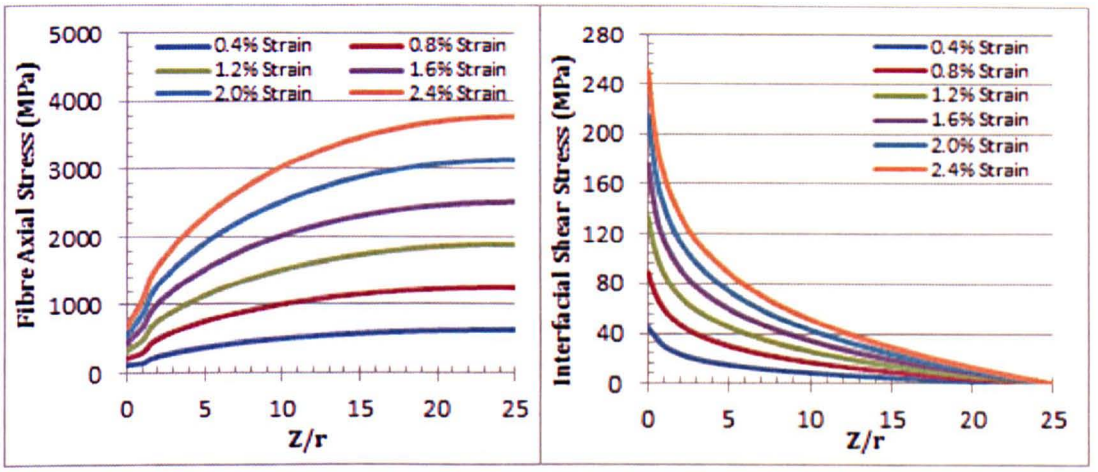

Figure 89 - Fibre axial stress (left) and interfacial shear stress (right) for the perfect bond interface model with elastic matrix properties.

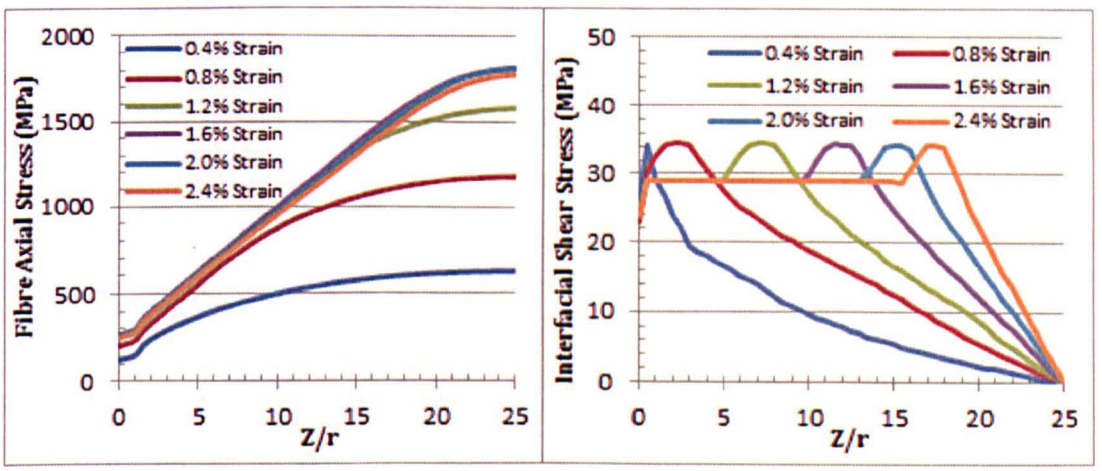

Figure 90 – Fibre axial stress (left) and interfacial shear stress (right) for the perfect bond interface model with EPP matrix properties.

Section 2: Debonding between fibre and matrix

The interfacial shear strength, τ_o, was set to 20MPa and the fracture toughness, G_C, of the cohesive elements was set to 220 J/m^2 for this study. The fibre axial stress and interfacial shear stress profiles for the debonding model with elastic matrix properties are shown in Figure 91. As expected, the introduction of debonding into the model greatly changes the fibre axial stress and interfacial shear stress profiles. The interfacial shear stress observed in the model does not exceed 20MPa, as damage is initiated in the cohesive element if stresses exceed this value. Once damage has been initiated in the cohesive element (point A in Figure 16), the fracture toughness dictates the rate at which the element decays before final failure of the element (point B in Figure 16). This leads to a damage processing zone between the elements which are fully damaged (debonded and carry zero stress) and the undamaged elements that are still active in the model.

The damage processing zone in this study is greater than that found by Pan [69], but this is attributable to the higher fracture toughness value (220 J/m^2) of the carbon/epoxy composite when compared to the fracture toughness of glass/epoxy composite (100 J/m^2). The fibre axial stress reduces to a near zero value along the length of the fibre when debonding has occurred in the interface. At strains greater than 0.4%, lower loads are transferred through the damaged interface from the matrix to the fibre. The fibre axial stress and interfacial shear stress profiles for the debonding model with EPP matrix properties are shown in Figure 92.

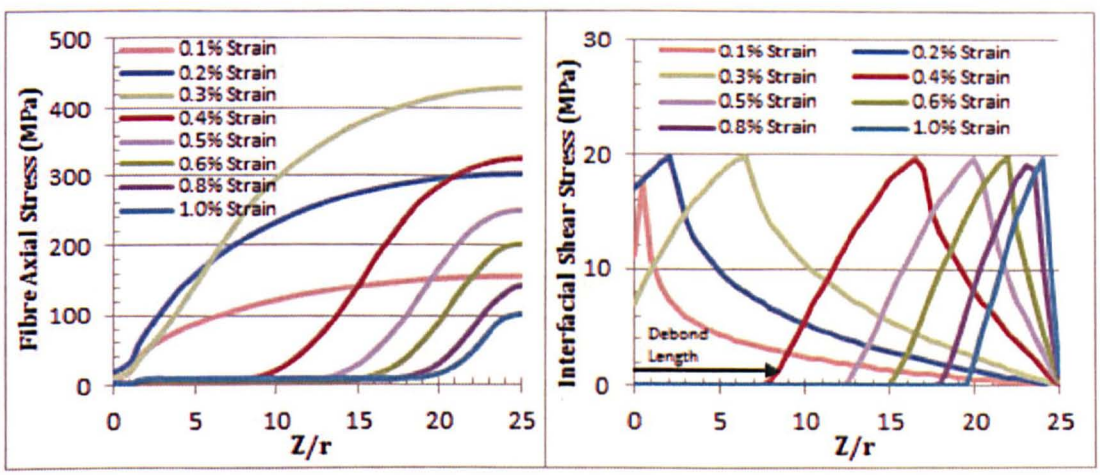

Figure 91 - Fibre axial stress (left) and interfacial shear stress (right) for the debonding interface model with elastic matrix properties.

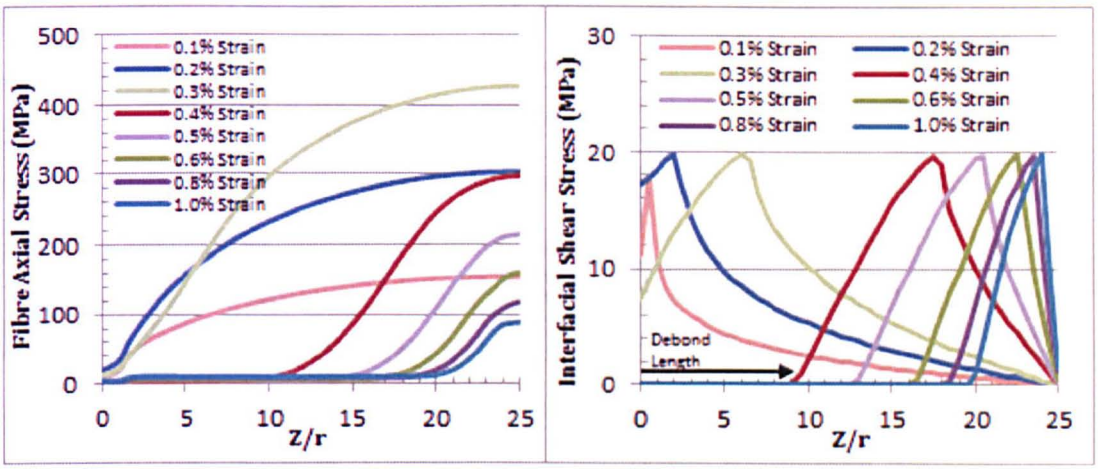

Figure 92 - Fibre axial stress (left) and interfacial shear stress (right) for the debonding interface model with EPP matrix properties.

The introduction of plasticity into the matrix material has only a slight impact on the debonding lengths observed in the single fibre composite. At low applied strains (less than 0.3%), prior to the onset of debonding, the fibre axial stress and interfacial shear stress profiles were identical. It was observed in [69] that the debonding length was lower in a glass fibre elastic matrix model when compared to an elastic-plastic matrix at lower applied strains, but at higher applied strains this trend reversed. The results from this study agree with Pan's findings. When the applied strain on the model was increased to between 0.4% and 0.6% strain, the debonding length in the interface of the EPP matrix models is greater (~10%) than that of the elastic matrix models. However, at strain levels greater than 0.8% the debonding lengths of both elastic and EPP matrix models are almost identical.

The onset of debonding occurred earlier and progressed faster in this study when compared to the work by Kim and Nairn [94], who performed experimental tests to predict the debond lengths of AS4-carbon fibres embedded in an epoxy matrix. In this study, a debond length of 9 fibre radii (9r) was predicted at 0.4% applied strain, rising to 20r at 1.0% applied strain - an increase of 11r over a net applied strain increase of 0.6%. The experimental results in [94] found a debond length of 6r at 1.0% applied strain, rising to 14r at 2.0% applied strain, an increase of 8r (28μm) over a net applied strain increase of 1.0%. The variation in experimental results and the FE models is consistent with the glass/epoxy single fibre composite model developed by Pan [69], with the discrepancy attributed to the

absence of the friction force and initial Residual Thermal Stress (RTS) on the interface in the FE models.

Section 3: Comparison of perfect bond, debonding and shear lag models

The fibre axial stress and interfacial shear stress profiles for the perfectly bonded interface and debonding models are compared to predictions from the shear lag model developed by Cox [50] in this section. Figure 93 shows the models compared at 0.2% applied strain, before the onset of damage in the cohesive elements at the interface. The peak shear stress prediction from the shear lag model is around 50% lower than the perfectly bonded interface FE models, which leads to a reduction in axial stress along the length of the fibre as the interface is responsible for transferring the load to the fibre from the matrix via shear in the composite material. The debonding models predict fibre axial stress values just below (~3.50%) the values obtained from the perfectly bonded models, attributable to the small processing zone which is observed in the interfacial shear strength plot in Figure 93 as the interface reaches the interfacial shear strength of 20MPa.

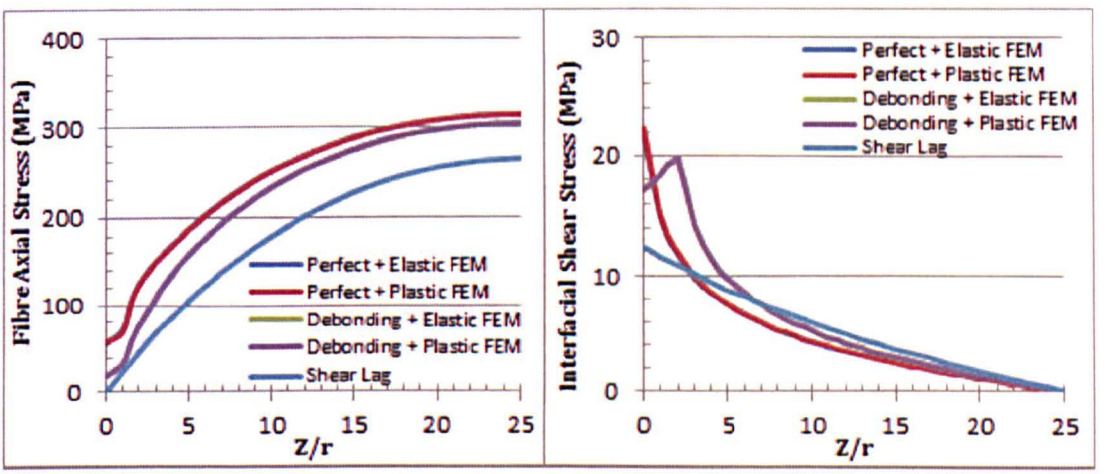

Figure 93 - Comparison of shear lag models to FE models with a perfectly bonded and debonding interface, with elastic and EPP matrix, at 0.2% applied strain.

Figure 94 compares the fibre axial stress and interfacial shear stress profiles for all the models at 0.4% applied strain, once debonding has initiated in the debonding models. A comparison is also made at 0.6% applied strain, Figure 95, to show the

variation in the stress plots as the debonding length increases along the fibre length in the models.

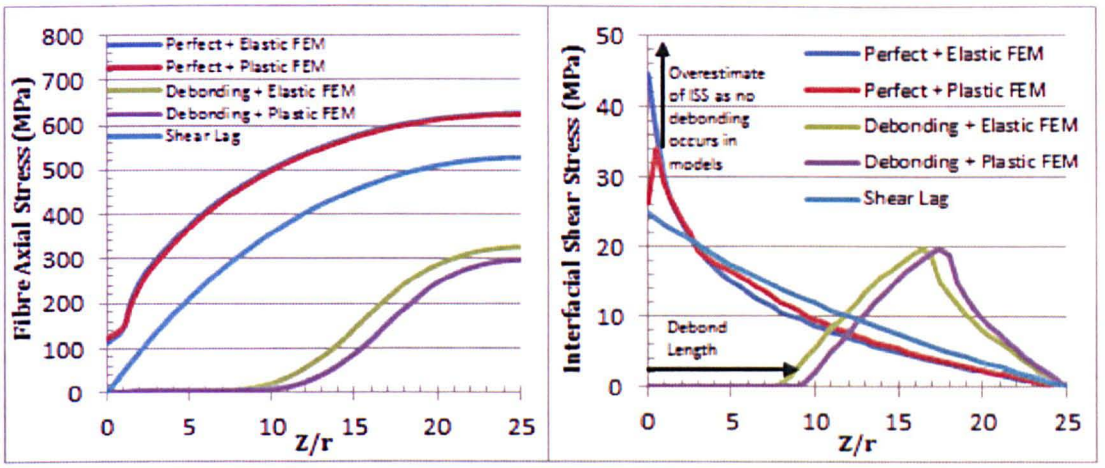

Figure 94 - Comparison of shear lag models to FE models with a perfectly bonded and debonding interface, with elastic and EPP matrix, at 0.4% applied strain.

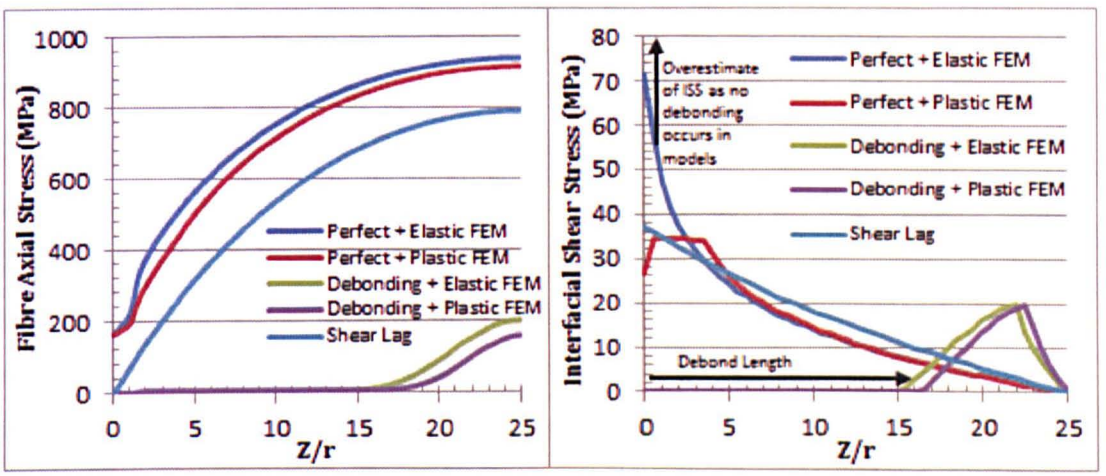

Figure 95 - Comparison of shear lag models to FE models with a perfectly bonded and debonding interface, with elastic and EPP matrix, at 0.6% applied strain.

At 0.4% applied strain, the shear lag prediction for the axial fibre stress lies between the perfectly bonded interface models and the debonding models (left, Figure 94). The reduced fibre axial stress observed in the debonding models is attributable to the debond length, also shown in the interfacial shear stress plot (right, Figure 94). The shear stress is zero across the full length of the debonded zone, with a processing zone found after this point, attributable to the fracture toughness of the interface, as the interfacial shear stress approaches the shear

strength of the interface elements – 20MPa. The interfacial shear stress in the perfectly bonded and shear lag models exceeds the shear strength of the interface in the debonding models as they do not account for interfacial damage, which provides the greater fibre axial stress levels observed (left, Figure 94).

As the applied strain is further increased on the models, to 0.6% in Figure 95, the discrepancy between the debonding models and the perfectly bonded models, and shear lag models, becomes even greater with the increase in debond length. This comparison has shown that the shear lag model and perfectly bonded models are valid for predicting the fibre axial stress and interfacial shear stress in a single fibre composite model at low applied strains (0.2% applied strain or less). Once the shear strength of the interface between the fibre and matrix is exceeded, at strains greater than 0.4%, both the shear lag model and perfectly bonded interface models are not suitable for predicting the fibre axial stress and interfacial shear stress for the current combination of constituent materials.

Section 4: Influence of interfacial fracture toughness on fibre debond length

The fracture toughness of the interface was varied in this study to analyse its influence on the debond length observed in the single fibre composite. Four fracture toughness values of 100 J/m^2, 220 J/m^2, 500 J/m^2 and 1000 J/m^2 were considered, with the interfacial shear strength kept constant at 20MPa in this analysis. The elastic matrix properties were used in this analysis to allow the influence of interfacial fracture toughness to be studied independently. The debond lengths are plotted for the range of interfacial fracture toughness values considered in Figure 96.

Damage initiates at the same point in all the fracture toughness models (~0.2% applied strain), as the interfacial shear strength is constant. However, by increasing the fracture toughness of the interface the onset of failure of the interface elements is delayed, with the length of the processing zone increasing with higher fracture toughness. A greater applied strain is therefore required to cause failure of the cohesive elements to propagate the crack along the length of the fibre, consistent with the findings in [69]. Figure 97 shows the fibre axial stress and interfacial shear stress profiles at 0.4% applied strain for the models

with increasing fracture toughness. The interfacial shear stress profiles in the models, (right, Figure 97), shows that the rate of interfacial debonding increases when lower values, 100 J/m^2 and 220 J/m^2, are used for the interfacial fracture toughness. This increase in debond length inherently reduces the fibre axial stress observed (left, Figure 97).

For the model with a fracture toughness value of 1000 J/m^2 the debond lengths are comparable with the experimental tests conducted by Kim and Nairn [94] for the AS4-carbon epoxy composite. A debond length of 2.5 fibre radii (2.5r) was predicted at 1.0% applied strain, rising to 14r at 2.0% applied strain for the single fibre composite model, an increase of 11.5r. The experimental results in [94] found a debond length of 6r at 1.0% applied strain, rising to 14r at 2.0% applied strain, an increase of 8r over the same range as the single fibre model.

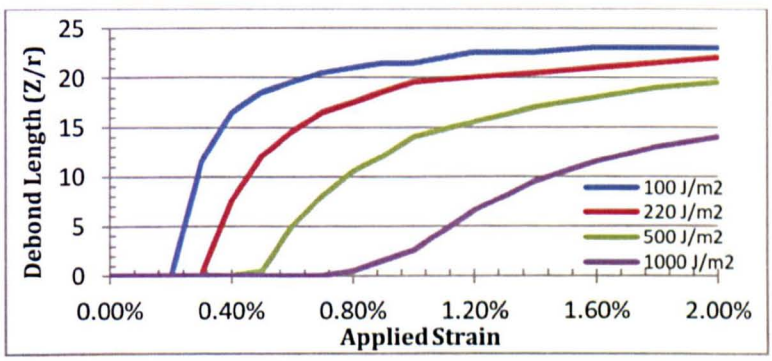

Figure 96 – Debond length in models with increasing interfacial fracture toughness

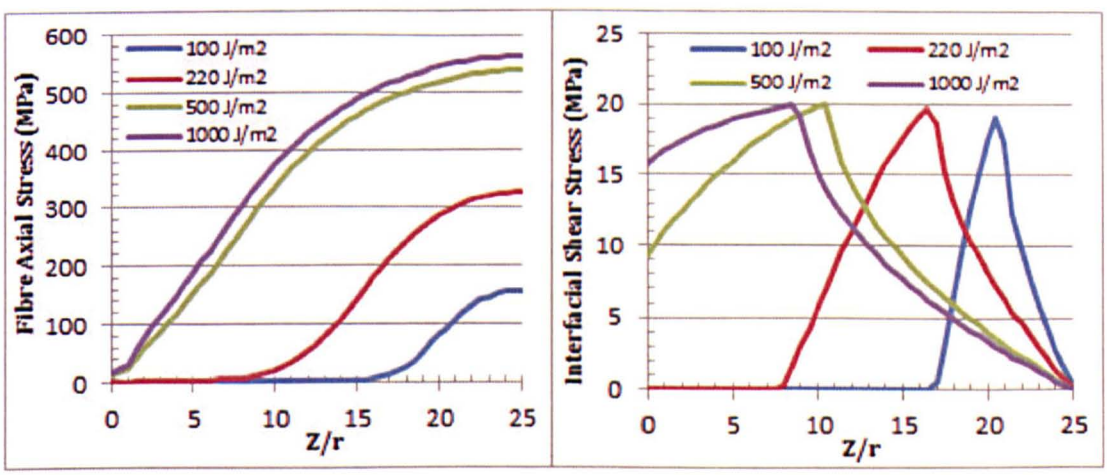

Figure 97 – Fibre axial stress (left) and interfacial shear stress (right) plots for the interfacial fracture toughness study, plotted at 0.4% applied strain.

4.1.2 Fibre ineffective length

The results from the analysis have been split into two sections. The first section will look at the stress plot and damage development in the model which uses the mid-values for the modulus of the fibre, interface and matrix. The ineffective length of the broken fibre will be calculated, along with the SCF observed in the unbroken fibre to show the methodology used for all the model variants. The second section will focus on the full factorial study to determine the influence of the three input parameters (fibre, interface and matrix stiffness) on the monitored output parameters (fibre ineffective length and SCF).

Stress and Damage Analysis for Mid-value Model

A typical von Mises stress plot for the model is shown in Figure 98. Stress builds along the length of the fractured fibre, with the unbroken fibre experiencing greater stress levels around the fracture site. The axial fibre stress along the length of the broken and unbroken fibre is shown in Figure 99, with the values taken at 0.2% applied strain for consistency with the von Mises stress plot in Figure 98.

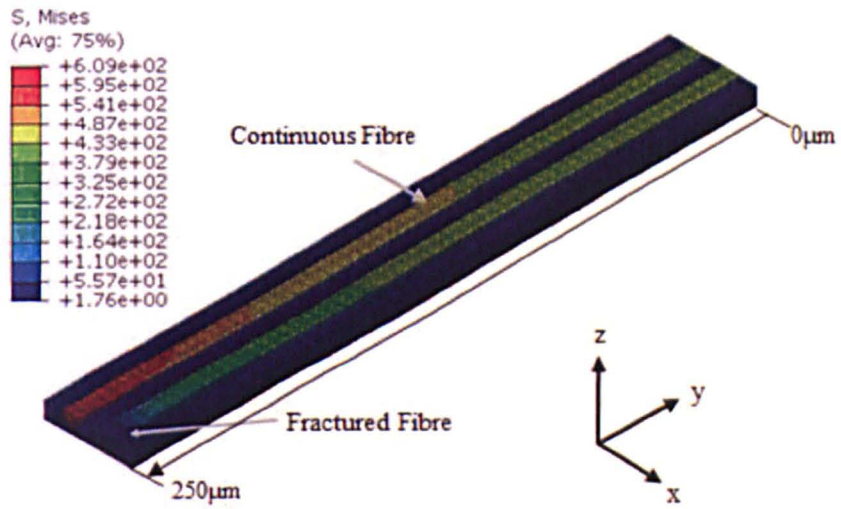

Figure 98 - von Mises stress plot at 0.2% strain for the fibre ineffective length model.

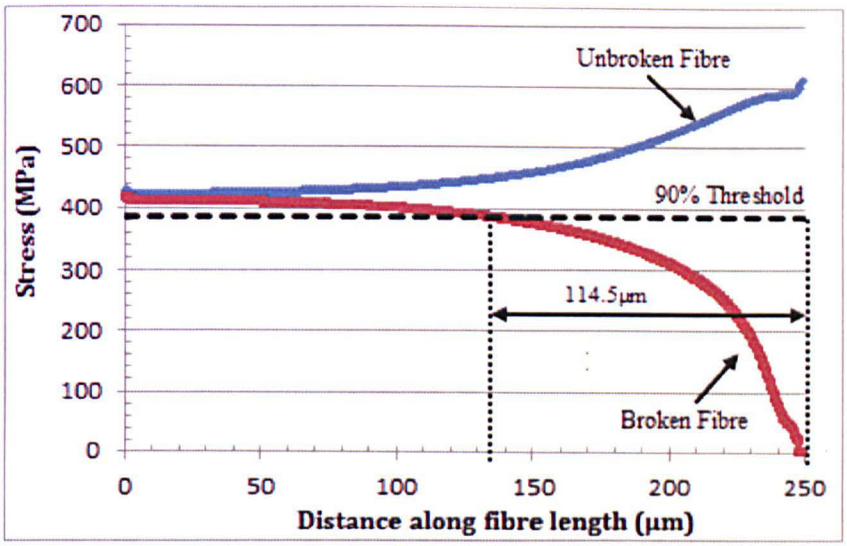

Figure 99 – Axial fibre stress plot along the half length of the broken and unbroken fibre at 0.2% applied strain.

The ineffective length of the broken fibre and the PAL of the unbroken fibre can be calculated using the data in Figure 99, with the 90% threshold plotted for clarity. A fibre ineffective length of 114.50μm was calculated in this analysis for the broken fibre, with a SCF of 1.4303 observed in the unbroken fibre. The SCF was calculated by dividing the peak stress in the unbroken fibre by the stress at which the fibre axial stress plateaus in the unbroken fibre. The SCF observed in this study is relatively high when compared to existing models in the literature (Figure 18), attributable to the fact that only one fibre is responsible for carrying the overload created by the fibre discontinuity.

Damage began to initiate in the matrix region at the tip of the broken fibre at 0.1% applied strain, at the site of the fibre fracture, before propagating along the length of the broken fibre down the interface. As the strain on the unit cell was increased to 0.4%, damage began to develop into the matrix region between the broken and unbroken fibre, shown in Figure 100. This damage then progressed across the matrix region at the base of the broken fibre at 1.6% applied strain, and ultimately caused failure of the unit cell as the matrix reached the failure strain criterion set in the UMAT. The unbroken fibre experienced further overloading around the site of the fibre fracture, which led to fibre failure in the initially unbroken fibre.

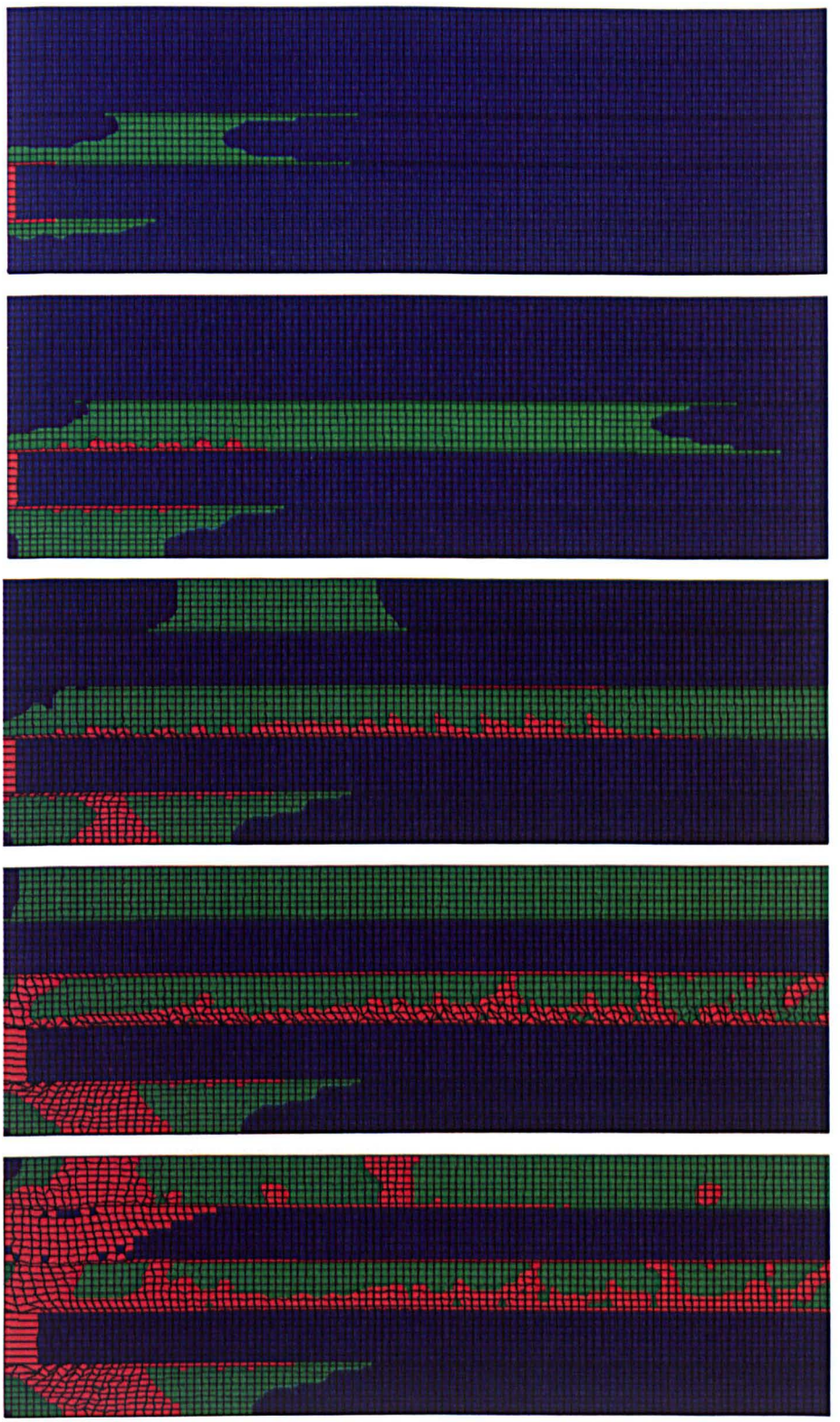

Figure 100 - Plan view of the damage progression in the fibre ineffective length model, focussed on the end of the fibre fracture.
(Top to bottom; 0.2%, 0.4%, 0.8%, 1.6% and 2.0% applied strain).
Undamaged elements (blue), plastic elements (green) and damaged elements (red).

Full Factorial Study

The 27 variants of the model were run in ABAQUS/Standard and the ineffective length of the broken fibre was calculated at 0.2% applied strain for each model. The SCF experienced by the unbroken fibre was also calculated, with the results presented in Table 17.

Table 17 - Results from full factorial study.

Fibre Modulus	Matrix Modulus	Interface Modulus	Ineffective Length (μm)	Stress Concentration Factor (SCF)
High	High	High	116.5	1.4442
Low	Low	High	107.5	1.4071
Mid	High	Mid	104.0	1.4046
Mid	Mid	Mid	114.5	1.4303
Low	High	Low	91.5	1.3548
Low	Mid	High	94.0	1.3617
Mid	Low	Low	136.5	1.4736
High	High	Low	125.5	1.4745
High	Low	Mid	156.5	1.5044
Low	High	Mid	86.5	1.3293
Mid	High	High	100.5	1.3894
High	Low	High	154.5	1.5111
Low	Low	Low	113.5	1.4221
High	Low	Low	165.0	1.5191
Mid	Mid	Low	120.0	1.4531
Mid	Mid	High	111.0	1.4193
Low	Mid	Low	100.5	1.3884
Mid	Low	Mid	131.5	1.4637
High	High	Mid	129.5	1.4589
Low	High	High	85.0	1.3258
High	Mid	Low	140.5	1.4977
Low	Mid	Mid	96.5	1.3709
Mid	High	Low	109.5	1.4309
Low	Low	Mid	109.0	1.4075
High	Mid	High	128.5	1.4635
Mid	Low	High	128.5	1.4607
High	Mid	Mid	133.0	1.4738

The results from the full factorial array were then analysed by performing a general linear analysis of variance (ANOVA) to evaluate the importance of the three input variables on the fibre ineffective length and SCFs in the models. Figure 101 shows the main effects plot for the fibre ineffective length of the broken fibre. The modulus of the fibre has the greatest influence on the fibre ineffective length in this study, with a 41.34% increase in the fibre ineffective length as the fibre modulus is increased from its lowest to highest values. The use of higher grade carbon fibres with greater mechanical properties increases the mismatch in the modulus between the fibre and matrix/interface (an increase in

the E_{fibre}/E_{matrix} ratio), which leads to an increase in the ineffective length of a broken fibre in the composite. Therefore, these results suggest that there is little point in using expensive, high-grade carbon fibres with a low performance resin. A high performance resin, or fibre coating, is needed to reduce the ineffective length of broken fibres in a composite material. A decrease in the fibre ineffective length was observed when the modulus of the matrix and interface were increased, with reductions of 21.12% and 6.94% respectively. The increase in the modulus of the matrix and interface promotes greater stress transfer efficiency between the fibres as the E_{fibre}/E_{matrix} ratio is decreased, which provides shorter fibre ineffective lengths. The interface only accounts for a small volume of the unit cell (0.5μm thickness around the fibres), yet it still significantly contributes to a reduction in the ineffective length of a broken fibre in the model (~7%). This provides a clear indication that the use of sizing on fibres can promote greater stress transfer efficiency between fibres in a composite, thus improving the mechanical properties of the material.

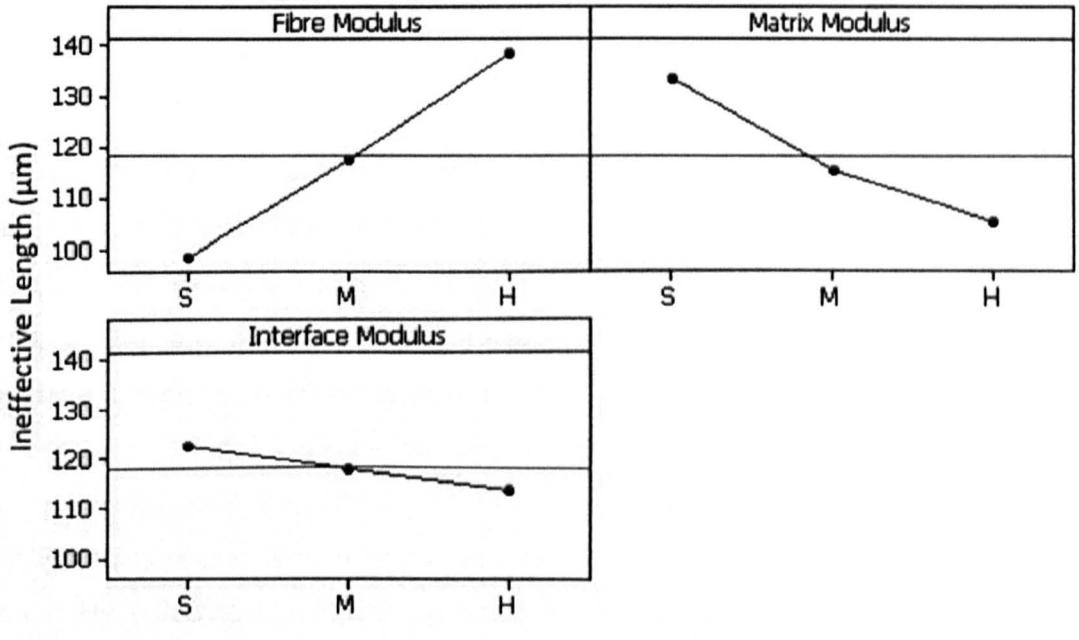

Figure 101 - Main effects plot for the fibre ineffective length of the broken fibre

The main effects plot for the stress concentration in the unbroken fibre in the model is shown in Figure 102. The SCF in the unbroken fibre increased by 7.93% when the fibre modulus was increased from its lowest to highest value (190.4GPa to 285.6GPa), in the analysis. The use of higher modulus carbon fibres will

produce a composite with greater stiffness; however around the site of a fibre fracture the SCF experienced by neighbouring fibres will be higher because of a greater mismatch in stiffness between fibre and matrix.

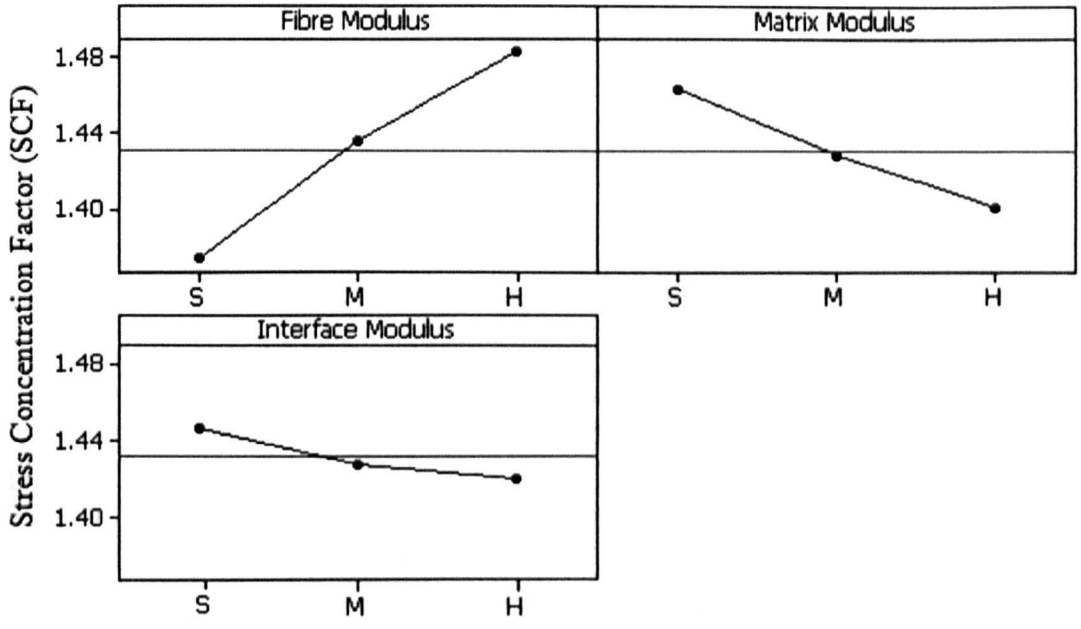

Figure 102 - Main effects plot for the stress concentration factor (SCF) experienced by the unbroken fibre in the model.

A reduction in SCF was observed with an increase in matrix and interface modulus, with a decrease of 4.24% and 1.80% respectively, similar to the results for the fibre ineffective length in Figure 101. By increasing the modulus of the matrix and interface the stress transfer efficiency between the fibres was increased, with the overload caused by the fibre break partially redistributed into the matrix material between the two fibres – leading to lower SCFs in the neighbouring, unbroken fibres. The fibre ineffective lengths of broken fibres and SCFs in adjacent unbroken fibres are both strongly dependent on the E_{fibre}/E_{matrix} ratio. By reducing the E_{fibre}/E_{matrix} ratio in the composite, the fibre ineffective length is reduced and lower SCFs will be found in adjacent fibres, providing an increase in the mechanical properties of the material.

According to Figure 103, an increase in matrix and interface modulus improves the failure strength of the composite material, whereas an increase in fibre modulus reduced the failure strength of the model. It was shown in Figure 101

and Figure 102 that the fibre ineffective length of the unbroken fibre and the SCF in the neighbouring fibre increased with increasing fibre modulus, which increases the stress levels in the matrix material between the two fibres. This increased stress level in the matrix and interface causes failure to initiate at lower applied strains in this region, so a reduction in failure strength was observed for this two fibre model. This study only considers two fibres at low volume fraction (~15%); with only one fibre responsible for carrying the overload caused by the fibre break. In practice, at higher volume fractions, multiple fibres will be responsible for carrying the additional load at the site of the fibre break; therefore the SCF values would be lower, as shown in Figure 18.

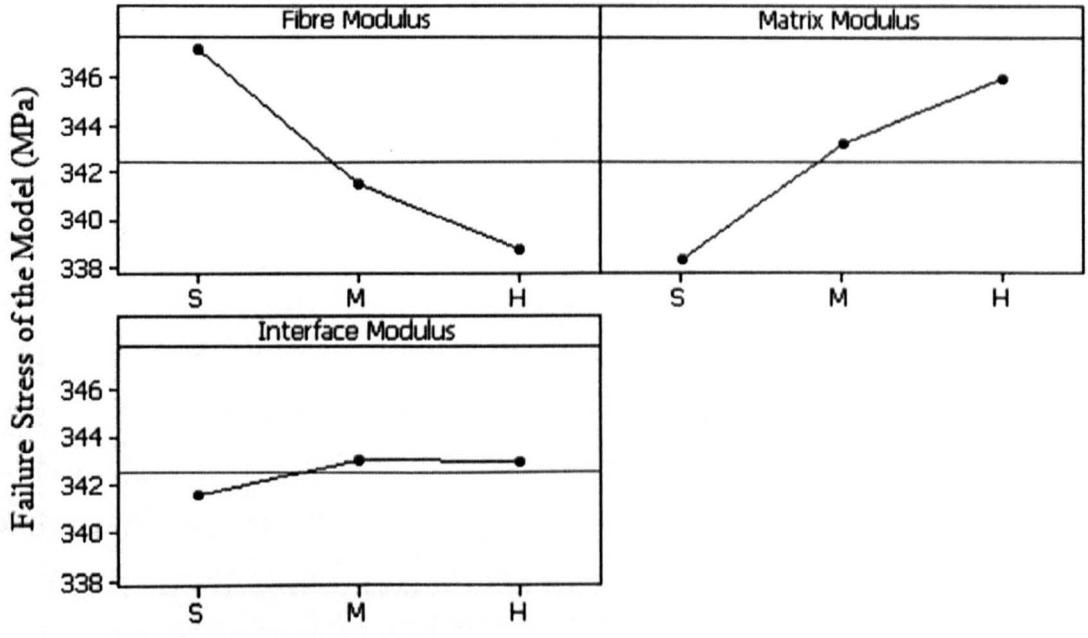

Figure 103 - Main effects plot for the failure stress of the model

In addition to looking at the influence of the input parameters (fibre, matrix and interface modulus) in isolation, interaction between the parameters has also been analysed by performing a general linear analysis of variance (ANOVA). The interaction plots for the fibre ineffective length of the broken fibre and the SCF experienced by the unbroken fibre are shown in Figure 105 and Figure 106 respectively. An interaction plot is a plot of means for each level of a factor with the level of a second factor held constant. Parallel lines in the plot indicate that little or no interaction is present between the variables under consideration and as the lines depart from the parallel state there is a higher the degree of interaction.

When determining the fibre ineffective length of a broken fibre, the interaction plot (Figure 105) indicates that there is little interaction between the variables in this analysis, with the lines in the plot remaining relatively parallel in each interaction cell. The interaction plot for calculating the SCF experienced by the unbroken fibre, Figure 106, shows that there is limited interaction between the variables in this analysis. The interface modulus and matrix modulus interaction cell, designated as cell X in Figure 106, suggests that there is an interaction between these two variables when determining SCF in fibres adjacent to a fibre break. With the interface and matrix responsible for transferring the overload from the fibre break to the adjacent fibre, it is unsurprising that the combination of the two variables influences the SCF in the unbroken fibre in the model.

The lower bound for fibre ineffective length of the broken fibre and SCF in the unbroken fibre found in the study was 85μm and 1.3258, respectively, for the model with low fibre stiffness and high matrix and interface stiffness. In contrast to this, the upper bound had a fibre ineffective length and SCF of 165μm (0.165mm) and 1.5191, respectively, for the model with high fibre stiffness and low matrix and interface stiffness. The high SCF values obtained in the study are attributable to only two fibres being considered in a low fibre volume fraction model, with only one fibre responsible for carrying the overload created by the fibre discontinuity, with Lane et al [48] reporting strain concentration values of 1.05 at volume fractions between 38-58% at 1% applied strain for carbon-epoxy composites. In addition to the influence of volume fraction on the SCFs, the cross-sectional shape of the fibre bundle will also influence the SCFs observed in fibres surrounding a failed filament, with two possible bundle shapes shown in Figure 104. If a greater number of intact fibres surround a failed filament then the SCFs are lower, therefore a more elliptical bundle shape would provide greater SCFs than if the fibre bundle was round. The influence of bundle cross-sectional shape is investigated further in section 4.2.1.

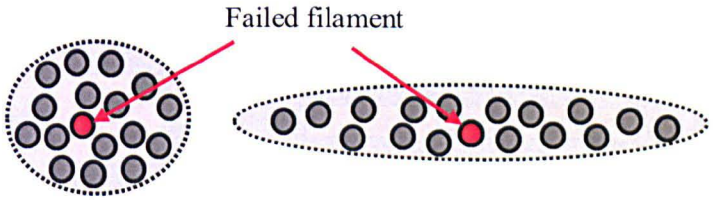

Figure 104 - Schematic showing the influence of bundle cross-section shape on the SCFs observed in filaments surrounding a failed filament

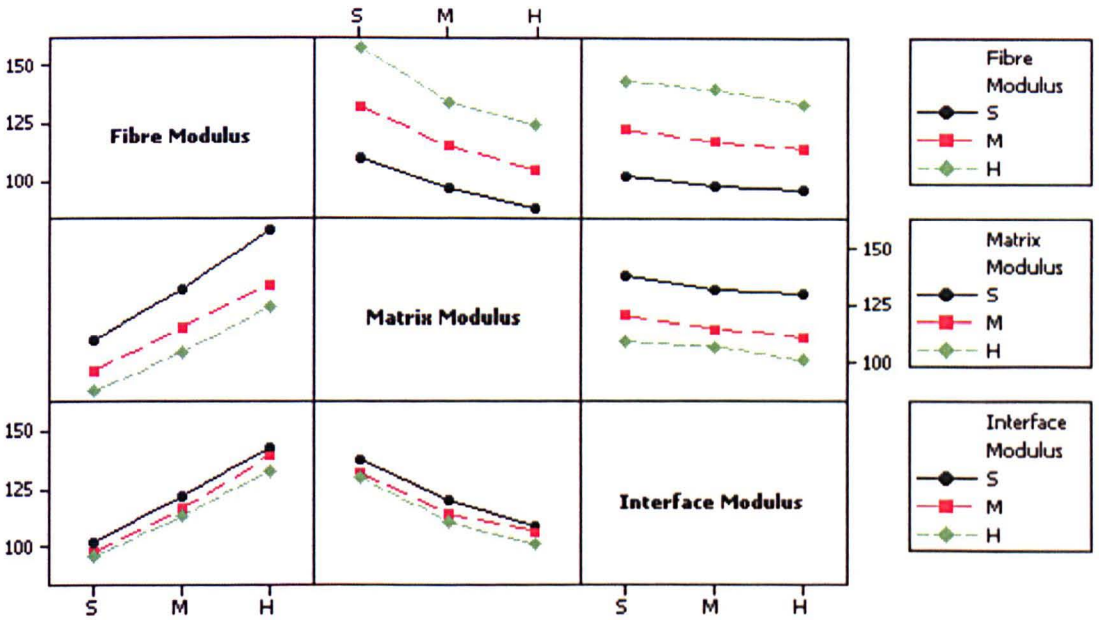

Figure 105 - Interaction plot for the fibre ineffective length of the broken fibre.

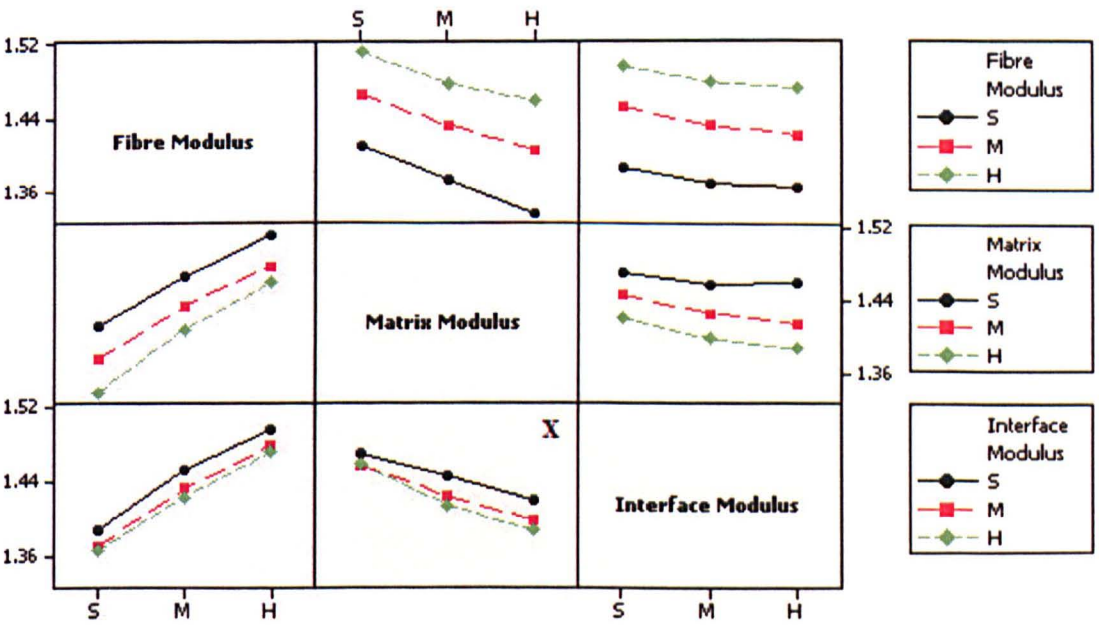

Figure 106 - Interaction plot for the stress concentration factor (SCF) experienced by the unbroken fibre in the model.

4.1.3 Fibre bundle properties

Mechanical properties have been calculated for a range of fibre volume fractions from 10 to 75%. For the nine volume fractions selected, the unit cells were generated and loaded in each principal direction. The model with 56% fibre volume fraction has been selected to show a representative von Mises stress and damage plot for each loading scenario, with longitudinal loading (z-direction) shown in Figure 107, transverse loading (x-direction) shown in Figure 108, and shear loading (xy-direction) shown in Figure 109. The values obtained for the modulus of the unit cell in each loading scenario is presented in Table 18.

When the representative fibre bundle model is subjected to longitudinal loading the matrix and interface regions become plastic as the applied strain is increased on the model, before fibre failure occurs, shown in the damage plot (right, Figure 107). When subjected to transverse loading, damage initiates in the interface region surrounding the fibres, before propagating into the matrix material between the fibres and ultimately causing final failure of the unit cell (right, Figure 108). For the shear load case, damage once again initiates in the interface before propagating to the outer boundary of the unit cell and causing final failure (right, Figure 109). As elements in the models are damaged, localisation can become apparent which can invalidate the periodicity of the model. The effects of localisation are not considered in this analysis and it is acknowledged that this could be a source of error in the results obtained for the fibre bundle models.

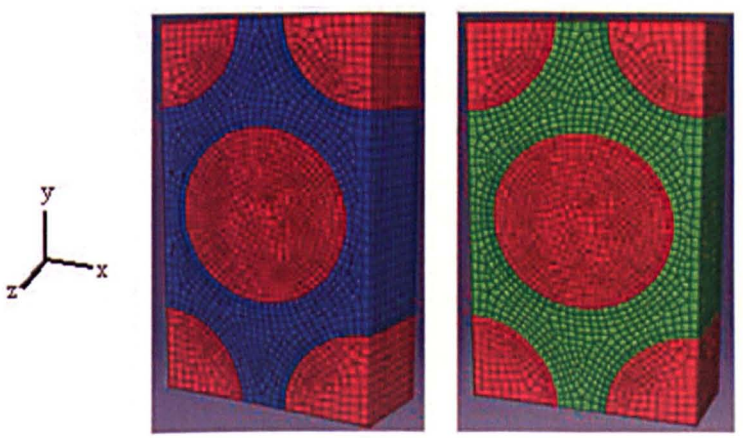

Figure 107 - Longitudinal loading of bundle unit cell (56% V_f). Both plots taken at 2% applied strain with the von Mises stress plot (left) and damage plot (right).

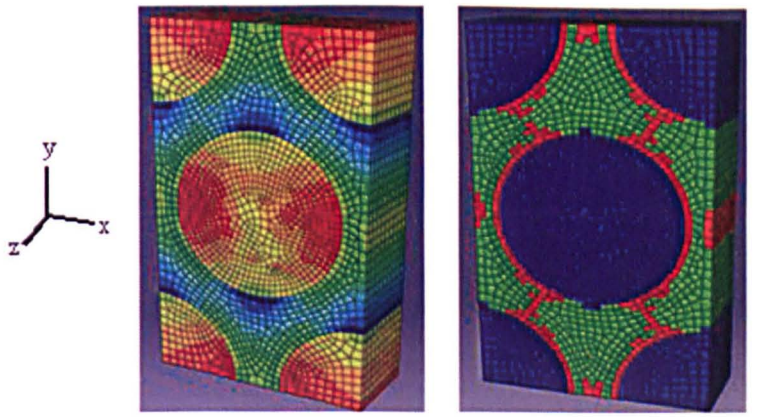

Figure 108 - Transverse loading of bundle unit cell (56% V_f). Both plots taken at 2% applied strain with the von Mises stress plot (left) and damage plot (right).

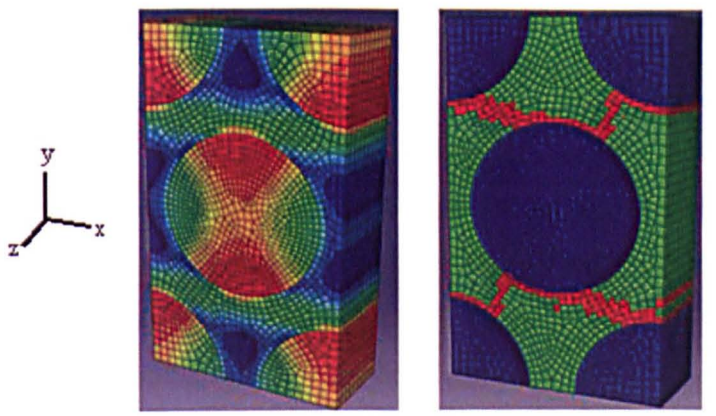

Figure 109 - Shear loading of bundle unit cell (56% V_f). Both plots taken at 2% applied strain with the von Mises stress plot (left) and damage plot (right).

Note: For the damage plots Figure 107 to Figure 109; undamaged elements (blue), plastic elements (green) and damaged elements (red).

Table 18 - Summary of the modulus properties in all principal directions for the fibre bundle model with increasing volume fraction.

V_f (%)	E_x (GPa)	E_y (GPa)	E_z (GPa)	E_{yz} (GPa)	E_{xz} (GPa)	E_{xy} (GPa)
10	4.207	4.207	25.142	1.381	1.381	1.349
19	4.752	4.752	46.971	1.597	1.597	1.528
28	5.358	5.358	68.787	1.852	1.852	1.743
37	6.074	6.074	90.592	2.160	2.159	2.008
46	6.949	6.949	112.386	2.536	2.536	2.346
56	8.033	8.034	134.169	3.010	3.009	2.785
65	9.373	9.374	155.942	3.627	3.626	3.356
70	10.149	10.150	166.826	4.013	4.013	3.700
75	11.001	11.001	177.708	4.473	4.473	4.088

To validate the modulus values obtained from the finite element study the results in Table 18 have been compared to a Rule of Mixtures (ROM) analytical model. The longitudinal modulus (z-direction) calculated by ROM shows good agreement with the numerical results, shown in Figure 110. As the fibre modulus is much greater than the matrix modulus in the z-direction (238GPa compared to 3.35GPa) the stiffness of the fibre dominates, with ROM providing a good estimate for the unidirectional composite for this load case. In this analysis, the fibre is modelled as continuous in the z-direction, which is an idealisation as discontinuous composites contain chopped bundles, which will inherently lead to stress concentrations forming at the bundle ends. Bundle length effects will be considered at the meso and macroscale using the experimental results obtained from bundle tensile testing in section 3.1.2.

Under transverse loading, the stress distribution in the unit cell (left, Figure 108) is much more complex than in the longitudinal load case, with the matrix and interface responsible for transferring the load between the fibres. This leads to failure in the interface and matrix, shown in the damage plot (right, Figure 108), which makes the mechanical properties of the unit cell more difficult to predict for transverse loading than for longitudinal loading. The complex stress distribution in the transversely loaded unit cell leads to poor predictions from ROM when compared to the results from the FE analysis; as shown in Figure 111. ROM under predicts the modulus of the unit cell, with an average discrepancy of 22% across the full range of fibre volume fractions considered in the analysis. The results from this study are consistent with the findings of Maligno [60], who also found that ROM was insufficient (~30% discrepancy between ROM and the numerical model for volume fractions greater than 50%) to predict the mechanical properties of transversely loaded unit cells due to the non-uniform distribution of stress across the model.

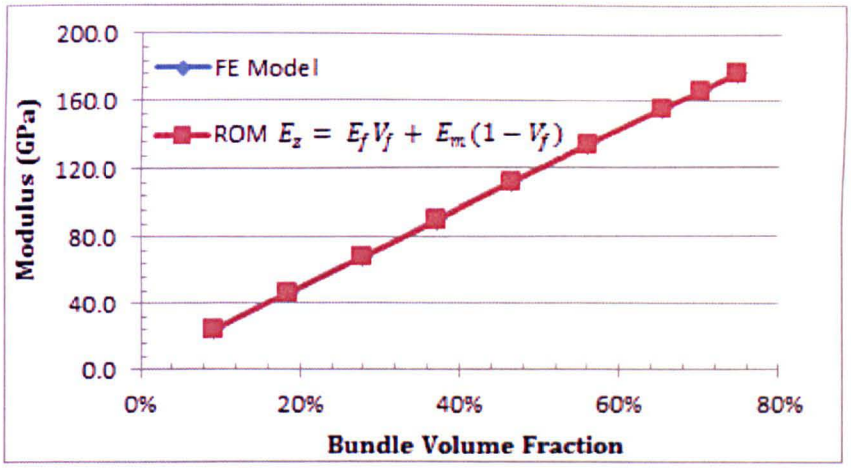

Figure 110 - Longitudinal modulus of ROM analytical model and FE model.

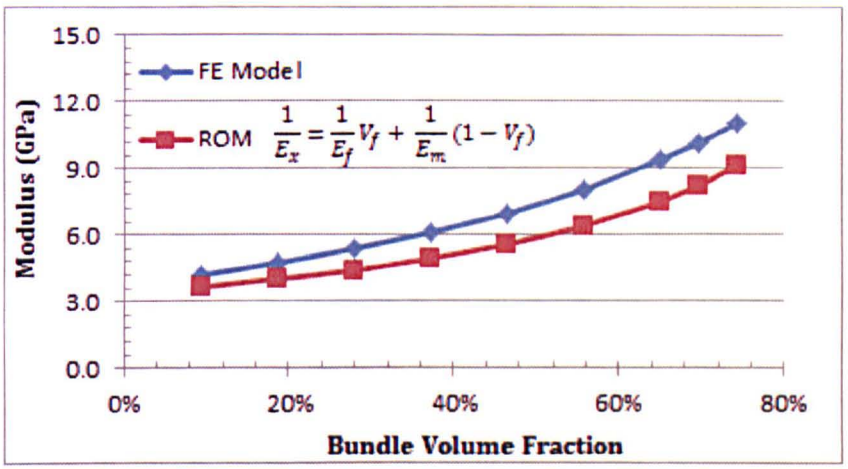

Figure 111 - Transverse modulus of ROM analytical model and FE model.

The strength and failure strain of the unit cells was recorded for all bundle volume fractions for each load case, with the strength values detailed in Table 19 and the failure strain values shown in Table 20. As expected, with increasing fibre volume fraction in the bundle the strength increases significantly in the z-direction, with a strength of 422.1MPa at 10% V_f, rising to 3037.3MPa at 75% V_f. The FE results for the z-direction strength are compared to ROM strength predictions in Figure 112, with good agreement found (~0.87%) as the fibre dominates the strength prediction. Tensile testing of bundles in section 3.1.2 showed that the strength of the bundle was lower than the FE predictions in this section, with the strength of the bundle also decreasing with increasing bundle length, attributable to the greater number of fibre flaws found in the bundle. For the analysis contained in this thesis, the failure stress of the bundle in the z-direction (σ_z) will be

determined using Equation 14, with failure stress values for a bundle volume fraction of 60% shown in Table 6.

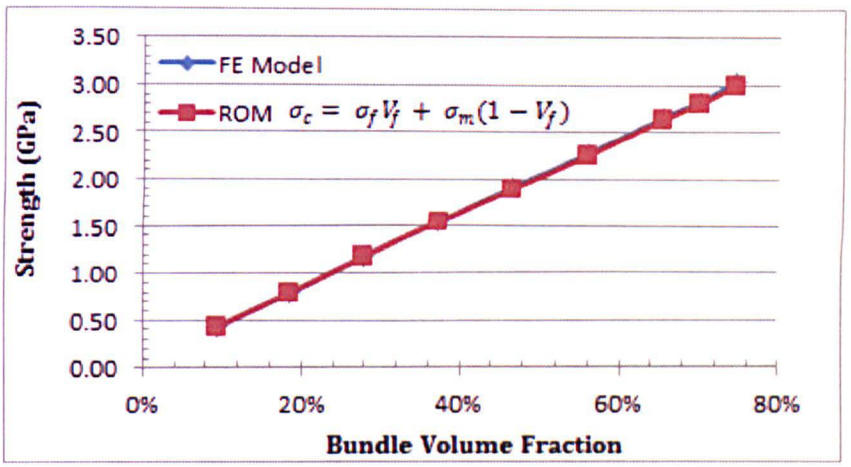

Figure 112 – Longitudinal strength of ROM analytical model and FE model.

The transverse strength of the bundle (x-direction) is almost constant with increasing fibre volume fraction. Failure is initiated in the matrix and interface regions, shown in Figure 108, therefore increasing the fibre content in the unit cell has little effect. It was observed that the strength of the unit cell was greater in the y-direction than in the x-direction, with a strength increase of approximately 20% in the y-direction for fibre volume fractions greater than 50%. The modulus of the unit cell is equivalent in the x and y-direction; see Table 18, but damage initiates in different areas of the matrix and interface for the different load cases due to the geometry of the hexagonal packing arrangement and the difference in the edge lengths on faces CDGH and EFGH (Figure 66). The results obtained are consistent with studies in [60], with a difference in strength of approximately 30% observed between transverse loading directions (x and y) for a hexagonal packing arrangement with glass fibre reinforcement.

The in-plane shear strength (xy-direction) of the bundle increased steadily with increasing fibre volume fraction, from 25.0MPa at 10% V_f to 30.9MPa at 75% V_f – an increase of 23.6%. The out-of-plane shear strengths (yz and xz directions) also increased with increasing V_f, but the shear strength of the unit cells remained relatively constant in all shear directions at bundle volume fractions greater than 50%, shown in Table 19.

Table 19 - Summary of the strengths in all principal directions for the fibre bundle model with increasing volume fraction.

V_f (%)	σ_x (MPa)	σ_y (MPa)	σ_z (MPa)	σ_{yz} (MPa)	σ_{xz} (MPa)	σ_{xy} (MPa)
10.0	42.3	43.6	422.1	23.0	23.1	25.0
19.0	43.1	45.7	793.6	24.3	24.4	26.4
28.0	42.9	47.1	1164.9	25.9	25.7	26.1
37.0	43.0	47.9	1536.1	27.4	27.1	25.7
46.0	42.9	48.6	1907.2	29.6	28.0	25.6
56.0	42.4	49.8	2278.1	31.7	28.9	26.5
65.0	42.7	50.7	2648.9	32.4	28.9	28.4
70.0	42.7	50.7	2834.2	32.3	28.3	29.4
75.0	42.3	50.9	3037.3	32.1	28.3	30.9

Table 20 - Summary of the failure strains in all principal directions for the fibre bundle model with increasing volume fraction.

V_f (%)	ε_x	ε_y	ε_z	ε_{yz}	ε_{xz}	ε_{xy}
10.0	1.08%	1.06%	1.70%	1.78%	1.78%	2.00%
19.0	0.98%	1.00%	1.70%	1.64%	1.64%	1.88%
28.0	0.86%	0.90%	1.70%	1.50%	1.50%	1.62%
37.0	0.76%	0.82%	1.70%	1.38%	1.34%	1.36%
46.0	0.66%	0.72%	1.70%	1.26%	1.18%	1.16%
56.0	0.56%	0.64%	1.70%	1.14%	1.02%	1.00%
65.0	0.48%	0.56%	1.70%	0.96%	0.84%	0.88%
70.0	0.44%	0.52%	1.70%	0.86%	0.74%	0.84%
75.0	0.40%	0.48%	1.70%	0.76%	0.66%	0.78%

In general, a reduction in failure strain is observed in each principal direction with increasing volume fraction, as shown in Table 20. This is attributable to the increased fibre content and reduced matrix content, with the fibre having a lower strain to failure than the matrix material. The failure strain in the z-direction remained constant for all fibre bundle volume fractions, due to the fibre failure in the unit cell for this load case, as shown in Figure 107. The mechanical properties calculated for the fibre bundles in this section are passed up to the meso and macroscale for the remainder of the analysis contained in this chapter.

4.2 Mesoscale Modelling

4.2.1 Bundle ineffective length

The von Mises stress plots for the four models at 0.2% applied strain, prior to the onset of damage, are shown in Figure 113. Similar to the fibre ineffective length model (section 4.1.2), stress builds up along the length of the fractured bundle, with the axial stress along the centre of the fractured bundle plotted in Figure 114. The fibre ineffective length was defined as the length over which 90% stress/strain recovery occurs in a broken fibre, and for consistency the bundle ineffective length has been defined using the same 90% threshold [135], plotted in Figure 114.

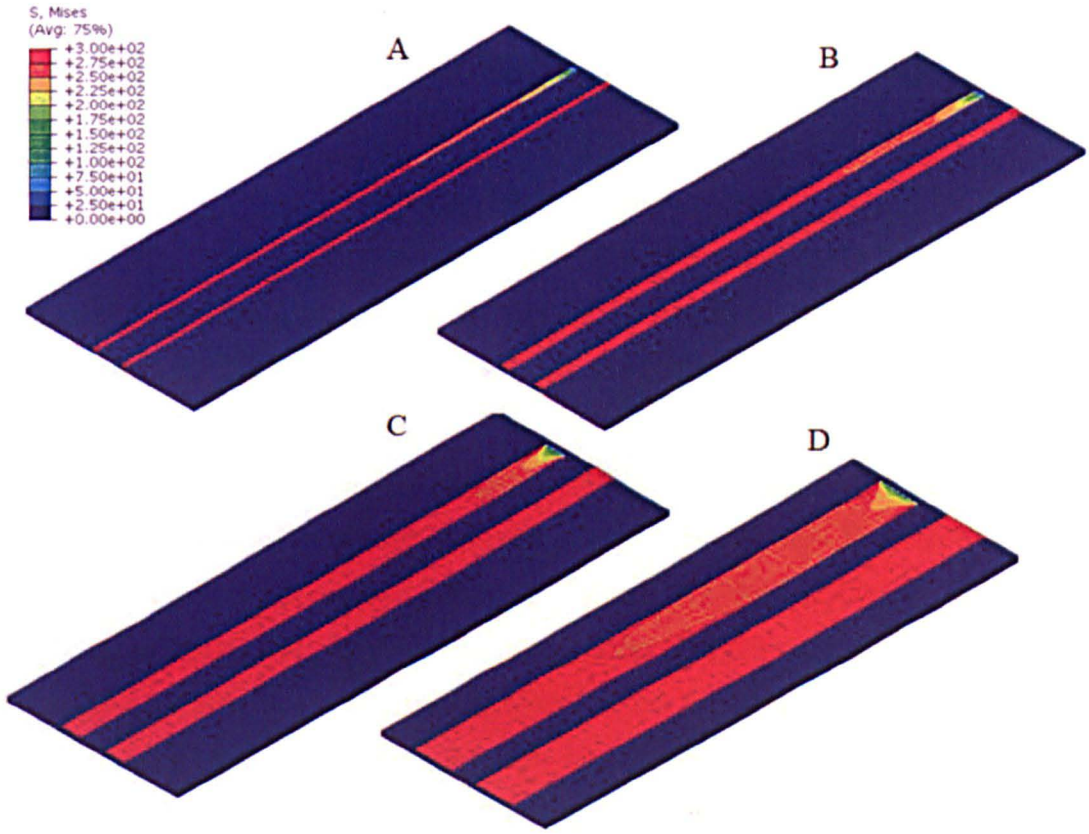

Figure 113 - von Mises stress plot at 0.2% applied strain for the four bundle ineffective length models. (Note: At 0.2% applied strain damage has yet to initiate in the models).

The bundle ineffective lengths are calculated at 0.2% applied strain for consistency with the fibre ineffective length model. If the ineffective lengths were

calculated at greater applied strains, more than 0.6% once the onset of damage has occurred; it would be difficult to quantify the ineffective length as the stress transfer from the fractured bundle to the unbroken bundle becomes restricted as the matrix elements between the two bundles begin to fail under shear. This failure is shown in the damage progression plots for each model in Figure 115, with damage initiating at the site of the bundle fracture before propagating across the width of the model and causing the neighbouring bundle to fail.

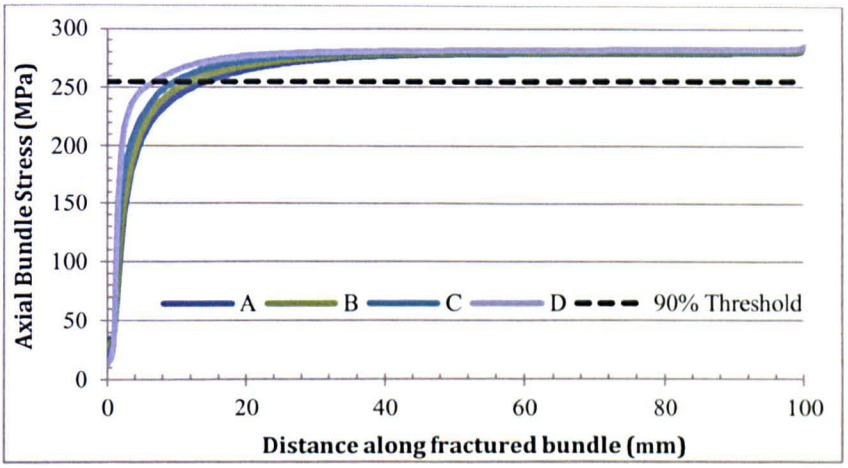

Figure 114 - Axial stress plotted along the centre of the fractured bundle for each model at 0.2% applied strain. (Note: 90% threshold plotted to show the point at which the broken bundles have achieved 90% stress recovery).

Figure 116 show the ineffective lengths for the four models, with a reduction in ineffective length observed with increasing bundle aspect ratio from model A to D. For a circular cross-section bundle (model A) the ineffective length is predicted to be 15mm, but when the aspect ratio of the bundle is increased this drops by over 50% down to 7mm for model D. As the aspect ratio of the bundle was increased, the contact area between bundle and matrix also increased by approximately 470%, from model A to model D, allowing the bundle to recover stress more efficiently from the site of the simulated fracture, providing a reduction in bundle ineffective length.

In a discontinuous composite material, a significant number of bundle ends will be found as the bundles are chopped to create the component. The discontinuity at the bundle ends will be similar to the fractured bundles in this analysis, and

reducing the ineffective length of the bundles by increasing the bundle aspect ratio will improve the load carrying capabilities of the material. The ultimate tensile strength (UTS) of the models was unaffected by the increase in aspect ratio of the bundles in this study as the damage initiated in the matrix material at the site of the bundle fracture.

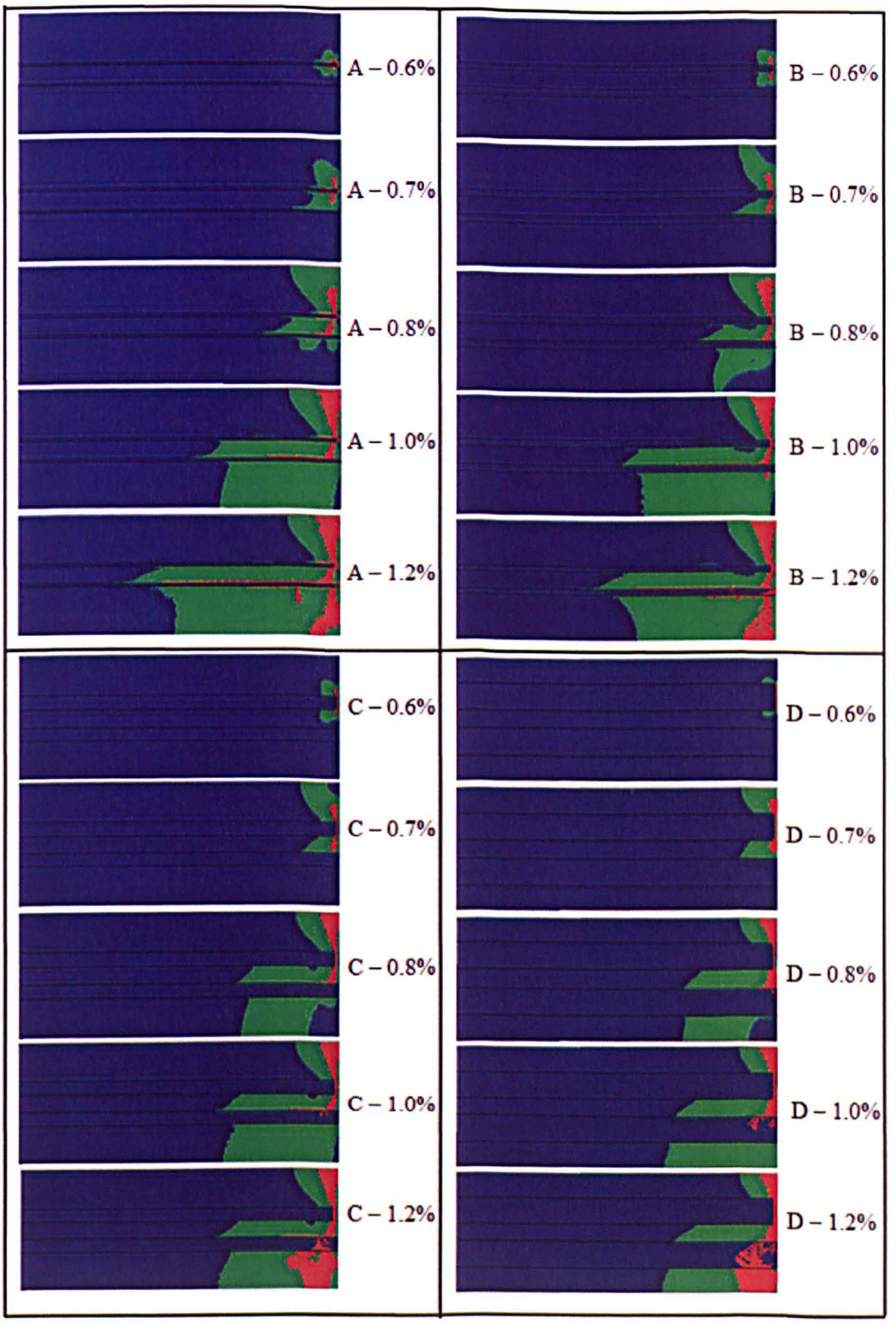

Figure 115 – Plan view of damage progression plots for bundle ineffective length models – letter refers to the aspect ratio of the bundles, shown in Table 13. (Note: The value next to each plot denotes the applied strain on the model). Undamaged elements (blue), plastic elements (green) and damaged elements (red).

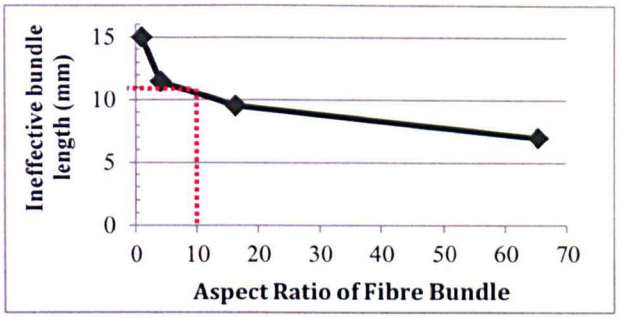

Figure 116 - Ineffective bundle lengths plotted against the aspect ratios for the four fibre bundle cross-sections (A to D – left to right) considered in the analysis.

The ineffective length values obtained in this analysis (Figure 116) suggest that if short fibre lengths are used in a discontinuous composite material, then the stress in the fibre will never achieve 90% recovery from the discontinuity at the fibre end. An aspect ratio of 10 is typical of a 12k bundle, based on microscopy measurements by Schubel et al [224], therefore bundle ineffective lengths of approximately 11mm would be expected for the constituents modelled in this analysis. If shorter bundle lengths are used there will be a reduction in the stiffness and strength of the material, with longer bundle lengths desirable, greater than 22mm (two times the bundle ineffective length) for a 12k tow, to improve the mechanical properties of the discontinuous composite.

The axial stress along the length of the unbroken bundle is plotted in Figure 117. Around the site of the bundle fracture, the unbroken bundle experiences elevated stress levels as it is responsible for carrying the stress overload created from the bundle fracture.

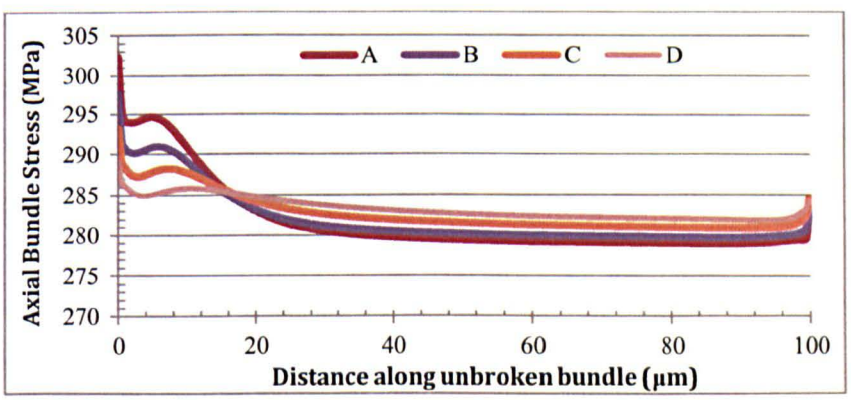

Figure 117 - Axial stress plotted along the length of the unbroken fibre bundle for each model at 0.2% applied strain.

SCFs were calculated in the unbroken bundle for each model by dividing the peak stress in the bundle by the far field axial stress (~80mm along the bundle length), with the results presented in Figure 118. A decrease in SCF was found as the aspect ratio of the bundle was increased; however, the far field axial stress in the bundle did increase as the bundle aspect ratio was increased. This analysis has shown that if the aspect ratio of the bundle is increased, the distribution of the overload in stress caused by the bundle fracture is more uniform along the bundle length, which makes the possibility of a second fracture occurring in the unbroken bundle less likely.

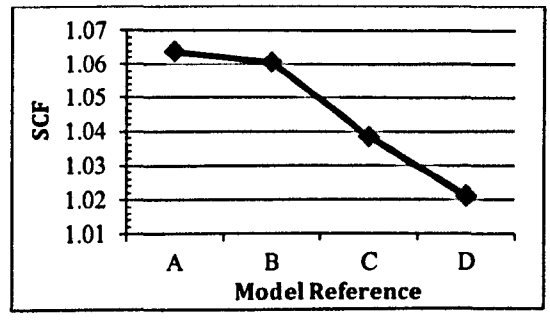

Figure 118 - Stress concentration factors (SCFs) obtained in the unbroken bundles.

The SCF values obtained in this study (Figure 118) have shown that the bundle aspect ratio influences the peak stresses observed in a bundle neighbouring a fractured bundle, or bundle end. The bundle aspect ratio can vary greatly across a discontinuous component at the macroscale, which can lead to greater SCFs being found in bundles with low aspect ratios. At the macroscale, the model is limited as the fibre bundles are represented by beam elements with a constant circular cross section. Therefore, as the SCFs calculated in this analysis are based on the bundle cross-sectional shape, they are unable to be carried forward. It is acknowledged that, according to the results in this study, this may be a source of error in the mechanical property predictions at the macroscale.

4.2.2 Bundle interaction

The results in this section are split into three parts. The first part calculates the contribution of an individual fibre bundle, at a range of orientations, on the modulus predictions of the unit cell. Using the contributions of the individual bundles at a range of orientations, a prediction is made for the modulus of a unit cell containing two fibre bundles. In the second part of this section, two bundles are modelled in the unit cell to calculate the actual modulus of the unit cell, with the difference between the predicted and actual modulus calculated to allow the influence of the SCFs induced by the interaction of the bundles to be quantified. The final part of this section assesses the influence of bundle separation distance on the SCFs found in the bundles in the unit cell.

4.2.2.1 Single bundle model

One fibre bundle was considered initially in this analysis and the modulus of the unit cell calculated for all bundle orientations, with the results presented in Table 21. The contribution of the fibre bundle to the modulus of the unit cell has been calculated by subtracting the modulus of the matrix, 3350MPa, from the modulus of the unit cell containing the single fibre bundle.

Using the contribution of the single fibre bundle to the modulus of the unit cell, a modulus prediction has been made for a unit cell containing two fibre bundles, shown in Table 22. To calculate the predicted modulus of the unit cells the contribution of the two bundles in the single bundle models have been added to the matrix modulus. For example, the 0° / 45° model is calculated using the values in Table 21 as follows; 3350MPa + 539.57MPa + 196.20MPa = 4085.77MPa.

Table 21 - Modulus of unit cells containing only one fibre bundle at all bundle orientations loaded in the longitudinal direction.

Bundle Orientation	Modulus of unit cell (MPa)	Contribution of the fibre bundle to the modulus of the unit cell (MPa)
0°	3889.57	(3889.57 – 3350) = 539.57
15°	3863.88	(3863.88 – 3350) = 513.88
30°	3680.53	(3680.53 – 3350) = 330.53
45°	3546.20	(3546.20 – 3350) = 196.20
60°	3498.80	(3498.80 – 3350) = 148.80
75°	3486.21	(3486.21 – 3350) = 136.21
90°	3480.56	(3480.56 – 3350) = 130.56

Table 22 - Predicted modulus for the unit cell containing two fibre bundles.

Bundle Orientation	Predicted modulus of unit cell containing two fibre bundles (MPa)
0° / 0°	4429.13
0° / 15°	4403.45
0° / 30°	4220.10
0° / 45°	4085.77
0° / 60°	4038.37
0° / 75°	4025.78
0° / 90°	4020.12

4.2.2.2 Two bundle model

The modulus of the unit cell containing two fibre bundles has been determined for all angular orientations of bundle 2, shown in Figure 69, for $\phi = 0°$ to 90°, with the results presented in Table 23. The actual modulus and predicted modulus values are plotted in Figure 119. It was found that the unit cell which contained two fibre bundles had a lower modulus than the predictions from the one bundle models, for the full range of angular orientations considered in this analysis. The mean difference between the modulus predictions was 1.60% across the full range of angular orientations considered, as shown in Table 23, with this analysis only considering one bundle-to-bundle interaction at low fibre volume fraction (~1.0% V_f).

Table 23 - Predicted modulus of the unit cells compared to the actual modulus of the unit cells containing two fibre bundles.

Bundle Orientation	Predicted modulus of unit cell containing 2 bundles (MPa)	Actual modulus of unit cell containing 2 bundles (MPa)
0° / 0°	4429.13	4320.45
0° / 15°	4403.45	4290.93
0° / 30°	4220.10	4177.90
0° / 45°	4085.77	4038.87
0° / 60°	4038.37	3981.93
0° / 75°	4025.78	3975.38
0° / 90°	4020.12	3972.76

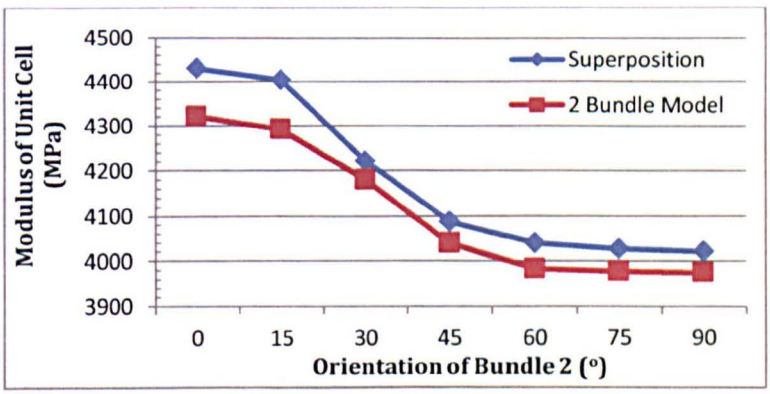

Figure 119 – Comparison of the predicted modulus of the unit cell plotted against the modulus of the unit cell containing two fibre bundles.

A sample damage plot is shown in Figure 120 (left) for the 45° orientation model, with the plot typical of the other orientations considered in the analysis. The matrix region that surrounds the fibre bundles in the centre of the unit cell remains undamaged throughout the analysis, with damage initiated at the site of the bundle ends. The damage then propagates across the width of the model before causing final failure of the unit cell. In addition to the damage plot, a sample stress plot can also be seen in Figure 120 (right) to show visually the stress distribution along the bundle lengths.

The stress in the centre of the unit cell, directly between the points of bundle crossover, is shown in Figure 121. As bundle 2 was rotated from 0° to 90° the stress gradually increased in the centre of the unit cell from 10.99MPa to 12.36MPa, an increase of 12.42%. The area of bundle overlap decreases in the models as bundle 2 is rotated; therefore a smaller region of matrix material is

responsible for transferring the load between the bundles, which results in the increased stresses in the centre of the model. Whilst the increase in stress in the centre of the models is significant, the magnitude of the stresses is unlikely to cause failure in the current model as there is a large volume of unreinforced matrix surrounding the fibre bundles. However, if the number of fibres in the model was to increase and the homogeneity improved, these elevated stresses could cause failure of the model. The damage in the models initiate at the bundle ends, with Figure 122 showing the stress at the end of bundle 1 at 0.5% applied strain, for all the angular orientations considered in the analysis.

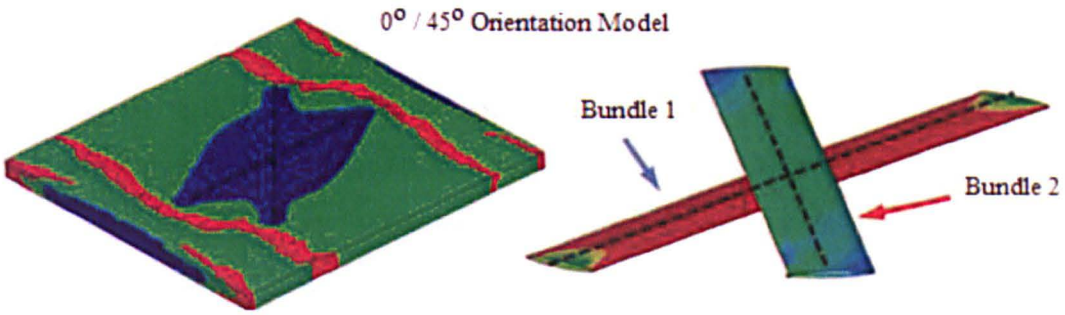

Figure 120 – Damage plot for the unit cell (left) and von Mises stress plot in the fibre bundles (right) for the 0°/45° model at 2.0% applied strain. For the damage plot; undamaged elements (blue), plastic elements (green) and damaged elements (red).

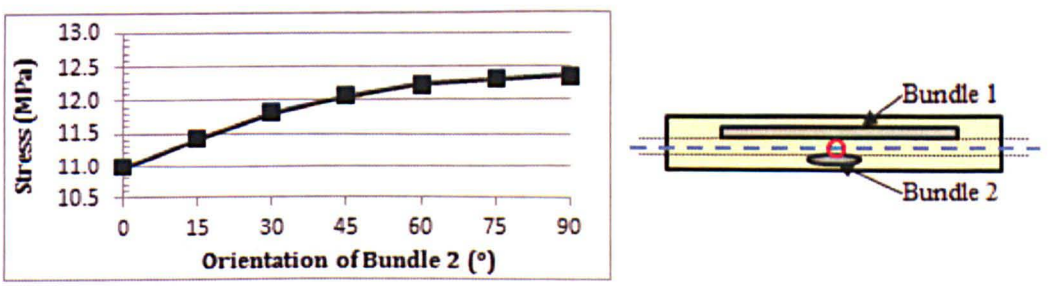

Figure 121 - Stress in the centre of the matrix (denoted by red circle in diagram) between the two fibre bundles at 0.5% applied strain.

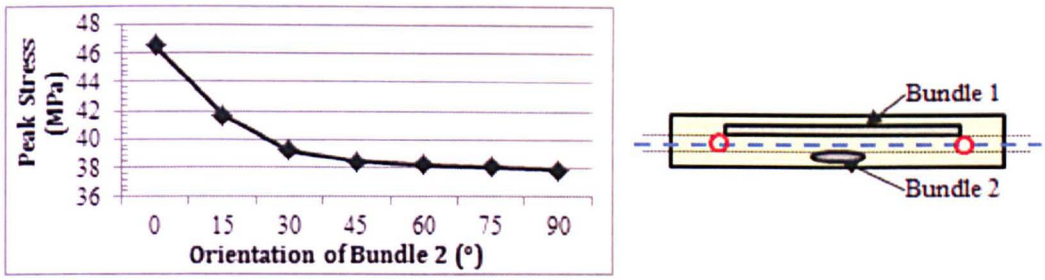

Figure 122 – Peak stress in the matrix between the two fibre bundles at the end of bundle 1 (denoted by red circles in diagram) at 0.5% applied strain.

Elevated stress levels were observed at the bundle ends, which was consistent with the findings in [139] where strain concentrations have been found at fibre ends in short fibre composite materials. The size of the stress concentrations found at the bundle ends, shown in Figure 122, is a function of the bundle orientation and it is at its greatest when the fibres are aligned to the loading direction in the 0° orientation model. As a discontinuous material is highly heterogeneous, if a matrix rich region is present in the composite, with multiple bundle ends, then this site is likely to experience high stress concentrations which could cause premature failure of the material. It is therefore important to ensure that good fibre bundle coverage is achieved in the manufacturing of the material if discontinuous composites are to be used for structural applications.

The stress along the length of the centre of the fibre bundles in the unit cell was monitored in the analysis to calculate SCFs in bundle 1 induced by the orientation of bundle 2 as it was rotated from 0° to 90°, with the stress profiles along the bundle lengths shown in Figure 123. Bundle 1 carried a greater load as the principal axis of bundle 2 was rotated away from the direction of loading, with the peak stress values found in the centre of bundle 1 shown in Table 24. The peak stress found in the single bundle models in Table 21 was 539.57MPa when bundle 1 was aligned to the direction of loading. SCFs in bundle 1 were calculated based on the increase in stress in bundle 1 with the incremental change in orientation of bundle 2 from 0° to 90°, using the stress in bundle 1 at 0° in the single bundle model as the benchmark, with the SCFs plotted in Figure 124.

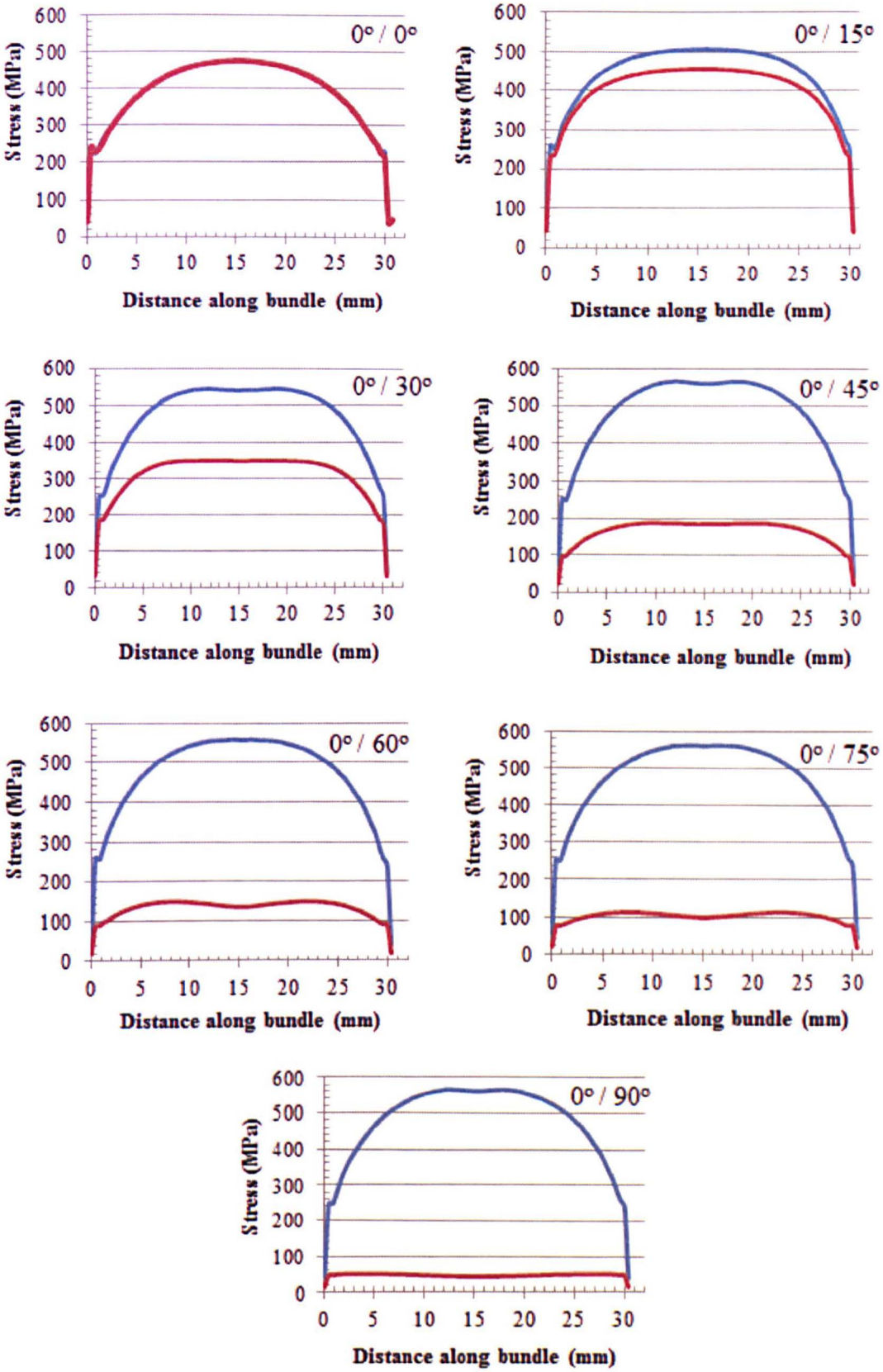

Figure 123 – Axial stress along the length of the fibre bundles at 0.5% applied strain. (Note: Blue line denotes stress along the 0^{o} bundle and the red line shows the stress along the incrementally rotated bundle).

Table 24 - Summary of peak stress values and SCFs in bundle 1 for all orientations at 0.5% applied strain. (Note: The benchmark stress for SCF calculations is 539.57MPa).

Model Ref.	Peak Stress in Bundle 1 (MPa)	SCF
0	492.435	No SCF
15	516.208	No SCF
30	551.342	1.0218
45	570.631	1.0576
60	580.714	1.0763
75	582.619	1.0798
90	584.952	1.0841

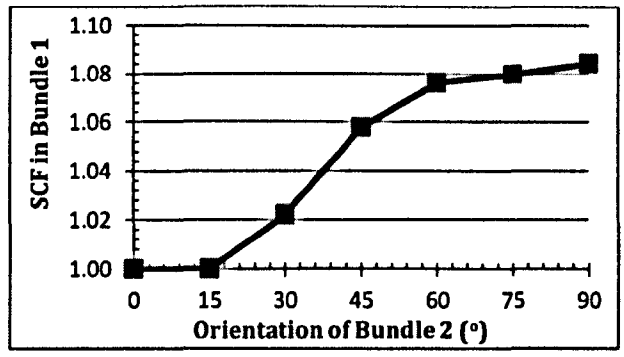

Figure 124 - SCFs in bundle 1 based on the angular orientation of bundle 2.

From this analysis it was found that bundle 1 can experience an increase in peak stress of up to 8.41%, which was observed when bundle 2 was oriented at 90° from bundle 1. When the orientation of bundle 2 is at 45° in the model, common in the random orientation in discontinuous materials, the SCF experienced by bundle 1 is 1.0576, shown in Figure 124. This could lead to bundle failures at higher levels of applied strain in models with a greater fibre volume fraction, which will inherently lead to a reduction in strength of the material.

Analytical models that are typically used to predict the modulus of discontinuous materials do not account for the interactions between the bundles [50, 225, 226], which leads to inaccuracies when predicting the mechanical properties of the material. It has been found in other studies that for components manufactured using discontinuous composites with volume fractions approaching 55% V_f, the contribution of the interaction of the overlapping bundles can reach up to 34.5%

when determining the mechanical properties of the material [43]. The results from this analysis have further highlighted the deficiencies in existing analytical models, with the interaction between bundles critical when calculating the modulus and strength of discontinuous materials.

4.2.2.3 Bundle separation distance

The distance between the fibre bundles has been varied in this section, to determine the influence of inter-bundle distance on the mechanical properties of the unit cell. Five separation distances (d, see Figure 68) have been considered; 0.20, 0.60, 1.20, 1.70 and 2.20mm, with models at each separation distance produced for all bundle orientations from $\phi = 0^{\circ}$ to 90°. The modulus values obtained for the unit cells at the five separation distances are shown in Figure 125. By reducing the separation distance between the fibre bundles from 2.20mm to 0.20mm, the modulus of the unit cell increased for the full range of bundle orientations considered in this analysis. An increase in modulus of 1.96% was observed for the $0^{\circ}/0^{\circ}$ model, with an increase of 1.93% observed when the bundles were orientated at $0^{\circ}/90^{\circ}$. The variation in modulus was relatively constant across the full range of orientations as the separation distance was reduced from 2.20mm to 0.20mm.

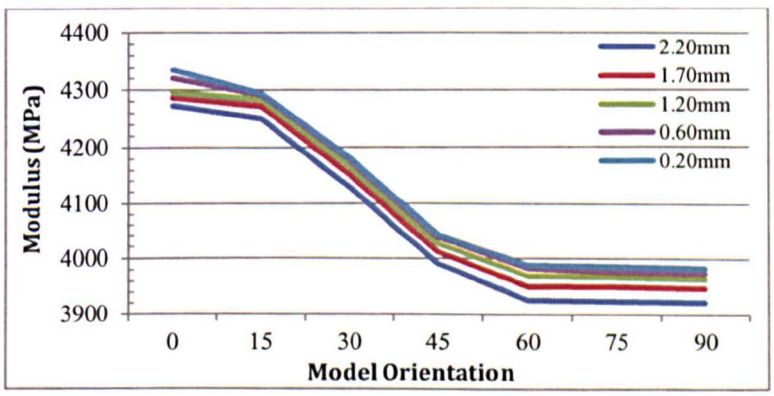

Figure 125 - Modulus variation in the unit cell for the five separation distances.

This slight increase in modulus is consistent with the findings in [43] where the separation distance between two perpendicular fibres was reduced from 5 to 1.05 fibre diameters, which provided an increase in modulus of 0.16% for the unit cell. Twenty interacting fibre pairs were also considered in the study by Pan et al [43], with an increase of modulus of 1.24% observed when reducing the inter-fibre

distance from 1.5 to 1.05 fibre diameters. Isotropic glass fibres with a circular profile were modelled in the analysis in [43], with Young's modulus values of 70GPa and 1GPa used for the fibre and matrix, respectively. There was a greater percentage increase in modulus of the unit cell in this analysis, when compared directly to the study in [43]; attributable to the greater difference in mechanical properties of the materials used and the higher fibre volume fraction of the unit cell.

As the separation distance between the bundles was decreased an increase in the peak stress in bundle 1 was observed, with the values shown in Table 25. The peak stress found in the single bundle models in Table 21 was 539.57MPa and this stress was again used as the benchmark, with the SCFs obtained in bundle 1 across the range of separations and orientations plotted in Figure 126. There was an increase in SCF with decreasing separation distance between the fibre bundles, with the peak SCF value of 1.0964 found when the two bundles were orientated at 0°/90° at a separation distance of 0.20mm in the unit cell. At high volume fractions in macroscale component, the bundle separation distance is likely to be even smaller (< 0.20mm), potentially leading to even higher SCF in the bundles and further reducing the mechanical properties of the discontinuous composite.

Table 25 - Peak stress values (MPa) found in bundle 1 as the separation distance between the bundles was reduced for the full range of orientations from 0° to 90°.

Model Ref.	Separation Distance, d (mm)				
	2.20	1.70	1.20	0.60	0.20
0	480.10	485.39	486.26	492.44	496.26
15	499.39	508.66	513.81	516.21	519.70
30	519.15	533.03	542.43	551.34	557.13
45	524.65	542.96	557.00	570.63	577.96
60	528.46	550.54	565.82	580.71	588.77
75	531.99	554.25	570.30	582.62	590.23
90	535.71	557.66	573.01	584.95	591.56

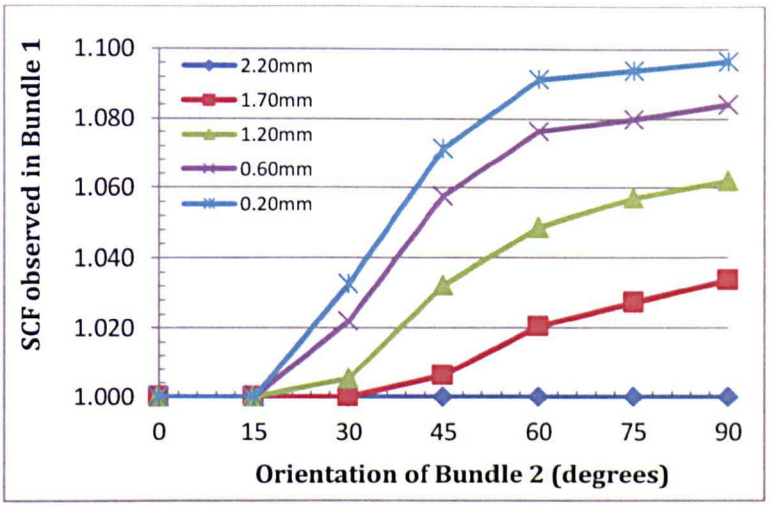

Figure 126 - SCFs in bundle 1 with varying separation distance and orientation.

The analysis contained in this section has shown that the interaction between bundles cannot be neglected when calculating the mechanical properties of the material at the macroscale. Both the in-plane orientation and separation distance directly influence the SCF observed in the bundle aligned to the direction of loading (bundle 1). At high volume fractions, the impact of the SCFs can lead to reductions in the mechanical properties of the discontinuous composite, therefore the influence of the SCFs needs to be captured. The developed macroscale model has 2D fibre bundle architectures, with the SCFs used to reduce the stiffness of the bundle elements at the point of bundle intersection to account for the 3D interaction between the bundles at the crossover point. The SCF values shown in Figure 126 have been used to develop a stiffness reduction scheme at the macroscale which is fully detailed in section 3.5.4.

4.3 Macroscale Modelling

The developed macroscale model (detailed fully in section 3.5) has been used to predict the mechanical properties of discontinuous composite materials. The models are benchmarked initially in section 4.3.1 against an existing 2D model that uses the embedded element technique to calculate the modulus and strength of the material [68]. For this study the interface between the fibre bundle and matrix is assumed to be perfect, with no debonding permitted between the bundles and matrix materials.

The second study looks at the influence of the interface on the mechanical property predictions of the macroscale model - section 4.3.2. The influence of interfacial stiffness and interfacial shear strength are evaluated at a range of fibre bundle lengths and volume fractions. SCFs are then introduced at the bundle intersections in section 4.3.3 to assess the impact of these reductions on the mechanical properties of the unit cell. The FE results obtained are then compared to experimental data and existing analytical models for discontinuous composites in section 4.3.4.

4.3.1 Comparison to embedded element model

This study compares the results obtained from the developed macroscale model to FE results from the embedded element model [68]. Identical fibre bundle architectures were generated for both models, embedded and free mesh, and the modulus and strength of each was then directly compared. Periodic boundary conditions were imposed on the models, with all models loaded in x, y and xy directions. Two different fibre bundle lengths were considered in this analysis, with the cell size kept constant for both models at 50x50x3.5mm.

Model 1 had a fibre bundle length of 5mm and model 2 had a bundle length of 25mm. Fibre volume fractions of 10%, 30% and 50% were considered with the bundle architectures for the models shown in Figure 127. The bundle size was set to 12k filaments for both models; with a global element size of 0.5 used to mesh the models. For this study, no failure was permitted in the interface between bundle and matrix materials, with a penalty stiffness of 10^6 N/mm^3 used to define

the connector stiffness in the models. Failure of the connector elements at the interface will be introduced in section 4.3.2.

Model 1 – 5mm bundle length

The results obtained from the FE analysis for the mechanical properties of the free mesh and embedded element unit cells are presented in Table 26. At low fibre volume fractions (10% V_f) good agreement was found between the free mesh model and the embedded element model when predicting the modulus and strength of the unit cell for each load case. The modulus predictions, averaged across the three load cases, were within 3.01% and the strength predictions varied by 4.15%. At 30% V_f, the mechanical property predictions for the two models were again similar, with 9.80% and 8.83% average variation observed between the free mesh and embedded models across the three load cases for the modulus and strength, respectively. A further increase in volume fraction, up to 50% V_f, saw a greater difference in the mechanical property prediction for the free mesh and embedded element unit cells, with average modulus and strength variations of 13.16% and 19.41%, respectively.

Table 26 - 5mm bundle length free mesh comparison with embedded element models

Model Type	V_f (%)	Modulus			Strength		
		x (GPa)	y (GPa)	xy (GPa)	x (MPa)	y (MPa)	xy (MPa)
Free Mesh	10	5.580	5.517	1.978	34.622	35.094	19.805
Embedded	10	5.780	5.677	2.034	34.434	33.401	18.537
Free Mesh	30	12.345	12.763	4.447	51.424	57.217	29.774
Embedded	30	13.716	14.155	4.918	58.243	64.510	30.847
Free Mesh	50	21.980	23.119	8.243	150.008	151.399	73.317
Embedded	50	25.403	26.552	9.483	184.021	187.183	92.368

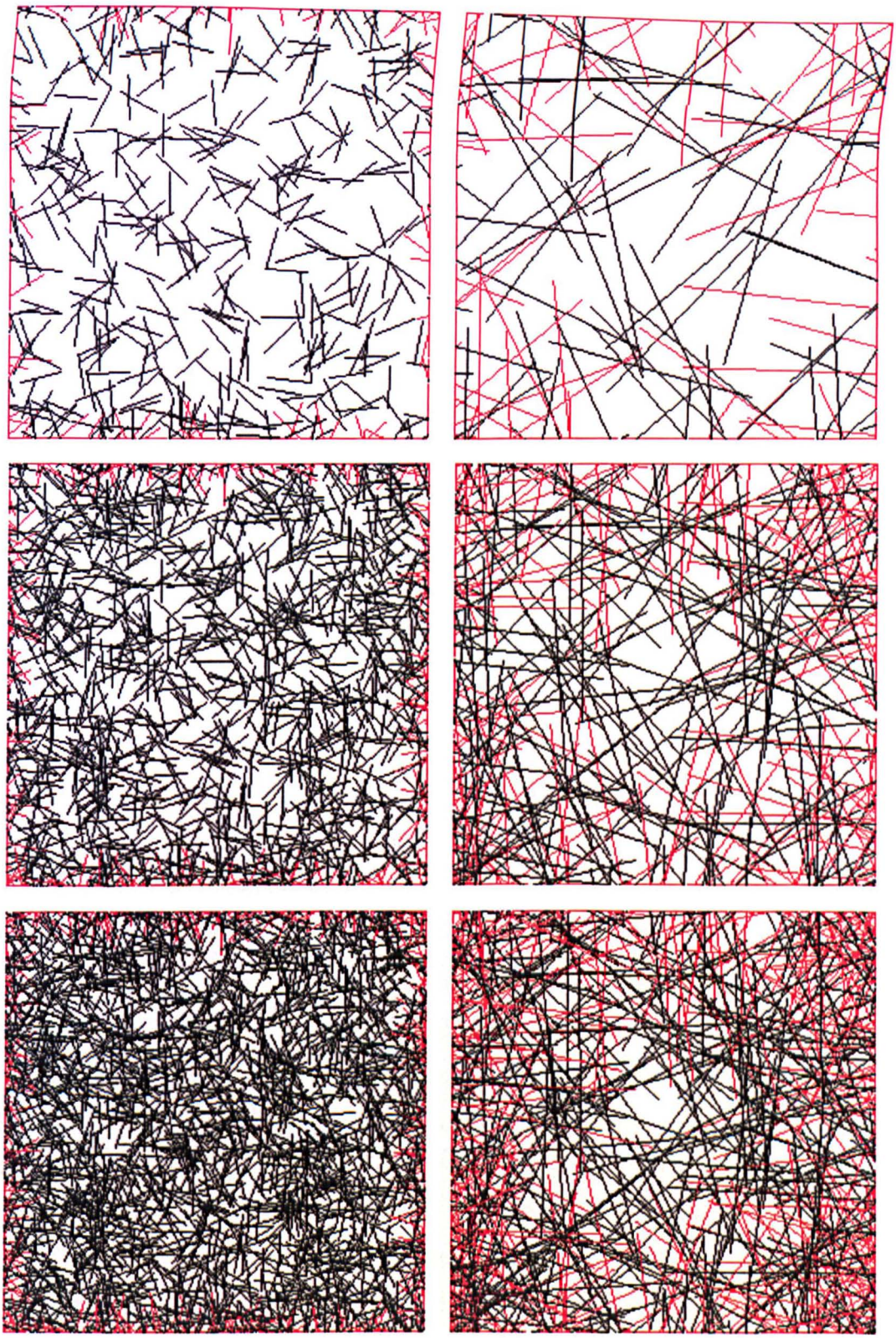

Figure 127 - Fibre bundle architectures for the embedded and free mesh models, with 5mm bundle length (left) and 25mm bundle length (right). Cell size is 50x50x3.5mm and a 12k bundle size is used. From top to bottom the fibre volume fractions are 10%, 30% and 50%, respectively. (Note: Red fibre bundles have been cropped when imposing periodicity on the unit cell).

Model 2 - 25mm bundle length

The results obtained from the FE analysis for the mechanical properties of the 25mm bundle length unit cells are presented in Table 27. The increase in bundle length from 5mm to 25mm saw a reduction in the variation of the predictions for the mechanical properties between the free mesh and embedded element models. The predictions for the modulus and strength were consistent across all volume fractions, with the models having good agreement for all three load cases. The average variation in modulus and strength, across all volume fractions, for all of the 25mm bundle length models was 1.85% and 1.93%, respectively.

Table 27 - 25mm bundle length free mesh comparison with embedded element models

Model Type	V_f (%)	Modulus			Strength		
		x (GPa)	y (GPa)	xy (GPa)	x (MPa)	y (MPa)	xy (MPa)
Free Mesh	10	8.790	7.591	3.477	60.647	44.775	29.566
Embedded	10	8.921	7.699	3.541	61.528	47.060	29.800
Free Mesh	30	21.086	23.114	8.378	184.033	173.877	87.807
Embedded	30	21.460	23.543	8.528	185.824	167.785	87.171
Free Mesh	50	34.381	36.538	13.389	264.066	355.227	133.142
Embedded	50	35.206	37.353	13.680	259.125	359.464	130.707

For longer bundle lengths (25mm) good agreement was found between the free mesh and embedded element model, with a comparison of the von Mises stress plots for the x-direction load case at 50% V_f shown in Figure 128. The stress distribution in both models is almost identical and the images to the right of Figure 128 show the stress profiles along the length of the fibres in the models. The mesh boundaries have been removed in the images to improve the clarity of the stress plots as the mesh is very fine across the model boundary. The von Mises stress plots for the shorter bundle length (5mm), for the 50% V_f free mesh and embedded element models, are shown in Figure 129. The stress distribution across the models (left, Figure 129) is again similar for both the embedded and free mesh models, however larger stresses were found along the length of the fibres in the embedded model when compared to the free mesh model (right, Figure 129).

The embedding of the fibres in the matrix material increases the modulus of the unit cell for each load case, at both fibre bundle lengths, across the range of volume fractions considered. The idealisation that the fibre bundles are embedded in the matrix leads to an over-estimation of the modulus of the material as the bundle elements are hosted by the resin elements, which also does not allow interfacial failures to be accounted for – a common failure mechanism at shorter bundle lengths. For the 5mm bundle length, more bundle segments are present in the model to provide the desired fibre volume fraction, as seen in Figure 127. This leads to an increased number of fibre bundle elements being hosted by the same matrix element, thus leading to the increased modulus prediction. The free mesh model meshes around the bundles to create the matrix elements, therefore it is expected that the modulus prediction of the free mesh model is more representative of the discontinuous material.

For the 25mm bundle length model, the failure of the model could be brought from the periodicity and imposed cropping of the bundles in the unit cell. The randomness of the fibre bundle distribution has been lost in the model as the fibre bundle density is higher around the model boundary when compared to the centre of the model. To overcome this problem Saint-Venant's principle has been used by some authors [149, 189], as discussed in section 2.5.3, to average the stresses and deformations across an inner sub-domain which is a prescribed distance from the model boundary. The use of Saint-Venant's principle, however, was not possible for the developed macroscale model due to the use of the connector elements at bundle-matrix interface and the unstructured free-mesh across the model boundary.

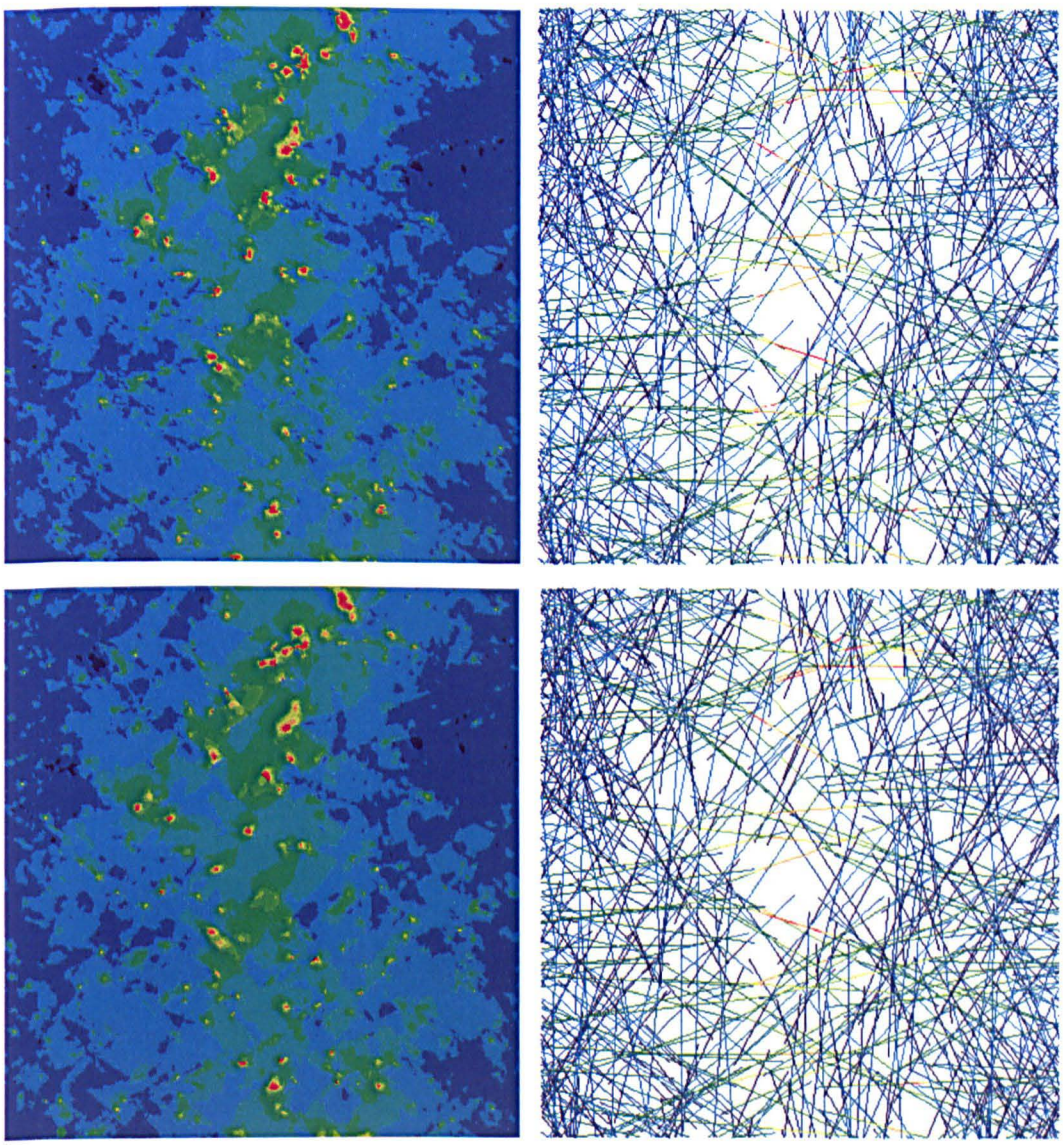

Figure 128 – Comparison of von Mises stress plots for 50% V_f 25mm bundle length free mesh and embedded element models, at 0.25% applied strain in the x-direction. (Top left – embedded element model; top right – embedded element model (fibres only); bottom left – free mesh model; and bottom right – free mesh model (fibres only). Note: Full plot images (left) and fibre plot images (right) are scaled to the same peak stresses of 40MPa and 650MPa, respectively.

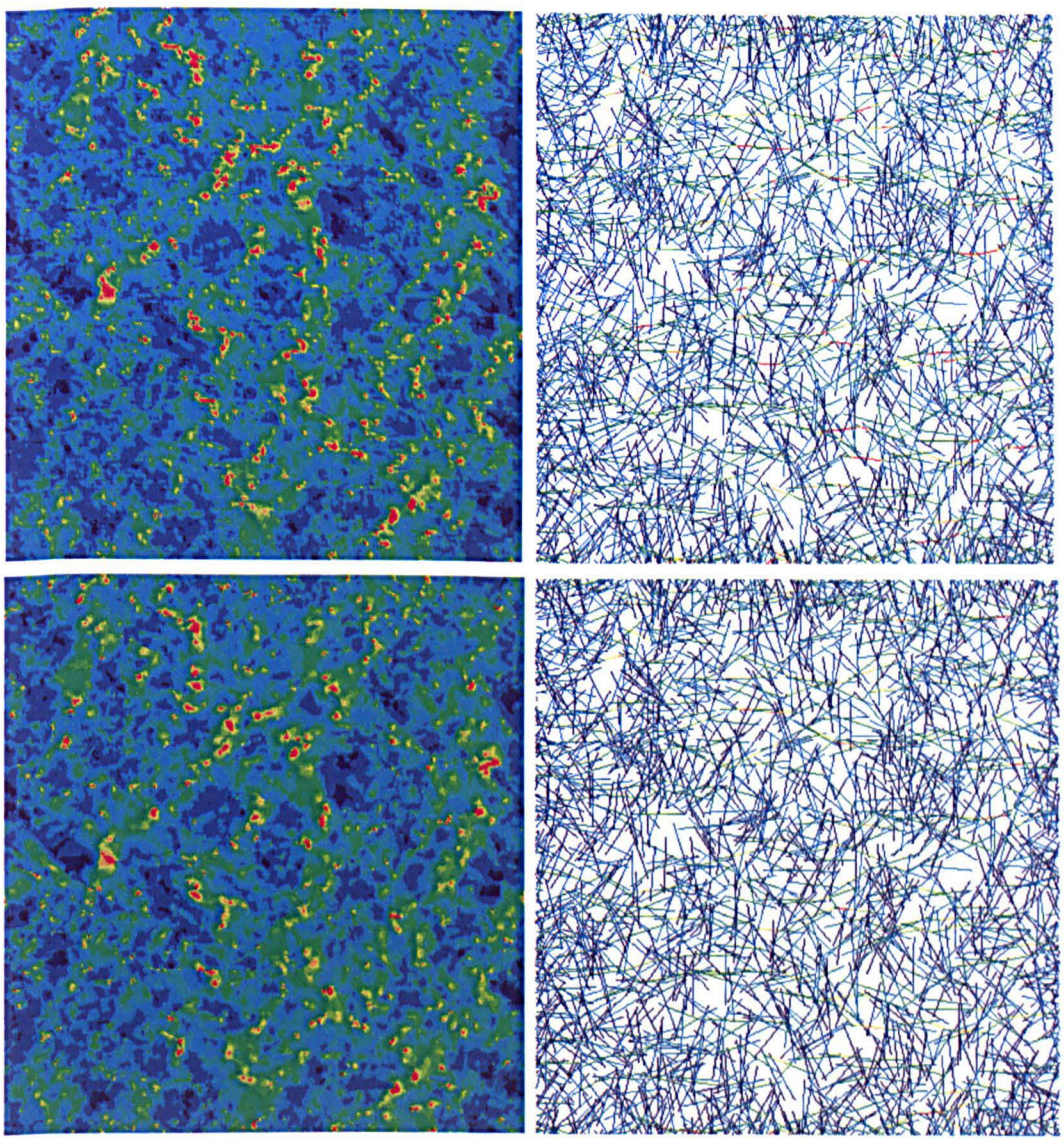

Figure 129 – Comparison of von Mises stress plots for 50% V_f 5mm bundle length free mesh and embedded element models, at 0.25% applied strain in the x-direction. (Top left – embedded element model; top right – embedded element model (fibres only); bottom left – free mesh model; and bottom right – free mesh model (fibres only). Note: Full plot images (left) and fibre plot images (right) are scaled to the same peak stresses of 40MPa and 500MPa, respectively.

Damage initiation and progression was monitored in the models to allow the determination of the strength of the unit cells. Figure 130 and Figure 131 show the damage plots at 2.5% applied strain in the x-direction for the 25mm and 5mm bundle length models, respectively. For the 25mm bundle length models, embedded and free mesh, the damage initiates in the resin rich region in the centre of the unit cell, before propagating vertically to the unit cell boundary. The

strength prediction for the 25mm bundle length free mesh model is within 1.9% of the prediction from the embedded element model, shown in Table 27. However, for the 5mm bundle length models (Figure 131) the damage plots for the embedded and free mesh models are less similar, with a difference in failure strength prediction of 18.5% observed, see Table 26.

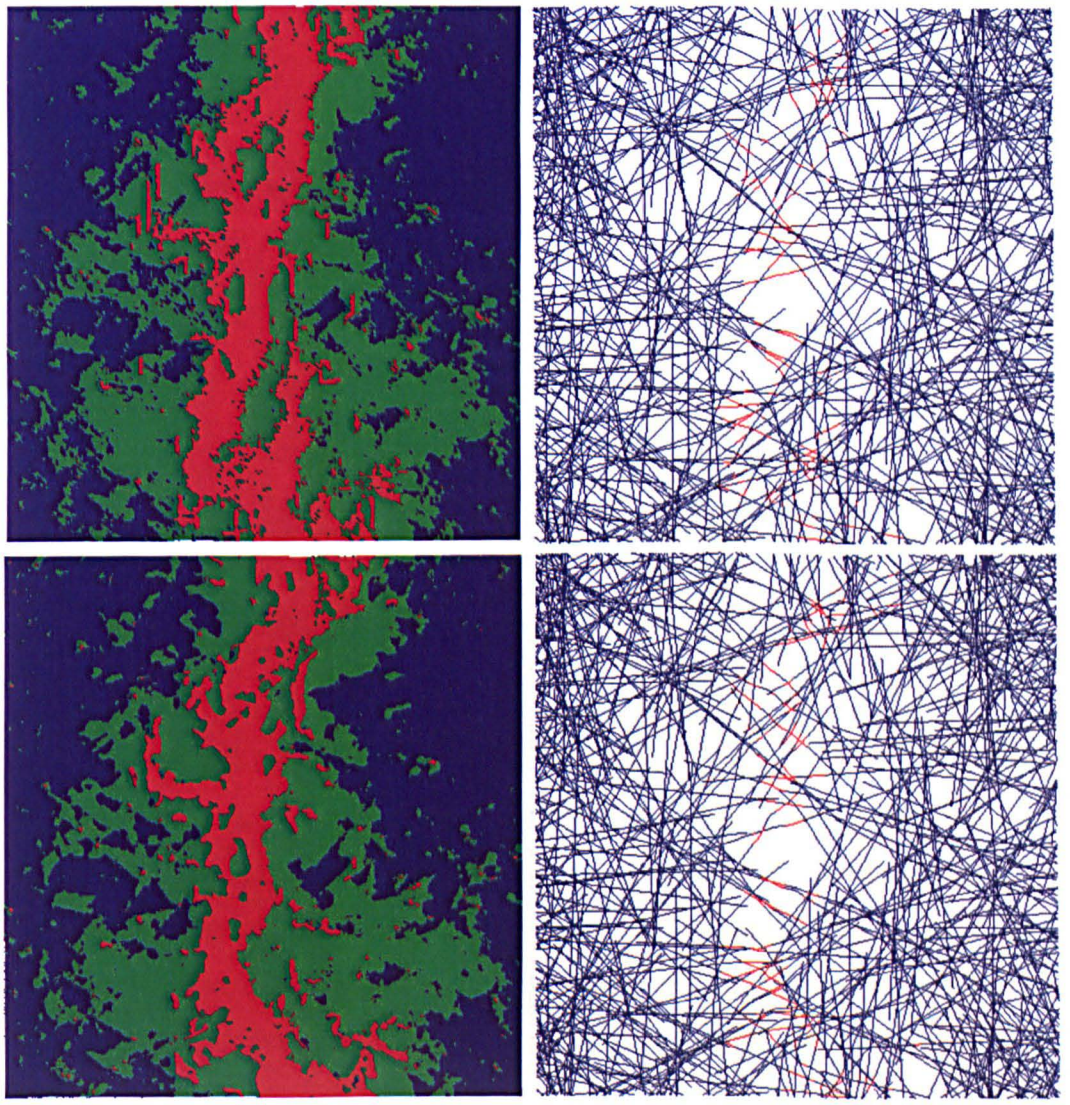

Figure 130 – Comparison of damage plots for 25mm bundle length free mesh and embedded element models at 2.5% applied strain for the 50% V_f models. (Top left – embedded element model; top right – embedded element model (fibres only); bottom left – free mesh model; and bottom right – free mesh model (fibres only). Note: undamaged elements (blue), plastic elements (green) and damaged elements (red).

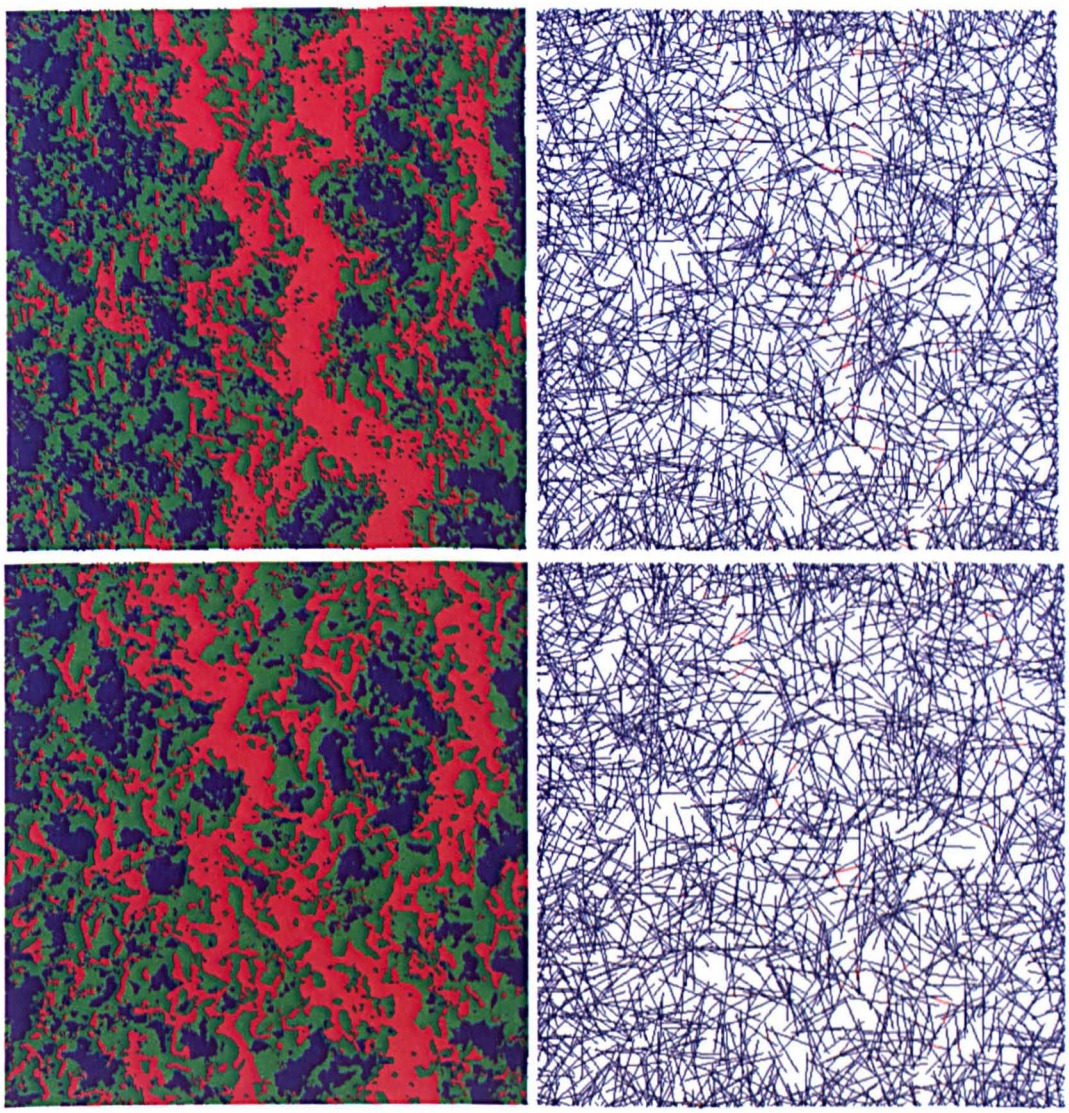

Figure 131 – Comparison of damage plots for 5mm bundle length free mesh and embedded element models at 2.5% applied strain for the 50% V_f models. (Top left – embedded element model; top right – embedded element model (fibres only); bottom left – free mesh model; and bottom right – free mesh model (fibres only). Note: undamaged elements (blue), plastic elements (green) and damaged elements (red).

This study has benchmarked the mechanical property predictions from the free mesh model developed against the embedded element model developed in [68]. Good agreement was found between the embedded and free mesh models for the mechanical property prediction at longer fibre lengths (25mm), however at shorter bundle lengths (5mm) the embedded element model predicted higher modulus and strength values for the unit cell.

4.3.2 Influence of the interface

To attempt to improve the strength predictions of the free mesh model the influence of the interfacial parameters has been investigated in this section. Two studies have been conducted. The first study looks at the influence of the stiffness of the interface on the modulus predictions of the unit cell – section 4.3.2.1. The second study allows failure of the connector elements at the interface between the bundle and matrix materials. The interfacial shear strength (ISS) is varied to quantify the influence of the ISS on the strength predictions of the free mesh model - section 4.3.2.2. The same fibre bundle architectures used in section 4.3.1 are considered in this study, shown in Figure 127, to allow direct comparisons to be made to models without interfacial failure to determine the influence of the ISS on the strength predictions of the unit cell.

4.3.2.1 Interface stiffness

Three interfacial stiffness values of $10e^6$, $10e^9$ and $10e^{12}$ N/mm^3 were considered in this analysis. The modulus values obtained for the 5mm and 25mm bundle length unit cells are shown in Table 28 and Table 29, respectively. It was found that by increasing the interface stiffness from $10e^6$ to $10e^9$ N/mm^3 there was a slight increase in modulus of the unit cell, but this increase in modulus was less than 0.15% across the full range of volume fractions for both bundle lengths. A further increase in interfacial stiffness from $10e^9$ to $10e^{12}$ N/mm^3 saw no further increase in the modulus of the unit cells.

Turon et al [123] found that the interface stiffness should be large enough to provide a reasonable stiffness but small enough to avoid numerical instabilities, such as spurious oscillations of the tractions in a connector or cohesive element. In this analysis the FE results converged to provide a solution, however as the interfacial stiffness was increased there was an increase in the number of equilibrium iterations required for each load increment. Based on the findings in this section and for consistency with the results presented in section 4.3.1, an interfacial penalty stiffness value of $10e^6$ N/mm^3 will be used for the remainder of the analysis contained in this thesis.

Table 28 – Modulus of 5mm bundle length unit cells with varying interfacial stiffness.

Interface Stiffness (N/mm^3)	V_f (%)	x (GPa)	y (GPa)	xy (GPa)
10^6	10	5.5801	5.5168	1.9782
10^9	10	5.5824	5.5183	1.9789
10^{12}	10	5.5824	5.5183	1.9789
10^6	30	12.3452	12.7628	4.4470
10^9	30	12.3563	12.7779	4.4517
10^{12}	30	12.3563	12.7779	4.4517
10^6	50	21.9804	23.1195	8.2426
10^9	50	22.0127	23.1408	8.2549
10^{12}	50	22.0127	23.1408	8.2549

Table 29 – Modulus of 25mm bundle length unit cells with varying interfacial stiffness.

Interface Stiffness (N/mm^3)	V_f (%)	x (GPa)	y (GPa)	xy (GPa)
10^6	10	8.7904	7.5907	3.4770
10^9	10	8.7940	7.5933	3.4784
10^{12}	10	8.7940	7.5933	3.4784
10^6	30	21.0859	23.1144	8.3781
10^9	30	21.0964	23.1277	8.3824
10^{12}	30	21.0964	23.1277	8.3824
10^6	50	34.3813	36.5380	13.3894
10^9	50	34.3989	36.5608	13.3961
10^{12}	50	34.3989	36.5608	13.3961

4.3.2.2 Interface shear strength

Failure at the interface between the bundle and matrix material was permitted in this section to attempt to improve the strength predictions of the free mesh model. The fibre bundle architectures in Figure 127 were used to allow comparisons to be made when predicting the strength of the unit cells. Three interfacial shear strength values were considered - 10MPa, 23.1MPa and 40MPa - based on the findings in section 3.5.3.2.

Table 30 and Table 31 present the strength predictions obtained for the 5mm and 25mm bundle length models, respectively. At low fibre volume fractions, for the 5mm and 25mm bundle length models, the interfacial shear strength (ISS) had little influence on the strength predictions of the unit cell, as the failure was initiated in the matrix region between the fibre bundles. When the fibre volume fraction was increased to 30%, the ISS began to dictate the strength of the unit cell. For the 5mm bundle length model (Table 30), when the ISS was at 40MPa the strength prediction of the unit cell was identical to the strength prediction when failure in the interface was not permitted. An average reduction in strength of 4.11% for the unit cell was observed, across all three load cases, as the ISS was reduced to 23.1MPa and then to 10MPa.

The influence of the interface became even more apparent at 50% volume fraction for the 5mm bundle length models, shown in Table 30, as the contact surface area between the bundles and matrix materials increased. For the models with an ISS of 23.1MPa, an average reduction in strength of 15.90% was observed across the three load cases. This reduction in strength increased significantly to 40.51% as the ISS was reduced further still to 10MPa.

The damage plots for the 50% V_f 5mm bundle length models loaded in the x-direction, with varying ISS, are shown in Figure 132. When the ISS was set to 10MPa, it can be seen that there was little fibre bundle failure in the models (right, Figure 132). As the ISS was low, the fibre bundles began to debond from the matrix material and consequently were unable to carry any load applied to the unit cell – leading to the reduction in failure strength of the unit cell. As the ISS was increased from 10MPa to 23.1MPa, and then further still to 40MPa, there was an increase in the number of bundle failures in the models, as there was less debonding between the bundle and matrix materials as the failure mechanism changed from bundle pull-out to bundle fracture. A strong interface allows the fibre bundles to continue to carry the load applied to the unit cell, which inherently leads to a higher material strength.

The interface had less influence on the strength predictions of the 25mm bundle length models, shown in Table 31. The force required to initiate debonding

between the bundle and matrix materials is proportional to the length of the fibre bundle encapsulated in the material, shown in Equation 36 and detailed in Table 14. Therefore the force required to initiate debonding in the connector elements for the 25mm bundle length models was five times greater than for the 5mm bundle length models. This resulted in no debonding of the bundles and matrix in the models when the ISS was set at 23.1MPa and 40MPa, with a small amount of debonding occurring when the ISS was reduced to its minimum value, 10MPa, where a small reduction in strength was observed – see Table 31 .

The damage plots for the 50% V_f 25mm bundle length models loaded in the x-direction, with varying ISS, are shown in Figure 133. As there is little change in the strength of the models, even at an ISS of 10MPa, the damage plots are almost identical for all the models.

Table 30 – Strength of 5mm bundle length unit cells with varying interfacial shear strength (ISS). (Note: Modulus did not vary as the penalty stiffness was kept constant).

Interface Shear Strength (MPa)	V_f (%)	x (MPa)	y (MPa)	xy (MPa)
No Failure	10	34.622	35.094	19.805
40.0	10	34.622	35.094	19.805
23.1	10	34.622	35.094	19.805
10.0	10	34.454	34.817	19.650
No Failure	30	51.424	57.217	29.774
40.0	30	51.424	57.217	29.774
23.1	30	51.380	56.529	29.774
10.0	30	48.943	53.644	29.398
No Failure	50	150.008	151.399	66.376
40.0	50	145.560	151.399	66.376
23.1	50	126.299	126.089	62.186
10.0	50	79.752	83.205	51.573

Table 31 – Strength of 25mm bundle length unit cells with varying interfacial shear strength (ISS). (Note: Modulus did not vary as the penalty stiffness was kept constant).

Interface Shear Strength (MPa)	V_f (%)	x (MPa)	y (MPa)	xy (MPa)
No Failure	10	60.647	44.775	29.566
40.0	10	60.647	44.775	29.566
23.1	10	60.647	44.775	29.566
10.0	10	59.471	44.775	28.911
No Failure	30	184.033	173.877	87.807
40.0	30	184.033	173.877	87.807
23.1	30	184.033	173.877	87.807
10.0	30	181.134	162.437	86.305
No Failure	50	264.066	355.227	133.142
40.0	50	264.066	355.227	133.142
23.1	50	264.066	355.227	133.142
10.0	50	263.523	314.341	132.522

This study has shown the importance of the ISS between bundles and matrix materials when determining the strength of discontinuous composite materials, particularly at shorter fibre bundle lengths (~5mm). If there is a weak interface (~10MPa) between the bundle and matrix materials then the strength of the material can reduce by up to 40% at high volume fractions (50% V_f) when compared to models with a strong ISS (~40MPa). The interface had less influence on the strength predictions of the unit cell as the bundle length was increased (~25mm), as the force required to initiate debonding was much larger due to the increase in the encapsulated bundle length – see section 3.5.3.2.

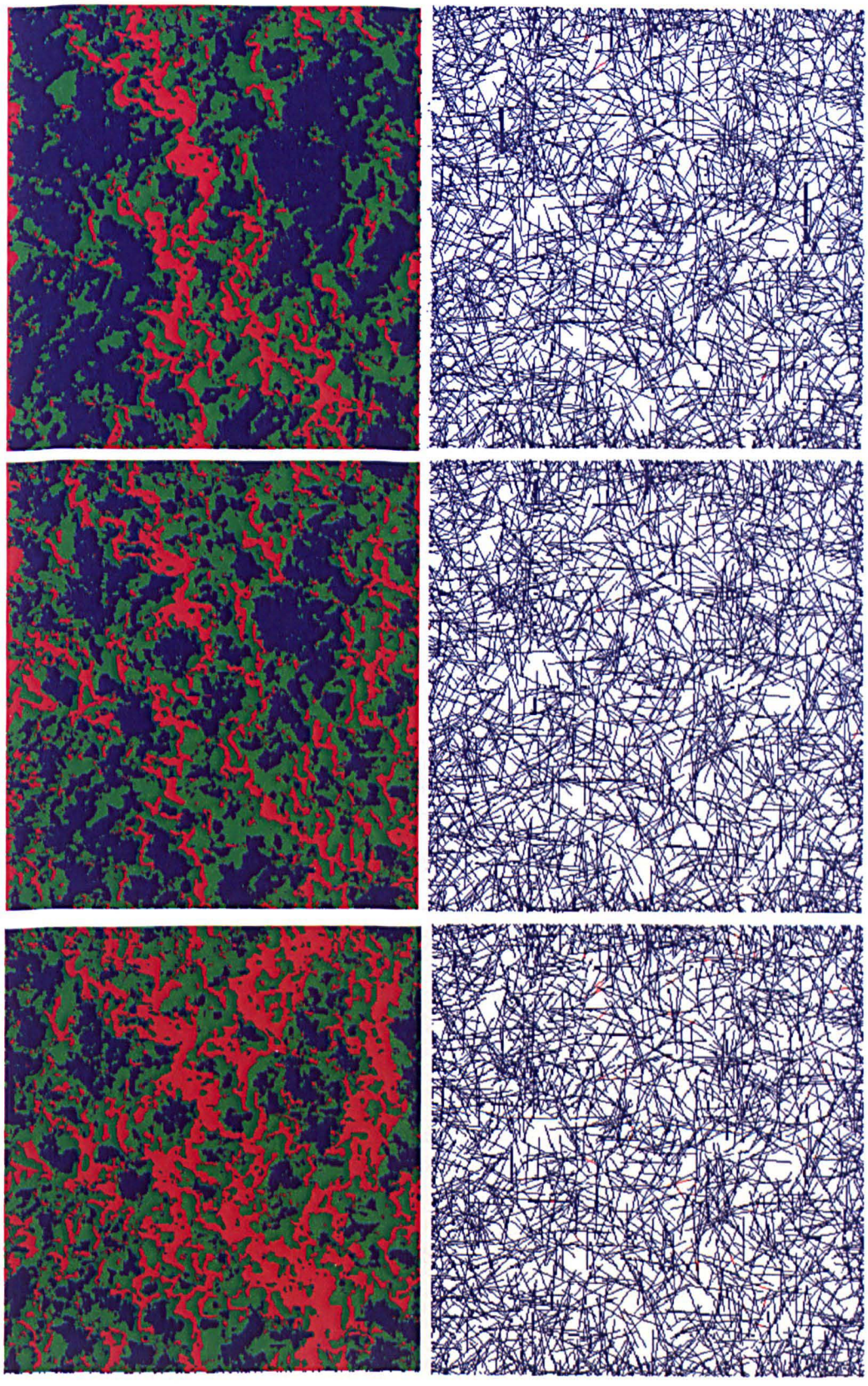

Figure 132 – Damage plots for 5mm bundle length free mesh models at 2.5% applied strain for the 50% V_f models with varying interfacial shear strength. Top – 10MPa, middle – 23.1MPa, and bottom – 40MPa. Note: undamaged elements (blue), plastic elements (green) and damaged elements (red).

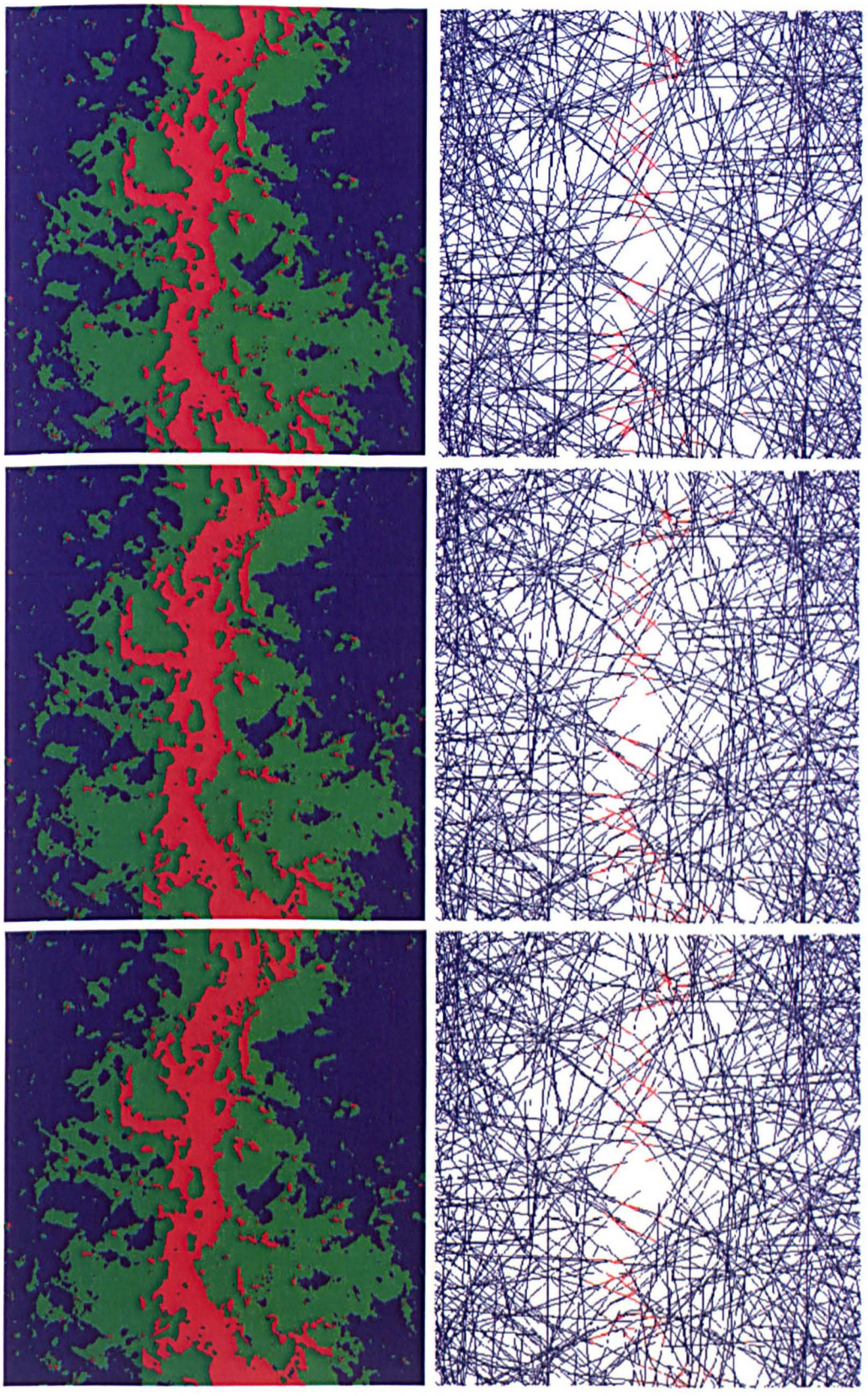

Figure 133 – Damage plots for 25mm bundle length free mesh models at 2.5% applied strain for the 50% V_f models with varying interfacial shear strength. Top – 10MPa, middle – 23.1MPa, and bottom – 40MPa. Note: undamaged elements (blue), plastic elements (green) and damaged elements (red).

4.3.3 Influence of SCFs at bundle intersections

This section presents the results for the two models, 5mm and 25mm bundle lengths with interfacial debonding between bundle and matrix, with the SCFs calculated in section 3.5.4 incorporated into the analysis. The number of intersections in each model, for all the volume fractions considered in this analysis, is shown in Table 32. At the point of the bundle intersections, the elements either side of the intersection (Figure 85) have their mechanical properties reduced by the values given in Table 16.

Table 32 – Number of intersections with varying bundle length and volume fraction.

Bundle Length	V_f (%)	Number of Intersections
5mm	10	463
25mm	10	476
5mm	30	4,194
25mm	30	4,375
5mm	50	11,575
25mm	50	12,518

The modulus and strength values obtained from FE analysis for the 5mm and 25mm bundle length models are shown in Table 33 and Table 34, respectively. At low fibre volume fractions (10% V_f) for both bundle lengths, the SCFs at the bundle intersections had little influence on the modulus (<2%) and strength (<0.5%) predictions of the unit cell; attributable to the low number of intersections, shown in Table 32.

As the fibre volume fraction of the unit cell was increased to 30% V_f, the difference in the modulus and strength predictions of the models with SCFs and those without increased. For the 5mm bundle length model, the modulus predictions were 5.1% lower with the introduction of the SCFs, with an average strength reduction of approximately 1.5% across the load cases. This difference increased further still for the 25mm bundle length model, with an average reduction in modulus of 5.9% across the three load cases with the introduction of the SCFs, however there was little reduction in the strength for the 25mm bundle model (~0.5%) at 30% V_f.

Table 33 - SCF modulus and strength values for the 5mm bundle length model.

		Modulus			Strength		
Model Reference	V_f (%)	x (GPa)	y (GPa)	xy (GPa)	x (MPa)	y (MPa)	xy (MPa)
SCF	10	5.507	5.451	1.958	34.781	35.200	19.914
No SCF	10	5.580	5.517	1.978	34.622	35.094	19.805
SCF	30	11.708	12.084	4.230	51.478	54.957	29.239
No SCF	30	12.345	12.763	4.447	51.380	56.529	29.774
SCF	50	20.362	21.401	7.650	122.047	117.287	61.584
No SCF	50	21.980	23.119	8.243	126.299	126.089	62.186

Table 34 - SCF modulus and strength values for the 25mm bundle length model.

		Modulus			Strength		
Model Reference	V_f (%)	x (GPa)	y (GPa)	xy (GPa)	x (MPa)	y (MPa)	xy (MPa)
SCF	10	8.533	7.415	3.381	60.923	44.824	29.556
No SCF	10	8.790	7.591	3.477	60.647	44.775	29.566
SCF	30	19.914	21.816	7.835	183.685	172.976	87.371
No SCF	30	21.086	23.114	8.378	184.033	173.877	87.807
SCF	50	31.818	33.634	12.192	262.564	353.376	132.498
No SCF	50	34.381	36.538	13.389	264.066	355.227	133.142

At 50% V_f, the difference in the mechanical property predictions of the unit cells with and without the SCFs at the bundle intersections was at its greatest, due to the greater number of intersections in the models, shown in Table 32. The modulus predictions were 7.3% and 8.1% lower for the models with the SCFs at the bundle intersections for the 5mm and 25mm bundle length models, respectively. The strength predictions were also 3.8% and 0.5% lower for the 5mm and 25mm SCF bundle length models, respectively.

The results from this study have shown that by incorporating the influence of the SCFs at the bundle intersections the modulus and strength of the unit cells reduce across the range of volume fractions and fibre lengths considered in this analysis. The introduction of the SCFs attempts to account for the 3D nature of the bundle intersections at the macroscale, which cannot be captured currently in the 2D fibre bundle architectures that the model generates.

4.3.4 Comparison to experimental data and analytical models

This section benchmarks the mechanical properties obtained using the free-mesh model against experimental data and an existing analytical model at a fibre volume fraction of 50%. Five repeats were performed for each fibre bundle length (3mm, 5mm, 7mm, 9mm, 12mm, 15mm, 20mm, 25mm and 40mm), with the mean of the modulus and strength predictions used for the comparisons. A cell size of 50x50mm was used in this analysis, apart from the 40mm bundle length model where a cell size of 80x80mm was used (two times the fibre bundle length). The interface penalty stiffness was set to $10e^6$ N/mm^3 and the interfacial shear strength was set to 23.1MPa.

The modulus predictions for the free-mesh model are compared to the analytical model developed in [169] and experimental test results from [36] in Figure 134. The analytical model has relatively good agreement with the experimental results for the bundle lengths considered in this analysis, with the analytical model providing an upper bound for the modulus prediction of the random discontinuous carbon composite material. The FE predictions for the free mesh model lie between the bounds set by the experimental test results, which provides a good approximation (~10%) for the stiffness of the material across the full range of bundle lengths considered in this analysis.

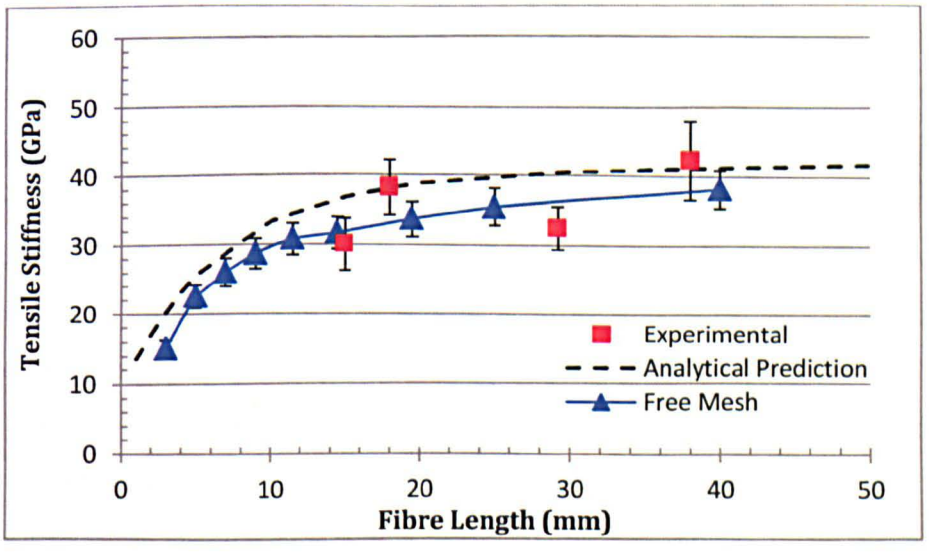

Figure 134 - Modulus predictions at a range of fibre bundle lengths at 50% V_f compared to experimental test results [36] and existing analytical model in [169].

The strength of the discontinuous material for the range of bundle lengths considered in this analysis can be seen in Figure 135. Good agreement (~18%) was found between the experimental results and the strength predictions from the free-mesh model for the fibre bundle lengths considered. This is a small improvement on the strength predictions from the existing embedded element model in [68], which provided strength predictions within 20% of the same experimental results in [36].

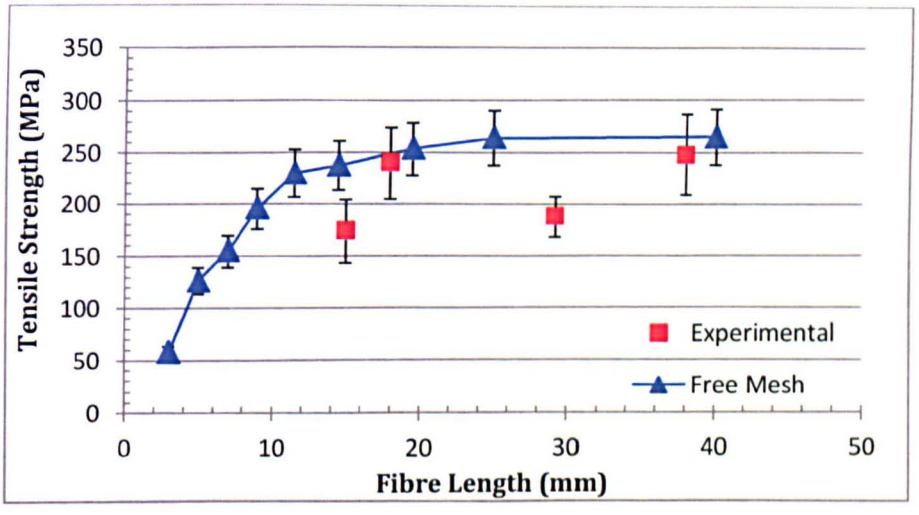

Figure 135 - Strength predictions at a range of fibre bundle lengths at 50% V_f compared to experimental test results from [36].

The 2D free-mesh model over-predicts the strength of the discontinuous material when compared to the experimental data from [36]. The model is a 2D idealisation of a 3D problem, with the 2D fibre bundle architecture providing higher strength predictions than would be expected for the discontinuous material. If the fibre bundles were in a 3D volume, matrix material would be present between the layers of fibres, which would be subjected to high stresses as load is transferred between the fibre bundles. An attempt to capture this was made by performing mesoscale analysis of bundle interactions in a unit cell, however, only two fibre bundles were considered in isolation in that analysis. Although the modulus predictions from the 2D free-mesh model are relatively good (~10%), after performing the analysis contained in this section a 3D model is seen as essential to further improve strength predictions for discontinuous composites at the macroscale.

Chapter 5 Discussion and Conclusions

The aim of this chapter is to discuss the findings and present the conclusions established during this work, with recommendations made for future study in the field. The thesis has been centred on the development of a 2D macroscale model that enables interfacial debonding between fibre and matrix to predict the mechanical properties of discontinuous composite materials, using multi-scale modelling techniques. Microscale and mesoscale analysis was performed and data was subsequently passed to the macroscale to improve the predictions of the in-plane tensile stiffness and strength. Experimental testing has also been conducted to provide the input data for the FE analysis for the fibre bundle and matrix materials. The results from the macroscale model have been benchmarked against existing analytical and numerical models, with comparisons also made to experimental results for discontinuous carbon composite materials. Whilst this methodology has only been applied to predict the performance of BRAC3D material in the current thesis, the methodology can be universally applied to other discontinuous fibre architectures, such as SMCs and BMCs.

5.1 Material characterisation and damage modelling

Damage models have been developed using FORTRAN, compatible with ABAQUS/Standard. The development of the user-defined material models (UMATs) allows damage initiation, damage progression and final failure to be monitored in FE models. Models have typically been produced to predict the stiffness of discontinuous composites; however, by integrating damage into the FE analysis, it was possible to also predict the failure strength of the discontinuous composite material. Experimental testing of the material constituents (section 3.1) allowed accurate data to be fed into user-defined material damage models (section 3.2), improving the modulus and strength predictions for discontinuous materials. UMAT's have been produced for 2D and 3D analyses, which were used at all material scales in this thesis – micro, meso and macroscale.

5.2 Microscale modelling

Micromechanical analysis of a single carbon fibre embedded in a matrix region has been conducted in section 4.1.1. By analysing one fibre in isolation, a robust and reliable model was developed to quantify the influence of the debonding parameters used at the interface between fibre and matrix. It was shown that a small interface, with a thickness of only 1% of the fibre radius, can greatly influence the stress transfer between the fibre and matrix materials. FE results have been benchmarked against the shear lag model, existing single fibre composite models and experimental results currently in the literature.

Limitations of existing analytical and numerical models were established and traction-separation laws, with suitable parameters for interface penalty stiffness ($K=10^6$ N/mm^3), interfacial shear strength (τ_o=20MPa) and interfacial fracture toughness (G_c=220 J/m^2), were determined at the microscale for use at the macroscale for high volume fraction discontinuous composite materials. The effect of constituent damage to the fibre and matrix was not considered in section 4.1.1, to allow the influence of the interfacial properties to be assessed independently. If fibre and matrix damage was considered in the analysis it is expected that the stresses achieved in the fibre would fall due to failures in the matrix material at the base of the embedded fibre, attributable to the discontinuity at the fibre end.

The fibre ineffective length study (section 4.1.2) has shown that the SCF found in fibres neighbouring a fractured fibre can strongly influence the mechanical properties of the material at the microscale for short fibre lengths (<1mm). The ineffective length of the broken fibre was calculated along with stress concentration factors in the adjacent fibres, with the material stiffness (fibre, matrix and interface) varied in a full factorial study to assess the change in the monitored output parameters. Both output parameters were found to be dependent on the E_{fibre}/E_{matrix} ratio, with a reduction in this ratio providing a reduced ineffective length of the broken fibre and lower SCFs in neighbouring fibre. Matrix failure initiated and propagated from the site of a fibre fracture, leading to increased stress levels in adjacent fibres and therefore more fibre failures in the

composite material. Although the fibre ineffective length almost doubled from 85μm to 165μm, the range of ineffective fibre lengths obtained are much lower than the fibre bundle lengths (>5mm) considered at the meso and macroscale; therefore, the proportion of the bundle length affected by the discontinuities was deemed to be negligible in this analysis.

Periodic unit cells were developed in section 4.1.3 to determine fibre bundle properties, represented as a unidirectional composite. Mechanical properties were determined for a range of bundle volume fractions to create a material library for use in analysis at the mesoscale and macroscale for discontinuous composite materials. Good agreement was found between the FE models and analytical predictions for loading along the length of the fibre (~1%), however for the transverse and shear load cases the analytical models provided poor predictions (~22%) as they failed to capture the complex stress distribution in the unit cells. The transverse and shear strengths of the bundle have been calculated from the FE models; however, the tensile strength of the bundle along its axis was determined from experimental tests, at a range of gauge lengths in section 3.1.2, to ensure the fractures present in the filaments along the length of the bundle were accounted for at the macroscale.

5.3 Mesoscale modelling

The objective of the mesoscale analysis was to understand and quantify the parameters that can influence the mechanical properties of a unit cell containing two discontinuous fibre bundles. It was shown that the stress transfer between two fibre bundles is complex, with many variables influencing the stress distribution in the unit cells. The redistribution of stress at a bundle end, or at the point of a bundle failure, in a discontinuous composite is important when predicting the strength of the material. It was found that by increasing the aspect ratio of the fibre bundle the ineffective length of the fractured bundle decreased by over 50%, for the bundle aspect ratios considered in this analysis. In addition to the reduction in bundle ineffective length, lower SCFs were also observed in the neighbouring bundle as the aspect ratio of the bundles was increased, with the overload caused

by the bundle fracture more evenly distributed along the length of the adjacent bundle.

The effect of bundle orientation and bundle separation distance on the SCFs found in discontinuous composites was investigated by monitoring the stress distribution and damage development in a unit cell containing two fibre bundles. As the separation distance between the fibre bundles decreased there was an increase in stiffness of the unit cell (~1.9%), however, this also coincided with greater stress concentrations in the bundle aligned to the direction of loading. The SCFs found in the bundles, based on orientation and separation, were carried forward to the macroscale to develop a stiffness reduction scheme for the bundle elements at the intersection points to account for the 3D nature of the bundle interactions.

5.4 Macroscale modelling

A macroscale model has been developed to predict the mechanical properties of discontinuous composite materials. 2D fibre bundle architectures were generated, with a free-meshing technique employed to mesh the unit cell ready for FE analysis. Bundle-matrix debonding was permitted in the analysis by the use connector elements at the interface, with the interface properties established at the microscale used to define the traction-separation relationship of the connector elements. The mechanical properties of the fibre bundles are also taken from the microscale analysis contained in this thesis.

Two fibre bundle lengths at a range of fibre volume fractions were considered initially in section 4.3.1, with no interfacial failure permitted, to allow the model to be benchmarked against an existing embedded element model developed in [68]. There was good agreement found between the embedded and free mesh models for the mechanical property prediction at longer fibre lengths (25mm), however at shorter bundle lengths (5mm) the embedded element model predicted higher modulus and strength values for the unit cell, with average modulus and strength variations of 13.16% and 19.41%, respectively, at 50% V_f. This was attributable to more bundle segments being present in the model for the short bundle length, with more bundle elements hosted by the same matrix in the

embedded element model. It is expected that the modulus prediction of the free mesh model is more representative of the discontinuous material as it does not host the bundle elements in the matrix like the existing embedded element model.

Interfacial failure was then considered in section 4.3.2 to assess the influence of interface penalty stiffness and interfacial shear strength on the strength predictions of the model. An increase in interfacial penalty stiffness from $10e^6$ to $10e^{12}$ N/mm^3 saw a slight increase in modulus of the unit cell, but this increase in modulus was less than 0.15% across the full range of volume fractions for both bundle lengths. A penalty stiffness of $10e^6$ N/mm^3 was selected to avoid numerical instabilities in the FE analysis, which can arise if the interface stiffness is too great, according to the findings in [123].

The interfacial shear strength was shown to strongly dictate the strength predictions of the discontinuous material, particularly at shorter fibre bundle lengths (~5mm). A weak interface (~10MPa) saw the strength of the material drop by up to 40% at high volume fractions (50% V_f) when compared to models with a strong ISS (~40MPa). At longer fibre bundle lengths (~25mm) the interfacial shear strength had less influence on the strength predictions of the discontinuous material, due to the larger force required to initiate bundle-matrix debonding for the greater encapsulated bundle length.

The characterisation of the fibre bundle architecture in discontinuous materials is difficult due to the heterogeneity of the material. The 2D macroscale model was able to capture the in-plane variation of the bundle geometry and an attempt was made to capture the out-of-plane bundle geometry at the mesoscale when considering two interacting fibre bundles. Using the mesoscale results from the mesoscale study (section 4.2.2), SCFs were introduced at the bundle intersections to account for the 3D nature of the interaction between the fibre bundles. A reduction in the modulus (~7.3% at 50% V_f) and strength (~3.8% at 50% V_f) predictions was observed for the 5mm bundle length model. A reduction in modulus (~8.1% at 50% V_f) was also observed at longer bundle lengths (~25mm), but the reduction in strength was only 0.5% when compared to the free-mesh models without the SCFs.

Finally, the model was validated against an existing analytical model and experimental test data in section 4.3.4. Good agreement (~10%) was found between the model and experimental test results when predicting the modulus of the discontinuous carbon composite material. The strength predictions provided by the free-mesh model have improved on the predictions made by the existing embedded element model [169], with an error of 18% found when compared to experimental test results for the bundle lengths considered in this analysis. This improvement will aid the development of discontinuous composite materials for semi-structural and structural applications, as designers will have more confidence in the mechanical property predictions from the macroscale model, which has previously been a barrier to acceptance of discontinuous materials.

5.5 Recommendations for future work

Areas that would benefit from further study are summarised below:

- It would be beneficial to conduct more extensive experimental testing on the material constituents (filament, bundle and matrix materials) to improve the modulus and failure stress/strain values used in the developed UMATs. This would improve the accuracy of the models at all scales.
- To further improve the modulus and strength predictions of the macroscale model it is essential that the 3D fibre bundle architecture is captured, which will account for bundle tortuosity throughout the thickness of the material. It is acknowledged that the generation and analysis of 3D bundle architectures would be computationally expensive, but it is seen as the only option to further improve the mechanical property predictions for discontinuous composite materials.
- The interfacial shear strength between bundle and matrix materials in the current models use values obtained from studies in the literature. To improve the accuracy of the values used for the interfacial shear strength it would be beneficial to perform a number of fibre bundle pull-out tests at a range of encapsulated bundle lengths. The shear strengths obtained from the experimental testing would help to improve strength predictions for the discontinuous material at the macroscale.

- Currently, the experimental data available to validate the model against is limited. Additional experimental testing of discontinuous carbon composite materials, especially at shorter fibre bundle lengths (~5mm), would allow the model to be validated against a greater range of bundle lengths.
- The Delaunay meshing algorithm used to mesh the model would benefit from further refinement to improve the speed that models can be meshed. A fine grid of points is required across the model boundary to ensure a good quality mesh is produced, which limits the cell size and bundle lengths that can be currently be considered for analysis.
- It would be beneficial to produce a number of models for a range of bundle sizes, which could be validated against some further experimental testing data. It is anticipated the mechanical property predictions of the model would improve for smaller bundle sizes as the bundle is represented by a beam element. However, the fine grid required to produce a good quality mesh currently makes it unfeasible to consider smaller bundle sizes at high fibre volume fractions for FE analysis.

Appendix A Publications

Conference Papers

1. *'Full Field Strain Measurement of Notched Discontinuous Carbon Fibre Composites'*, M D Bond, L T Harper, T A Turner, N A Warrior - 17th International Conference of Composite Materials, Edinburgh, 2009.
2. *'Numerical Macro Scale Modelling of Discontinuous Fibre Architectures'*, R Luchoo, L T Harper, M D Bond, A Dodworth, N A Warrior - 14th European Conference on Composite Materials, Budapest, June 2010.
3. *'Automated Charge Placement for Structural Moulding Compounds'*, L T Harper, R Luchoo, M D Bond, N A Warrior, A Dodworth - SAMPE Seattle, WA, Washington State Convention Centre, 2010.

Journal Papers

4. *'Net-Shape Spray Deposition for Compression Moulding of Discontinuous Fibre Composites for High Performance Applications'*, R Luchoo, L T Harper, M D Bond, N A Warrior and A Dodworth - Plastics Rubber and Composites, Volume 39, Issue 3-5, 2010, Pages 216-231.
5. *'Automated Charge Placement for Structural Moulding Compounds (SMC)'*, L T Harper, R Luchoo, M D Bond, N A Warrior, A Dodworth - SAMPE Journal, Volume 46, Issue 5, September/October 2010.
6. *'Three dimensional Numerical Modelling of Discontinuous Fibre Composite Architectures'*, R Luchoo, L T Harper, M D Bond, N A Warrior and A Dodworth - Plastics Rubber and Composites (accepted for publication).

Appendix B Program User Interface

The user interface for the macroscale model is shown in Figure 136, with the screen split into five cells (A to E) to explain what parameters the user can specify when generating a discontinuous model. Each cells function is listed below:

Cell **A** – The user can specify the size, length and filament diameter of the carbon fibre bundles. A target V_f can also be specified for the unit cell, along with the bundle volume fraction. When the constants are calculated, a target volume for the unit cell is returned, along with the actual V_f obtained in the unit cell and the relative percentage error associated with it.

Cell **B** – The length, width and depth of the unit cell is defined in this section. The user is also able to specify whether they wish to produce a periodic unit cell, tensile specimen or a non-repeating RVE.

Cell **C** – The filamentisation distribution of the fibre bundles can be specified in this section. Data can be exported into the model for the distribution from an external source – in Excel spread-sheet format.

Cell **D** – The fibre orientation distribution is defined in this section, with the user able to specify if they want a 100% random orientation or a certain level of fibre alignment.

Cell **E** – Delaunay triangulation parameters are specified in this section. An element dimension size is set initially, before a point set is generated for the fibre bundle and matrix materials to allow meshing of the models. Connector elements are then generated between the fibre and matrix interface, before finally performing a mesh quality assessment to ensure the mesh is of adequate quality for analysis. If the mesh is unacceptable, it is recommended a smaller value is used for the element dimension size.

Figure 137 shows the as-deposited state, cropped state and filamentisation levels of the fibre bundle architecture that is generated from the specified input

parameters shown in Figure 136. The next step for the program is to generate the ABAQUS input files for FE analysis of the free mesh models. The user interface developed to define these parameters is shown in Figure 138, with a description of the parameters that need to be defined in each cell shown below:

Cell **F** – The mechanical properties for the fibre bundle and matrix materials for the FE analysis are defined in this cell.

Cell **G** – The number of increments for the FE analysis is specified in this cell. A stiffness only analysis can be selected, which applies the prescribed strain over one increment. The level of applied strain and the direction in which it is applied is also defined in this cell.

Cell **H** – To allow comparisons with the embedded element model in section 4.3.1, models with identical fibre bundle architecture can be produced that use the embedded element technique. The fibre and matrix element sizes needs to be defined prior to generating the ABAQUS input file.

Cell **I** – The interface penalty stiffness, the shear strength of the interface, and the fracture toughness of the interface is defined in this cell for the free mesh model. A check box also allows the user to implement the SCF knockdowns at the bundle intersection points if it is desired for the FE analysis, as discussed in section 3.5.4. Following the definition of these parameters, an ABAQUS input file for the free mesh model can be generated ready for FE analysis.

After the input file has been successfully generated an ABAQUS job is created for the model and it is submitted in parallel with the developed UMAT - discussed fully in section 3.2. This allows the damage in the unit cell to be monitored as the applied strain is increased and allows strength predictions to be made for the discontinuous material.

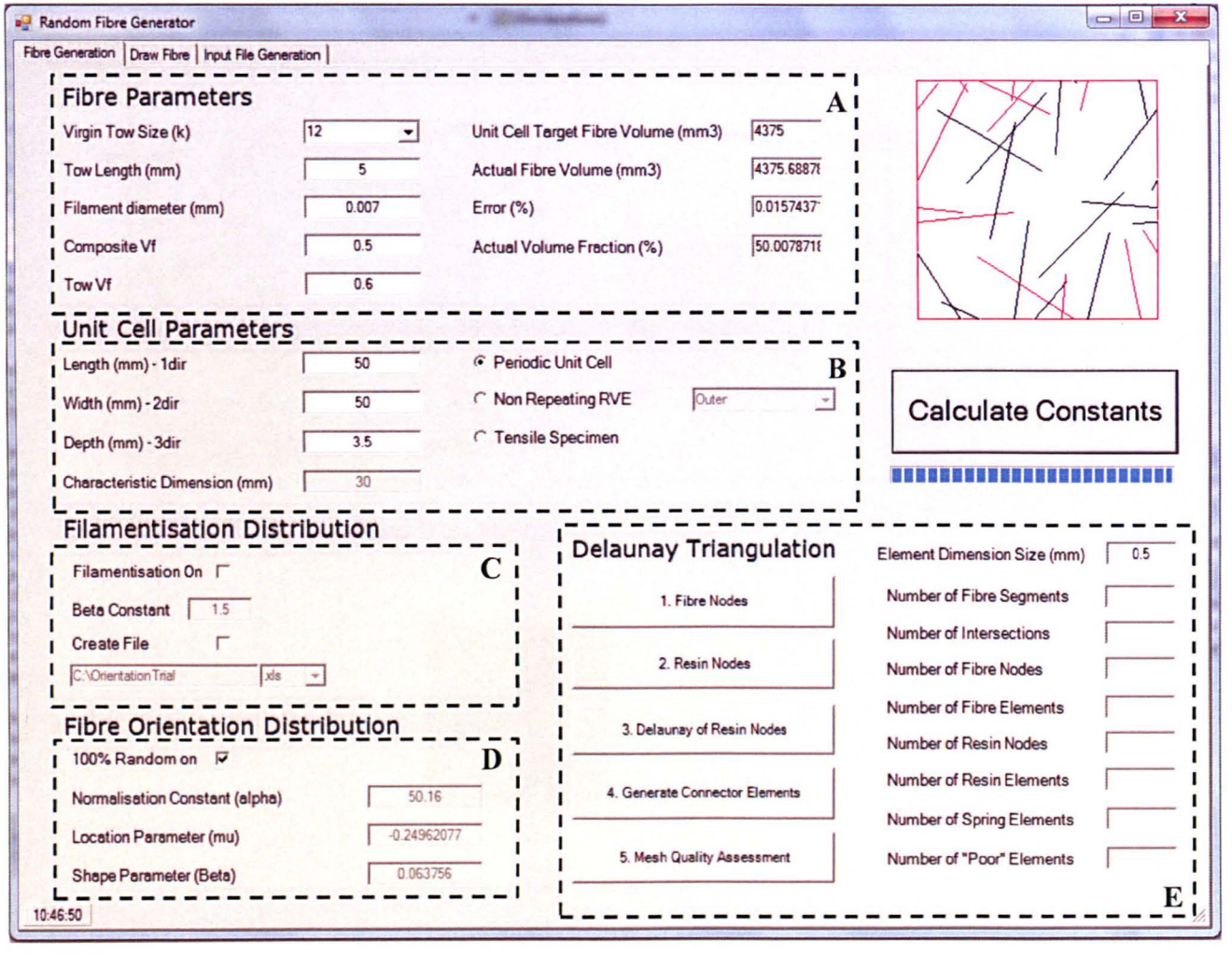

Figure 136 - User interface for the developed macroscale model.

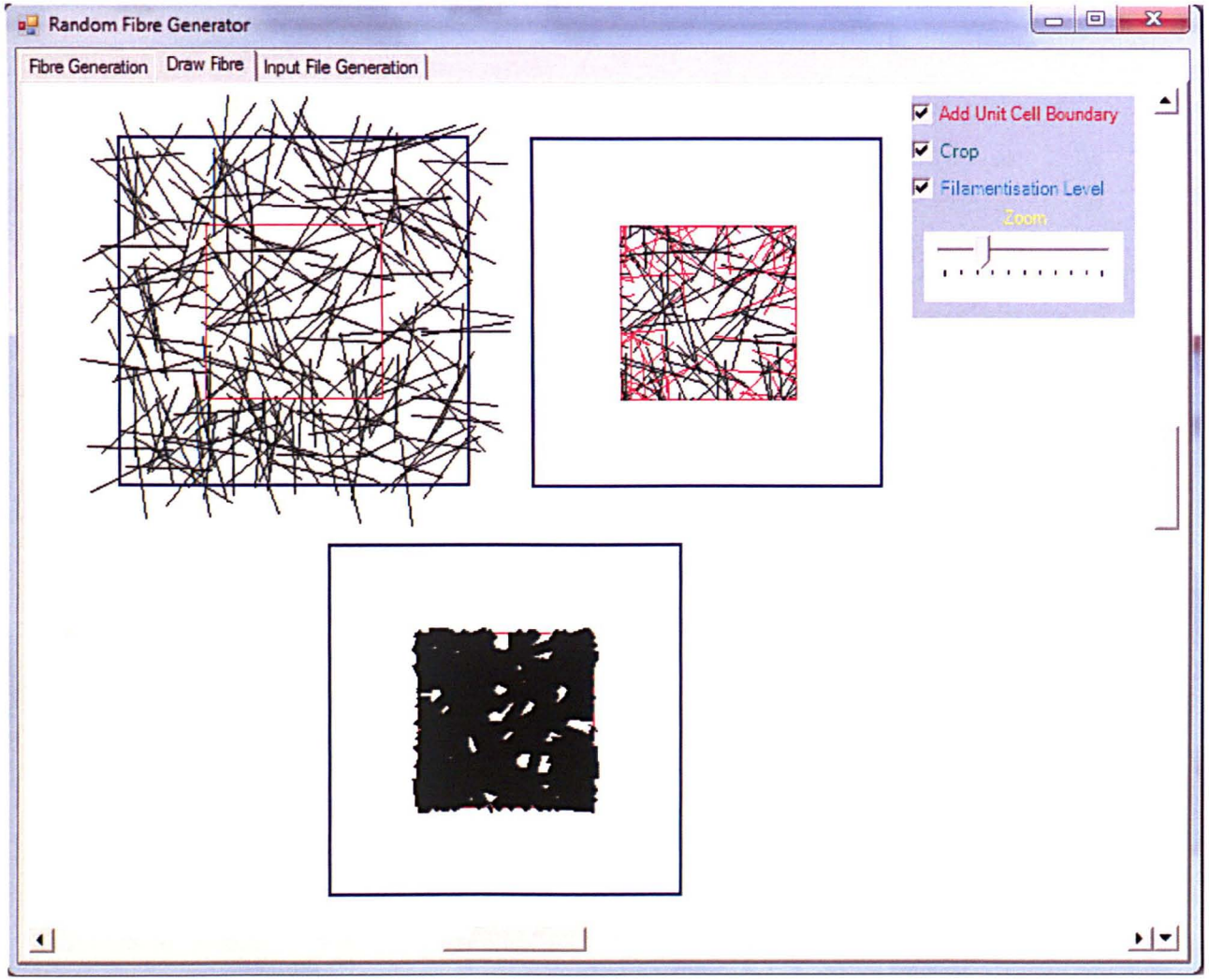

Figure 137 – As-deposited state (top left) and cropped state (top right), with filamentisation level of the bundles (bottom).

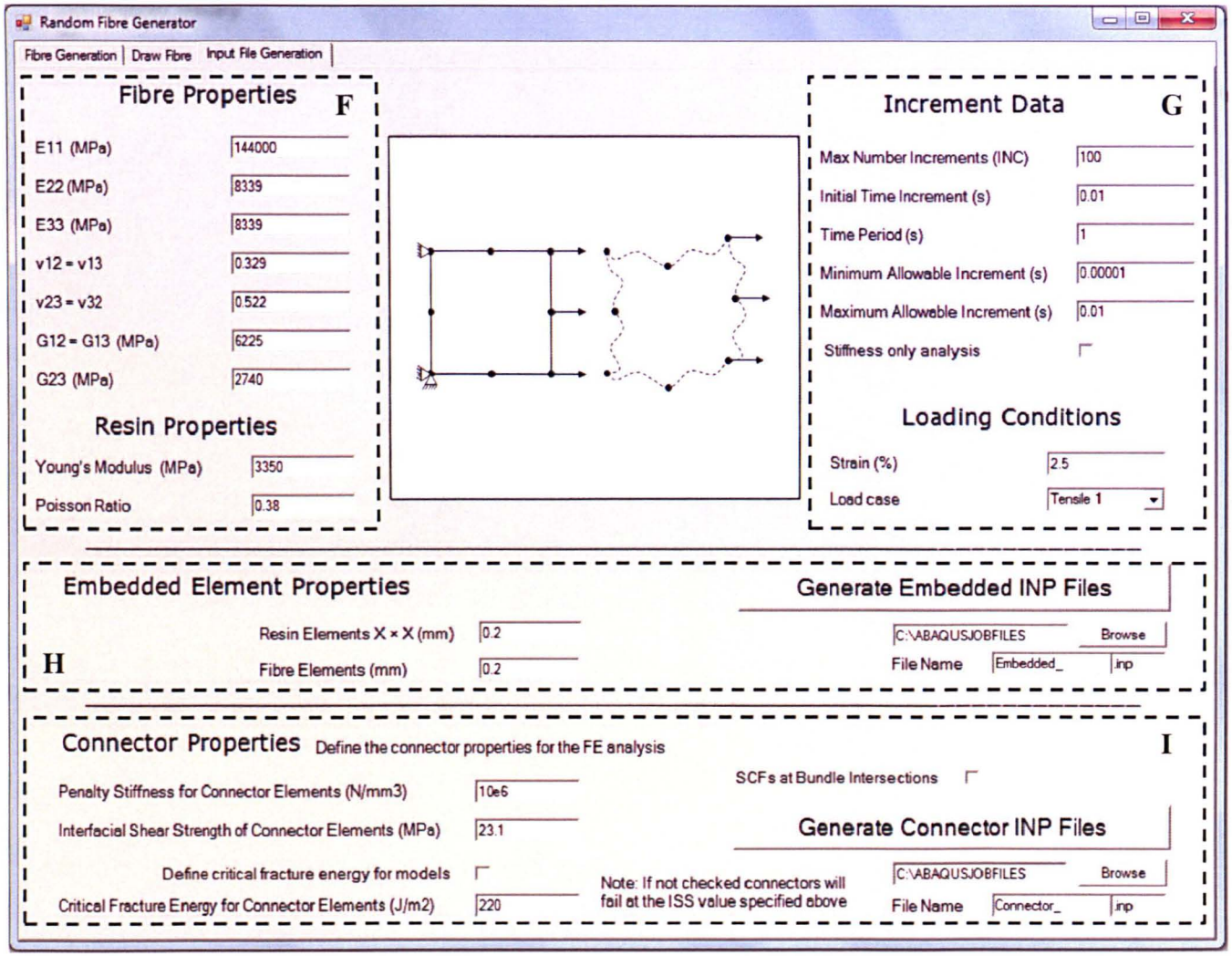

Figure 138 - Input file generation screen for the developed macroscale model.

Appendix C Failure Criterion for 3D Analysis

This section details the failure criterion used to develop damage models for 3D analysis. The development of damage models for 2D analysis is detailed fully in section 3.2, but the equations shown in that section only define the 2D failure envelopes for the materials. Equation 38 and Equation 39 show the von Mises and Maximum Stress criterion failure criterions, respectively, which were used in the 3D analysis at the microscale and mesoscale.

Von Mises

$$\sigma_o = \frac{1}{\sqrt{2}}\sqrt{(\sigma_1 - \sigma_2)^2 + (\sigma_2 - \sigma_3)^2 + (\sigma_3 - \sigma_1)^2} \qquad \text{Equation 38}$$

Maximum Stress criterion

$$-\sigma_c < \{\sigma_1, \sigma_2, \sigma_3\} < \sigma_t \; ; \quad \{|\tau_{12}|, |\tau_{13}|, |\tau_{23}|\} \geq \tau_s \qquad \text{Equation 39}$$

Appendix D Periodic boundary conditions

The following equation constraints are imposed on the macroscale model when periodic boundary conditions are selected:

```
**Constraint: Equations for dummy nodes for a 5x5 unit cell
** Periodic Boundary Conditions
*EQUATION
**Edges of the periodic unit cell
3
Left, 1, -1, Right, 1, 1, DUMMY1, 1, -5
2
Left, 2, -1, Right, 2, 1
3
Bottom, 1, -1, Top, 1, 1, DUMMY3, 1, -5
3
Bottom, 2, -1, Top, 2, 1, DUMMY2, 1, -5
**
**Vertices (corners) of the periodic unit cell
3
TOPLEFT, 1, -1, TOPRIGHT, 1, 1, DUMMY1, 1, -5
2
TOPLEFT, 2, -1, TOPRIGHT, 2, 1
4
BOTTOMLEFT, 1, -1, TOPRIGHT, 1, 1, DUMMY1, 1, -5, DUMMY3, 1, - 5
3
BOTTOMLEFT, 2, -1, TOPRIGHT, 2, 1, DUMMY2, 1, -5
3
BOTTOMRIGHT, 1, -1, TOPRIGHT, 1, 1, DUMMY3, 1, -5
3
BOTTOMRIGHT, 2, -1, TOPRIGHT, 2, 1, DUMMY2, 1, -5
```

Key for the above node sets in the equation constraints for periodic boundary conditions:

Left – left edge of the unit cell.

Right – right edge of the unit cell.

Top – top edge of unit cell.

Bottom – bottom edge of unit cell.

TOPLEFT – top left node of unit cell.

TOPRIGHT – top right node of unit cell.

BOTTOMLEFT – bottom left node of unit cell.

BOTTOMRIGHT – bottom right node of unit cell.

DUMMY1, DUMMY2, DUMMY3 – dummy nodes used to apply displacement to unit cell in the x, y and xy directions respectively.

References

1. SHERBURN, M., *Geometric and Mechanical Modelling of Textiles*, in *The School of Mechanical, Materials and Manufacturing Engineering*. 2007, The University of Nottingham: Nottingham.
2. PAN, Y., L. IORGA, and A. PELEGRI, *Numerical generation of a random chopped fiber composite RVE and its elastic properties.* Composites Science and Technology, 2008. **68**(13): p. 2792-2798.
3. WARRIOR, N.A., et al. *Affordable Lightweight Body Structures (ALBOS).* in *JSAE Annual Congress*. 2004. Pacifico, Yokohama.
4. BROSIUS, D. *ECONOMIC COMPARISON OF AUTOCLAVE AND QUICKSTEP PROCESSES FOR HIGH VOLUME ADVANCED COMPOSITE AUTOMOTIVE COMPONENTS.* 2004; Available from: www.quickstep.com.au].
5. BROSIUS, D. *CARBON FIBER: THE AUTOMOTIVE MATERIAL OF THE TWENTY-FIRST CENTURY STARTS FULFILLING THE PROMISE.* 2004; Available from: http://www.speautomotive.com/SPEA_CD/SPEA2003/pdf/f01.pdf].
6. WEILGAT, A., *Composites use up in auto industry - Supplier technology - Brief article*, in *Automotive Industries*. 2002.
7. MARSH, G., *Composites on the road to the big time?* Reinforced Plastics, 2003. **Automotive supplement**(February): p. 33-47.
8. HARPER, L.T., *Discontinuous carbon fibre composites for automotive applications*, in *PhD Thesis*. 2006, The University of Nottingham: Nottingham.
9. *Bulk Molding Compound.* Owens Corning 2012 20th Dec 2012]; Available from: http://composites.owenscorning.com/processes/Bulk_Molding_Compound.aspx.
10. TEODORESCU, H., et al. *Modelling of Tensile Behaviour of Sheet Moulding Compounds in Proceedings of the World Congress on Engineering 2007.* July 2-4, London, U.K.
11. TEODORESCU-DRAGHICESCU, H. and S. VLASE, *Homogenization and averaging methods to predict elastic properties of pre impregnated composite materials.* Computational Materials Science, 2011. **50**(4): p. 1310-1314.
12. *Silver Arrow has lightweight SMC parts.* Reinforced Plastics, 2005. **February**: p. 8.
13. DOCKUM, J.F. and P.L. SCHELL. *Fiber directed preform reinforcement: Factors that may influence mechanical properties in liquid composite molding.* in *6th Annual ASM/ESD Advanced Composites Conference*. 1990. Detroit, Michigan: ASM International.
14. BRANDT, M.R. and S.R. REEVE. *Directed fibre preform case studies.* in *Composites 2001 Convention and Trade Show*. 2001. Tampa FL USA: Composite Fabricators Association.
15. CORUM, J.M., et al., *Durability-based design criteria for a chopped-glass-fiber automotive structural composite.* Composites Science and Technology, 2001. **61**: p. 1083-1095.

16. BROOKE, L., *Making composites cost-effective. (Automotive Composites Consortium's P4 Process)*, in *Automotive Industries*. 1998.
17. HARPER, L.T., et al., *Fiber Alignment in Directed Carbon Fiber Preforms - A Feasibility Study.* Journal of Composite Materials, 2008. **44**(8): p. 931-951.
18. TURNER, T.A., et al., *Low cost carbon-fibre based automotive body panel systems - a performance and manufacturing cost comparison.* Journal of Automobile Engineering - Proceedings of the Institution of Mechanical Engineers Part D, 2008. **222**(1): p. 53-64.
19. BRUDERICK, M., et al., *Carbon fiber composite body structures for the 2003 Dodge Viper.*
20. *Boeing 787 features composite window frames.* Reinforced Plastics, 2007. **51**(3): p. 4.
21. RONDEAU, R., S.R. REEVE, and G. BOND. *The effect of tows and filament groups on the properties of discontinuous fiber composites.* in *44th International SAMPE Symposium & Exhibition*. 1999. Long Beach, CA, USA.
22. REEVE, S.R., et al. *Mechanical property translation in oriented, discontinuous carbon fiber composites.* in *SAMPE International Symposium*. 2000.
23. GRIFFIN, D.A. and T.D. ASHWILL. *Alternative composite materials for megawatt-scale wind turbine blades: Design considerations and recommended testing.* in *2003 ASME Wind Energy Symposium*. 2003: American Institute of Aeronautics and Astronautics.
24. GRIFFIN, D.A., *Blade system design studies Volume 1: Composite technologies for large wind turbine blades.* 2002, Global Energy Concepts: Kirkland, Washington.
25. FERABOLI, P., et al., *Notched behavior of prepreg-based discontinuous carbon fiber/epoxy systems.* Composites Part A, 2009. **40**: p. 289-299.
26. FERABOLI, P., et al., *Defect and damage analysis of advanced discontinuous carbon/epoxy composite materials.* Composites Part A, 2010. **In Press**.
27. HARPER, L.T., et al., *Fiber Alignment in Directed Carbon Fiber Preforms - Mechanical Property Prediction.* Journal of Composite Materials, 2009. **43**(57): p. 57-74.
28. CORDELL, T., T. BENSON TOLLE, and R. RONDEAU. *The programmable powdered preform process for aerospace: Affordable performance through composites.* in *45th International SAMPE Symposium and Exhibition*. 2000.
29. DAS, S. *Cost assessment of carbon-reinforced composite automotive part.* in *14th International Conference on Composite Materials*. 2003. San Diego, Calafornia: ASC.
30. *SRIM pick-up box competitive with steel*, in *Reinforced Plastics*. 2001. p. 18.
31. CHAVKA, N.G., et al., *Automotive lightweighting materials program annual progress report - P4 carbon fibre preform development.* 2000, U.S. Department of Energy. p. 89-96.
32. CHAVKA, N.G., et al., *Automotive lightweighting materials program annual progress report - Development of manufacturing methods for fiber preforms.* 2001, U.S. Department of Energy. p. 93-95.

33. DAHL, J.S., et al., *Automotive lightweighting materials program annual progress report - Development of manufacturing methods for fiber preforms.* 2002, U.S. Department of Energy. p. 93-97.
34. DAHL, J.S., et al., *Automotive lightweighting materials program annual progress report - Development of manufacturing methods for fiber preforms.* 2003, U.S. Department of Energy. p. 93-99.
35. DeVRIES, J.E., N.G. CHAVKA, and J.S. DAHL. *Recent advances in glass fiber preforming: Implementation of the Ford Programmable Preform Process (F3P).* in *International Conference for Manufacturing of Advanced Composites.* 2001. Belfast.
36. LUCHOO, R., et al., *Net-shape spray deposition for compression moulding of discontinuous fibre composites for high performance applications* Plastics, Rubber and Composites: Macromolecular Engineering, 2010. **39**(3-5): p. 216-231.
37. HARPER, L.T., et al., *Low cost carbon fibre-based automotive body panel systems*, in *27th International SAMPE Europe Conference* 2006: Paris.
38. CHAVKA, N.G. and J.S. DAHL. *P4 preforming technology development utilizing E-glass and carbon fibers.* in *SAMPE International Symposium.* 1999. Detroit, Michigan.
39. HARPER, L.T., et al. *Automated preform manufacture for affordable lightweight body structures.* in *26th International SAMPE Europe Conference.* 2005. Paris.
40. HEXCEL. *Product data sheet - carbon epoxy hexmc / c / 2000 / r1a Hexel Corporation.* 2008; Available from: http://www.hexcel.com/NR/rdonlyres/037544D8-2EBE-40E1-B5A2-9CFD06189753/0/HEXCELHEXMCMOULDING2.pdf].
41. MENZOLIT. *Preliminary data sheet - menzolit advancedsmc 1300 2004.* Available from: http://www.menzolit.com/templates/rhuk_solarflare_ii/pdf/list_new/AdvancedSMC_1300.pdf].
42. YLA. *Product bulletin - ms-4a TenCate Advanced Composites USA Inc. 2009.* Available from: http://www.tencate.com/TenCate/Aerospace_composites/documents/TCAC%20USA%20docs/TCAC%20USA%20Datasheets/DataSheet/MS-4A_PB_DS_Web.pdf].
43. PAN, Y., L. IORGA, and A.A. PELEGRI, *Analysis of 3D random chopped fiber reinforced composites using FEM and random sequential adsorption.* Composites Materials Science, 2008. **43**: p. 450-461.
44. HARPER, L.T., et al., *Characterisation of random carbon fibre composites from a directed fibre preforming process: Analysis of microstructural parameters.* Composites Part A: Applied Science and Manufacturing, 2006. **37**(11): p. 2136-2147.
45. IONITA, A. and Y.J. WEITSMAN, *On the mechanical response of randomly oriented reinforced chopped fibre composites: Data and model.* Composites Science and Technology, 2006. **66**(14): p. 2566-2579.
46. FERABOLI, P., et al., *Stochastic laminate analogy for simulating the variability in modulus of discontinuous composite materials.* Composites Part A, 2010. **44**(4): p. 557-570.

47. HAYES, S.A., R. LANE, and F.R. JONES, *Fibre/matrix stress transfer through a discrete interphase. Part 1: single-fibre model composites.* Composites Part A, 2001. **32**: p. 379-389.
48. LANE, R., S.A. HAYES, and F.R. JONES, *Fibre/matrix stress transfer though a discrete interphase: 2. High Volume fraction systems.* Composites Science and Technology, 2001. **61**: p. 565-578.
49. KELLY, A. and W.R. TYSON, *Tensile properties of fiber-reinforced metals copper/tungsten and copper/molybdenum.* Journal of Mechanical Physics, 1965. **Solids 13**: p. 329.
50. COX, H.L., *The elasticity and strength of paper and other fibrous materials.* Journal of Applied Physics, 1952. **3**: p. 72.
51. *Special issue of journal, World-wide Failure Exercise (WWFE): Part 1.* Composites Science and Technology, 1998. **58**.
52. *Special issue of journal, World-wide Failure Exercise (WWFE): Part 2.* Composites Science and Technology, 2002. **62**.
53. *Special issue of journal, World-wide Failure Exercise (WWFE): Part 3.* Composites Science and Technology, 2004. **64**.
54. SODEN, P.D., A.S. KADDOUR, and M.J. HINTON, *Recommendations for designers and researchers resulting from the world-wide failure exercise.* Composites Science and Technology, 2004. **64**: p. 589-604.
55. CROOKSTON, J., *Prediction of elastic behaviour and initial failure of textile composites*, in *Mechanical Engineering*. 2004, The University of Nottingham.
56. RUJITER, W., *Analysis of mechanical properties of woven textile composites as a function of textile geometry, in PhD thesis*. 2008, University of Nottingham: Nottingham.
57. BLACKETTER, D.M., D.E. WALRATH, and A.C. HANSEN, *Modelling damage in a plain weave fabric-reinforced composite material.* Journal of Composites Technology and Research, 1993. **15**(2): p. 136-142.
58. NICOLETTO, G. and E. RIVA, *Failure mechanisms in twill-weave laminates: FEM predictions vs. experiments.* Composites Part A, 2004. **35**: p. 787-795.
59. ZAKO, M., Y. UETSUJI, and T. KURASHIKI, *Finite element analysis of damaged woven fabric composite materials.* Composites Science and Technology, 2003. **63**: p. 507-516.
60. MALIGNO, A.R., *Finite Element Investigations on the Microstructure of Composite Materials*, in *PhD Thesis*. 2007, The University of Nottingham: Nottingham.
61. ZHAO, L.G., N.A. WARRIOR, and A.C. LONG, *Finite element modelling of damage progression in non-crimp fabric reinforced composites.* Composites Science and Technology, 2006. **66**: p. 36-50.
62. SUN, C.T. and J. TAO, *Prediction of failure envelopes and stress/strain behaviour of composite laminates.* Composites Science and Technology, 1998. **58**: p. 1125-1136.
63. ERICSON, M.L. and L.A. BERGLUND, *Deformation and fracture of glass mat reinforced polypropylene.* Composites Science and Technology, 1992. **43**: p. 269-281.
64. KACIR, L., M. NARKIS, and O. ISHAI, *Oriented short glass fiber composites. III. Structure and mechanical properties of molded sheets.* Polymer Engineering and Science, 1977. **17**(4): p. 234-241.

65. efunda.com. *Maximum Normal Stress Criterion.* 2011; Available from: http://www.efunda.com/formulae/solid_mechanics/failure_criteria/failure_criteria_brittle.cfm.
66. JENKINS, C.F., *Materials of construction used in aircraft and aircraft engines.* Report to the Great Britain Aeronautical Research Committee, 1920.
67. *Handbook of Composites. Vol.3 Failure Mechanics of Composites.* 1985: Elsevier Science Publishers B.V.
68. HARPER, L.T., et al., *Fiber Alignment in Directed Carbon Fiber Preforms - Mechanical Property Prediction.* Journal of Composite Materials, 2010. **44**(8): p. 931-951.
69. PAN, Y., *STIFFNESS AND PROGRESSIVE DAMAGE ANALYSIS ON RANDOM CHOPPED FIBER COMPOSITE USING FEM.* 2010, The State University of New Jersey: New Brunswick, New Jersey.
70. TSAI, S.W. and E.M. WU, *A general theory of strength for anisotropic materials,* . Journal of Composite Materials, 1971. **5**: p. 58-80.
71. JIANG, Y.Q., P.S. LU, and Z.J. GU, *Mechanics of composite materials*, in *Xi'an Jiaotong Publications.* 1990: Xi'an, China.
72. TSAI, S.W. and H.T. HAHN, *Introduction to composite materials.* 1980: Techomic Publishing Co.
73. LIU, K.S. and S.W. TSAI, *A progressive quadratic failure criterion for a laminate.* Composites Science and Technology, 1998. **58**: p. 1023-1032.
74. HOFFMAN, O., *The brittle strength of orthotropic materials.* Composite Materials, 1967. **1**: p. 200-206.
75. HUYSMANS, G., I. VERPOEST, and P. VAN HOUTTE, *A damage model for knitted fabric composites.* Composites: Part A, 2001. **32**: p. 1465-1475.
76. TSAI, S.W. *Strength characteristics of composite materials.* in *North American Space Agency (NASA) Contractor Report, CR-224.* 1965. USA.
77. HILL, R., *A theory of the yielding and plastic flow of anisotropic materials.* Proceedings of the Royal Society, 1948. **A193**: p. 189-297.
78. efunda.com. *Von Mises Criterion.* 2011; Available from: http://www.efunda.com/formulae/solid_mechanics/failure_criteria/failure_criteria_ductile.cfm.
79. DRUCKER, D.C. and W. PRAGER, *Soil mechanics and plastic analysis of limit design.* Quart Appl Math, 1952. **10**: p. 157-165.
80. EDGREN, F., et al., *Formation of damage and its effect on non-crimp fabric reinforced composites loaded in tension.* Composites Science and Technology, 2004. **64**: p. 675-692.
81. GOH, K.L., R.M. ASPDEN, and D.W.L. HUKINS, *Review: Finite element analysis of stress transfer in short-fibre composite materials.* Composites Science and Technology, 2004. **64**: p. 1091-1100.
82. JOHNSON, A.C., et al., *Influence of a matrix crack on stress transfer to an alpha-alumina fibre in epoxy resin using FEA and photoelasticity.* Composites Science and Technology, 2006. **66**: p. 2023-2029.
83. SIRIVEDIN, S., et al., *Matrix crack propagation criteria for model short-carbon fibre/epoxy composites.* Composites Science and Technology, 2000. **60**: p. 2835-2847.

84. FEIH, S., et al. *Testing procedure for the single fiberfragmentation test.* 2004 11th October 2011]; Available from: http://130.226.56.153/rispubl/AFM/afmpdf/ris-r-1483.pdf.
85. van der HEUVEL, P.V.J., *Failure Phenomena in Carbon/Epoxy Microcomposite Model Systems*, in *Department of Mechanical Engineering, Centre for Polymers and Composites.* 1995, Eindhoven University of Technology: Eindhoven.
86. JOHNSON, A.C., S.A. HAYES, and F.R. JONES, *An improved model including plasticity for the prediction of the stress in fibres with an interface/interphase region.* Composites Part A, 2005. **36**: p. 263-271.
87. ANDERSON, J., et al., *Fibre fragmentation distribution in single-fibre composite tension tests.* Composites Part B, 2001. **32**: p. 323-332.
88. CHEN, F., D. TRIPATHI, and F.R. JONES, *Effect of support matrix on interfacial shear strength determination by the bimatrix fragmentation technique.* Composites Part A, 1996. **27A**: p. 505-515.
89. WU, W., et al., *An improved analysis of the stresses in a single-fibre fragmentation test: I Two-phase model.* Composites Science and Technology, 1997. **57**: p. 809-819.
90. KANG, S.-K., D.-B. LEE, and N.-S. CHOI, *Fibre/epoxy interfacial shear strength measured by the microdroplet test.* Composites Science and Technology, 2009. **69**: p. 245-251.
91. TRIPATHI, D. and F.R. JONES, *Measurement of the load-bearing capability of the fibre/matrix interface by single-fibre fragmentation.* Composites Science and Technology, 1997. **57**: p. 925-935.
92. PAIPETIS, A. and C. GALIOTIS, *Effect of fibre sizing on the stress transfer efficiency in carbon/epoxy model composites.* Composites Part A, 1996. **27A**: p. 755-767.
93. PAIPETIS, A. and C. GALIOTIS, *A study of the stress-transfer characteristics in model composites as a function of material processing, fibre sizing and temperature of the environment.* Composites Science and Technology, 1997. **57**: p. 827-838.
94. KIM, B.W. and J.A. NAIRN, *Experimental Verification of the Effects of Friction and Residual Stress on the Analysis of Interfacial Debonding and Toughness in Single Fiber Composites.* Journal of Materials Science, 2002. **37**: p. 3965-3972.
95. GALIOTIS, C., et al., *The study of model polydiacetylene/epoxy composites.* Journal of Materials Science, 1984. **19**: p. 3640-3648.
96. FUKUDA, H. and T.W. CHOU, *An advanced shear-lag model applicable to discontinuous fiber composites.* Journal of Composite Materials, 1981. **15**: p. 79-91.
97. SHIOYA, M. and A. TAKARU, *Estimation of fibre and interfacial shear strength by using a single-fibre composite.* Composites Science and Technology, 1995. **55**: p. 33-39.
98. ANAGOSTOPOULOS, G., et al., *An experimental and theoretical study of the stress transfer problem in fibrous composites.* Acta Materialia, 2005. **53**: p. 4173-4183.
99. COPPONNEX, T.J., *Analysis and evaluation of the single-fibre fragmentation test.* Composites Science and Technology, 1996. **56**: p. 893-909.

100. YANG, Q.S., Q.H. QIN, and X.R. PENG, *Size effects in the fibre pullout test.* Composite Structures, 2003. **61**: p. 193-198.
101. JOHNSON, A.C., S.A. HAYES, and F.R. JONES, *Data reduction methodologies for single fibre fragmentation test: Role of the interface and interphase.* Composites Part A, 2009. **40**: p. 449-454.
102. WU, W., I. VERPOEST, and J. VARNA, *An improved analysis of the stresses in a single-fibre fragmentation test – II. 3-phase model.* Composites Science and Technology, 1998. **58**: p. 41-50.
103. FIELDER, B. and K. SCHULTE, *Stress Distribution in single-fibre model composites with perfect bonding.* Composites Science and Technology, 1997. **57**: p. 1331-1339.
104. MALIGNO, A.R., N.A. WARRIOR, and A.C. LONG, *Effects of inter-fibre spacing on the damage evolution in unidirectional (UD) fibre-reinforced composites.* European Journal of Mechanics A/Solids, 2008.
105. PARK, J.M., S.I. LEE, and J.H. CHOI, *Cure monitoring and residual stress sensing of single-carbon fibre reinforced epoxy composites using electrical restivity measurement.* Composites Science and Technology, 2004. **65**: p. 571-580.
106. DiBENEDETTO, A.T., *Evaluation of fibre surface treatments in composite materials.* Pure and Applied Chemistry, 1985. **57**(11): p. 1659-1665.
107. KARI, S., et al., *Evaluation of influence of interphase material parameters on effective material properties of three phase composites.* Composites Science and Technology, 2008. **68**: p. 684-691.
108. WU, W., et al., *Variational approach to the stress-transfer problem through partially debonded interfaces in a three-phase composite.* Composites Science and Technology, 1999. **59**: p. 519-535.
109. WU, W., I. VERPOEST, and J. VARNA, *A novel axisymmetric variational analysis of stress transfer into fibres through a partially debonded interface.* Composites Science and Technology, 1998. **58**: p. 1863-1877.
110. KARI, S., *Micromechanical Modelling and Numerical Homogenization of Fibre and Particle Reinforced Composites*, in *Institute of Mechanics Department.* 2005, Otto-von-Guericke University Magdeburg: Magdeburg.
111. SWAMINATHAN, S., N.J. PAGANO, and S. GHOSH, *Analysis of interfacial debonding in three-dimensional composite microstructures.* Journal of Engineering Materials and Technology, 2006. **128**: p. 96-106.
112. SCHEIDER, I., *Micromechanical based derivation of traction-separation laws for cohesive model simulations.* Procedia Engineering, 2009. **1**: p. 17-21.
113. SUN, C.T. and Z.-H. JIN, *Modeling of composite fracture using cohesive zone and bridging models.* Composites Science and Technology, 2006. **66**: p. 1297-1302.
114. JIN, H.Z. and C.T. SUN, *Cohesive fracture model based on necking.* International Journal of Fracture, 2005. **134**: p. 91-108.
115. JIN, H.Z. and C.T. SUN, *A cohesive zone modeling of interface fracture in elastic bi-materials.* Engineering Fracture Mechanics, 2005. **72**: p. 1805-17.

116. LIN, G., P.H. GEUBELLE, and N.R. SOTTOS, *Simulation of fiber debonding with friction in a model composite pushout test.* International Journal of Solids and Structures, 2001. **38**: p. 8547-8562.
117. GEUBELLE, P.H. and J. BAYLOR, *Impact-induced delamination of laminated composites: a 2D simulation.* Composites B, 1998. **29**: p. 589-602.
118. NEEDLEMAN, A., *A continuum model for void nucleation by inclusion debonding.* Journal of Applied Mechanics, 1987. **54**(3): p. 525-531.
119. NEEDLEMAN, A., *Numerical modelling of crack growth under dynamic loading conditions.* Computational Mechanics, 1997. **19**(6): p. 463-469.
120. LI, S., et al., *Use of a cohesive-zone model to analyze the fracture of a fiber reinforced polymer–matrix composite.* Composites Science and Technology, 2005. **65**: p. 537-49.
121. TVERGARRD, V. and J.W. HUTCHISON, *The relation between crack growth resistance and fracture process parameters in elastic-plastic solids.* Journal of Mechanics, Physics and Solids, 1992. **40**: p. 1377-1397.
122. NISHIKAWA, M., T. OKABE, and N. TAKEDA, *Determination of interface properties from experiments on the fragmentation process in single-fiber composites.* Materials Science and Engineering A, 2008. **480**: p. 549-557.
123. TURON, A., et al., *An Engineering Solution for solving Mesh Size Effects in the Simulation of Delamination with Cohesive Zone Models.* Engineering Fracture Mechanics, 2007. **74**: p. 1665-1682.
124. ZOU, Z., et al., *Modelling interlaminar and intralaminar damage in filament wound pipes under quasi-static indentation.* Journal of Composite Materials, 2002. **36**: p. 477-499.
125. CAMANHO, P.P., C.G. DAVILA, and M.F. De MOURA, *Numerical simulation of mixed- mode progressive delamination in composite materials.* Journal of Composite Materials, 2003. **37**(16): p. 1415-1438.
126. MEI, H., et al. *INITIATION AND PROPAGATION OF INTERFACIAL DELAMINATION IN INTEGRATED THIN-FILM STRUCTURES.* 2010 [cited 2012 3rd Feb]; Available from: http://imechanica.org/files/ITherm2010.pdf.
127. BEHZADI, S. and F.R. JONES, *The effect of temperature on stress transfer between a broken fibre and the adjacent fibres in unidirectional fibre composites.* Composites Science and Technology, 2008. **68**: p. 2690-2696.
128. MARSTON, C., et al., *Failure characteristics in carbon/epoxy composite tows.* Composites Part A, 1996. **27A**: p. 1183-1194.
129. van der HEUVEL, P.V.J., et al., *Failure phenomena in two-dimensional multi-fibre model composites: 5. A finite element study.* Composites Part A, 1998. **29A**: p. 1121-1135.
130. NEDELE, M.R. and M.R. WISNOM, *Stress concentration factors around a broken fibre in a unidirectional carbon fibre-reinforced epoxy.* Composites Part A, 1994. **25**(7): p. 549-557.
131. NEDELE, M.R. and M.R. WISNOM, *Three-dimensional finite element analysis of the stress concentration at a single fibre break.* Composites Science and Technology, 1994. **51**(4): p. 517-524.

132. HEDGEPATH, J.M. and P. van DYKE, *Local stress concentrations in imperfect filamentary composite materials.* Journal of Composite Materials, 1967. **1**(3): p. 294-309.
133. FIELDER, B., A. KILSCH, and K. SCHULTE, *Stress concentrations in multiple fibre model composites.* Composites: Part A, 1998. **29A**: p. 1013-1019.
134. OCHIAI, S. and M. HOJO, *Stress disturbances arising from cut fibre and matrix in unidirectional metal matrix composites calculated by means of a modified shear lag analysis.* Journal of Materials Science, 1996. **31**(14): p. 3861-3869.
135. BEHZADI, S., P.T. CURTIS, and F.R. JONES, *Improving the prediction of tensile failure in unidirectional fibre composites by inducing matrix shear yielding.* Composites Science and Technology, 2009. **69**: p. 2421-2427.
136. van der HEUVEL, P.V.J., T. PEIJS, and R.J. YOUNG, *FAILURE PHENOMENA IN TWO-DIMENSIONAL MULTI-FIBRE MICROCOMPOSITES: 2. A RAMAN SPECTROSCOPIC STUDY OF THE INFLUENCE OF INTER-FIBRE SPACING ON STRESS CONCENTRATIONS.* Composites Science and Technology, 1997. **57**: p. 899-911.
137. van der HEUVEL, P.V.J., T. PEIJS, and R.J. YOUNG, *Failure phenomena in two-dimensional multi-fibre microcomposites—3. A raman spectroscopy study of the influence of interfacial debonding on stress concentrations.* Composites Science and Technology, 1998. **58**(6): p. 933-944.
138. van der HEUVEL, P.V.J., et al., *Failure phenomena in fibre-reinforced composites. Part 6: a finite element study of stress concentrations in unidirectional carbon fibre-reinforced epoxy composites.* Composites Science and Technology, 2004. **64**: p. 645-656.
139. MEHAN, M.L. and L.S. SCHADLER, *Micromechanical behavior of short-fibre polymer composites.* Composites Science and Technology, 2000. **60**: p. 1013-1026.
140. ZHAO, L.G., N.A. WARRIOR, and A.C. LONG, *A micromechanical study of residual stress and its effect on transverse failure in polymer-matrix composites.* International Journal of Solids and Structures, 2005. **43**: p. 5449-5467.
141. ZHAO, L.G., N.A. WARRIOR, and A.C. LONG, *A thermo-viscoelastic analysis of process-induced residual stress in fibre-reinforced polymer–matrix composites.* Materials Science and Engineering A, 2007. **452-453**: p. 483-498.
142. SIRIVEDIN, S., et al., *Effects of inter-fibre spacing and matrix cracks on stress amplification factors in carbon-fibre/epoxy matrix, composites, Part II: Hexagonal array of fibres.* Composites Part A, 2006. **37**: p. 1936-1943.
143. MALIGNO, A.R., N.A. WARRIOR, and A.C. LONG, *Effects of interphase properties in unidirectional fibre reinforced composites.* Composites Science and Technology, 2009. **In Press**.
144. L. MISHNAEVSKY JR. and P. BRONDSTED, *Micromechanisms of damage in unidirectional fibre reinforced composites: 3D Computational analysis.* Composites Science and Technology, 2009. **69**: p. 1036-1044.

145. DOMNANOVICH, A., H. PETERLIK, and K. KROMP, *Determination of interface parameters for carbon/carbon composites by the fibre-bundle pull-out test.* Composites Science and Technology, 1996. **56**: p. 1017-1029.
146. McConnell, V. *The making of carbon fiber.* 2009 8th October 2010]; Available from: http://www.compositesworld.com/articles/the-making-of-carbon-fiber.
147. JACOBS, E. and I. VERPOEST, *Finite element modelling of damage development during longitudinal tensile loading of coated fibre composites.* Composites Part A, 1998. **29A**: p. 1007-1012.
148. HILL, R., *Elastic properties of reinforced solids: some theoretical principles.* Journal of the Mechanics and Physics of Solids, 1963. **11**: p. 357.
149. WONGSTO, A. and S. Li, *Micromechanical FE analysis of UD fibre-reinforced composites with fibres distributed at random over the transverse cross-section.* Composites: Part A, 2005. **36**: p. 1246-1266.
150. LI, S., *On the unit cell for micromechanical analysis of fibre-reinforced composites.* Mathematical, Physical and Engineering Sciences, 1999. **455**: p. 815-838.
151. LI, S., *General unit cells for micromechanical analyses of unidirectional composites.* Composites: Part A, 2001. **32**: p. 815-826.
152. LI, S., *Boundary conditions for unit cells from periodic microstructures and their implications.* Composites Science and Technology, 2008. **68**: p. 1962-1974.
153. MULLIGAN, D.R., et al., *Fibre-bundling in a short-fibre composite: 1. Review of literature and development of a method for controlling the degree of bundling.* Composites Science and Technology, 2003. **63**: p. 715-725.
154. MULLIGAN, D.R., et al. *The effect of fibre-bundling on the mechanical properties of a short-fibre composite.* in *ICCM-11.* 1997. Australia.
155. MEI, T. and M.R. PIGGOT, *Mesostructure development during molding of sheet molding compounds.* Polymer Composites, 1996. **17**(4): p. 548-555.
156. WORRALL, C.M. and G.M. WELLS. *Fibre distribution in discontinuous fibre reinforced plastics: Characterisation and effect on material performance.* in *ECCM 7.* 1996. London.
157. PIGGOTT, M.R., *Mesostructures and their mechanics in fibre composites.* Advanced Composite Materials, 1996. **6**: p. 75-81.
158. YURGARTIS, S.W., *Techniques for the quantification of composite mesostructures.* Composites Science and Technology, 1995. **53**: p. 145-154.
159. LUCHOO, R., et al. *MACRO-SCALE MODELLING OF DISCONTINUOUS FIBRE COMPOSITES.* in *ICCM 18.* 2011. Jeju Island, S. Korea.
160. HARPER, L.T., T.A. TURNER, and N.A. WARRIOR. *A random fibre network model for predicting the stochastic effects of discontinuous fibre composites.* in *16th International Conference of Composite Materials.* 2007. Kyoto, Japan.
161. COLEMAN, B.D., *On the strength of classical fibers and fiber bundles.* Journal of Mechanics and Physics of Solids, 1958. **7**: p. 60-70.

162. BADER, M.G. and A.M. PRIEST. *Statistical aspects of fibre and bundle strength in hybrid composites.* in *4th International Conference on Composite Materials (ICCM-IV).* 1982. Tokyo, Japan.
163. GOMMER, F., A. ENDRUWEIT, and A.C. LONG. *Stochastic description of fibre reinforced composites* in *ICMAC 2011: International Conference on Manufacturing of Advanced Composites.* 2011. Belfast, N. Ireland.
164. YANG, Q.S. and Q.H. QIN, *Fiber interactions and effective elasto-plastic properties of short-fiber composites.* Composites Structures, 2001. **54**: p. 523-528.
165. TOLL, S., *Packing mechanics of fiber reinforcements.* Polymer Engineering and Science, 1998. **38**(8): p. 1337-1350.
166. LUCHOO, R., et al., *Three dimensional numerical modelling of discontinuous fibre composites for high performance applications.* Plastics, Rubbers and Composites, 2010. **IN PRESS.**
167. ERICSON, M.L. and L.A. BERGLUND, *The effect of microstructure on the elastic modulus and strength of preformed and commercial GMTs.* Polymer Composites, 1993. **14**(1): p. 35-41.
168. HARPER, L.T., et al. *AUTOMATED CHARGE PLACEMENT FOR STRUCTURAL MOLDING COMPOUNDS.* in *SAMPE Seattle.* 2010. WA, Washington State Convention Center.
169. HARPER, L.T., et al., *Characterisation of random carbon fibre composites from a directed fibre preforming process: The effect of tow filamentisation.* Composites: Part A: Applied Science and Manufacturing, 2007. **38**(3): p. 755-770.
170. CARLEY, E.P., J.F. DOCKUM, and P.L. SCHELL. *Preforming for Liquid Composite Molding.* in *Polymer Composites for Structural Automotive Applications.* 1990. Detroit, Michigan.
171. HARPER, L.T., et al., *Characterisation of random carbon fibre composites from a directed fibre preforming process: Effect of fibre length.* Composites Part A: Applied Science and Manufacturing, 2006. **37**(11): p. 1863-1878.
172. IORGA, L., Y. PAN, and A.A. PELEGRI, *Numerical characterisation of material elastic properties for random fiber composites.* Journal of Mechanics of Materials and Structures, 2008. **3**(7): p. 1279-1298.
173. HARPER, L.T., et al., *Representative Volume Elements for Discontinuous Carbon Fibre Composites. Part 1: Boundary Conditions.* Composites Science and Technology, 2011. **In Press, Corrected Proof.**
174. DUSCHLBAUER, D., H.J. BOHM, and H.E. PETTERMANN, *Computational simulation of composites reinforced by planar random fibers: Homogenization and localization by unit cell and mean field approaches.* Journal of Composite Materials, 2006. **40**(24): p. 2217-2234.
175. GUSEV, A.A., *Representative volume element size for elastic composites: A numerical study.* Journal of the Mechanics and Physics of Solids, 1997. **45**(9): p. 1449-1459.
176. EVANS, K.E. and M.D. FERRAR, *The packing of thick fibres.* Journal of Physics D: Applied Physics, 1989. **22**: p. 354-360.
177. DUMONT, P.J.J., et al., *A numerical analysis of the evolution of bundle orientation in concentrated fibre-bundle suspensions.* Journal of Non-Newtonian Fluid Mechanics, 2009. **160**: p. 76-92.

178. LE CORRE, S., et al., *Behavior of a net of fibers linked by viscous interactions: theory and mechanical properties.* Journal of Mechanics, Physics and Solids, 2004. **52**: p. 395-421.
179. LE CORRE, S., et al., *Rheology of highly concentrated fiber suspensions.* Journal of Rheology, 2005. **49**(5): p. 1029-1058.
180. EVANS, K.E. and A.G. GIBSON, *Prediction of the maximum packing fraction achievable in randomly.* Composites Science and Technology, 1986. **25**: p. 149-162.
181. BOHM, H.J., A. ECKSCHLAGER, and W. HAN, *Multi-inclusion unit cell models for metal matrix composites with randomly oriented discontinuous reinforcements.* Computational Materials Science, 2002. **25**(1-2): p. 42-53.
182. PAN, N., *Analytical characterization of the anisotropy and local heterogeneity of short fiber composites: Fiber fraction as a variable.* Journal of Composite Materials, 1994. **28**(16): p. 1500-1531.
183. GITMAN, I.M., H. ASKES, and L.J. SLUYS, *Representative volume: Existence and size determination.* Engineering Fracture Mechanics, 2007. **74**: p. 2518-2534.
184. HARPER, L.T., et al., *Representative volume elements for discontinuous carbon fibre composites. Part 1: Boundary conditions.* Composites Science and Technology, 2012. **72**(2): p. 225-234.
185. TRIAS, D., et al., *Determination of the critical size of a statistical representative volume element (srve) for carbon reinforced polymers.* Acta Materialia, 2006. **54**: p. 3471-3484.
186. TRIAS, D., et al., *Random models versus periodic models for fibre reinforced composites.* Computational Materials Science, 2006. **38**(2): p. 316-324.
187. MISHNAEVSKY, L.L., *Three-dimensional numerical testing of microstructures of particle reinforced composites.* Acta Materialia, 2004. **52**(14): p. 4177-4188.
188. NAKAMURA, S. and R.S. LAKES, *Finite element analysis of saint-venant end effects in micropolar elastic solids.* Engineering Computations, 1995. **12**(6): p. 571-587.
189. HARPER, L.T., et al., *Representative volume elements for discontinuous carbon fibre composites – Part 2: Determining the critical size.* Composites Science and Technology, 2012. **72**(2): p. 204-210.
190. TORAY CARBON FIBERS AMERICA, I. *T700S DATA SHEET.* 2010 4th June 2010]; Available from: http://www.toraycfa.com/pdfs/T700SDataSheet.pdf.
191. BEYERLEIN, I.J. and S.L. PHOENIX, *Statistics for the strength and size effects of microcomposites with four carbon fibers in epoxy resin.* Composites Science and Technology, 1996. **56**: p. 75-92.
192. PAN, N., et al., *Investigation on the strength-size relationship in fibrous structures including composites.* Journal of Materials Science, 1998. **33**: p. 2667-2672.
193. PAN, N., S. ZHAO, and T. HUA, *Relationship between scale effect and structure levels in fibrous structures.* Polymer Composites, 2000. **21**(2): p. 187-195.

194. SUTHERLAND, L.S., R.A. SHENOI, and S.M. LEWIS, *Size and scale effects in composites: I. Literature review.* Composites Science and Technology, 1999. **59**(2): p. 209-220.
195. ZWEBEN, C., *Is there a size effect in composites?* Composites, 1994. **25**(6): p. 451-453.
196. WEIBULL, W., *A statistical theory of strength of materials.* Ingeniorsvetenscapsakademien Handlingar, 1939. **151**: p. 1-29.
197. van Hattum, F.W.J. and C.A. Bernado, *A model to predict the strength of short fibre composites.* Polymer Composites, 1999. **20**(4): p. 524-533.
198. HWANG, T.-K., C.-S. HONG, and C.-C. KIM, *Size effect on the fiber strength of composite pressure vessels.* Composite Structures, 2003. **59**: p. 489-498.
199. BULLOCK, R.E., *Strength ratios of composite materials in flexure and in tension.* 1974: p. 200-205.
200. PARDINI, L.C. and L.G.B. MANHANI, *Influence of the Testing Gage Length on the Strength, Young's Modulus and Weibull Modulus of Carbon Fibres and Glass Fibres.* Materials Research, 2002. **5**(4).
201. ZWEBEN, C. and B.W. ROSEN, *A statistical theory of material strength with application to composite materials.* Journal of the Mechanics and Physics of Solids, 1970. **18**: p. 189-206.
202. *Glass fibre reinforced plastics. Tensile test*, in *British Standard.* BS EN 2747 - 1: 1998.
203. *Plastics. Determination of compressive properties*, in *British Standard.* BS EN ISO 604:1997.
204. *Standard test method for shear properties of composite materials by V-notched rail shear method*, in *The American Society for Testing and Materials.* D7078/D7078M - 05.
205. MatWeb. *Tensile Property Testing of Plastics.* 2012 31st Jan 2012]; Available from: http://www.matweb.com/reference/tensilestrength.aspx.
206. efunda.com. *Polymer Material Properties: Epoxy.* 2012 31st Jan 2012]; Available from: http://www.efunda.com/materials/polymers/properties/polymer_datasheet.cfm?MajorID=epoxy&MinorID=2.
207. *Standard Test Method for Shear Strength of Plastics by Punch Tool*, in *The American Society for Testing and Materials.* ASTM D732 - 10.
208. *FX-751 LV Hydro-Ester® Epoxy.* Fox Industries 2nd Feb 2012]; Available from: http://www.fox-ind.com/products/low_viscosity_epoxy/fx751_LV_hydro_ester_epoxy.
209. *Sikadur® 22, Lo-Mod.* Sika Construction 2nd Feb 2012]; Available from: http://www.ktc.uky.edu/kytc/kypel/downloadAttachment.php?fileIndex=1039.
210. LIDGETT, M., et al., *Virtual modelling of microscopic damage in polymer composite materials at high rates of strain.* Plastics, Rubbers and Composites, 2011. **40**(Numbers 6-7): p. 324-332.
211. SPROULL, B. and W.M. NEWMAN, *Principles of interactive computer graphics. International Edition ed. 1973.* McGraw-Hill: p. 124 and 252.
212. BOURKE, P. *Intersection point of two lines (2 dimensions).* 1989 20th Jan 2012]; Available from: http://paulbourke.net/geometry/lineline2d/.

213. LEGRAND, S., V. LEGAT, and E. DELEERSNIJDER, *Delaunay mesh generation for an unstructured-grid ocean general circulation model.* Ocean Modelling 2, 2000: p. 17-28.
214. SECCHI, S. and L. SIMONI, *An improved procedure for 2D unstructured Delaunay mesh generation.* Advances in Engineering Software, 2003. **34**: p. 217-234.
215. YU, B., M.J. LIN, and W.Q. TAO, *Automatic generation of unstructured grids with Delaunay triangulation and its application.* Heat and Mass Transfer, 1999. **35**: p. 361-370.
216. MathWorks. *Delaunay Triangulation.* 1984-2012 7th April 2011]; Available from: http://www.mathworks.co.uk/help/techdoc/math/bspqjle-1.html.
217. WEISSTEIN, E.W. *Delaunay Triangulation.* 7th April 2011]; Available from: http://mathworld.wolfram.com/DelaunayTriangulation.html.
218. PETERSON, S. *Computing Constrained Delaunay Triangulations.* 2011 7th April 2011]; Available from: http://www.geom.uiuc.edu/~samuelp/del_project.html.
219. CHEW, L.P., *Guaranteed-quality mesh generation for curved surfaces.* Proceedings of the Ninth Annual Symposium on Computational Geometry, 1993: p. pp 274-280.
220. RUPPERT, J., *A Delaunay refinement algorithm for quality 2-dimensional mesh generation.* Journal of Algorithms, 1995. **18**(3): p. 548-585.
221. PADRON, M.A., J.P. SUAREZ, and A. PLAZA, *Refinement based on the longest-edge and self-similar four-triangle partitions.* Mathematics and Computers in Simulation, 2007. **75**: p. 251-262.
222. GERLACH, R., et al., *The interface between matrix pockets and fibre bundles under impact loading.* Composites Science and Technology, 2009. **69**: p. 2024-2026.
223. MICHAELI, W. and K. KOCKER, *Fibre Bundle Pull-Out Test for Thermoplastic Matrix Materials*, in *Proceedings of ICCM-10.* 1995: Whistler, B.C., Canada.
224. SCHUBEL, P.J., N.A. WARRIOR, and C.D. RUDD, *Surface Roughness Modelling of Textile Composites using TexGen*, in *8th International Conference on Textile Composites (TEXCOMP-8).* 2006: Nottingham, UK.
225. NIELSEN, L.E. and P.E. CHEN, *Young's modulus of composites filled with randomly oriented fibers.* Journal of Materials, 1968. **3**(2): p. 352-358.
226. KRENCHEL, H., *Fibre Reinforcement.* Copenhagen: Akademisk Forlag, 1964.